School of Electrical Engineering, Computing, and Mathematical Sciences
Curtin Institute of Radio Astronomy

Three-Dimensional Tomography of Pulsar Magnetospheres

Samuel James McSweeney

This thesis is presented for the Degree of
Doctor of Philosophy
of
Curtin University

5 September 2019

To the best of my knowledge and belief this thesis contains no material previously published by any other person except where due acknowledgement has been made. This thesis contains no material which has been accepted for the award of any other degree or diploma in any university.

Samuel James McSweeney

5 September 2019

"Like every scientist, she appreciated that to make her mark, what she needed to do was find a hard problem and solve it."

— Margaret Heffernan

Acknowledgements

I would like to thank, first and foremost, Dr. Ramesh Bhat, for the three and a half years it has been my pleasure to count him as both my supervisor and my friend, for giving me the latitude to explore new ideas, and for his encouragement and support. The help, support, and advice of my other supervisors, Dr. Avinash Deshpande and Dr. Steven Tremblay, have been invaluable, and helped me to maintain intellectual integrity and rigour, producing the best quality work of which I am capable. The chance meeting of Dr. Geoff Wright during the "Pulsar Astrophysics" conference in 2017 led to the most fruitful and rewarding collaboration I have yet had the privilege of enjoying, and I hope this collaboration may continue for many years ahead. I also thank Dr. Stephen Ord and Dr. Jean-Pierre Macquart for their instruction and guidance during the undergraduate and Honours years, whose clear thinking and keen insight have been inspirational. Finally, I want to express appreciation for the whole Pulsar and Transients research team at CIRA, who have made the whole journey fun and worthwhile.

Outside of academia, the people in my life who have contributed both directly and indirectly to this effort are too many to list. My parents and siblings have always been supportive, no matter what direction my career thus far has taken—I hope this achievement makes you proud. Above all, my thanks and love go to my partner and the love of my life, Gary Namestnik, who has been by my side throughout my PhD, lifting, supporting, inspiring, and reminding me constantly of the joys of life. The last year, in particular, has been amazing, and I've loved every minute of it, despite the stresses of trying to finish a PhD, simply because you've been there, Gary. I dedicate this thesis to you, with all my heart.

Abstract

Pulsars are nature's premier laboratories for high-energy physics. They were discovered in the late 1960's via the detection of bright, strongly pulsed radio emission, caused by the intersection of the line of sight with highly collimated beams of radiation, rotating with the central neutron star. Since that time, the mechanism by which the radio emission beams are produced has remained one of the most tantalising mysteries in astrophysics.

This thesis attempts to shed light on the emission physics by following a program of mapping out the quasi-stable subbeams (i.e. discrete components of the total emission beam) that are hypothesised to give rise to the phenomenon of subpulse drifting. If the subbeams are arranged in a circular pattern about the magnetic axis, and rotate steadily around it, as conjectured by the carousel model (Ruderman and Sutherland, 1975), then the mapping can be achieved by means of the Cartographic Transform (Deshpande and Rankin, 2001).

The application of the Cartographic Transform to obtain the average polar pattern of the carousel depends on steady, uninterrupted rotation of the subbeam carousel. However, in practice, in some pulsars, the pattern of subpulse drifting is quite irregular, thereby presenting a natural challenge to the assumptions underlying the carousel model. This thesis focuses on one such pulsar, PSR B0031−07, whose drifting pattern is shown to exhibit both sudden changes (due to multiple drift modes and nulling) and gradual changes (accelerations of the drift rate). The characterisation of the gradual changes reveals that, unlike other pulsars showing similar behaviour, the acceleration period is not confined to the period of time following a null sequence, but is ubiquitous, occurring throughout the entire duration of the drift sequences.

B0031−07's subpulses are also shown to appear at slightly different rotation phases when viewed at different frequencies, a feature that cannot be straightforwardly explained with the carousel model alone. In general, asymmetric phase shifts of integrated pulse profile features can be explained by the well-established

effects of aberration and retardation (AR), two relativistic effects which are related to the height of the emission regions above the pulsar's surface. In this thesis, AR effects are applied to the carousel model for the first time in order to determine whether they can be responsible for the subpulse phase shifts observed in B0031−07 and other pulsars. The analysis is explored both analytically and numerically, the latter being developed into an open source software suite, PSRGEOM, which can simulate pulsar data from given carousel parameters, and can be applied to the study of any pulsar exhibiting subpulse drifting.

A carousel configuration is inferred for B0031−07, which explains how its different drift modes can appear to have different drift rates while maintaining a single carousel rotation rate, namely, by changing the number of sparks in the carousel. This is a major advance in our understanding of this pulsar, which can now have its carousel rotation rate measured and compared with the predictions of the carousel model. They are found to agree to first order, but it is understood that both the measurement of the carousel rotation rate and the theoretical model must be refined before such measurements can be used to discriminate between alternative models.

The challenges of understanding B0031−07's complex drifting dynamics are not unique to this pulsar, and the analyses undertaken here may be applied to other, similar pulsars. Characterising B0031−07's unusual drifting behaviour has brought the goal of mapping out its emission regions within reach. Future observations of this and other pulsars with current- and next-generation telescopes, especially those with large frequency coverage and high time resolution, promise to resolve several outstanding mysteries for how and why the drifting behaviour of so many pulsars appears to depart from that which is predicted by the carousel model. In this way, the radio pulsar emission mechanism is slowly, but surely, revealing its secrets.

Statement of originality

The content of Chapters 3-5 is my own work, with the following qualifications. In Chapter 3, the MWA-VCS observations were scheduled and undertaken by Dr Steven Tremblay, and processed with the beamformer software by myself under the supervision of Dr Ramesh Bhat, Dr Steven Tremblay, and Dr Stephen Ord. Further analysis of the data (including the development of bespoke software) was undertaken by myself, under close supervision of, and with many suggestions from, Dr Ramesh Bhat, Dr Steven Tremblay, and Dr Avinash Deshpande. In Chapter 4, I wrote the numerical code that underpins this paper (PSRGEOM). Error (and sanity) checking the PSRGEOM code was achieved through multiple discussions with all the co-authors. Dr Ramesh Bhat and Dr Avinash Deshpande guided the discussion relating the simulations to real data, and Dr Avinash Deshpande provided the SPULSES software that was used to make cartographic maps of the simulated beam. Dr Geoff Wright provided derivations of results relating to AR effects that made possible the connection between our results and previous works on AR effects. In Chapter 5, the MWA and GMRT observations were planned by myself, Dr Ramesh Bhat, and Dr Steven Tremblay. Dr Steven Tremblay scheduled and executed the MWA-VCS observations; Dr Ramesh Bhat and Dr Sanjay Kudale coordinated and executed the GMRT observations. The idea to argue for a first-order-aliasing solution came originally from Dr Geoff Wright, and I undertook the subsequent analysis of the data under the supervision of Dr Ramesh Bhat, Dr Avinash Deshpande, and Dr Geoff Wright. These three also provided many suggestions and insight into the theory relating AR effects to subpulse phase shifts, which I originally derived, and the discussion thereof.

(Signature of Candidate)

(Signature of Supervisor)

Contents

List of Figures

Chapter 1

Background and Introduction

1.1 Overview and Aims

Pulsars are rapidly-rotating compact neutron stars with typical masses of $1.4\,M_{\odot}$ and rotation periods ranging from a few milliseconds to over 20 seconds (Tan et al., 2018). In the vicinity of the star, gravitational and magnetic fields are extremely strong, making them unique environments for studying physical regimes that can't be replicated in Earth-based laboratories. Neutron stars were first predicted by Baade and Zwicky (1934), and confirmed more than 30 years later when newly discovered pulsed radio sources were positively identified as rotating neutron stars (Hewish et al., 1968; Gold, 1968).

It was long assumed that these objects would only be detectable by indirect means (Zwicky, 1939)—their direct detection by means of pulsed radio waves came as a complete surprise. Moreover, the radio emission is so intrinsically bright that it was quickly realised that the radio emission mechanism, whatever it is, must be a coherent process and that the emission must be strongly beamed owing to the fact that the observed signal is strongly pulsed. Work immediately began in the late 1960's to model the emission process; even though steady progress was made over the succeeding decades, understanding the physics that governs the radio emission remains one of the most important open problems in astrophysics.

The primary reason for the difficulty of the problem is evidently the complexity of the pulsars themselves as well as their detected signals which vary on a huge range of timescales and frequencies, with no two pulsars behaving the same way. Although some of this behaviour is attributable to propagation effects through the interstellar medium (ISM) along the line of sight, it is clear that much of the variation is intrinsic to the pulsar itself. In particular, the radio emission is thought to originate in the pulsar's magnetosphere—the dynamic plasma that surrounds the central star—at some altitude, or range of altitudes, above the stellar surface. The necessary existence of the magnetosphere was deduced within only a couple of years of the pulsars' discovery (Goldreich and Julian, 1969), and all leading models of pulsar emission are predicated on the assumption that it is the magnetospheric particles travelling at relativistic speeds that produce the observed radio emission. Thus, understanding the emission mechanism is tantamount to understanding the behaviour of relativistic plasma in the ultra-strong gravity and magnetic field regimes.

Observing the structure of magnetospheres on short time and spatial scales is the most direct way to study the behaviour of relativistic plasma. Unfortunately, neutron star magnetospheres have minuscule angular diameters when viewed from Earth ($\lesssim 1\,\mu$as), putting them well beyond the ability of even the best telescope systems to image them directly at typical pulsar frequencies[1]. On the other hand, the fact that the pulsar is rotating means that an Earth-bound observer samples a different part of the emission beam as a function of the pulsar's rotation phase. Thus, although direct imaging magnetospheres is impossible, one can make inferences about their three-dimensional structure and dynamics from their "one-dimensional" signals, i.e. their time series.

In this chapter, pulsar signals are introduced from a purely observational perspective, that is to say, without reference to the physical models that give rise to

[1] At higher radio frequencies, the Event Horizon Telescope has achieved $\sim 35\,\mu$as resolution using a global Very Long Baseline Interferometer (VLBI) network (Event Horizon Telescope Collaboration et al., 2019)

them. The raw signals as they appear at the telescope are described in Section §1.2, as well as some basic transformations that allow us to view the signals in more intuitive ways. The received signal is necessarily a distorted version of the intrinsic pulsar signal, since it has passed through the cold plasma of the ISM, the Earth's ionosphere, and the telescope itself, before being recorded and analysed. Section §1.2.5 outlines the theory describing these distortions as well as the available techniques for mitigating or removing them to recover the intrinsic signal. Next, Section §1.3 showcases the sheer variety of pulsar signals. One class of signal is given particular emphasis: those that exhibit the phenomenon of **subpulse drifting**, which is where the rotation phases of subpulses (the discrete bursts of emission observed from pulse to pulse) drift gradually over time. Subpulse drifting is described in detail in Section §1.3.6.

The central theme of this thesis is subpulse drifting and its interpretation by one of the most popular models that attempts to explain them, the **carousel model**, originally proposed by Ruderman and Sutherland (1975). The carousel model holds that there are quasi-stable, discrete structures that exist very close to the stellar surface and that the observed modulation of subpulses is the signature of the structures' regular, periodic motion around the pulsar's magnetic axis. Despite its popularity, the carousel model is somewhat controversial. This is partly because it implicitly relies on a specific emission mechanism—coherent curvature radiation—which, from a plasma physics point of view, is argued to be untenable (see, e.g. Melrose, 2017), and partly because there are a number of more complex pulsar behaviours which, in its simplest form, it cannot easily explain (e.g. Edwards, 2006). Although alternative models exist (e.g. the non-radial oscillation model of Rosen et al., 2011), only the carousel model is investigated in this thesis.

The description of the carousel model starts with the physical objects themselves—neutron stars and their immediate environments—which is given in Section §1.4. The physical assumptions of the carousel model are stated explicitly, drawing at-

tention to the main differences between this model and alternative emission mechanisms. Finally, the cartographic transform of Deshpande and Rankin (2001) is introduced in Section §1.5.3.1. This is a transformation from the time coordinate of the pulsar signal to two-dimensional spatial coordinates of the emission beam, centred on the magnetic axis.

Every pulsar is observationally unique, and studies of the emission mechanism can either focus on explaining the peculiarities of individual pulsars, or making a comparative study of a large sample of pulsars. This thesis takes the former approach, with the primary object under investigation being PSR B0031−07. This pulsar was chosen because its single pulses exhibit many interesting behaviours that are associated with subpulse drifting and, hence, the carousel model. Specifically, three aspects of subpulse drifting (both in B0031−07 and in a few other pulsars) are investigated in detail:

1. Observational evidence that the carousel rotation speeds up, or slows down, on relatively short time scales (the model predicts a constant rotation rate),

2. The carousel rotation rate itself (which is difficult to measure, but often found to be slower than the model predicts), and

3. The subpulse drifting behaviour changing as a function of observing frequency (the model itself predicts no frequency dependence whatsoever).

The difficulty in either proving or disproving the carousel model itself is that one can almost always extend the model to incorporate one or more of the above phenomena. Some such extensions are specifically tailored to explain the observed behaviour in terms of the carousel model, while others enjoy wider observational support and are therefore more established. The question posed here is twofold: (1) Can pulsars like B0031−07 be understood in terms of the carousel model without stretching the model too far to accommodate their observed peculiarities? and (2) Is there a way to test the carousel model definitively? The answers to

these questions require both careful modelling of the observed pulsar behaviour and the subtle predictions of the carousel model and its extensions.

1.2 Properties of observed pulsar signals

1.2.1 Raw signals

A telescope trained on a pulsar signal is able to record the incoming flux only over a limited range of frequencies and at some time resolution, determined by the available hardware and software comprising the complete telescope system. The signal can thus be described as intensity as a function of time and frequency, $\tilde{I}(\tilde{t}, \tilde{\nu})$, where the tilde signifies the quantities measured by the telescope. As $\tilde{I}$ is both a function of time and frequency, we refer to it as a *dynamic spectrum*. In the event that the telescope is equipped with the means of sampling linearly independent polarisations, full polarimetric information of the signal can be obtained, yielding the full-Stokes parametrisation:

$$\begin{gathered} \tilde{I}(\tilde{t}, \tilde{\nu}), \quad \tilde{Q}(\tilde{t}, \tilde{\nu}), \quad \tilde{U}(\tilde{t}, \tilde{\nu}), \quad \tilde{V}(\tilde{t}, \tilde{\nu}), \\ \tilde{Q}^2 + \tilde{U}^2 + \tilde{V}^2 \leq \tilde{I}^2 \end{gathered} \tag{1.1}$$

The received signal is composite—it contains information about both the intrinsic pulsar emission and any distortions introduced en route to the observer, including distortions and noise introduced by the electronic subsystems of the telescope. Since the primary goal of this thesis is to study the intrinsic emission, both kinds of distortion are a hindrance. Fortunately, many of the most significant distortions can be accounted for and "undone", in the sense that the measured signals $\tilde{I}(\tilde{t}, \tilde{\nu})$, etc., can be transformed into an "undistorted" signal that approximates the intrinsic signal.

$$I(t, \nu) \leftarrow \tilde{I}(\tilde{t}, \tilde{\nu}), \text{ etc.} \tag{1.2}$$

The causes of these distortions—and the methods used to either rectify or mitigate them—are varied, and are discussed in Section §1.2.5. In the meantime, the reader may assume that the data presented in the following sections have already been transformed according to Eqn. (1.2), and represent the closest possible approximations to the intrinsic signal.

1.2.2 Pulsar time series

The characteristic feature of observed pulsar signals is the fact that they appear temporally pulsed, and, moreover, that the period of the pulses is on average extremely regular. Very often, the signal-to-noise of an individual frequency channel is too low to observe individual pulses—it can be boosted by summing the available frequency channels together. In this way, we produce the time series:

$$I_{\rm ts}(t) = \sum_{i=1}^{N} I(t, \nu_i), \tag{1.3}$$

where ν_i is the ith frequency channel (out of N); similarly for the other polarisations. This procedure, called *frequency scrunching*, naturally obliterates any information about frequency-dependent structure in the signal, trading it in for increased signal-to-noise. In the most optimistic case (no frequency structure across the observing band), frequency scrunching boosts the signal-to-noise by a factor of $\sqrt{N}$.

Fig 1.1 shows a portion of the frequency-scrunched time series of the pulsar B0950+08. The pulses have period[2] of $P_1 \approx 0.253\,\mathrm{s}$, with the pulses themselves being $\lesssim 10\,\mathrm{ms}$ wide.

[2]The subscript "1" in P_1 serves to distinguish the pulse period, associated with the pulsar's rotation, with other periods associated with the subpulse drifting phenomenon, introduced in later sections.

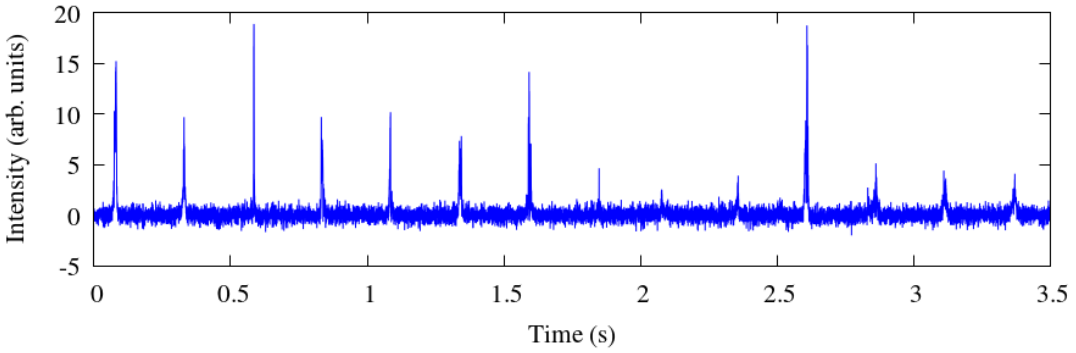

Figure 1.1 A sequence of 14 consecutive pulses of B0950+08 recorded using the Murchison Widefield Array. The original 3072 frequency channels (spanning 170-200 MHz) have been scrunched to produce this time series. Even in this short example, it is apparent that the individual pulses vary by more than the noise.

1.2.3 Pulse stacks

It will be argued later more rigorously (§1.4.1) that the periodicity of the pulses is due to the rotation of the neutron star, with the average elapsed time between pulses, P_1, being identified with the rotation period of the neutron star. Hence, it is of theoretical interest to view the data as a function of rotation phase rather than a function of time. One can do this by transforming the time series into a two-dimensional image via

$$\begin{gathered} I_{\mathrm{ps}}(p,\varphi) \leftarrow I_{\mathrm{ts}}(t), \\ p \leftarrow \left\lfloor \frac{t}{P_1} \right\rfloor, \qquad \varphi \leftarrow 2\pi\left(\frac{t}{P_1} - p\right), \end{gathered} \tag{1.4}$$

where $p \in \mathbb{Z}$ is the pulse number and $0 \leq \varphi < 2\pi$ is the rotation phase in radians. Actually, the transform given above is only a first-order approximation that assumes a constant period. With a long enough time series, it is possible to measure the first-order perturbation of the period, i.e. its first time derivative

$$\dot{P}_1 \equiv \frac{\mathrm{d}P_1}{\mathrm{d}t} \tag{1.5}$$

Where such a measurement is possible, all pulsars are shown to have non-zero values of $\dot{P}_1$, and the vast majority have $\dot{P}_1 > 0$—i.e. the rotation is slowing down (Fig. 1.2).

Where observations span a long enough time (years, decades), a variation in $\dot{P}_1$ can been measured, yielding approximate values of the next highest order derivative, $\ddot{P}_1$ (e.g. Hobbs et al., 2004). Moreover, some pulsars *glitch*, the term used to describe a sudden and dramatic change in P_1 that is thought to be caused by a sudden reconfiguration of the neutron star's internal structure (Baym et al., 1969; Espinoza et al., 2011)[3]. The historical measurements of the period and its derivatives are summarised in publicly available pulsar ephemerides[4] (Manchester et al., 2005), which can then be used to calculate the correct form of the transform (1.4).

Conveniently, the algorithms for transforming a raw time series into one as a linear function of rotation phase have been implemented in the open source software packages TEMPO and TEMPO2 (Hobbs et al., 2006). TEMPO2, which is used in this thesis, also includes a host of other algorithms designed to counter other timing distortions that are discussed more fully in Section §1.2.5. A full description of these algorithms can be found in Edwards et al. (2006), and references therein.

The duration of pulsar observations presented in this thesis (∼hours) is short relative to the time scale over which the non-zero $\dot{P}_1$ would cause significant departure from a model that assumes $\dot{P}_1 = 0$ (∼months). Thus, Eqn. (1.4) can be considered a convenient, simple, and still very accurate approximation for our purposes. In practice, however, all the data were processed using TEMPO2 using the most up-to-date ephemerides available.

The result of Eqn. (1.4) is a two-dimensional image called a *pulse stack* (see Fig. 1.3), with pulse numbers running up the vertical axis, the rotation phase along the horizontal axis, and the colour scale representing the intensity, I. For

[3] `http://www.jb.man.ac.uk/pulsar/glitches.html`
[4] `http://www.atnf.csiro.au/research/pulsar/psrcat`

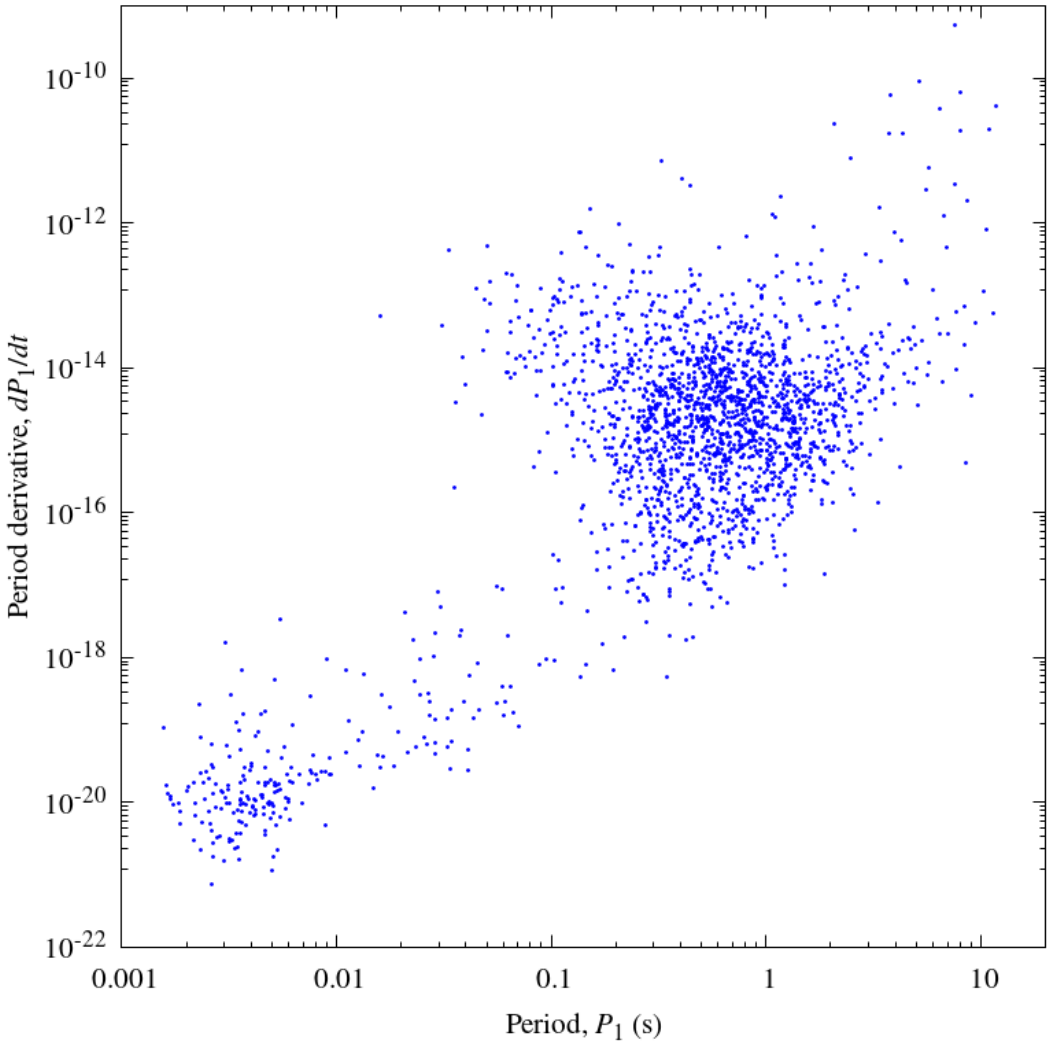

Figure 1.2 A plot of pulsar periods, P_1, against period derivatives, $\dot{P}_1$. The lower left population are the so-called *millisecond pulsars* (MSPs). The data are from the ATNF Pulsar Catalogue (Manchester et al., 2005), catalogue version 1.60.

convenience, the pulse itself is usually centred in the pulse stack and the phase allowed to run from $-\pi$ to π (or, equivalently, from -180° to 180°), rather than from 0 to 2π.

1.2.4 Pulsar profiles

Pulse-to-pulse variation is a feature of all pulsars which speaks to the dynamic nature of the emission process. Nevertheless, even a cursory inspection of pulse stacks of different pulsars reveals that they can have vastly different *average* properties. A pulsar's *integrated pulse profile* (also sometimes called its *average profile*, or more succinctly, its *profile*) is the curve that results from averaging the intensity at each rotation phase:

$$I_{\rm pr}(\varphi) = \frac{1}{N}\sum_{k=1}^{N} I_{\rm ps}(p_k, \varphi), \tag{1.6}$$

where N is the number of pulses taken in the average. The process of applying Eqn. (1.6) is called *folding*. As in the case of frequency scrunching (Eqn. (1.3)), forming a profile increases the signal-to-noise by up to a factor of $\sqrt{N}$; however, this process obliterates information about pulse-to-pulse variation.

Because the phase is assumed to be associated with the neutron star's rotation, the shape of a pulsar's profile contains information about the geometry of the emission regions in the vicinity of the pulsar. The variety of profile shapes is astounding, considering the small number of parameters needed to describe the Earth-pulsar geometry. Profiles of individual pulsars can also change as a function of both time (Section §1.3.6.6) and observing frequency (see Section §1.3.5).

Once a profile has been formed, one can readily identify the range of rotation phases that show emission, termed the *pulse window*. Two standard profile width measurements are w_{50}, measured at 50% of the peak height, and w_{10}, measured at 10% of the peak height. From either of these, one can estimate the duty cycle, $\delta = w_{50}/P_1$ or $\delta = w_{10}/P_1$. The approximate signal-to-noise ratio can be found

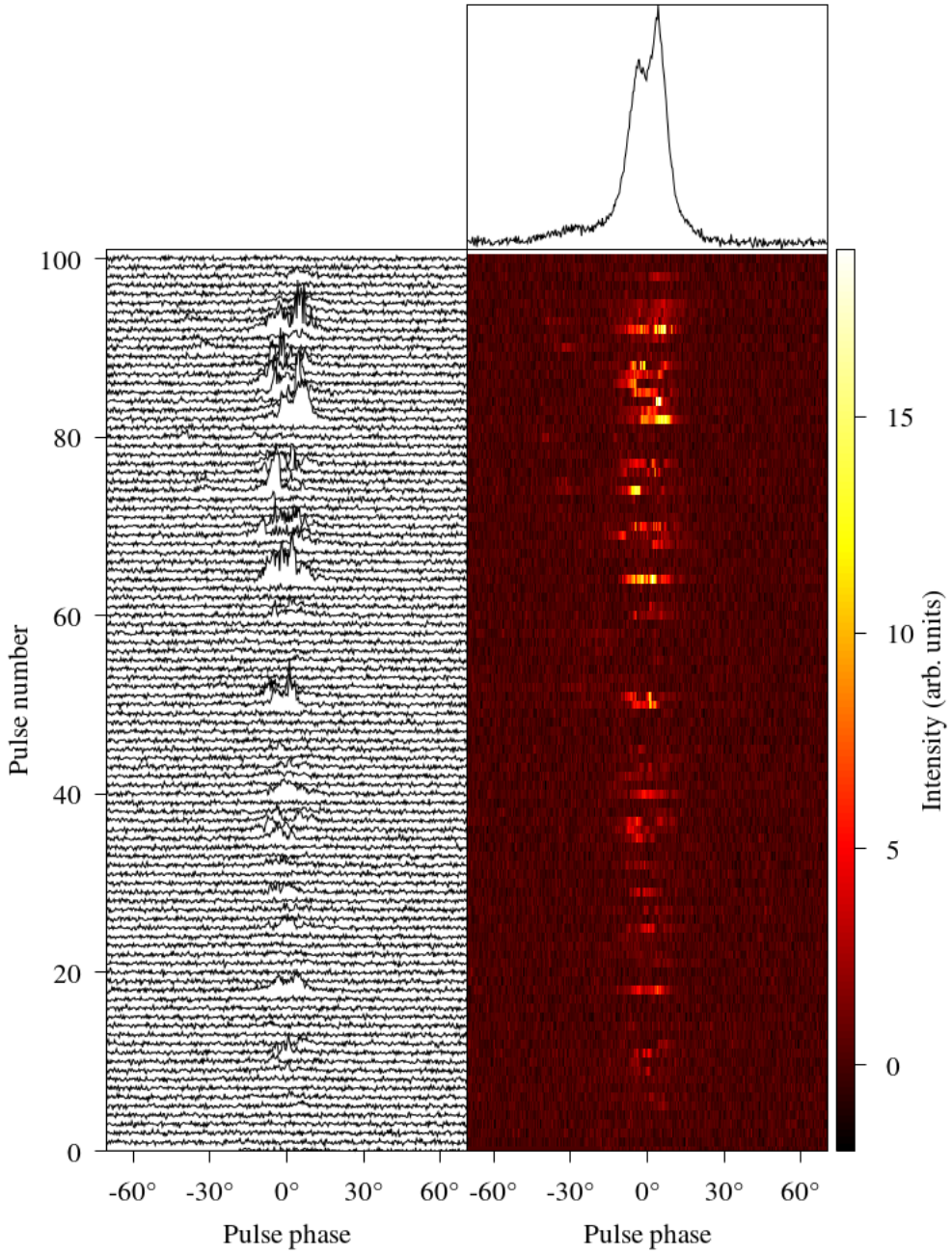

Figure 1.3 A sequence of 100 pulses of B0950+08 from observations made with the Murchison Widefield Array (MWA) at 185 MHz. The data are displayed in a two equivalent forms of a pulse stack image, where intensity is shown either as height (left) or as colour (right). In both cases, the plots are zoomed into the 140° centred on the region of brightest emission. The pulse-to-pulse variation is again clearly evident (cf. Fig. 1.1). The top panel shows a normalised pulse profile, calculated from the entire observation (785 pulses).

by comparing the peak signal to a section of the noise outside the pulse window.

Frequently, individual pulses are not bright enough to be observed above the noise, and forming the pulse profile is the only way to affirm a detection of the pulsar. This is how pulsars are often discovered (albeit via Fourier analysis in the frequency domain rather than in the time domain), with most pulsars being too dim and/or distant to see their individual pulses. Thus, the number of pulsars that are amenable to analyses of their pulse-to-pulse variation is limited to those that are sufficiently bright in the observing frequency range.

1.2.5 Distortions due to propagation effects

Once the signal has left the immediate environment of the pulsar, it is susceptible to distortion by the interstellar medium (ISM) through which it propagates. In order to study the intrinsic emission, it is therefore necessary to model these distortions and, to the extent possible, invert them to recover the original signal. In the notation used above, the process of recovering the intrinsic signal is described by the transformations

$$\begin{aligned} I(t,\nu) &\leftarrow \tilde{I}(\tilde{t},\tilde{\nu}) \\ Q(t,\nu) &\leftarrow \tilde{Q}(\tilde{t},\tilde{\nu}) \\ U(t,\nu) &\leftarrow \tilde{U}(\tilde{t},\tilde{\nu}) \\ V(t,\nu) &\leftarrow \tilde{V}(\tilde{t},\tilde{\nu}) \end{aligned} \tag{1.7}$$

or, more compactly in vector notation,

$$\mathbf{S}(t,\nu) = f(\tilde{\mathbf{S}}(\tilde{t},\tilde{\nu})), \tag{1.8}$$

for some function f yet to be determined, and where the two arguments of $\tilde{\mathbf{S}}(\tilde{t},\tilde{\nu})$ are understood to map respectively to the unadorned arguments of $\mathbf{S}$. If a particular distortion cannot be undone during post-processing (i.e. f is not an invertible function), an alternative strategy is avoidance—one can often choose to observe different pulsars, or the same pulsars at different frequencies, where the

distortions are minimised.

Distortions come in three different flavours: (1) *timing*, (2) *flux*, and (3) *polarimetric* modulations. *Timing* distortions retard the arrival time of the signal at the telescope by a non-uniform amount. *Flux* distortions augment or diminish the intensity of the signal without affecting the arrival time. *Polarimetric* distortions (such as a change in the signal's polarisation angle) can technically be decomposed into coupled timing and flux distortions of the four Stokes parameters, but it is conceptually simpler to think of it as its own class.

All of the propagation effects considered here arise from the fact that the propagating medium, the ISM, is a cold, tenuous plasma whose constituent particles are to all intents and purposes collisionless.

1.2.5.1 Dispersion

Dispersion[5] is the frequency-dependent delay caused by the ISM's greater-than-unity refractive index. The dispersion delay of a photon with frequency ν is given by (e.g. Lorimer and Kramer, 2005)

$$\tau(\nu) = \mathcal{D} \times \frac{\mathrm{DM}}{\nu^2}, \tag{1.9}$$

where DM is the *dispersion measure*, defined as the column density of free electrons along the line of sight,

$$\mathrm{DM} \equiv \int_0^D n_\mathrm{e}(\ell)\, d\ell, \tag{1.10}$$

where $n_e(\ell)$ is the electron number density, D is the Earth-pulsar distance, and $d\ell$ is a line segment along the line of sight. The dispersion constant, $\mathcal{D}$, is related

[5]In the context of pulsar signals, and throughout this thesis, the term "dispersion" always means the effect that is due to the ISM.

to the plasma frequency, and is given by

$$\mathcal{D} \equiv \frac{e^2}{4\pi^2 m_\mathrm{e} \varepsilon_0}, \tag{1.11}$$

where e is the charge of an electron, m_e is its mass, and ε_0 is the permittivity of free space. Converting to more commonly used units, Eq. (1.9) can be more conveniently expressed

$$\tau(\nu) = 4.148808 \pm 0.000003\,\mathrm{ms} \times \left(\frac{\mathrm{DM}}{\mathrm{pc\,cm^{-3}}}\right)\left(\frac{\nu}{\mathrm{GHz}}\right)^{-2}, \tag{1.12}$$

Pulsars at low Galactic latitudes ($|b| \lesssim 15°$) have higher DMs ($\gtrsim 100\,\mathrm{pc\,cm^{-3}}$) than pulsars at higher Galactic latitudes ($\lesssim 100\,\mathrm{pc\,cm^{-3}}$) on account of the higher concentration of free electrons in the Galactic disk. Along any given line of sight, the measured DM provides a first-order estimate of the distance to the pulsar if the average density of free electrons is approximately known (Cordes and Lazio, 2002; Yao et al., 2017).

Some pulsars show evidence of either a time-variable DM (Backer et al., 1993) or small deviations from the expected ν^{-2} dispersion sweep (due to chromatic dispersion effects, Cordes et al., 2016). However, such deviations are smaller than the precision to which DMs are often measured (e.g. on account of the intrinsic evolution of pulsar profiles over the observed frequency range, Ahuja et al., 2007), on the order of $\lesssim 10^{-3}\,\mathrm{pc\,cm^{-3}}$. Across the MWA's observing frequency range of 170 to 200 MHz, this is equivalent to a relative time delay of ~ 0.04 ms, which is much smaller than the finest time resolution used here (~ 1 ms)[6]. For these reasons, we use the historically measured DMs for the pulsars studied in this thesis, and treat them as both constant and accurate up to the stated precision.

In the high time and frequency resolution limit, the dynamic spectrum that is measured by the observer is a transformed version of the intrinsic dynamic

[6]However, Kaur et al. (2019) have recently reported DM variations of $\sim 10^{-4}\,\mathrm{pc\,cm^{-3}}$ using the MWA.

spectrum, where the transformation is given by

$$\tilde{\mathbf{S}}(\tilde{t}, \tilde{\nu}) = \mathbf{S}(t + \tau(\nu), \nu). \tag{1.13}$$

An illustration of this effect is given in Fig. 1.4. The intrinsic dynamic spectrum is easily recovered by the inverse process of *dedispersion*:

$$\mathbf{S}(t, \nu) = \tilde{\mathbf{S}}(\tilde{t} - \tau(\tilde{\nu}), \tilde{\nu}). \tag{1.14}$$

In practice, a problem arises due to the finite size of the frequency channels. The reason is that a single frequency channel has already effectively been scrunched over the small bandwidth of the channel at some point during the signal processing chain. Consequently, the signal is temporally smeared over an interval that corresponds to the dispersive delay between the top and the bottom of the channel. By a suitable Taylor expansion of Eq. (1.12), the time scale of the resulting *dispersion smear* is, to first order,

$$\Delta\tau_{\mathrm{DM}} \approx 8.3\,\mu\mathrm{s} \times \left(\frac{\mathrm{DM}}{\mathrm{pc\,cm^{-3}}}\right)\left(\frac{\nu}{\mathrm{GHz}}\right)^{-3}\left(\frac{\Delta\nu}{\mathrm{MHz}}\right), \tag{1.15}$$

where $\Delta\nu$ is the bandwidth of the given frequency channel.

Dispersion smear can be entirely mitigated by a process known as *coherent dedispersion* (Hankins and Rickett, 1975) whenever the signal phase is known (recall that $\tilde{I}$, $\tilde{Q}$, etc. are complex quantities). However, it is not necessary to do so if the dispersion smear is smaller than the time scale of the temporal structures being studied, as is the case for the pulsar observations analysed in this thesis. Thus, Eq. (1.14) is applied to a whole channel with impunity, with $\tilde{\nu}$ chosen to be the centre frequency of that channel.

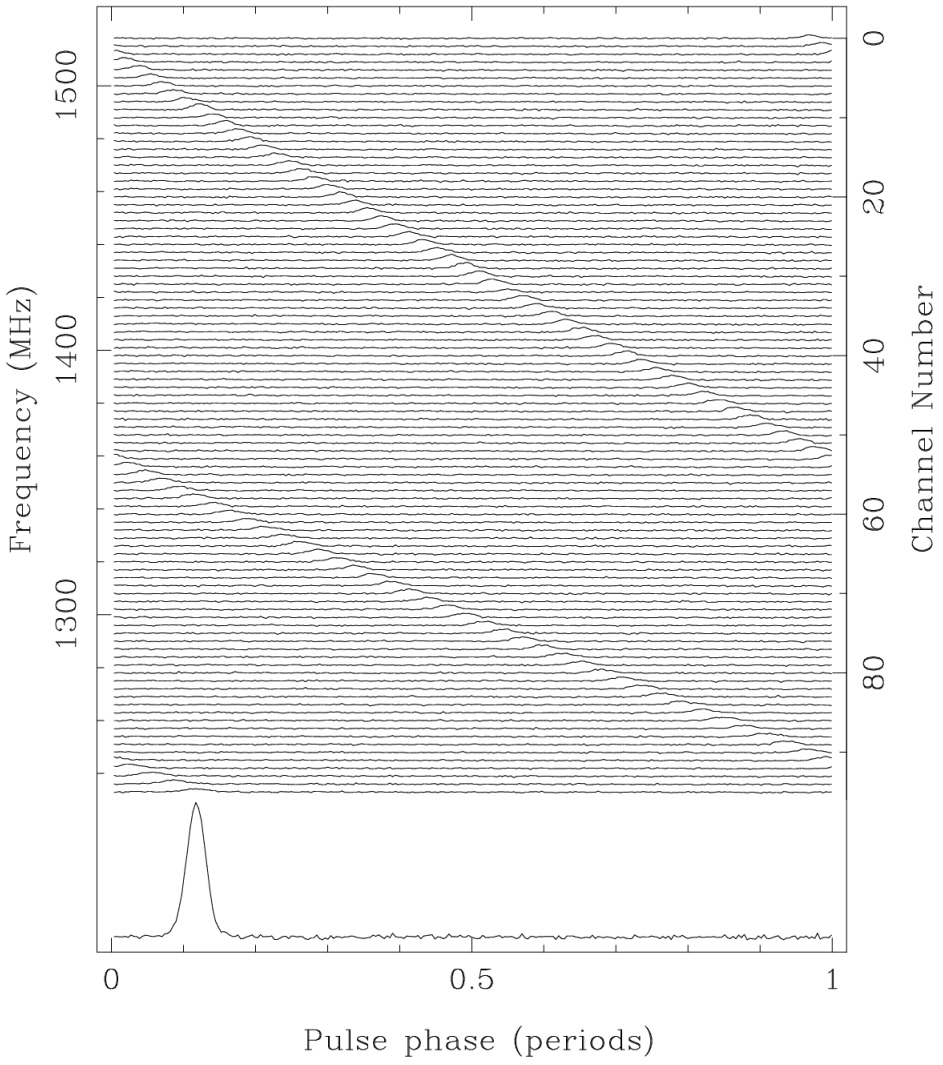

Figure 1.4 An example of ISM dispersion in B1356−60, where the dispersion measure is DM = 295 pc cm^{-3}. Pulses at low frequencies arrive at the telescope later than those at high frequencies due to the dispersion effects of the ISM (Lorimer and Kramer, 2005).

1.2.5.2 Scattering

A single photon leaving a pulsar may take one of several routes to Earth, due to the refractive nature of the ISM. Consequently, an ensemble of photons leaving the pulsar simultaneously will not all arrive at the telescope simultaneously. Those which take a longer route (i.e. more refraction) will arrive later than those that take a more direct route. The image of a pulsar is therefore smeared over a finite angular range with the photons viewed along the boresight arriving slightly earlier than those arriving off-axis. Typically, the angular broadened image, called the *scattering disk* ($\sim$mas at $\sim$ 300 MHz), is still much smaller than the resolving power of individual radio telescopes, although ground-space interferometry has recently successfully resolved the scattering disk of PSR B0329+54 (Smirnova et al., 2014).

The temporal smearing of the pulse power can be modelled as a kernel $H(t)$ which is convolved with the intrinsic pulse such that

$$\tilde{\mathbf{S}}(\tilde{t}, \tilde{\nu}) = H(t, \nu) * \mathbf{S}(t, \nu). \tag{1.16}$$

In the mathematically simple case that the material responsible for the scattering resides in a thin screen[7], the theoretical form of $H(t)$ is a one-sided exponential,

$$H(t, \nu) = \begin{cases} 0, & t < 0, \\ H_0 e^{-t/\tau_s} & t \geq 0, \end{cases} \tag{1.17}$$

where H_0 is a normalisation factor (scattering preserves flux) and the *scattering time scale*, τ_s, is, in general, a strong function of the Earth-pulsar distance, d, the observing frequency, ν, and the distribution of scale lengths of the inhomogeneities in the ISM. If we assume that the scale lengths have a Kolmogorov distribution,

[7]Thin, relative to the Earth-pulsar distance.

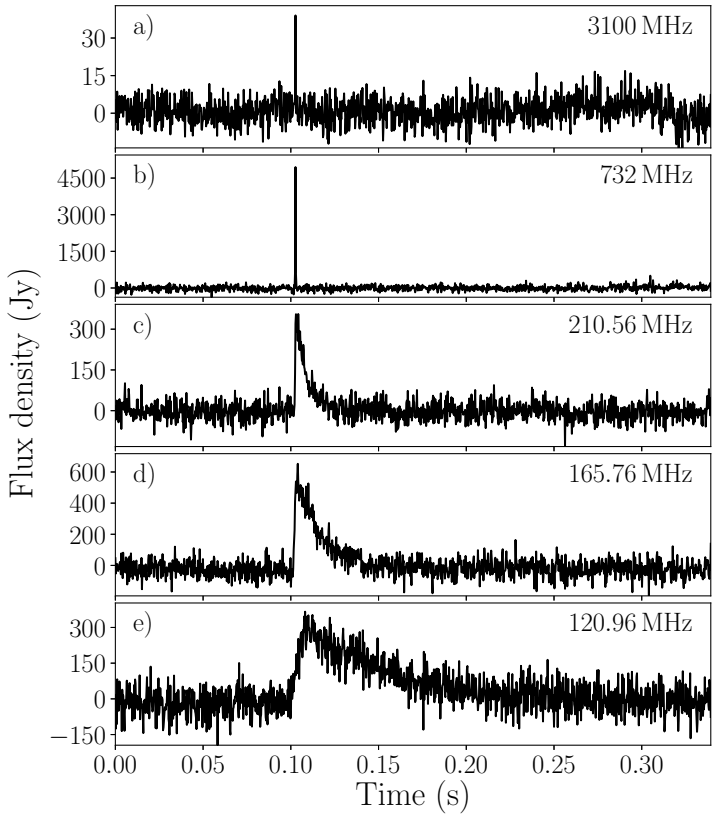

Figure 1.5 A giant pulse from the Crab pulsar, B0531+21, simultaneously observed at frequencies from $\sim$ 100 MHz to $\sim$ 3 GHz. An increase in scattering time can be clearly seen at lower observing frequencies. (a) and (b) are from the Parkes radio telescope, and (c), (d), and (e) are from the MWA (Meyers et al., 2017).

then the scattering time scale obeys the proportionality (Cordes et al., 1985)

$$\tau_s \propto \nu^{-4.4}. \tag{1.18}$$

The larger the scattering time scale τ_s, the more temporal broadening suffered by each pulse—and because Eqn. (1.16) preserves flux, the signal-to-noise decreases, as can be seen in Fig. 1.5. In addition, τ_s can sometimes be larger than the pulsar's rotation period, in which case the flux from one pulse can bleed into the next, further masking the pulsating nature of the signal.

The filter function $H(t, \nu)$ was defined above for a simplified model of the

ISM; in reality, the ISM is more complicated and therefore the proportionality above should be taken as a first order approximation. In any case, however, the scattering time scale is a very strong function of observing frequency, and in cases where scattering would interfere with one's particular science goals, the most common strategy is avoiding the effects of scattering by observing the pulsar at higher frequencies. In general, the convolution is not invertible, but various deconvolution schemes such as cyclic spectroscopy (Demorest, 2011) and CLEAN-based deconvolution (Bhat et al., 2003) have been advanced that, to one extent or another, succeed in undoing the effects of scattering.

Similar to dispersion, since the scattering time scale is smaller than the temporal structures being studied in this thesis, scattering effects are neglected.

1.2.5.3 Scintillation

The multipath propagation described in the previous section has another knock-on effect: the constructive or destructive interference of two (or more) wavefronts that have arrived at the telescope at the same time along different routes. Whether the net superposition of the arriving light rays is constructive or destructive depends sensitively on the geometry of the scattering medium in relation to the Earth and the pulsar. As the pulsar moves relative to the ISM, and as the Earth orbits the Sun, the observer passes through the interference pattern, seeing semi-regular amplifications or attenuations of the pulsar signal. Moreover, because the angle of refraction and, hence, the size scale of the interference pattern depend on frequency, the observed modulation of the intrinsic signal is a function of both time and frequency:

$$\tilde{\mathbf{S}}(\tilde{t}, \tilde{\nu}) = A(t, \nu)\mathbf{S}(t, \nu). \tag{1.19}$$

When $A(t,\nu) > 1$, we say that the pulsar is "scintillating up"; when $A(t,\nu) < 1$, "scintillating down"[8].

The function $A(t,\nu)$ embodies two characteristic properties which are of interest to the pulsar observer, known as the *scintillation bandwidth* and the *scintillation time scale*, which are the average bandwidth and the average time scale, respectively, over which the signal modulation goes from constructive to deconstructive interference. Both the scintillation bandwidth and time scale are themselves functions of frequency, given by the proportionalities (Cordes et al., 1986; Romani et al., 1986)

$$\begin{aligned} \Delta\nu_{\mathrm{sc}} &\propto \nu^{4.4} \\ \Delta\tau_{\mathrm{sc}} &\propto \nu^{1.2} \end{aligned} \tag{1.20}$$

There are different regimes of scintillation, which differ observationally in both the bandwidth and time scale. For example, the time scale of diffractive scintillation is typically of order minutes and hours (at $\sim 300\,\mathrm{MHz}$), while that of refractive scintillation is on the order of weeks and months.

Of the distortions discussed so far, scintillation is the arguably the least damning since the signal is not spread into other time/frequency bins, not to mention the fact that often the pulsar can sometimes appear even brighter than average, aiding its detection. If $A(t,\nu)$ were known, the inversion would be straightforward:

$$\mathbf{S}(t,\nu) = \frac{1}{A(\tilde{t},\tilde{\nu})}\tilde{\mathbf{S}}(\tilde{t},\tilde{\nu}). \tag{1.21}$$

In principle, scintillation is only distinguishable from fluctuations in the intensity of the intrinsic signal by the time scales involved. Generally, the scintillation time scale (in any regime) is much longer than the rotation period, P_1, so pulse-to-pulse variations in intensity can be considered an intrinsic characteristic of the pulsar signal. Although the scintillation timescale is often shorter than the length

[8]Here, $A(t,\nu)$ is being treated as a real scalar, but in reality scintillation is more accurately modelled as a complex transfer function, not unlike Eq. (1.16) above. The phase information can, via cyclic spectroscopy, be used to completely "undo" the effects of scintillation (e.g. Walker et al., 2013).

of an observation, it can be easily identified in the dynamic spectrum (see, e.g., Fig. 2.4). Fortunately, when observations cover a wide enough frequency range (i.e. for observing bandwidths $\gg \Delta\nu_{\rm sc}$), the value of $A(t,\nu)$ will average out to ≈ 1 in any given time bin. Thus, even though scintillation effects are known to be present in the observations discussed in this thesis, they are neglected—partly for the reason just given, and also because the analyses, which are mainly concerned with pulse-to-pulse variations, are not greatly affected.

1.2.5.4 Faraday rotation

The final propagation effect to consider is *Faraday rotation*, which is the rotation of the polarisation angle of the incident light as it passes through the ISM. It occurs because the ambient magnetic field permeating the ISM introduces an asymmetrical effect on oppositely circularly polarised light (into which any arbitrary polarisation state can be decomposed). Left-handed circularly polarised light will thereby experience a slightly different refractive index than its right-handed counterpart, with the net effect that the superposition of the two (i.e. the total propagating wave) will experience a net rotation.

Like the other distortions, Faraday rotation is strongly frequency-dependent. The total amount of rotation experienced by the incident ray as it passes through the ISM is (e.g. Lorimer and Kramer, 2005)

$$\Delta\psi = \mathrm{RM}\,\lambda^2, \tag{1.22}$$

where $\lambda = c/\nu$ is the ray's wavelength, and RM is the *rotation measure*

$$\mathrm{RM} \equiv \frac{e^3}{8\pi^2\varepsilon_0 m_{\rm e}^2 c^3}\int_0^d n_{\rm e}(\ell)B_{\parallel}(\ell)\,d\ell, \tag{1.23}$$

where $B_{\parallel}(\ell)$ is the component of the magnetic field at distance ℓ which is parallel to the line of sight, and the other terms are as defined in Eq. (1.11). Like the DM, the value of RM is measured empirically on a pulsar-by-pulsar basis, for

example, by the method of RM-synthesis (Burn, 1966; Brentjens and de Bruyn, 2005).

Faraday rotation affects only the Stokes parameters Q and U. The transformation between the intrinsic quantities (I, Q, etc.) and the observed quantities ($\tilde{I}$, $\tilde{Q}$, etc.) under a Faraday rotation of $\Delta\psi$ radians is

$$\tilde{\mathbf{S}}(\tilde{t}, \tilde{\nu}) = \mathbf{M}_{\rm rot}\mathbf{S}(t, \nu), \tag{1.24}$$

where

$$\mathbf{M}_{\rm rot} = \begin{bmatrix} 1 & 0 & 0 & 0 \\ 0 & \cos(2\Delta\psi) & \sin(2\Delta\psi) & 0 \\ 0 & -\sin(2\Delta\psi) & \cos(2\Delta\psi) & 0 \\ 0 & 0 & 0 & 1 \end{bmatrix} \tag{1.25}$$

Correcting for Faraday rotation, once the RM is known, is accomplished by inverting Eq. (1.25):

$$\mathbf{S}(t, \nu) = \mathbf{M}_{\rm rot}^{-1}\tilde{\mathbf{S}}(\tilde{t}, \tilde{\nu}). \tag{1.26}$$

1.2.5.5 Pulsar ephemerides

The effects of dispersion, scattering, scintillation, and Faraday rotation as they apply to a given pulsar signal are summarised, along with a host of other timing-related effects, in published pulsar ephemerides. These ephemerides are most commonly used to facilitate the transformation from the raw signal $\tilde{\mathbf{S}}(\tilde{t}, \tilde{\nu})$ to the intrinsic signal $\mathbf{S}(t, \nu)$.

An excellent, publicly available catalogue of pulsar ephemerides is maintained at `http://www.atnf.csiro.au/people/pulsar/psrcat/` (Manchester et al., 2005). The contents of the catalogue are also available via a program called PSRCAT, which can be downloaded from the same website. An example of an ephemeris file, generated by PSRCAT, is shown in Fig. 1.6.

```
PSRJ            J0034-0721
RAJ             00:34:08.8703               1.000e-04
DECJ            -07:21:53.409               2.000e-03
DM              10.922                      6.000e-03
PEPOCH          46635.00
F0              1.0605004987209             1.900e-12
F1              -4.59098E-16                7.000e-21
PMRA            10.37                       8.000e-02
PMDEC           -11.13                      1.600e-01
POSEPOCH        52275
DMEPOCH         56843
F2              2.1E-28                     6.000e-29
RM              9.89                        7.000e-02
PX              0.93                        8.000e-02
EPHVER          2
UNITS           TDB
```

Figure 1.6 Example of a pulsar ephemeris file (B0031−07). The columns are (1) property name, (2) property value, (3) uncertainty

1.3 Properties of intrinsic pulsar emission

Once propagation effects of the ISM have been accounted for (see the previous section), the resulting dynamic spectrum is expected to be a close approximation to the intrinsic pulsar signal. The ultimate goal of studying intrinsic pulsar signals is to produce a physical model of the radio emission mechanism. This, however, has proved challenging over the decades, for several reasons. Firstly, the environment around a pulsar is thought to be in an extreme regime (strong magnetic and gravitational fields, ultra-relativistic particle energies) that do not exist on Earth. That is to say, the relevant plasma models cannot be easily reproduced and tested in laboratory settings. Secondly, intrinsic pulsar signals exhibit an impressively large range of behaviours and morphologies; each pulsar appears to have characteristics that are unique to it. Thus, many models are capable of explaining some subset of pulsar behaviours but ultimately fail to explain *all* pulsars.

The goal of this section is to introduce some properties of intrinsic pulsar

signals that are common (if not ubiquitous) in the population of known pulsars, and to make some elementary deductions, where possible, about the nature of the underlying radio emission mechanism. Often the interpretation of these properties depends on the specific emission mechanism being considered. In these cases, the interpretation is deferred until the main emission mechanism treated in this thesis has been introduced.

1.3.1 Brightness

1.3.1.1 Brightness temperature

In the radio regime of pulsars, we can define the measured brightness temperature to be (Cordes, 1979)

$$\begin{aligned} T_b &\equiv \frac{SD^2}{2\pi k_{\rm B}(\nu\Delta t)^2}, \\ &\simeq 10^{30}\,{\rm K} \times \left(\frac{S}{\rm Jy}\right)\left(\frac{\nu}{\rm GHz}\right)^{-2}\left(\frac{\Delta t}{\mu{\rm s}}\right)^{-2}\left(\frac{D}{\rm kpc}\right)^{2} \end{aligned} \tag{1.27}$$

where ν is the observing frequency, S is the peak flux density measured in Jy ($= 10^{-26}\,{\rm W\,m^{-2}\,Hz^{-1}}$), $k_{\rm B}$ is the Boltzmann constant, Δt is the time scale of pulsar signal variations, and D is the distance to the pulsar. For even modest values of S, Δt, and D, the implied brightness temperature is several orders of magnitude above the *inverse Compton limit* of approximately $10^{12}\,{\rm K}$, which is the theoretical upper limit for an incoherent source of synchrotron radiation (Kellermann and Pauliny-Toth, 1969; Melrose, 1992). In extreme cases, such as the Crab pulsar which emits "giant" pulses ($S > 100\,{\rm kJy}$) on nanosecond time scales, measured brightness temperatures can reach approximately 10^{39} to $10^{42}\,{\rm K}$ at 4 to 6 GHz (Hankins et al., 2003; Jessner et al., 2005; Hankins et al., 2016). Because the brightness temperatures are so much higher than the inverse Compton limit, the radio emission mechanism must be a coherent process. That is, if one considers the overall emitted wave as the sum of contributions by individual photons, then

the phases of the photons (treated as wave packets) must be strongly correlated. Understanding how this is accomplished in the vicinity of pulsars remains the central challenge of understanding the radio emission mechanism.

1.3.1.2 Spectral index

Pulsars that have been observed for long enough for scintillation effects to be averaged out can have their spectra reliably measured. In general, pulsars have negative spectral indices in the radio band—i.e. they are brighter at lower frequencies. In many cases, this trend continues down to the lowest frequencies that can be observed from Earth's surface, but there are also pulsars which show a turn-over at low frequencies ($\lesssim 200\,\mathrm{MHz}$).

The spectral index, α, is defined assuming a power-law relationship between flux density and frequency:

$$S_\nu \propto \nu^\alpha, \tag{1.28}$$

where S_ν is the flux density at frequency ν. Population studies show the spectral index to have a mean value of -1.4 and a standard deviation of 1 (Bates et al., 2013), although it should be noted that there are many pulsars whose spectra are not well described by a simple power law model (Jankowski et al., 2018). Naturally, a viable model of the emission mechanism must be able to predict the observed spectra.

1.3.2 The time scales of intensity variation

Pulsar time series show that the pulse-to-pulse emission is highly stochastic in nature, and that the duration of individual bursts of emission is usually much shorter than the pulse window. Because of this, we use the word *pulse* as a collective term for all emission that occurs within one period, P_1, and *subpulse* to denote an individual burst of emission within a pulse. Thus, a pulse may contain any number of subpulses (including zero). The meaning of these terms is illustrated in Fig. 1.7

The question naturally arises whether the subpulse is the basic unit of emission, or whether temporally finer structures exist. When the autocorrelations of the time series were computed, structures on microsecond time scales were revealed as a distinct distribution from subpulse time scales (Cordes, 1979, 1981). That is to say, when sufficiently high time resolution is available, subpulses are seen to be made up of much shorter discrete emission events, collectively termed *microstructure*. In a similar manner, a population of events on the order of nanoseconds (*nanostructure*) has been discovered in a few, very bright pulsars (e.g. the Crab pulsar, B0531+21; Hankins et al., 2003), but it remains unclear if this phenomenon is widespread.

The existence of distinct regimes of time scales of emission events over so many orders of magnitude (from $\sim 10^{-9}$ to 10^{-3} s) implies a complex hierarchy of different spatial structures in the emitting medium, offering important clues to the nature of the emission mechanism. However, whether or not *all* pulsars exhibit microstructure or nanostructure, or whether there are different emission mechanisms responsible for emission on different timescales, is as yet unknown. This thesis, however, deals only with subpulses, whose time scales are typically between 2 and 3 orders of magnitudes shorter than the period, P_1. For "ordinary" pulsars ($P_1 \sim 1$ s), this implies time scales on the order of a few milliseconds, and emission beam substructures of no more than a few degrees of rotation phase.

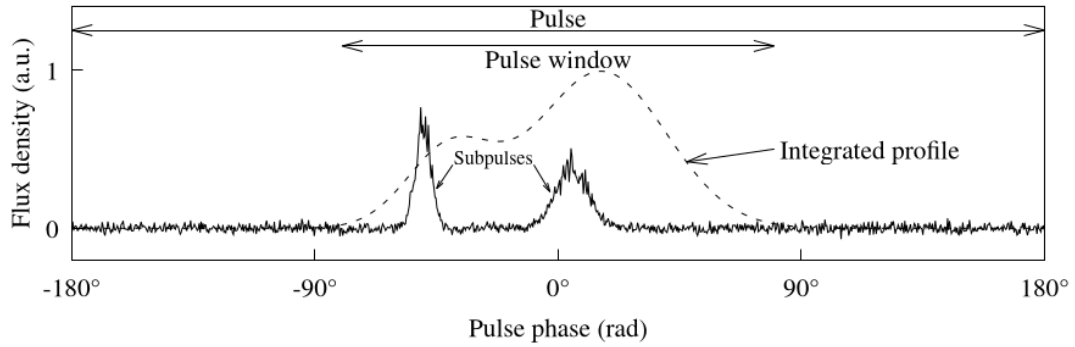

Figure 1.7 A diagram illustrating the meaning of the terms *pulse*, *subpulse*, *integrated profile*, and *pulse window*.

1.3.3 Nulling

In many pulsars, there are sporadic time intervals during which no emission is detected, a phenomenon called *nulling* (Backer, 1970b; Ritchings, 1976; Wang et al., 2007). Both the onset and cessation of nulling appears to be universally rapid, with the transition from the "on"-state (sometimes called a *burst* sequence) to the "off"-state (a *null* sequence), and vice versa, occurring within a single pulsar rotation (e.g. Fig. 1.8). The fraction of time that a given pulsar is in a nulling state is called its *nulling fraction*, and reported values of null fractions run the gamut from 0% to almost 100%. The duration of individual nulling events can also vary widely for a single pulsar. B0031−07, for example, contains both short-duration nulls lasting a few pulses interspersed with long-duration nulls lasting hundreds of pulses (Joshi and Vivekanand, 2000).

Nulling occurs pseudo-randomly in time, and thus unconnected to explanations such as eclipsing by a companion object, or precession of the pulsar beam away from our line of sight, which imply strictly periodic nulling. Nulling appears to be intrinsic to the emission mechanism, representing a distinct "emission" state. That is to say, they are not merely the tail end of an energy distribution that dips below the detection threshold (Ritchings, 1976). This is further supported by the widespread observational fact that nulling is a broadband phenomenon (Gajjar et al., 2014), although exceptions are known (e.g. Bhat et al., 2007). Nulling is known to affect the properties of the burst emission just preceding and following a null sequence (e.g. Lyne and Ashworth, 1983). Despite the preponderance of nulling in the known pulsar population, it is not well understood; emission mechanism models tend to focus on explaining the properties of burst states rather than the existence of null states.

1.3.4 Polarisation

Light can be completely unpolarised ($Q = U = V = 0$), completely polarised ($Q^2+U^2+V^2 = I^2$), or partially polarised ($0 < Q^2+U^2+V^2 < I^2$). For partially

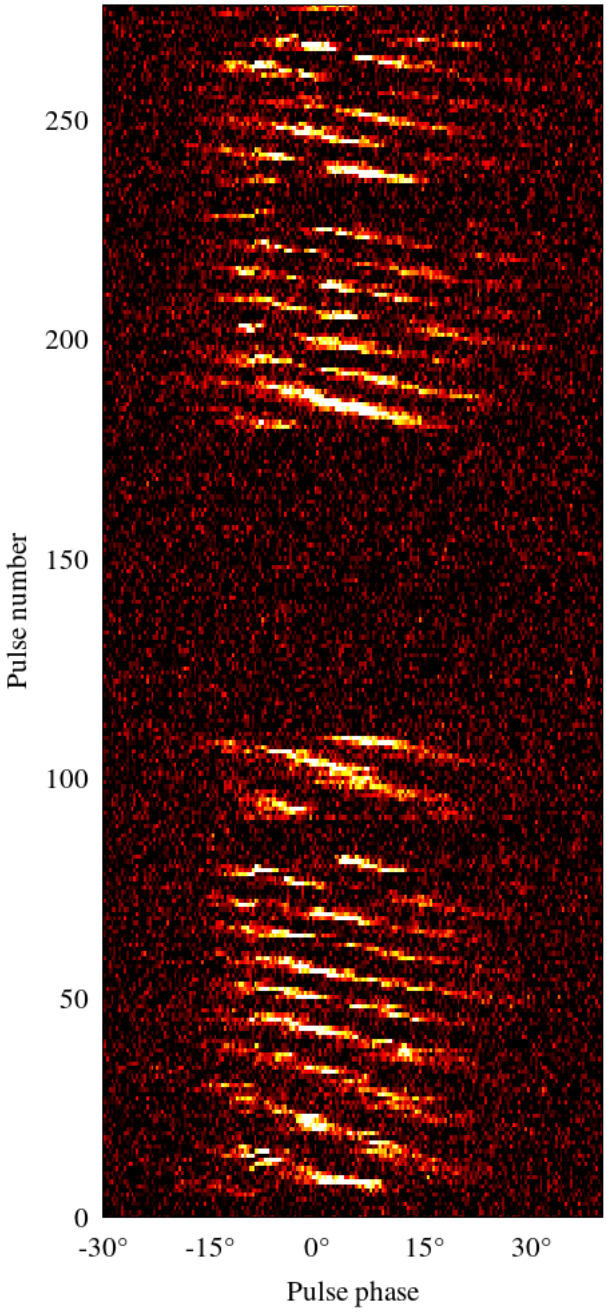

Figure 1.8 A pulse stack of B0031−07 showing both relatively short (pulses 83-90) and long (pulses 110-179) null sequences.

or completely polarised light, the polarisation state is generally elliptical, which can be described in terms of *linear* and *circular* components. Together with the *polarisation position angle* (PPA) and the total intensity, these comprise an alternative basis for describing the polarisation state that is more amenable to physical interpretation. The transformation from Stokes parameters to the new basis is

$$\begin{aligned} I &\leftarrow I \\ L &\leftarrow \sqrt{Q^2 + U^2} \\ V &\leftarrow V \\ \psi &\leftarrow \frac{1}{2} \arctan\left(\frac{U}{Q}\right), \end{aligned} \tag{1.29}$$

where L is the linear polarisation, V is the circular polarisation, and ψ is the PPA.

Pulsars are generally highly polarised sources with the fraction of linear polarisation, L/I, reaching almost 100% in some cases (Lyne and Smith, 1968; Manchester et al., 1975; Gould and Lyne, 1998; Noutsos et al., 2015). By the same token, the fraction of circular polarisation, $|V|/I$, is generally lower than the linear, but still present in significant quantities ($\sim$ 10-20%), making the polarisation generally elliptical. The *polarisation profile* is a convenient way to show how the polarisation state changes as a function of pulse phase (Fig. 1.9).

1.3.4.1 Orthogonal polarisation modes

When the signal-to-noise is high enough for single pulse observations, it is possible to investigate the statistics of polarisation for each time sample. This was first done for PSR B0329+54 by Clark and Smith (1969) and for a handful of other pulsars by Ekers and Moffet (1969), who both observed that

1. the polarisation fraction ($\sqrt{Q^2 + U^2 + V^2}/I$) of individual pulses is usually stronger than the polarisation fraction of the integrated profile—i.e. the operation of forming the integrated profile must *depolarise* it;

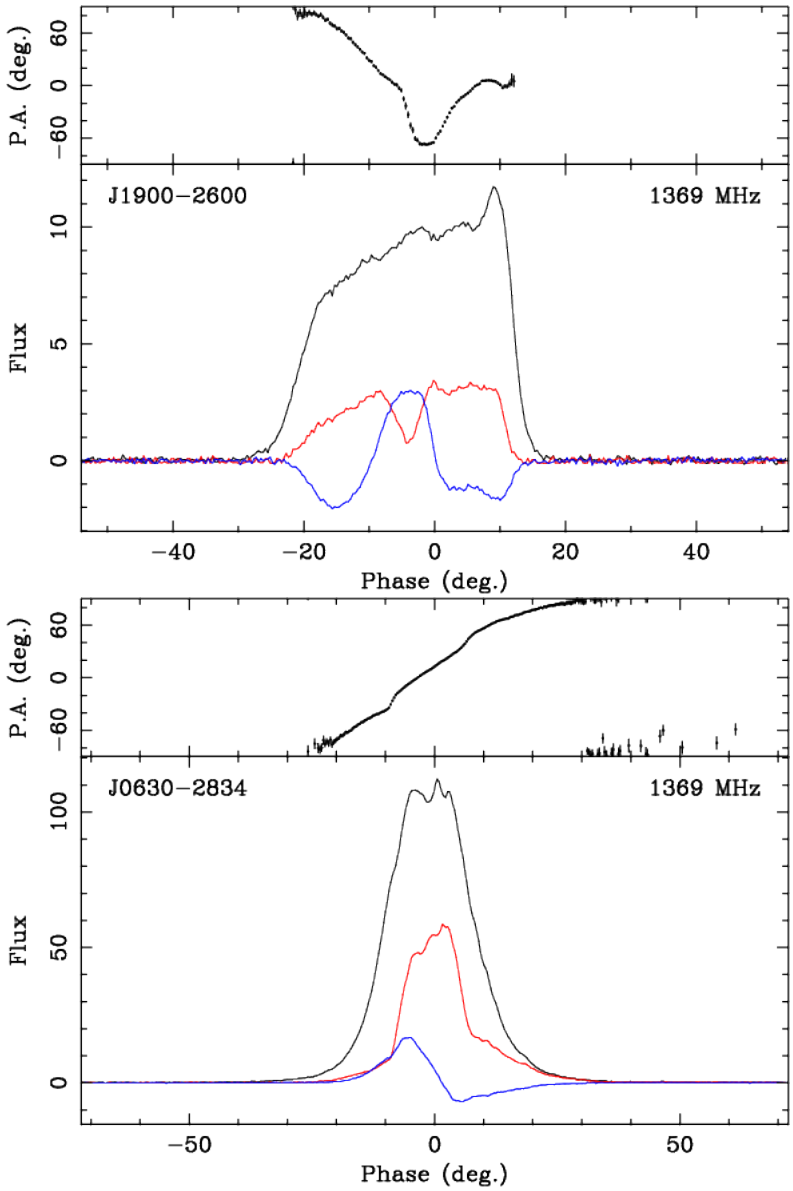

Figure 1.9 Two examples of polarisation profiles from Parkes observations of B1857−26 (top) and B0628−28 (bottom). The black, red, and blue curves are I, L, and V, respectively. The top panels show the polarisation position angle (abbreviated to "P.A." by the plotting software). The B0628−28 PPA curve has the characteristic "S" shape, i.e. steepest near the middle and flattening out near the edges of the pulse window.

2. the polarisation varies from pulse to pulse (explaining the depolarisation above), but within a single pulse the polarisation angle varies smoothly across the pulse window; and

3. the distribution of polarisation angles observed in a single phase bin is often bimodal, with the two components of the distribution typically separated by approximately 90°. The two modes are called *orthogonal polarisation modes*, or OPMs.

The presence of OPMs naturally affects the polarisation characteristics of the integrated profile. In any given phase bin, the average PPA will reflect whichever of the two OPMs is more dominant. Thus, it is not uncommon to see one or more discontinuous jumps of 90° in the polarisation angle of the profile.

1.3.4.2 PPA as a function of pulse phase

Except for discontinuous jumps due to OPMs, the average PPA typically varies smoothly across the pulse window. When the pulse window is wide enough, the PPA curve often has a distinctive "S" shape, i.e. steepest in the middle and flattening out towards the periphery (e.g. B0628−28 in Fig. 1.9). If OPM discontinuities are present, the S-shape can be recovered by artificially rotating one of the OPMs by 90° (Backer and Rankin, 1980).

The S-shape was recognised to be consistent with the orientation of magnetic field lines of an inclined, rotating dipole as it sweeps past the observer's line of sight. This association between the PPA and the magnetic field geometry, as originally outlined by Radhakrishnan and Cooke (1969) and Komesaroff (1970), has become known as the Rotating Vector Model (RVM), which is discussed further in §1.5.2.

1.3.5 Profile evolution with frequency

The shape of a pulsar's integrated profile changes as a function of observing frequency. This is true for all pulsars; however, the degree and type of change differs from pulsar to pulsar. The changes can be described in terms of the individual components that make up the integrated profile, which can change in three ways: (1) intensity, (2) width, and (3) pulse phase.

Intensity changes are common, and can affect different components within the same profile by different degrees. In these cases, one can speak meaningfully of the spectral index of individual components, which can sometimes differ drastically from each other. The overall spectral index of the pulsar is really just a conflation of the spectral indices of the individual components.

The width of profile components tends to increase at lower frequencies, and, similarly, the profile components tend to spread out in pulse phase. The first systemic study of this effect by Cordes (1978) models the component separation, $\Delta\theta$ as a broken power law

$$\Delta\theta = \begin{cases} A\nu^{\alpha}, & \nu \leq \nu_c \\ B, & \nu > \nu_c \end{cases} \tag{1.30}$$

where A and B are constants, and typically $-0.5 \leq \alpha \leq -0.08$ below some critical frequency ν_c which is specific for each pulsar. This general trend is borne out in more recent studies (Pilia et al., 2016); however, some pulsars are known to have the opposite trend (e.g. B1944+17; Kloumann and Rankin, 2010). Fig. 1.10 shows the profile evolution of three pulsars.

Thorsett (1992) argues that the broken power law model just described does not capture the true behaviour very well, and introduces the empirical relationship

$$\Delta\theta = A\nu^{\alpha} + \Delta\theta_{\min}, \tag{1.31}$$

where $\Delta\theta_{\min}$ is a high-frequency asymptote.

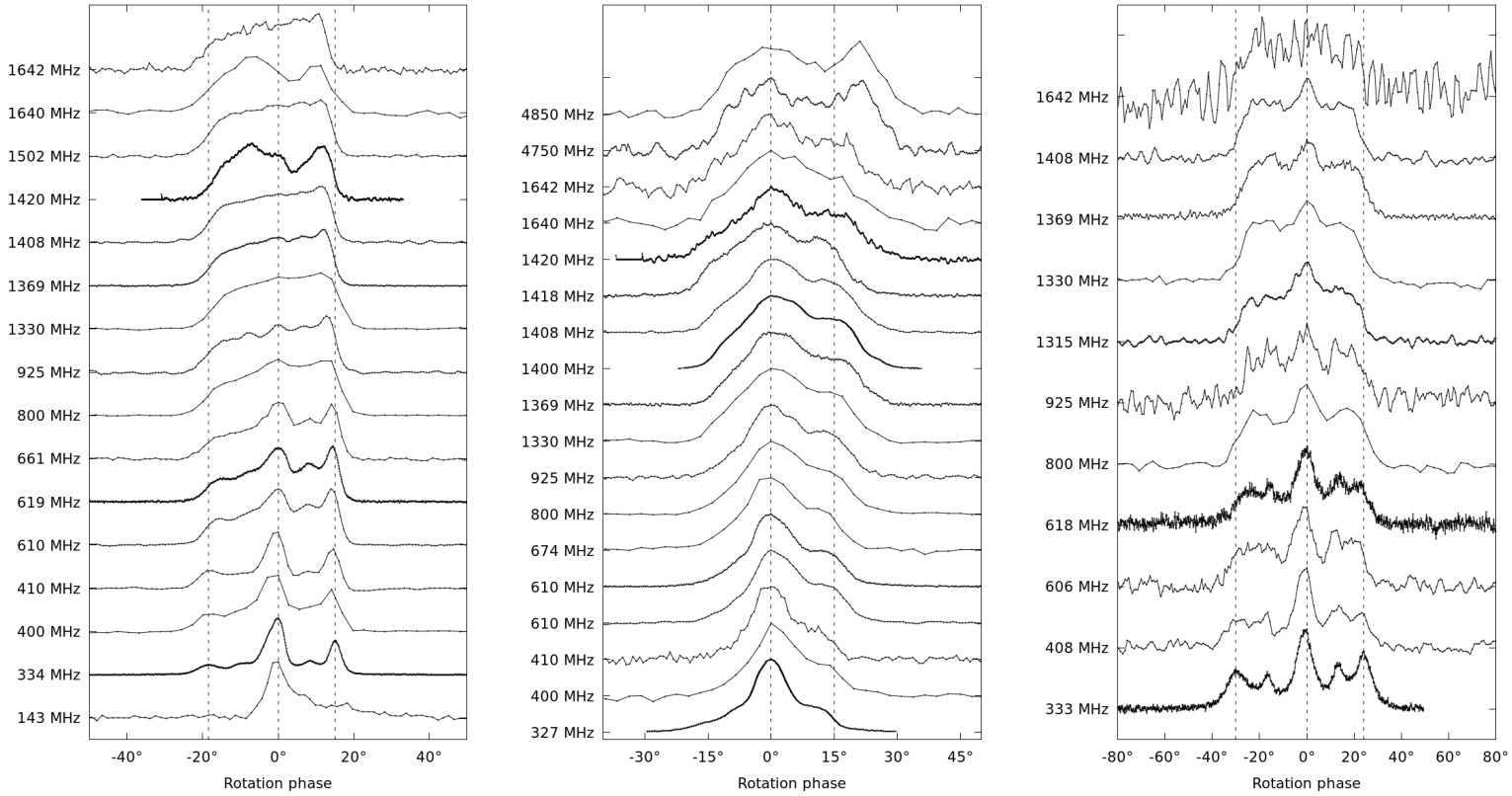

Figure 1.10 The frequency evolution of the profiles of B1857−26 (left), B1944+17 (middle), and B2003−08 (right). The separation between components usually becomes smaller at higher frequencies; however, B1944+17 is an exception. The 610 and 1369 MHz profiles for B1944+17 were produced from our own Giant Metrewave Radio Telescope (GMRT) and Parkes observations, respectively; the rest are from the European Pulsar Network database (`http://www.epta.eu.org/epndb/`).

Profile evolution is widely taken as evidence for the existence of a *radius-to-frequency mapping* (RFM), i.e. that the frequency of emission is a function of the height above the pulsar surface at which it is generated (Cordes, 1978). The tendency for profile features to be broader at lower frequencies suggests (in the context of a dipolar magnetic field) that lower frequencies are emitted at greater heights, where the magnetic field lines make a greater angle to the magnetic axis, while higher frequencies are generated closer to the pulsar surface. The consequences of RFM for emission mechanism models are explored further in Section §1.4.4.1.

1.3.6 Subpulse drifting

In many pulsars, subpulses occur stochastically within the pulse window, i.e. the phases of subpulses in one pulse is not correlated with the phases of the subpulses in the next pulse. However, in other pulsars there is a very strong correlation in subpulse phases from pulse to pulse. In many such cases, subpulses appear to march gradually and systematically in phase, emerging on one side of the pulse window and, several pulses later, disappearing from the other side. This phenomenon, called *subpulse drifting*, was first observed in PSR B1919+21 by Drake and Craft (1968) and was subsequently found to occur in several other pulsars (e.g Taylor et al., 1975). A more recent study by Weltevrede et al. (2006, 2007) suggests that "at least half of the total population of pulsars have drifting subpulses when observations with a high enough signal-to-noise ratio would be available."

The study of subpulse drifting is the main focus of this thesis. Among the various phenomena that require observations of individual pulses, subpulse drifting seems to offer unique insights into the underlying emission mechanism (Rankin, 1986). Indeed, the main model considered here (the *carousel* model, to be discussed in detail in a later section) has its origins in one of the earliest comprehensive models of pulsar emission which was motivated (in part) by the effort to

account for subpulse drifting (Ruderman and Sutherland, 1975). The continuing popularity of this early model (or, at least, its main ideas) has inspired methods for inferring the emission geometry from subpulse drifting properties (Deshpande and Rankin, 1999, 2001), which, if valid, are powerful tools for investigating the details of the emission mechanism. In this section, the main properties of subpulse drifting are set forth, as well as some advanced techniques for quantifying its behaviour.

1.3.6.1 Drift bands, the drift rate, P_2, and P_3

When the time series data are arranged in pulse stacks, subpulse drifting manifests as diagonal tracks of emission called *drift bands* (e.g. Fig. 1.11). Drift bands are most simply characterised by (1) their *drift rates* (i.e. the rate of change of rotation phase per pulse, whose visible manifestation in pulse stacks is the slope of the drift band) and (2) the spacing between them. On a pulse stack image, one may choose either the "horizontal" spacing or the "vertical" spacing. The horizontal spacing is equal to the temporal separation of two successive subpulses (within a single pulse), and is therefore considered a kind of secondary period, denoted by the symbol P_2. The vertical spacing, denoted by P_3, is equal to the time it takes a subpulse to appear at the same rotation phase[9]. The drift rate, D, is thus related to P_2 and P_3 via

$$\frac{D}{P_1} = \pm\frac{P_2}{P_3}. \tag{1.32}$$

where D, P_1, P_2, and P_3 are all given in units of time. The sign indicates the drift direction (i.e. the subpulses drift either towards positive or negative phases), since P_2 and P_3 are conventionally always positive quantities. Fig. 1.11 illustrates the interpretation of these quantities on a pulse stack. On account of Eq. (1.32), one can choose any pair of the three quantities (D, P_2, P_3) to characterise the

[9]This intuitive definition is adequate when the drift bands are clearly defined, but is problematic for certain types of subpulse modulation. The pulsars studied in this thesis all have clearly defined drift bands.

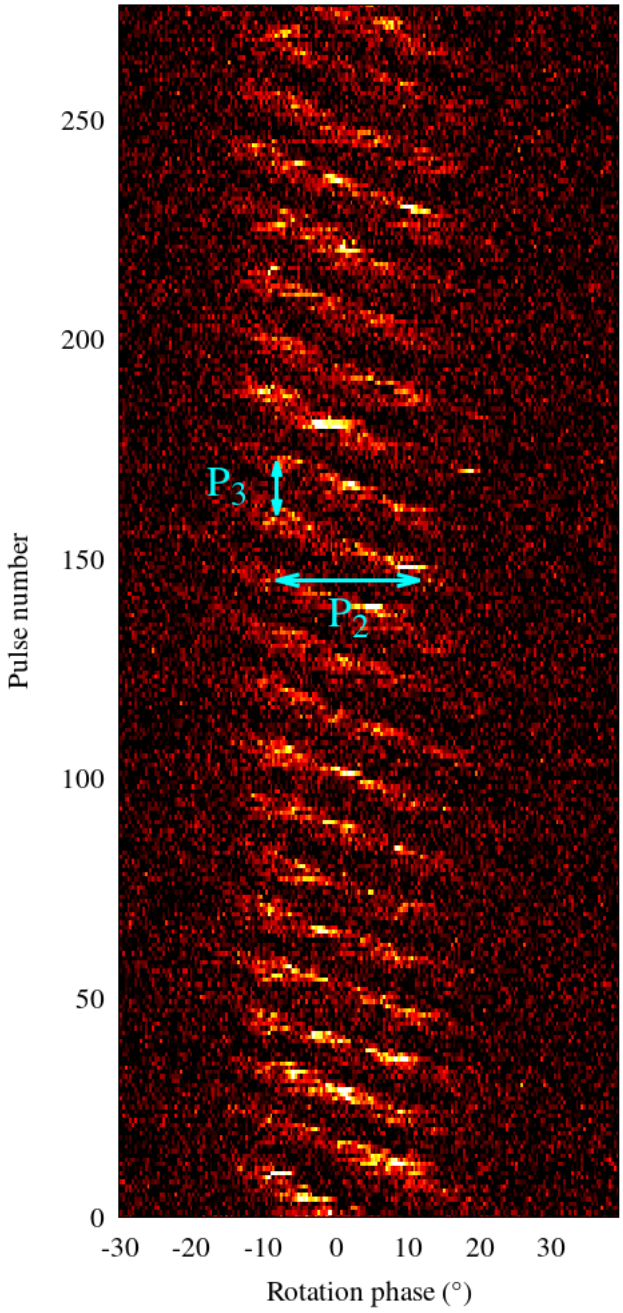

Figure 1.11 A pulse stack drawn from 185 MHz observations of B0031−07 obtained with the MWA (McSweeney et al., 2017), exhibiting the phenomenon of subpulse drifting. The diagonal strips of subpulses in successive pulses form the so-called *drift bands*. If the spacing between subpulses is short enough with respect to the pulse window, a drift band may appear before the previous one vanishes. The horizontal and vertical "spacing" between the drift bands are called P_2 and P_3 respectively. Since the drift pattern moves towards more negative phases as time progresses, this is an example of a *negative* drift rate.

drift bands.

1.3.6.2 The longitude-resolved fluctuation spectrum (LRFS) and the subpulse phase track

Shortly after the discovery of subpulse drifting, Backer (1970b) pioneered the application of Fourier techniques to detect and measure both the phase and amplitude modulations of subpulses over time. His original technique involved taking the discrete Fourier transform (DFT) of each phase bin in a pulse stack over the duration of an observation to produce a complex image called the *longitude-resolved fluctuation spectrum*, or LRFS,

$$I_{\rm lrfs}(\nu_p, \varphi) \equiv \sum_{k=0}^{N-1} I_{\rm ps}(p_k, \varphi)\, e^{i2\pi k\nu_p/N}, \tag{1.33}$$

where $i = \sqrt{-1}$ and N is the number of pulses in the pulse stack. Naturally, the same analysis can also be applied to the other Stokes parameters, Q, U, and V; however, unless otherwise indicated, the term "LRFS" implies Stokes I. If the subpulse modulation is stable over the pulse window and over a sufficiently long period of time, the LRFS will reveal a thin region of power at the frequency of the modulation, $\nu_p = 1/P_3$, as illustrated in Fig. 1.12.

P_3 is a constant function of pulse phase in all pulsars for which P_3 has been measured, and the corresponding feature in the LRFS therefore occupies only a single row of pixels (up to spectral leakage effects caused by the DFT). The complex phases of this row are collectively called the *subpulse phase track*, and it encodes information about the *horizontal* spacing of the drift bands, i.e. P_2. to be precise, P_2 is proportional to the inverse of the rate of change of phase as a function of pulse phase (cf. Wolszczan et al., 1981):

$$P_2(\varphi) = P_1 \left(\frac{{\rm d}\theta}{{\rm d}\varphi} \right)^{-1}, \tag{1.34}$$

where $\theta(\varphi)$ is the complex phase of the subpulse phase track at pulse phase φ.

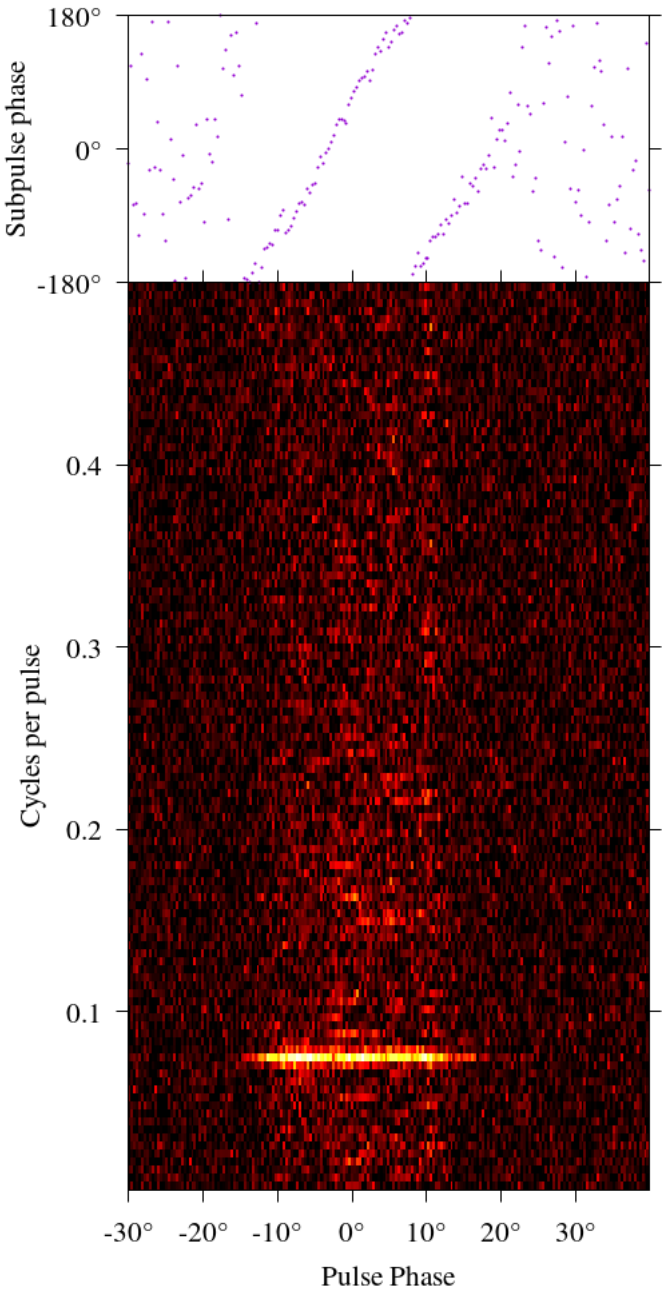

Figure 1.12 The LRFS of the pulse stack shown in Fig. 1.11, excluding the first 25 pulses (during which the separation of the drift bands is irregular). **Bottom**: The amplitudes of the LRFS, as defined in Eq. (1.33). The first row of pixels (containing the "DC" component of the Fourier transform) is not shown. The brightest feature occurs at approximately 0.075 cycles per pulse, corresponding to a value of $P_3 \approx 13.35$. **Top**: The phases of the brightest non-DC row of the LRFS. The slope of the curve encodes information about P_2.

An example of a subpulse phase track is shown in the upper panel of Fig. 1.12.

In general, P_2 is not a constant function of phase (manifest as non-zero curvature in the subpulse phase track). Since P_3 is a constant function of phase, a non-constant P_2 implies that the drift bands themselves ought to exhibit curvature, which is indeed common. However, often the pulse window is narrow enough that both the drift bands and the subpulse phase track appear linear in the visible phase range.

1.3.6.3 Drifting categories

Broadly speaking, we can classify subpulse modulation into four categories, based on the LRFS phases, following the convention of Basu et al. (2016):

1. *Positive drifting:* The subpulse phase track has a consistently negative slope across the phase window (corresponding to subpulses that move towards positive phases over time).

2. *Negative drifting:* The subpulse phase track has a consistently positive slope across the phase window (corresponding to subpulses that move towards negative phases over time).

3. *Amplitude modulated drifting:* The subpulse phase track is flat across the phase window (corresponding to subpulses whose amplitude is modulated over time, but which do not change their position in phase).

4. *Other:* Subpulse phase tracks that have a complicated structure, such as those few pulsars that exhibit both positive and negative drifting simultaneously in distinct phase ranges (*bi-drifting*) or otherwise hard to classify into the above three types, can be put into this category.

Basu et al. (2016) reported that 46% of their observational sample of 123 pulsars were observed to have some degree of subpulse modulation, with roughly equal numbers in each category. The remaining pulsars in their sample showed no discernible pattern in their subpulse modulation.

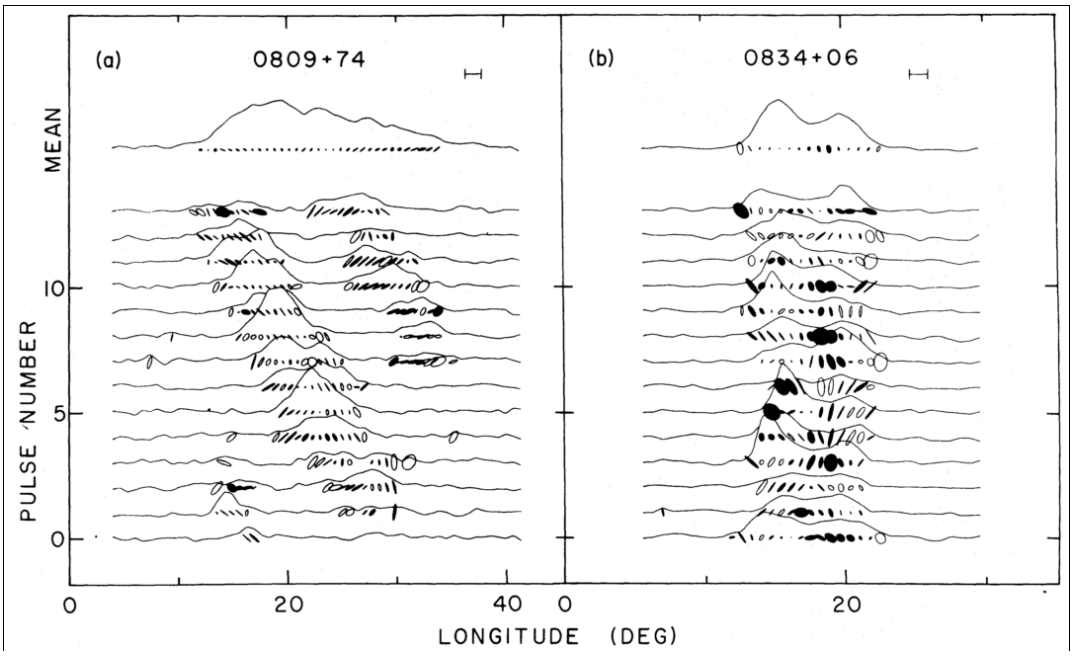

Figure 1.13 The polarisation of individual subpulses of PSRs B0809+74 and B0834+06. The polarisation ellipses are shown below the individual pulses (filled ellipses are left-hand circularly polarised; open ellipses are right-handed). The dependence of the polarisation angle on both pulse phase and subpulse phase is clearly evident in the case of B0809+74 (left). Image from Manchester et al. (1975).

1.3.6.4 The polarisation of subpulses

The investigation of the 12 pulsars conducted by Manchester et al. (1975) showed that the PPA of subpulses is both a function of pulse phase *and* subpulse phase. That is, the observed PPA depends on both the phase position of the emission within the pulse window, but also the phase position of the subpulse in which it resides (Fig. 1.13).

This fact is, on the face of it, difficult to reconcile with the basic RVM model introduced in Section §1.3.4.2, which predicts that the observed polarisation is purely a function of pulse phase. However, Ramachandran et al. (2002) argue that these early observations were severely limited by the sensitivity of the telescopes, and that, at least in the case of PSR B0809+74, the apparent gradual change in PPA over the duration of a subpulse is an artificial side-effect of mixing the two

OPMs. If the OPMs are offset in rotation phase, then an individual emission event (i.e. a single "pixel" of a pulse stack) will have a smaller or greater probability of being dominated by one of the OPMs depending on its longitude. When multiple drift bands are averaged together, as done, e.g., by Taylor et al. (1971), the resulting dependence of polarisation angle on longitude looks smooth, even though the polarisation angles of individual pixels are drawn from a distinctly bimodal distribution.

1.3.6.5 Aliasing of the drift rate

The enduring patterns of subpulse drifting strongly suggest that the physical structures that give rise to emission on subpulse time scales are long-lived. However, it does not necessarily follow that a single drift band contains emission from only a single emitting structure. Given that the subpulses drift in pulse phase, it is unclear whether a given subpulse has drifted only a little (so that it appears in the same drift band in the next pulse) or a lot (so that it appears in a different drift band). In the latter case, we say that the subpulse drifting is *aliased*.

If aliasing is present, both the drift rate, D, and the vertical separation P_3 give a false indication for how individual subpulses drift in pulse phase. If the true drift rate is D_{true}, then the time it takes for a given subpulse to arrive at the pulse phase of its predecessor (i.e. the "true" value of P_3) is

$$\frac{P_{3,\mathrm{true}}}{P_1} = \frac{P_2}{D_{\mathrm{true}}} = \frac{P_3}{P_1 + kP_3} \tag{1.35}$$

where P_3 is apparent, measured vertical spacing of the drift bands if aliasing was assumed *not* to be present, and $k \in \mathbb{Z}$ is the aliasing order.

The true drift rate, D_{true}, is an important prediction of several emission mechanism models, including the carousel model. Unfortunately, it is usually very difficult, if not impossible, to ascertain the value of k in practice, as there is very little to distinguish an aliased instance of subpulse drifting from an unaliased one.

1.3.6.6 Drift mode changing

An implicit assumption in the formation of pulse profiles (see Eqn. (1.6)) is that the average properties of the emission as a function of rotation phase does not change significantly over time. However, there are several pulsars for which this assumption does not hold (Bartel et al., 1982, and references therein). These pulsars appear to undergo a sudden change from one emission mode to the other, referred to as *mode changing*. When there is a high enough signal-to-noise that individual pulses can be seen, the sudden nature of the transition is evident (Fig. 1.14). Mode changes in dimmer pulsars can also be detected as statistically significant changes in the pulse profile over time. The time scale of the transition between modes, similar to nulling (see §1.3.3 below), is generally shorter than one pulsar rotation (Wang et al., 2007), but the duration of modes (i.e. between changes) can last anywhere from a few pulses to longer than days, according to the pulsar (e.g. Wang et al., 2012).

Mode changing, as just described, is a phenomenon that can occur in pulsars regardless of whether subpulse drifting is present. If, however, the mode change is distinguished by a measurable change in the drifting properties (i.e. the drift rate and/or P_3), then it is specifically referred to as *drift mode changing* (e.g. Redman et al., 2005). Like (non-drift) mode changing and nulling, drift mode changing occurs pseudo-randomly, with the average time between changes being different for different pulsars. The number of distinct drift modes present in a single pulsar ranges from zero (i.e. no evidence of drifting subpulses) to three (e.g. B0031−07, B1944+17).

1.4 Physical properties of neutron stars

Having surveyed the properties of intrinsic pulsar signals, we can now seek to build up a picture of the physical objects that give rise to them. We begin with a justification for the association of pulsars with neutron stars, an interpretation

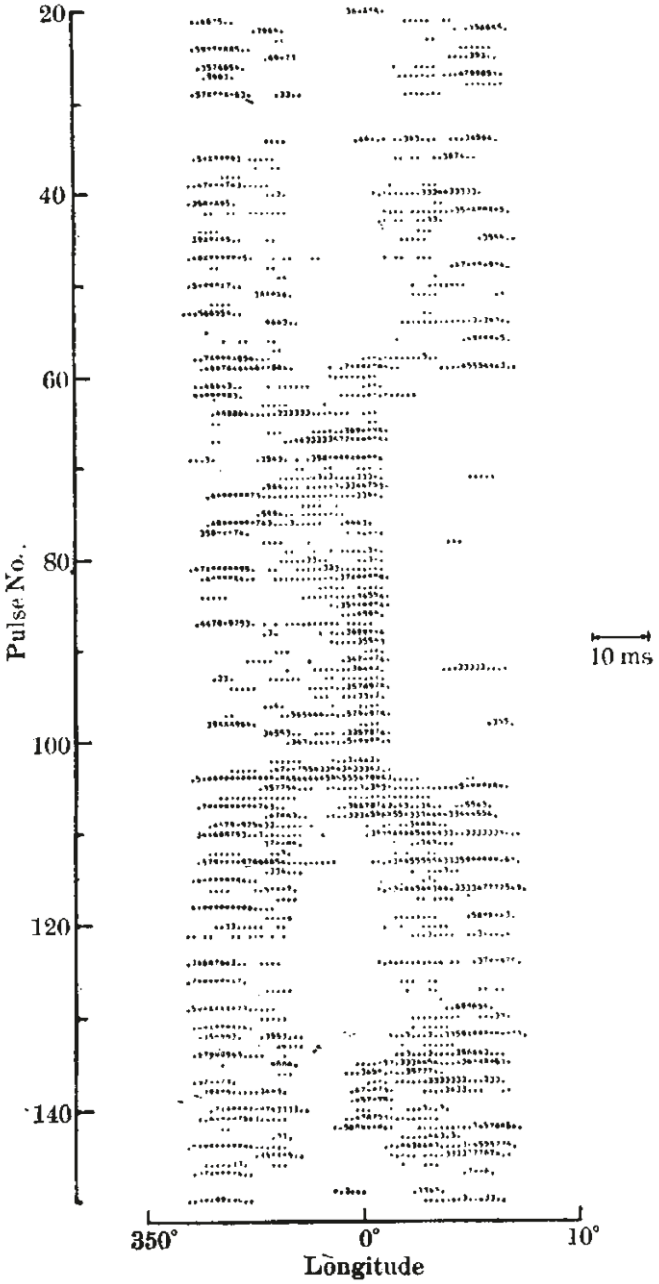

Figure 1.14 One of the earliest detections of the phenomenon of mode changing, as observed in PSR B1237+25, in which the statistics of pulse emission undergo rapid transitions between multiple states (Backer, 1970c).

which rapidly converged soon after the discovery of pulsars, and confirmed with the discovery of the Crab pulsar, B0531+21 (Gold, 1968, 1969).

1.4.1 Justification for neutron stars

Michel (1991) presents a concise argument for rotation of a single object as the cause of pulsar signals, and is summarised here. Naturally, rotation of a single object is not the only way to produce a time series of steady, regular pulses. Two alternatives are orbital motion (e.g. planetary motion) and regular, radial pulsation (e.g. Cepheid variables). Orbital motion can be ruled out by the fact that orbiting bodies, as they lose energy (by whatever means), will migrate to closer orbits with shorter periods, whereas the vast majority of pulsars have been measured to have $\dot{P}_1 > 0$ (see Fig. 1.2)—i.e. the periods are increasing. Radial pulsation can be ruled out by the fact that large bodies tend to distribute the oscillation energy among a spread of modes with different fundamental frequencies, whereas pulsars invariably exhibit a single, stable fundamental frequency. Also, objects pulsating at typical pulsar periods must be smaller than white dwarf stars and larger than the theoretical size of neutron stars, so it is unclear what these objects might be.

If we accept that rotation is the most probable explanation, then one may ask what possible kinds of object could be rotating. There is a natural upper limit to the size of the object set by the smallest observed period: the centrifugal force at the surface cannot exceed the gravitational attraction, or else the object would break apart. The smallest observed period is only a few milliseconds, corresponding to an upper radius limit of a few tens of kilometres. The only known object, either confirmed or theoretical, that fits these constraints is the neutron star.

1.4.2 The canonical pulsar

Although the properties of pulsars necessarily differ from each other, it is often useful to have a mental conception of properties of a "typical" pulsar. Therefore, we introduce the *canonical pulsar*, which has a mass of $1.4\,M_\odot$, a radius of 10 km, a rotation period of 1 s, and a surface magnetic field strength of 10^{12} G. These properties are chosen on both theoretical and observational grounds, and justified in the following sections. Real pulsars, of course, have different masses, radii, etc., all of which affect the observed radio emission to one degree or another, so it is important to remember that the canonical pulsar is merely a mathematical construct for conveniently describing average pulsar properties.

1.4.3 The gravitational field

The enormous density of neutron stars implies that the gravitational fields surrounding them must be extremely strong. For the canonical pulsar, the gravitational field strength at the surface is $\sim 2 \times 10^{12}$ N/kg, approximately 11 orders of magnitude greater than the Earth's. Neutron stars generate the strongest gravitational fields of any astrophysical object, with the exception of black holes. Therefore, they furnish natural laboratories for testing theories of gravity (especially General Relativity) in regimes that cannot be reproduced in terrestrial laboratories, nor which exist anywhere in the Solar System.

The gravitational effects on pulsar signals are twofold. Firstly, if the pulsar is in a binary system with a compact object, the gravitational effect of the companion can affect the times of arrivals of pulses originating at the pulsar and passing through the companion's gravitational well. This is called *Shapiro delay* and is one of the sources of timing error[10] that is corrected for in the TEMPO2 software package (see §1.2.5). Secondly, a pulsar's own gravitational field will affect the properties of its *own* emission, due partly to its effect on the motion of the

[10]The Shapiro delay caused by the Sun and the planets in the Solar System is also significant, and also modelled by TEMPO2.

emitting particles, and partly to its effect on the emitted photons as they climb out of the pulsar's gravitational well.

1.4.4 The magnetosphere

The term *magnetosphere* connotes both the ambient magnetic field of a neutron star and any matter embedded in or flowing though it. The question of whether or not the magnetospheres of neutron stars were filled was first addressed by Goldreich and Julian (1969), who provided an early proof that an empty magnetosphere was untenable. If the space surrounding the star was a vacuum, they argued, the electrostatic potential acting on the outer layer of particles on the surface would exceed the gravitational potential by several orders of magnitude, ripping particles off the surface and into the surrounding space. The argument is an argument by contradiction. Whether or not it is the surface itself that supplies the particles that ultimately fill the magnetosphere, or whether the particles are sourced some other way (e.g. pair-production or from the ISM) is irrelevant to the point being made here: The magnetosphere cannot be a vacuum.

In their seminal paper, they went on to calculate the space-charge density of the particles in the resulting magnetosphere (in SI units),

$$\rho(\vec{\boldsymbol{r}}) = -\frac{2\varepsilon_0 \vec{\boldsymbol{\omega}} \cdot \vec{\boldsymbol{B}}}{1 - r_\perp^2 / r_L^2}, \tag{1.36}$$

where $\vec{\boldsymbol{\omega}}$ is the angular rotation, $r_\perp$ is the component of $\vec{\boldsymbol{r}}$ that is perpendicular to the $\vec{\boldsymbol{\omega}}$ (i.e. the magnitude of the vector rejection of $\vec{\boldsymbol{r}}$ from $\vec{\boldsymbol{\omega}}$), and $r_L = c/\omega = cP/(2\pi)$ is the *light cylinder radius*, the distance at which the corotation speed is equal to the speed of light. Clearly, this quantity depends on the strength of the magnetic field itself, which, as the following section shows, is of order $10^{12}\,\mathrm{G}$ at the neutron star surface.

1.4.4.1 The magnetic field

The existence of a strong magnetic field can be inferred by the fact that the magnetic flux of the progenitor star must be conserved during its transition into a neutron star. If we take a typical stellar surface magnetic field strength of $B_* \approx 100\,\mathrm{G}$ (see, e.g., the catalogue in Bagnulo et al., 2015), then we can obtain a first-order estimate of the surface magnetic field strength of a neutron star by considering the reduction in surface area during its formation. A typical star with radius $\sim 10^9\,\mathrm{m}$ is reduced to a theoretical neutron star with radius $\sim 10^4\,\mathrm{m}$, implying a reduction of surface area by a factor of $(10^9/10^4)^2 = 10^{10}$. Consequently, the surface magnetic field at the surface of the neutron star must be of order $10^{10} \times 100\,\mathrm{G} \sim 10^{12}\,\mathrm{G}$, which is the value used for the canonical pulsar.

Magnetic fields of real pulsars are estimated by assuming that the slowing down of the pulsar's rotation is largely due to the loss of rotational kinetic energy to magnetic dipole radiation. In that case, the (equatorial) magnetic field is (e.g. Ostriker and Gunn, 1969; Lorimer and Kramer, 2005)

$$B \approx 3.2 \times 10^{19}\,\mathrm{G} \times \frac{1}{\sin\alpha}\left(\frac{P_1\dot{P}_1}{\mathrm{s}}\right)^{1/2}, \tag{1.37}$$

where α is the angle between the rotation axis and the (assumed dipolar) magnetic axis. The constant factor in Eqn. (1.37) is in general a function of pulsar mass and size, with the value stated above being derived for the canonical pulsar. For an ordinary, slow rotator with $P_1 = 1\,\mathrm{s}$ and $\dot{P}_1 = 10^{-15}$, the minimum magnetic field is $B \approx 10^{12}\,\mathrm{G}$. For a typical millisecond pulsar, whose spin-down rates are much smaller, $B \approx 10^8\,\mathrm{G}$. It should be noted that Eq. (1.37) represents a greatly simplified model of the pulsar's magnetic field, which can be seen by the fact that the expression blows up as α approaches zero. Nevertheless, it is sufficient to obtain an order-of-magnitude estimation of the magnetic field strength near the pulsar's surface.

The precise shape of the magnetic field of an idealised rotating star in a

vacuum was first worked out by Deutsch (1955). Without loss of generality, the field can be described in a right-handed coordinate system in which the z-axis is parallel to the rotation axis, and the x-axis is chosen such that the magnetic moment lies in the xz-plane. Its full expression is (Arendt and Eilek, 1998)[11]

$$\begin{aligned}\vec{\mathbf{B}}(\vec{r}) = {} & \mu\cos\alpha\,\boldsymbol{F}_1\frac{1}{r^5}+ \\ & \mu\sin\alpha\,\boldsymbol{F}_2\frac{\cos(\phi_*)}{r^3 r_L^2} + \mu\sin\alpha\,\boldsymbol{F}_3\left(\frac{\cos(\phi_*)}{r^5}+\frac{\sin(\phi_*)}{r^4 r_L}\right)- \\ & \mu\sin\alpha\,\boldsymbol{F}_4\frac{\sin(\phi_*)}{r^3 r_L^2} - \mu\sin\alpha\,\boldsymbol{F}_5\left(\frac{\sin(\phi_*)}{r^5}-\frac{\cos(\phi_*)}{r^4 r_L}\right)\end{aligned} \tag{1.38}$$

where μ is the magnetic dipole strength; $\phi_* = (r - r_p)/r_L$ is the time delay (measured in terms of rotation phase) of the neutron star's surface rotation (at stellar radius r_p) seen by an observer at radius r; and

$$\begin{aligned}\boldsymbol{F}_1 &= 3xz\,\hat{x} + 3yz\,\hat{y} + (3z^2 - r^2)\,\hat{z} \\ \boldsymbol{F}_2 &= (r^2 - x^2)\,\hat{x} - xy\,\hat{y} - xz\,\hat{z} \\ \boldsymbol{F}_3 &= (3x^2 - r^2)\,\hat{x} + 3xy\,\hat{y} + 3xz\,\hat{z} \\ \boldsymbol{F}_4 &= -xy\,\hat{x} + (r^2 - y^2)\,\hat{y} - yz\,\hat{z} \\ \boldsymbol{F}_5 &= 3xy\,\hat{x} + (3y^2 - r^2)\,\hat{y} + 3yz\,\hat{z}\end{aligned} \tag{1.39}$$

Essentially, the field is equivalent to a dipole field in a rotating frame of reference. Near the star ($r \ll r_L$), the relativistic correction required to transform from the rotating frame to an observer's inertial frame is minimal, and therefore the field is approximately equal to a rigidly rotating dipole field oriented according to the star's magnetic moment (which is not necessarily coincident with its rotation axis). In particular, if the radio emission region turns out to be located well within the light cylinder, then it is understood that the geometry of the field lines in that region can be locally well described by a simple dipole field.

Further afield ($r \gg r_L$), the field takes on the form of an oscillating radiation

[11] The notation follows Arendt and Eilek (1998), but several sign corrections have been made here. Compare also the Appendix of Dyks and Harding (2004).

field whose Poynting vector has both radial and tangential components. This is the dipole radiation discussed above, whose tangential component is responsible for robbing the star's angular momentum and increasing its rotation period P_1 over time.

The Deutsch field was constructed for a perfectly conducting star in a vacuum, which as argued above is certainly not the case for neutron stars. However, the equilibrium state of the magnetosphere in the co-rotating frame is believed to be "force-free", i.e. the magnetospheric plasma screens the electric fields. Therefore, the only forces acting on particles must be generated by the central star itself, which in the corotating frame is dipolar. This does not preclude the possibility that higher order multipole components of the magnetic field exist, which must certainly be the case if the internal structure of the neutron star is more complicated than the perfectly conducting sphere assumed by Deutsch. How higher order multipoles might affect pulsar emission is not well understood; however, since they fall off with radius much more rapidly than the dipole component, it is expected that even at moderate emission heights the dipole component dominates.

1.4.4.2 The viewing geometry

Pulsar geometry is defined by three principal axes: (1) the rotation axis, $\hat{\boldsymbol{\omega}}$; (2) the magnetic axis, $\hat{\boldsymbol{\mu}}$; and (3) the line of sight, $\hat{\boldsymbol{n}}$, which by convention points from the (centre of the) neutron star to the observer. The vectors $\hat{\boldsymbol{\omega}}$ and $\hat{\boldsymbol{n}}$ can be considered constant, but the direction of $\hat{\boldsymbol{\mu}}$ depends on the rotation phase, φ. The angle between the rotation and magnetic axes is the *inclination angle*, α, and is constant. The angle between the rotation axis and the line of sight, ζ, is also constant. Finally, the angle between the magnetic axis and the line of sight, Γ, is called the half-beam opening angle, and is a function of φ.

We are free to choose any phase angle as a reference point (i.e. where $\varphi = 0$), but the natural choice is the plane spanned by the rotation axis and the line of

sight, called the *fiducial plane*. In the observer's frame of reference, these two axes are non-moving vectors, and the fiducial plane is therefore fixed in space. The magnetic axis, on the other hand, is a rotating vector, and it passes through (i.e. is coplanar with) the fiducial plane twice per rotation. Of those two moments, the one in which the magnetic axis is pointing more towards the observer (i.e. $\vec{\boldsymbol{\mu}} \cdot \vec{\boldsymbol{n}} > 0$) is called the *fiducial point*. The angle that the magnetic axis makes with the line of sight at the fiducial point is called the *impact parameter* $\beta \equiv \Gamma(0) = \zeta - \alpha$.

At some arbitrary rotation phase φ, the three vectors $(\hat{\boldsymbol{\omega}}, \hat{\boldsymbol{\mu}}, \hat{\boldsymbol{n}})$ define a spherical triangle on the unit sphere. The relationship between these vectors and the angles between them are illustrated in 1.15. The angle subtended between the rotation axis and the line of sight at the magnetic pole is called the *magnetic azimuth*, and denoted in this thesis by the symbol σ. Finally, the angle subtended between the rotation axis and the magnetic pole "at" the line of sight is (as will be justified later) the polarisation position angle, PPA, denoted as ψ. As is true of all spherical triangles, at least three of the six sides and angles must be known to completely determine the geometry.

1.4.4.3 Last open field lines and the polar cap

The definition of the light cylinder radius (r_L, the perpendicular distance at which the corotation speed equals the speed of light) naturally divides magnetic field lines into two categories: (1) those which extend beyond the light cylinder and (2) those contained entirely within it. The first category, which we will call *open field lines* have the following properties:

1. They emerge from the neutron star's surface close to the magnetic axis.

2. Their shape and dynamics necessarily departs from that of a co-rotating dipole upon approaching the light cylinder radius.

3. They do not reconnect to the neutron star, but, upon escaping the light

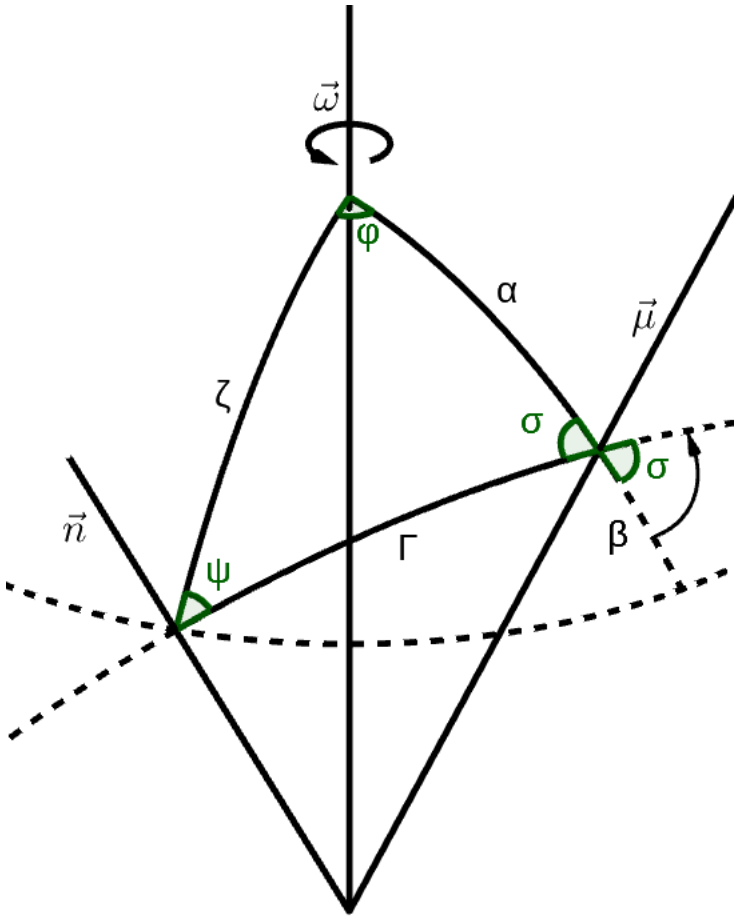

Figure 1.15 The spherical triangle formed by the rotation axis, $\hat{\boldsymbol{\omega}}$, the magnetic axis, $\hat{\boldsymbol{\mu}}$, and the line of sight, $\hat{\boldsymbol{n}}$. The other symbols are defined in the text.

cylinder, become components of the dipole radiation that propagate outwards in waves. It is this feature that justifies the term "open".

The second category, the *closed field lines*, have the complementary properties:

1. They emerge from the neutron star's surface closer to the equatorial regions.
2. They resemble a co-rotating dipole.
3. They reconnect to the neutron star, being entirely contained within the light cylinder.

The boundary between the two categories of field lines is marked by the so-called *last open field lines*. The intersection of these lines with the surface of

the neutron star defines the perimeter of the *polar cap*, from which all open field lines emerge. In the special case of the aligned rotator ($\alpha = 0°$), the polar cap is a circle that makes an angle $\theta = \arcsin\sqrt{r_p/r_L}$ with the magnetic axis, which for the canonical pulsar amounts to $\lesssim 1°$, or about 150 m on the surface. The shape of the polar cap becomes more complicated for inclined rotators ($\alpha > 0°$), but was shown to remain roughly circular (still with $\theta \approx \arcsin\sqrt{r_p/r_L}$) for the Deutsch field geometry (Arendt and Eilek, 1998).

1.5 Emission mechanisms

In the previous section, §1.4, we developed a physical picture of pulsars as rapidly rotating neutron stars with strong, roughly dipolar magnetic fields that were filled with charged particles. In this section, we show how charged particles are expected to behave in this environment, and how this can explain the general features of pulsar emission introduced in Section §1.3.

1.5.1 Particle motion

This sections begins with a review of charged particle motion in weak, uniform magnetic fields, and then extended to the strong, magnetic fields around pulsars. See, e.g., Jackson (1975) for a general treatment of electrodynamics and radiative processes.

In a uniform magnetic field $\vec{\boldsymbol{B}} = B\hat{\boldsymbol{z}}$ (and no electric field), a charged particle with charge q and arbitrary (non-relativistic) velocity $\vec{\boldsymbol{v}}$ will experience the Lorentz force

$$\vec{\boldsymbol{F}} = q\vec{\boldsymbol{v}} \times \vec{\boldsymbol{B}}. \tag{1.40}$$

Because this force is perpendicular to $\vec{\boldsymbol{B}}$, the particle will move in a gyratory motion whose radius of motion is

$$r = \frac{mv_\perp}{qB}, \tag{1.41}$$

where m is the particle's mass and $v_\perp$ is the component of the velocity that is perpendicular to $\hat{\boldsymbol{z}}$. The component of the velocity parallel to the magnetic field, $v_\parallel = \vec{\boldsymbol{v}} \cdot \hat{\boldsymbol{z}}$, remains constant, so that the shape of the trajectory is generally helical.

However, a gyrating particle is necessarily an accelerating one, and all accelerating charged particles emit radiation. The radiation associated with this motion is called *cyclotron radiation*, which causes the particle to lose energy at a rate

$$\frac{\mathrm{d}E}{\mathrm{d}t} \propto B^2 v_\perp^2. \tag{1.42}$$

The generalisation of Eq. (1.42) for relativistic particles is *synchrotron radiation*. For electrons (or positrons) the radiative energy loss per particle is

$$\frac{\mathrm{d}E}{\mathrm{d}t} \approx -159\,\mathrm{W} \times \left(\frac{B}{10^{12}\,\mathrm{G}}\right)^2 \beta_\perp^2 \gamma^4, \tag{1.43}$$

where $\beta_\perp = v_\perp/c$ is the perpendicular speed of the particle normalised to the speed of light, and $\gamma = 1/\sqrt{1 - v^2/c^2}$ is the particle's Lorentz factor.

As the particle loses energy, its radius of gyration decreases, as implied by Eq. (1.41). For strongly relativistic particles, $\beta_\perp \approx 1$ and $\gamma \gg 1$, implying a very rapid decay of the gyration radius. This process does not continue indefinitely, however, because the energy levels are quantised—in this context, the energy levels are called *Landau levels*. Like the energy levels in the quantum harmonic oscillator, there is a minimum allowed Landau level, which, for electrons and positrons, has energy

$$E_0 = \frac{1}{2}\hbar\omega_c \approx 9.27 \times 10^{-16}\,\mathrm{J} \times \left(\frac{B}{10^{12}\,\mathrm{G}}\right), \tag{1.44}$$

where $\omega_c = qB/m$ is the gyration frequency of the particle. The time scale for

the decay to the lowest level is (Luo, 1998)

$$\tau \simeq 10^{-16}\,\mathrm{s} \times \left(\frac{B}{10^{12}\,\mathrm{G}}\right)^{-2} \gamma, \tag{1.45}$$

so that the perpendicular energy is radiated away extremely rapidly and the particle is only free to move in a direction parallel to the local magnetic field lines, analogous to beads on a wire. The presence of a magnetospheric plasma (which was argued to exist in Section §1.4.4) guarantees that the quantity $\vec{\boldsymbol{E}} \cdot \vec{\boldsymbol{B}}$ vanishes in the reference frame corotating with the pulsar (Goldreich and Julian, 1969; Ruderman and Sutherland, 1975). In such regions, particles will not experience any significant acceleration parallel to the local magnetic field. Taking all of the above considerations together, it is argued that the magnetospheric plasma has a very constrained motion: it must corotate with the pulsar, and its constituent particles are only permitted to move along the magnetic field lines (which are also corotating), and are not allowed to "cross" field lines transversely.

The picture developed so far is widely accepted within the pulsar community, but is insufficient to account for the observed radio emission. The only significant radiation that has been explicitly mentioned so far (i.e. the synchrotron radiation associated with the decay to the lowest Landau level, Eq. (1.43)) is extremely energetic, well above observed radio frequencies ($\nu \gg 1\,\mathrm{GHz}$; Melrose, 1979). Thus the question is, what other forces are present to provide the acceleration required to generate the observed radio spectra of pulsars?

1.5.2 Curvature radiation and the rotating vector model (RVM)

One of the earliest considered emission mechanisms invoked the large-scale curvature of the magnetic field lines as the source of the emission-generating acceleration, termed *curvature radiation*. Curvature radiation shares many of the same characteristics as synchrotron radiation (Jackson, 1975):

1. The spectrum peaks near (but drops off rapidly above) the *characteristic frequency*,

$$\nu_c = \frac{3\gamma^3 c}{4\pi\rho}, \tag{1.46}$$

where ρ is the radius of curvature of the particle's trajectory.

2. The emission is beamed in the direction of the particle's velocity at the moment of emission with a characteristic beam width proportional to $1/\gamma$.

3. The emission is strongly polarised in the plane of motion, with a negligible amount of the radiation polarised perpendicular to it.

1.5.2.1 Observable predictions

Taking these properties together with the dipole geometry of the magnetic field provides, in one fell swoop, an explanation for several broad features of pulsar emission (Radhakrishnan and Cooke, 1969). First and foremost of these is the fact that the observed emission is pulsed. If the emission region is restricted to a sufficiently small volume of the magnetosphere (limiting the local magnetic field to a relatively small range of directions), the strong beaming of the emission from individual particles implies that the "global" emission will also be beamed. As long as the global beam axis is offset from the rotation axis, the beam will sweep through some area of the (pulsar's) sky with a period equal to the pulsar's rotation, analogous to a lighthouse. If the emission region is centred on the magnetic axis, then the observed pulse width, W, of a given pulsar will then be a function of the inclination angle, α, the half beam opening angle, Γ, and the viewing angle, ζ. Using elementary spherical geometry, these are related via

$$\cos\Gamma = \cos\alpha\cos\zeta + \sin\alpha\sin\zeta\cos\left(\frac{W}{2}\right). \tag{1.47}$$

Secondly, the negative spectral indices can be at least qualitatively explained by the fact that the individual particle beam width is wider at low frequencies

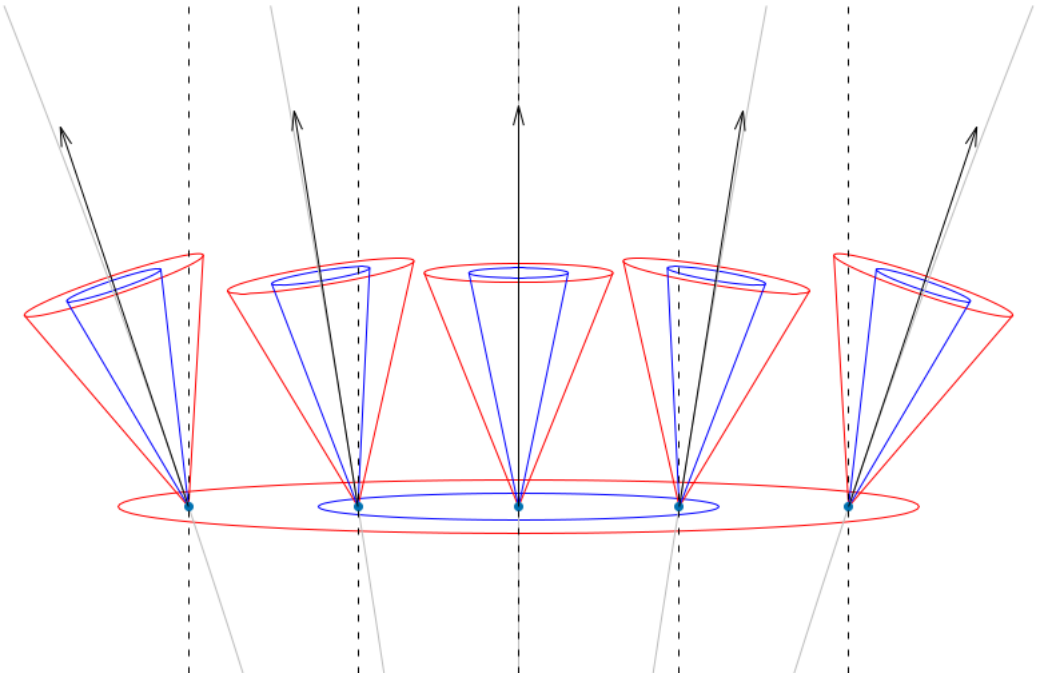

Figure 1.16 Particles streaming along neighbouring, diverging dipolar field lines (grey solid lines) will emit radiation that is beamed towards their direction of motion (black arrows). The width of the beam is proportional to $1/\gamma$, so higher frequencies beams (blue) will be narrower than their lower frequency counterparts (red). For a given line of sight (dashed black lines), the cross-sectional area of the visible emission region (large ellipses at the bottom of the figure) and hence the number of visible particles will be larger at lower frequencies, resulting in a negative spectral index.

and narrower at high frequencies. At a fixed moment in time, an observer will detect radiation from all particles whose emission angular range (which goes as $1/\gamma$) includes the line of sight. This implies that the volume of an emission region that contributes radiation towards the observer is proportional to the square of the particle beam width. Assuming a roughly equal charge density in the regions involved, more radiation would therefore be detected at lower frequencies by virtue of the fact that a greater number of particles are found within the larger volume sampled[12]. This is schematically illustrated in Fig. 1.16.

Thirdly, the radius-to-frequency mapping emerges as a consequence of the dipolar geometry of the magnetic field. To a first order approximation (i.e. ne-

[12]Note that this does not explain low-frequency spectral turnovers.

glecting rotation effects), the curvature of the particle's trajectory is equal to the curvature of the magnetic field line on which it resides, which increases with radial distance, at least in the inner regions of the magnetosphere. Thus, as a given particle streams outward along its unique field line, the characteristic frequency of its curvature radiation, Eq. (1.46), necessarily decreases at greater altitudes, where the magnetic field line tangent (and hence the emission direction) makes a larger angle with the magnetic axis.

The relation between frequency and pulse width (or profile component separation) can be partially derived as follows. A dipolar field line whose maximum extent is at a distance R from the origin has the formula in polar coordinates

$$r = R \sin^2 \theta \tag{1.48}$$

where θ is measured from the magnetic axis. The radius of curvature is then given by

$$\rho = \frac{r(3\cos^2\theta + 1)^{3/2}}{3\sin\theta(\cos^2\theta + 1)}. \tag{1.49}$$

In regions close to the magnetic axis ($\theta \ll 1$),

$$\rho \approx \frac{4r}{3\theta} \approx \frac{4\sqrt{rR}}{3} \approx \frac{4R}{3}\theta, \tag{1.50}$$

where the latter approximations come from the small angle approximation of Eq. (1.48), $r \approx R\theta^2$. This shows that ρ increases with distance from the origin along a given field line (i.e. fixed R). The half beam opening angle is equal to the tangent of the magnetic field,

$$\tan\Gamma = \frac{3\sin\theta\cos\theta}{3\cos^2\theta - 1}, \tag{1.51}$$

or, in the same small angle approximation,

$$\Gamma \approx \frac{3}{2}\theta \approx \frac{9}{8R}\rho. \tag{1.52}$$

Substituting Eqs. (1.52) and (1.50) into the formula for the characteristic frequency (Eq. (1.46), which we now identify with the observing frequency, $\nu \approx \nu_c$),

$$\nu \approx \frac{27\gamma^3 c}{32\pi R\Gamma}. \tag{1.53}$$

Beyond Eq. (1.53), a testable prediction of how the integrated profile changes with frequency requires some extra constraints on ν, R, γ and Γ. For instance, if one considers only emission restricted to field lines with some fixed R (e.g. the last open field lines, $R \approx r_L = cP/(2\pi)$ for small inclination angles, α) and fixed γ (e.g. $\gamma = 1000$), then Eq. (1.53) becomes

$$\nu \approx 1.69\,\mathrm{GHz} \times \frac{1}{\Gamma}\left(\frac{\gamma}{1000}\right)^3 \left(\frac{P}{\mathrm{s}}\right)^{-1}. \tag{1.54}$$

Recall that the half beam opening angle is related to the pulse width (and, if applicable, to the separation between profile components) via (1.47). Some examples of RFM curves produced by this equation are illustrated in Fig. 1.17. It should be remembered, however, that the values of R and γ here were arbitrarily chosen, and that in all likelihood emission occurs on a range of field lines and a range of particle energies. Various specific RFM relations have been advanced (e.g. $\nu \propto r^{-3/2}$ in Ruderman and Sutherland, 1975) which have specific implications for the location of the emission regions, but these continue to be debated in the literature and we do not explore these further here. For our purposes, it is sufficient to note that the curvature radiation model is capable of producing predictions about how the integrated profile evolves as a function of observing frequency, which, at least, qualitatively agree with observations (cf. Fig. 1.17 and Thorsett, 1992).

Finally, curvature radiation and the dipolar field line geometry can explain the characteristic shapes of the PPA curves described in Section §1.3.4.2. Indeed, curvature radiation was originally invoked for precisely this purpose (Radhakrishnan and Cooke, 1969). Recall that curvature radiation is inherently strongly

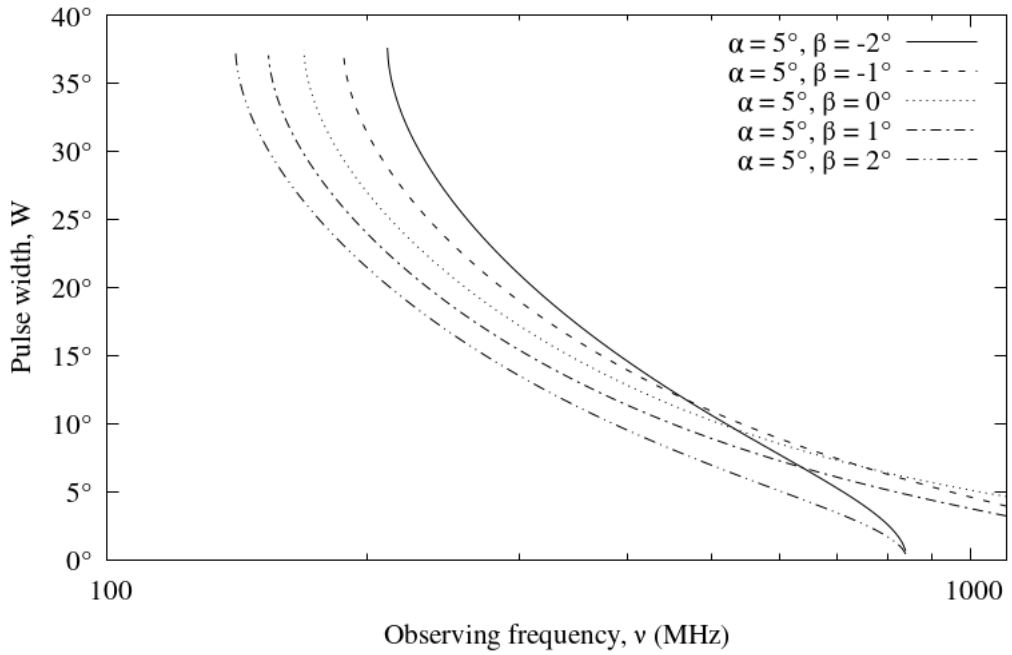

Figure 1.17 A prediction of the width of the pulse window as a function of observing frequency, for particles with $\gamma = 1000$ streaming along the last open field lines ($R = r_L$) for a nearly-aligned rotator ($\alpha = 5°$). The observed RFM depends also on the impact angle of the line of sight $\beta = \zeta - \alpha$, a few values of which a plotted. Compare these curves with, e.g., Thorsett (1992).

linearly polarised in the plane of motion, which (neglecting rotation effects) is equal to the plane of the magnetic field line from which it emerges. As the pulsar rotates through the phase angle φ, the "visible" magnetic field lines are precisely those whose planes are instantaneously parallel to the line of sight (up to the particle beam width), and the observed PPA would equal the angle of the magnetic field line projected onto the plane of the sky. This justifies the identification of the angle ψ in Fig. 1.15 with the PPA. Thus, as the pulsar rotates, ψ rotates according to the spherical geometric relationship between α, ζ (which are both fixed), and φ. On account of the rotation of ψ, the model has become known as the *rotating vector model* (RVM)[13].

The spherical geometry implied by the RVM was first stated explicitly by

[13]It should be noted that Radhakrishnan and Cooke never referred to this model by the name "RVM", but we use it in this thesis because it has become the de facto name within the pulsar community.

Komesaroff (1970). For a dipolar magnetic field, the PPA is

$$\psi = \arctan\left(\frac{\sin\alpha\sin\phi}{\sin\zeta\cos\alpha - \cos\zeta\sin\alpha\cos\phi}\right), \tag{1.55}$$

from elementary spherical geometry. The steepest slope of the PPA curve occurs at the fiducial point, and is

$$\left.\frac{d\psi}{d\varphi}\right|_{\varphi=0} = \frac{\sin\alpha}{\sin\beta}. \tag{1.56}$$

The primary usefulness of this model is that the PPA curve can be fitted to Eq. (1.55) to deduce the angles α and ζ (see, e.g., Rankin, 1993). If the pulse window is small enough that only a small section of the total PPA curve can be observed, the constraints on α and ζ may be rather poor, but usually the point of steepest slope can be identified, and, by virtue of Eq. (1.56), many geometries can be ruled out.

1.5.2.2 Criticisms of the curvature radiation model

Curvature radiation as the main emission mechanism has been criticised on both theoretical and observational grounds. The main theoretical argument comes from the difficulty of making the curvature radiation produce coherent emission, since incoherent curvature emission cannot produce the observed brightness temperatures (Jackson, 1975). An early idea came from Ruderman and Sutherland (1975), who noted that if the local density of emitting particles was sufficiently high, spatially localised particles would emit in phase, and the observed intensity would grow in proportion to N^2, where N is the number of particles packed within a volume $V < \lambda^3$, where $\lambda = c/\nu$ is the wavelength of the emission. To accomplish this, they invoked a mechanism by which very high energy particles cause the relatively lower energy particles to bunch together (also see Cheng and Ruderman, 1977). Later, mechanisms that invoked maser emission were also suggested (e.g. Beskin et al., 1988; Luo and Melrose, 1992; Luo, 1993; Luo and

Melrose, 1995).

Melrose and Yuen (2016) and Melrose (2017) summarise the main categories of coherent emission mechanisms[14]. In the following, it is understood that the particles that constitute the magnetosphere will, at any given moment, have some distribution in position, in velocity, and in acceleration, $f(\mathbf{r}, \mathbf{v}, \mathbf{a})$.

Emission by bunches : If there is a sufficiently large number of particles occupying a small enough region of the phase space $\mathbf{r} \otimes \mathbf{v}$ ($\otimes$ is the outer product), electromagnetic waves emitted from each particle will have the same phase and direction, resulting in a superposed wave with a power that goes as N^2, where N is the number of particles in the bunch. The size of the physical region containing the particles cannot exceed the wavelength of the emission, or else the emission of particles at one spatial extreme will decohere with emission of particles at the other, placing very strict limits on the allowed densities for producing this type of coherent emission. If more than one species of particle is considered, the bunching must occur in the phase space $\mathbf{r} \otimes \mathbf{p}$, where $\mathbf{p}$ is the momentum of the particle.

Reactive instability : Plasma waves can result in correlated motions of constituent particles that are separated by physical distances longer than the wavelength of the emission, relaxing the requirement of emission by bunches such that the particles only need to be confined to a small region in $\mathbf{v}$ (or $\mathbf{p}$, but not necessarily in $\mathbf{r}$.

Kinetic instability : If there is an external source of energy, the conditions for stimulated emission may be achieved, not unlike astrophysical masers. In this view, the requirement for bunching in $\mathbf{r}$ is again relaxed, and the energy (or momentum) distribution must exceed the local stable equilibrium for sustaining the resulting coherent radiation.

[14]Note that this discussion is not limited to coherent curvature radiation, but other forms of coherent emission as well.

(Melrose, 2017) argues that of the three, kinetic instability is the most likely, since the other two are dynamically unstable in the sense that under magnetospheric conditions, they would naturally decay into the third. It is widely acknowledged, however, that the behaviour of relativistic plasmas is not yet sufficiently well understood to provide a firm theoretical basis for theories of pulsar emission (including coherent curvature radiation).

Curvature radiation is also criticised on the basis that the body of pulsar observations contain many examples which depart from the model predictions. For example, PPA curves of many pulsars do, in fact, depart significantly from the shape defined by Eq. (1.55) (e.g. Noutsos et al., 2015; Mitra et al., 2016), particularly for MSPs (Xilouris et al., 1998). In this regard, OPMs have already been mentioned, which have no natural explanation within the context of curvature radiation. However, even allowing for OPM jumps, other deviations persist. Some of these deviations can be modelled by appropriate extensions to the RVM, most prominently relating to secondary effects of converting between the corotating frame of reference (in which the above treatment of the RVM is traditionally derived) to the observer's inertial frame. Some of these are explored further in the next section.

1.5.2.3 Extensions to the RVM

In the corotating frame of reference, the conditions in the magnetosphere are determined by the magnetic field, which is axisymmetric about the magnetic axis. Therefore, the emission beam is expected to also be axisymmetric about the magnetic axis. For example, multi-component profiles may be a result of the emission beam being a hollow cone, or a set of nested cones, which the line of sight may traverse in various ways to produce symmetrical sets of components about the fiducial point (Rankin, 1983, and other papers in the series). However, profile components are rarely symmetrical: pairs of "matched" components often differ in intensity, width, and "distance" from the fiducial point (obtained from

the PPA curve) or from some more centralised component.

Several important effects were identified that would produce profile asymmetries. The first recognises that emission produced in different parts of the magnetosphere will take different amounts of time to reach the observer by virtue of the fact that the direct line-of-sight distance to the observer is different from emission region to emission region. More specifically, two photons simultaneously emitted at radii $r_1 < r_2$ respectively will arrive at the observer's telescope separated by time $\Delta t_{\rm ret} \approx -\Delta r/c = -(r_2 - r_1)/c$. The equivalent time difference expressed in terms of rotation phase is (Dyks et al., 2004)

$$\Delta\varphi_{\rm ret} = \frac{2\pi\Delta t_{\rm ret}}{P} \approx -\Delta r', \tag{1.57}$$

where $r' \equiv r/r_L$ is normalised to the light cylinder radius. Thus, light emitted at lower magnetospheric altitudes would appear to arrive at a retarded pulse phase relative to light emitted at higher altitudes at the same time and magnetic azimuth. This effect, called *retardation*, is purely a function of geometry and the finite speed of light.

Another effect, called *aberration*, is a consequence of transforming from the corotating frame to the observer's inertial frame. In the corotation frame, all points along a given magnetic field lines, as well as all other, coplanar field lines, emit radiation in the same plane, namely, the plane of the field line. However, the corotation velocity at higher altitudes is larger than at lower altitudes, and so the Lorentz transformation between frames implies that the higher altitude emission undergoes a greater degree of relativistic aberration than the lower altitude emission. The aberration apparently bends the emission out of the plane of the field line, on the "leading" side of the pulsar's rotation. Thus, the net effect is qualitatively similar to that of retardation: light emitted at lower magnetospheric altitudes would appear to arrive later than light emitted at higher altitudes, all else being equal. Coincidentally, it is quantitatively similar as well (a proof is

provided by Dyks et al., 2004), with

$$\Delta\varphi_{\rm ab} \approx -\Delta r', \tag{1.58}$$

so that the joint effects of both aberration and retardation (often abbreviated to "AR effects") shift components by $\Delta\varphi \approx -2\Delta r'$ (e.g. Gangadhara and Gupta, 2001).

Other important effects that have been investigated over the decades include the effect of the frame transformation on the PPA curve (Blaskiewicz et al., 1991; Dyks, 2008), the curvature of the particles' trajectories (Thomas and Gangadhara, 2007; Thomas et al., 2010), and the distortion of the magnetic field due to the torque responsible for pulsar slow-down (called *rotational sweepback*; Shitov, 1983; Dyks and Harding, 2004). However, even all of these effects combined do not completely explain the variety of observed pulse profiles and PPA curves.

1.5.3 The carousel model

Nothing discussed so far in this section has addressed the observational fact that subpulse drifting is common in pulsars (see Section §1.3.6). Indeed, the curvature radiation model and its geometric corollaries (the hollow/nested cones), in and of themselves, do not even offer an explanation for pulse-to-pulse variability, including the existence of subpulses and other structures at finer time scales. In this section, we introduce the carousel model, originally introduced by Ruderman and Sutherland (1975) to explain subpulse drifting, which has enjoyed a continued, albeit controversial, popularity up until the present time (e.g. Edwards, 2006).

The original statement of the carousel model was given in the context of coherent curvature radiation by particle bunching. Ruderman and Sutherland (1975) argue that the charge around a rotating neutron star would be distributed in such a way that a subset of the open field lines, whose footpoints are near the outer perimeter of the polar cap, would experience a net negative outward current

as charges escape from the magnetosphere. The resulting charge depletion along those lines facilitates the build-up of a voltage potential gap near the surface, called the *polar gap*. For the canonical pulsar, they calculated that the potential across this gap would be $\sim 6.6 \times 10^{12}\,\mathrm{V}$; any charge entering this region would be accelerated to ultra-relativistic speeds in a very short time. The high energy curvature radiation of these particles would catalyse the spontaneous production of a (slightly less energetic) electron-positron pair on neighbouring field lines, which, in turn, become the seeds for two new pairs by the same process. The resulting pair-production "avalanche" finally results in a population of particles which are not energetic enough to instigate new pair-production, but which are in the correct energy regime to produce curvature radiation in the radio part of the spectrum—i.e. the radiation we ultimately observe.

In this model, the polar gap plays a key role in the dynamics of charged particles near the stellar surface. The pair production avalanche not only produces outward-flowing particles that escape the magnetosphere, but also inward-flowing particles that serve to "short the circuit" and temporarily close the voltage gap. Because pair-production in one location induces pair-production on neighbouring field lines, the resulting avalanches occur over some finite area of the surface, called a *spark event*, or more concisely, a *spark*. The duration of a spark is set by the time scale of the avalanche process (i.e. the time it takes an initial seed particle to diffuse its energy into a population of secondary particles) and the time it takes the (now depleted) local voltage gap to build up again via charge outflow to a level where it can again support sustained pair-production, while the its spatial extent is set by the (relatively long range) depression of the voltage gap on surrounding field lines, which inhibits pair-production there. During the lifetime of a spark, its constituent charges move in an azimuthal direction (relative to the magnetic axis) due to the electric and magnetic field present inside the polar gap. The velocity of this azimuthal motion, the so-called $\vec{\boldsymbol{E}} \times \vec{\boldsymbol{B}}$ drift,

is given by

$$\vec{\boldsymbol{v}} = \frac{\vec{\boldsymbol{E}} \times \vec{\boldsymbol{B}}}{B^2}. \tag{1.59}$$

Because the presence of one spark affects the likelihood of a spark forming nearby in the polar gap, and because of the common $\vec{\boldsymbol{E}} \times \vec{\boldsymbol{B}}$ drift experienced everywhere in the polar gap, it is reasonable to suppose that the global pattern of sparks is both regular and quasi-stable, rotating around the magnetic axis at the drift velocity in Eq. (1.59). The resulting picture of equally spaced spark events rotating in a circle around a common axis resembles a fairground carousel, justifying the name *carousel model*.

The connection between the spark carousel and subpulse drifting is direct. A magnetic field line is called *active* if, at some given moment in time, its footpoint is the site of spark activity, rendering the field line capable of producing observable coherent curvature radiation. Any given field line will therefore become periodically active and inactive as the carousel rotates beneath it. Consequently, the geometry of the emission beam would mirror that of the sparks: a carousel of *beamlets* (or *subbeams*) circling around a common point in the pulsar's sky, instead of a static cone (or cones) of emission. With each pulsar rotation, the emission beam would present a differently rotated pattern of beamlets as the line of sight cuts through it, resulting in a temporally displaced pattern of subpulses.

By virtue of Eq. (1.59), the carousel model makes very specific predictions of the carousel rotation time and the observed drift rate. Let P_4 be the carousel rotation period (i.e. the time it takes a single spark to make one whole revolution about the magnetic axis). If the carousel consists of n equally-spaced and equally-shaped sparks, then the carousel will return to the same apparent configuration after $1/n$ rotations. Therefore, the (unaliased) period of the repeating subpulse pattern will be

$$P_{3,\mathrm{true}} = \frac{P_4}{n}. \tag{1.60}$$

In the general case of an aliased drift rate with aliasing order k, the relationship

between the carousel rotation period and the measured vertical spacing of the drift bands, P_3, is

$$\frac{P_4}{P_1} = \frac{nP_{3,\mathrm{true}}}{P_1} = \frac{nP_3}{P_1 + kP_3}. \tag{1.61}$$

Ruderman and Sutherland (1975) also derive P_4 from Eq. (1.59) for the expected electric and magnetic fields in the polar gap of a canonical pulsar, showing it to be approximately

$$P_4 \approx 5.7\,\mathrm{s} \times \left(\frac{P_1}{\mathrm{s}}\right)^{-1/2} \left(\frac{\dot{P}_1}{10^{-15}}\right)^{1/2}. \tag{1.62}$$

Measuring P_4 for pulsars with drifting subpulses therefore constitutes a first-order test for the carousel model. Unfortunately, the aliasing order, k, and the number of sparks, n, are not *a priori* known, and are difficult to determine. In a few cases where P_4 has been measured, the evidence suggests that the observed carousel rotation rate is much slower than predicted by Eq. (1.62) (e.g. Mitra and Rankin, 2008), although it remains unclear if the correct aliasing order was assumed in these cases.

Eq. (1.61) connects the carousel rotation period, P_4, with measured periodicity of the subpulse modulation pattern, P_3. The connection between P_4 and P_2 is at once more direct and more subtle. When two or more subpulses appear in the same pulse, it is because the line of sight is cutting through multiple beamlets. Thus, there is a direct connection between the "spacing" of the subpulses, which can be measured directly, and the spacing of the beamlets in the carousel. Like P_3 above, the relation between P_2 and P_4 depends on n and k, but it also depends on the viewing geometry (α and ζ), and the pulse phase (φ) according to the spherical triangle shown in Fig. 1.15. The exact relation is derived in Chapter 5.

The carousel model is most applicable to pulsars whose subpulse drifting modulation is stable on long time periods. This is because the electric and magnetic fields that dictate conditions in the polar gap are themselves expected to be stable. However, several features of subpulse drifting reviewed in Section §1.3 show changes on short time scales, e.g. nulling, drift mode changes, and (more grad-

ual) changes of the drift rate after a null sequence. In the context of the carousel model, these phenomena seem to indicate equally sudden changes in either the magnetospheric conditions or the carousel configuration and dynamics, which would require revisions of (or at least extensions to) the carousel model in order to properly account for them. It is still unclear just how widespread some of these features are (as most pulsars are not bright enough to see in single pulses), and therefore whether they represent "normal" behaviour or whether they are present in only a few pathological cases.

1.5.3.1 The cartographic transform

Using spherical geometry, Deshpande and Rankin (1999, 2001) derived the one-to-one relationship between the "pixels" of a pulse stack and the location of the line of sight in a coordinate frame centred on the magnetic axis and corotating with the carousel. The transformation, which requires knowledge of the viewing geometry (α, ζ) and the carousel rotation period (P_4), maps the (possibly aliased) drift bands onto their respective parent sparks, and displayed in magnetic polar coordinates. The transformation[15] is (cf. Deshpande and Rankin, 2001)

$$\sigma = \pm\sigma_{\rm rot} \pm \sigma_{\rm trans}, \tag{1.63}$$

where the signs on each term depend on the drift direction and the slope of the PPA.

$$\sigma_{\rm rot} = \frac{2\pi}{P_4}\left(p - p_0 + \frac{\varphi}{2\pi}\right), \tag{1.64}$$

$$\sigma_{\rm trans} = \arcsin\left(\frac{\sin\zeta\sin\varphi}{\sin\Gamma}\right), \tag{1.65}$$

where p is the pulse number, p_0 is a reference pulse, φ is measured relative to the fiducial point (usually, but not always, assumed to lie at the centre of the profile), and where one expression relating the half beam opening angle to the

[15]The notation has been changed to conform with the conventions used in this thesis.

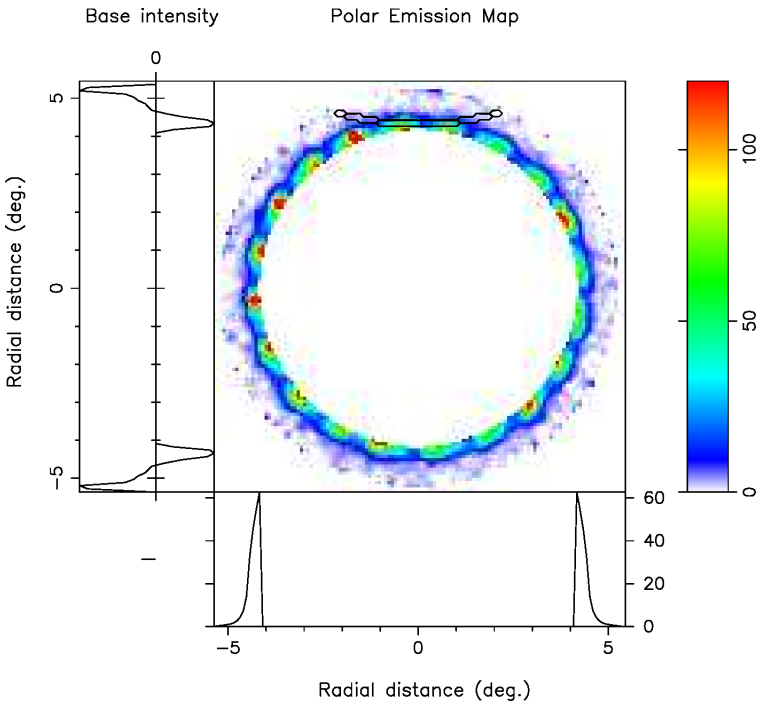

Figure 1.18 The result of the cartographic transform defined by Eq. (1.63), applied to a sequence of B0943+10 pulses. The figure is taken from Deshpande and Rankin (2001).

other terms is

$$\Gamma = 2 \arcsin \sqrt{\sin^2\left(\frac{\varphi}{2}\right) \sin\alpha \sin\zeta + \sin^2\left(\frac{\beta}{2}\right)}. \tag{1.66}$$

An example showing the result of the transform is shown in Fig. 1.18.

1.6 This thesis: direction and scope

The cartographic transform (§1.5.3.1) is potentially a powerful tool for investigating the emission mechanism. At a single observing frequency, the maps generated by the transform provide a window into the average emission processes at whichever emission height corresponds to that frequency according to the RFM. Moreover, they reveal the carousel configuration (i.e. the number and size of sparks) and dynamics (i.e. the carousel rotation rate), which are believed to be

determined by physical conditions just above the neutron star's surface. If simultaneous observations can be made over a wide frequency range or at widely spaced frequencies and the cartographic transform applied, the emission columns above individual sparks can be sampled at multiple heights, providing much-needed insight into the relationship between the local magnetic field and the conditions required to produce coherent radiation.

This ambitious program of mapping out the emission beams of individual sparks at multiple frequencies simultaneously has already begun to be carried out. Maan et al. (2013) have used a multi-band receiver designed for the Green Bank Telescope to take simultaneous observations of B0809+74 in four distinct frequency bands spanning 117-330 MHz. An image of their results, after applying the cartographic transform and arranging them schematically according to relative emission height, is reproduced in Fig. 1.19: The choice of Maan et al. (2013) to trial the new multi-band system on B0809+74 was deliberate: it is very bright, and its subpulse modulation pattern is well known for its long-term stability.

The original motivation of this thesis was to continue this program, using multiple telescopes in concert (described in Chapter 2) to observe a selection of bright pulsars that exhibit subpulse drifting, in order to map out their respective emission beams in a similar way to Maan et al. (2013). However, it quickly became apparent that the stability of the subpulse drifting behaviour required by the cartographic transform is relatively rare, and that the stability is often interrupted and influenced by null sequences. Such was the case for B0031−07, which stood out as an archetypal example of subpulse drifting behaviour that differed in many respects from the behaviour expected from the original carousel model of Ruderman and Sutherland (1975). The attention was thus turned towards characterising these exceptions, and to explore the ways in which the carousel model might be extended in order to accommodate them.

Chapter 3 (published as McSweeney et al., 2017) begins this investigation by measuring how the drift rate of B0031−07's subpulses changes during the course

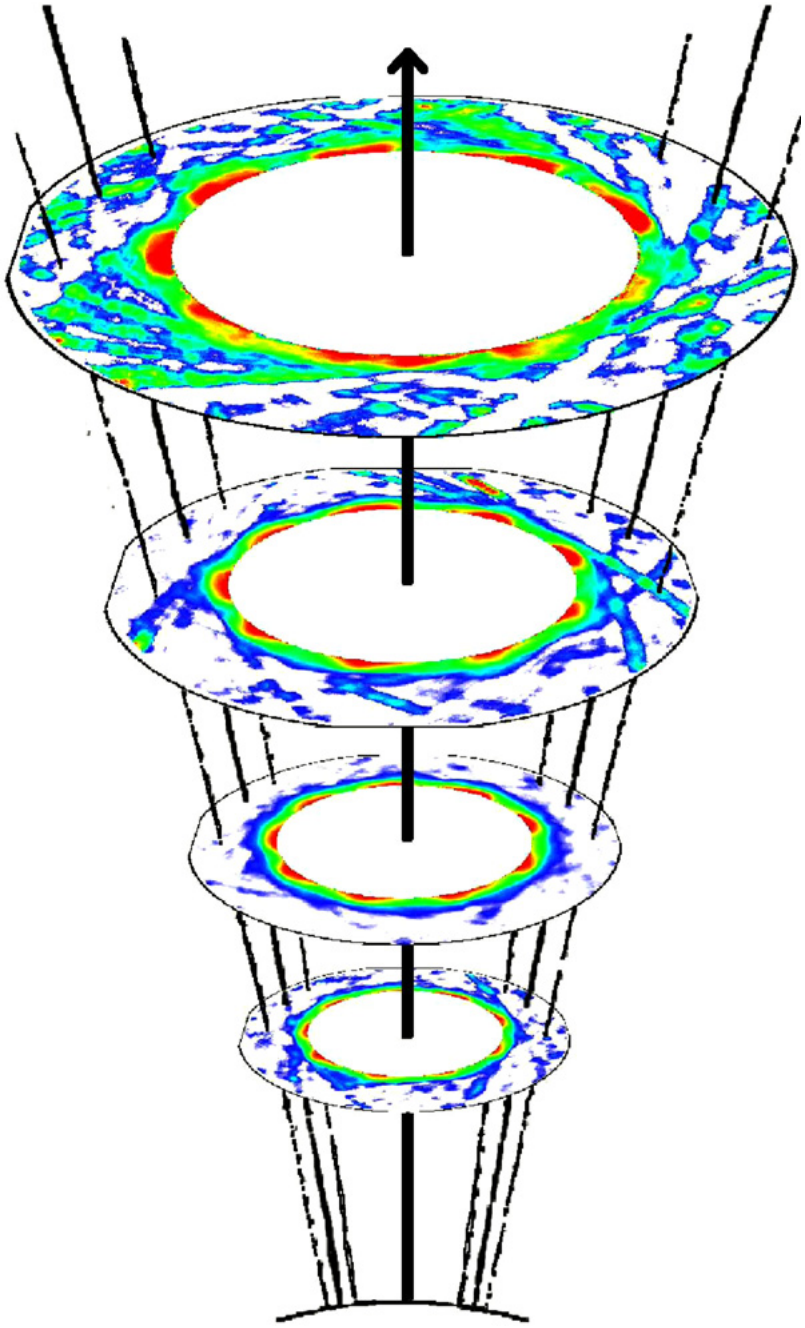

Figure 1.19 A reproduction of Fig. 12 in Maan et al. (2013), showing the reconstructed emission beam maps of B0809+74 at four frequencies (ranging from 117 to 330 MHz). The data were obtained using the multi-band receiver installed at the Green Bank Telescope, and transformed into emission maps via the cartographic transform introduced by Deshpande and Rankin (2001).

of a drift sequence. This study showcased the MWA's relatively new capability as a viable instrument for observing single pulses within the frequency range $\sim$ 170-200 MHz. Subsequent observations of the same pulsar taken simultaneously with the MWA ($\sim$ 185 MHz) and the GMRT ($\sim$ 610 MHz) revealed another curious feature: the drift bands were displaced in phase at the two frequencies. Originally, it was thought that the displacement (whose magnitude depended on which drift mode was present) might be indicative of a non-dipolar component of the emission columns above the sparks, which might be revealed in maps made via the cartographic transform, if they could be reliably produced for this pulsar (McSweeney et al., 2017). However, it was also possible that the already well-known and well-established effects of aberration and retardation (AR) might be responsible, if the different drift modes were associated with different emission heights, as suggested by Smits et al. (2005, 2007). To investigate this possibility, the effect of AR on emission beams caused by a carousel of surface sparks was modelled numerically. The resulting software suite, called PSRGEOM is written in C++ and the source code is available online for the wider pulsar community to use. The algorithms used in PSRGEOM are described in Chapter 4 (published as McSweeney et al., 2019).

Whether AR effects could explain B0031−07's specific behaviour had not yet been determined. Part of the reason for the difficulty was the fact that neither B0031−07's emission geometry nor its carousel geometry was very well constrained, which hindered efforts to use PSRGEOM to model its drift bands at different frequencies. Chapter 5 (published as McSweeney et al., 2019) tackles these difficulties head on by seeking carousel configurations that are consistent with B0031−07's behaviour in all three drift modes. The strategy was to find, if possible, a single carousel rotation rate which could explain the (average) drift rates seen in each drift mode as artefacts of aliasing due to a differing number of sparks. The derived rotation rate thus set the scene for an investigation into the possibility that its frequency-dependent behaviour could be explained by AR

effects.

The major results from Chapters 3 to 5 are summarised and developed further in Chapter 6. In particular, since the former chapters dealt with individual aspects of B0031−07's subpulse drifting behaviour, an attempt is made to synthesise the wisdom gained from the three chapters. Future research directions are also discussed, both in regard to B0031−07 and to the phenomenon of subpulse drifting generally.

Chapter 2

Methodology: Data Acquisition and Preprocessing

This chapter contains a description of the methods used to obtain and process pulsar data from the two telescopes that were used for the work presented in this thesis: the Murchison Widefield Array (MWA), located in the Shire of Murchison, Western Australia; and the Giant Metrewave Radio Telescope (GMRT), located $\sim 90\,\mathrm{km}$ north east of Pune, India. The end result of the preprocessing stages is the data product described in Eq. (1.1), i.e., a dedispersed, high time resolution ($\sim 100\,\mu\mathrm{s}$) time series. If and when polarimetry was available, full Stokes (IQUV) parameters were also obtained; otherwise, only Stokes I. This chapter describes the general methodology and pre-processing procedures only. Details specific to the data sets used in this thesis are given in subsequent chapters when the data themselves are presented.

Figure 2.1 A few "tiles" that make up the MWA telescope. Each tile has 16 cross-dipole antennas connected to an analog beamformer (white box), the first part of the signal processing chain used to generate pulsar time series. (Image credit: *The Geraldton Guardian*).

2.1 Telescopes and pre-processing

2.1.1 The Murchison Widefield Array (MWA)

2.1.1.1 Physical Description and On-Site Signal Processing

The MWA is an aperture array telescope consisting of pairs of cross dipole antennas (one for each orthogonal polarisation direction) arranged into regular, square 4×4 grids. The grids, referred to as *tiles*, are distributed in a pseudo-random fashion over a ~ 5 km-diameter region of Western Australian desert within the Murchison Radio Observatory (see Fig. 2.2). The MWA is capable of several observation modes, but only those aspects relevant to the taking of pulsar data will be described here.

The instrument is being actively developed; here we will describe the telescope during "Phase 1" of its deployment, which is relevant to the time period in which the observations were taken, i.e., approximately between December 2015 and

December 2016. The full specifications of the Phase 1 MWA are given in Tingay et al. (2013), and a description of the current (as of this writing) Phase 2 MWA is given in Wayth et al. (2018).

The Phase 1 MWA consisted of 128 tiles. The analog signals from the individual dipoles are initially passed through a low noise amplifier before arriving at a signal processing unit called the *analog beamformer*. The analog beamformer delays the signals from each dipole (of a single polarisation species) by different, calculated amounts in order to enable the coherent addition of any planar signals coming from a preselected look direction, and then sums the signals together. The result of this process is that the tile's gain pattern becomes more localised, achieving maximum sensitivity at the user-specified pointing centre, and dropping off with increasing angle[1]. The solid angle, Ω, whose sensitivity is above some pre-specified fraction of the peak sensitivity is called the *primary beam*. The angular diameter of the primary beam follows the general law of diffraction-limited resolution,

$$\theta_{\mathrm{beam}} \approx \frac{\lambda}{D}, \tag{2.1}$$

where λ is the observing wavelength and D is the aperture diameter, which in the context of a single MWA tile can be interpreted as the average distance between any two individual dipole elements, approximately 4.5 m. This gives approximate fields of view of 375 deg^2 and 610 deg^2 for observing frequencies of 200 MHz and 150 MHz respectively (Tingay et al., 2013).

After analog beamforming, there are a total of 256 independent, real voltage signals (2 polarisations for each of 128 tiles) which are then digitised at a native sampling rate of 655.36 MHz. Channelisation of the signals is undertaken by a two-stage polyphase filterbank (PFB). The output of the first PFB stage is 256×1.28 MHz-wide "coarsely" channelised data, of which 24 (selected by the user) are recorded. These output data streams are complex-valued, sampled at

[1]At even larger angles, the sensitivity can again increase, analogous to higher-order peaks in, for example, Fresnel diffraction patterns. These secondary (etc.) peaks are called sidelobes, but are not relevant to the present discussion.

the reduced rate of 1.28 MHz. The second PFB stage channelises each 24 coarse channels further, increasing the frequency resolution to 10 kHz and decreasing the time resolution to 100 μs. The output of the second-stage, or "fine" PFB are downsampled to $4i + 4$ complex samples, which are then recorded to on-site RAID disks at a data rate of $\sim 4.2\,\mathrm{GB\,s^{-1}}$ per polarisation, with enough capacity to store ~ 100 min of data (amounting to ~ 45 TB) before the data need to be transferred off-site.

Before finally committing the samples to disk, one more action is performed on the data: a reordering of the samples in order that they have the following hierarchical structure:

$$[\text{time}][\text{channel}][\text{tile/polarisation}][\text{complexity}]. \tag{2.2}$$

That is, all the samples belonging to a single time step are grouped together, then for each time step, all the channels are grouped together, etc. "Tile/polarisation" means one of the 256 signal channels uniquely identified by a physical tile and polarisation combination. "Complexity" means either the real or imaginary part. This reorganisation of the data is called *recombination*.

The signal chain described above comprises the Voltage Capture System (VCS), the MWA's subsystem that is amenable for pulsar observations, and is described in fuller detail in Tremblay et al. (2015).

2.1.1.2 Beamforming

The completion of the VCS on-site signal processing pipeline is a data cube consisting of (per second, per 1.28 MHz coarse channel)

$$10000 \times 128 \times 128 \times 2 = 327,680,000 \tag{2.3}$$

complex samples, each 2×4 bits $= 1$ byte in size. The meaning of each multiplicand is apparent by analogy to Eq. (2.2).

Beamforming (when used without the qualifier "analog") means the coherent summation of the samples within these data cubes over tiles, in order to increase sensitivity in a particular direction at the expense of sensitivity elsewhere. Unlike analog beamforming, which occurs in real time on site, beamforming of MWA-VCS high time resolution data must be accomplished offline, after the data have already been transported offsite to the Pawsey Supercomputing Centre[2] located in Perth, Western Australia. This differs notably from other telescopes which have dedicated pulsar backends.

Because beamforming sums coincident samples produced at each tile, the resulting data sets are reduced in size[3] by a factor of 128. An important difference between beamforming and analog beamforming is that, in the former, the tiles themselves can be considered the individual elements, and their relative spacing is what determines the aperture distance, D, of Eq. (2.1). The maximum tile-to-tile distance, or *baseline*, of the Phase 1 array was $\sim 3\,\mathrm{km}$, resulting in a so-called *tied-array beam* only a few arcminutes in diameter (dependent, of course, on the observing frequency). The narrowness of the tied-array beam also justifies the use of the term *pencil beam*, which can be used interchangeably with "tied-array beam". The important point to be made here is that the angular size of the emitting regions of even the nearest pulsars is still several orders of magnitude smaller than the MWA's pencil beam, so the goal of beamforming is not so much to try to spatially resolve pulsars, but instead to focus the maximum amount of sensitivity onto the single pixel containing the pulsar signal.

We can estimate the increase in sensitivity of the tied-array beam compared to the primary beam by noting the general, ideal result that the signal-to-noise (S/N) grows in proportion to the number of elements, N. If on the other hand, the signals from each tile were added incoherently (by detecting the pulsar at each telescope first, and then summing the resulting power measurements together),

[2] `https://pawsey.org.au/`

[3] This does not include other factors such as a change in data format or the conversion of the dual polarisation to full Stokes parameters.

the signal would still increase with N, but the uncorrelated noise would increase as $\sqrt{N}$, so that the S/N would only increase as $\sqrt{N}$. Incoherent summation does not, however, reduce the field of view, so one is still sensitive to pulsar signals anywhere within the primary beam.

The goal and the challenge of beamforming, then, is to ensure that the signals from each tile are being added *coherently*—that is, the phase information inherent in the complex samples are artificially delayed or advanced in such a way that the wavefronts of the pulsar signal (which can be approximated as a planar wave) are aligned. This involves a calculation of the geometric time delay between the arrival of a signal at a given tile and some (arbitrary) reference point, usually taken to be the centre of the array. The details of these procedures are well documented in the MWA beamformer description paper, Ord et al. (2019).

The geometry of the array is not the only reason that the signal at a given tile will arrive out of alignment with the others. Other effects include the length of the cables through which the signals are propagated before the samples are digitised and time-stamped; the diffractive nature of the ionosphere on radio signals, which distort the incoming wavefronts; and a host of other electronic and instrumental effects inherent in the design of the MWA's hardware. The first of these, the cable length, is known for each tile and can be accounted for exactly. The determination of the other effects requires an independent calibration step, which involves an iterative process of comparing the correlated signals from each pair of tiles, called *visibilities*, with the expected visibilities given a model of the radio sources within the primary beam. The pulsar observation can itself be used as the calibration observation—which we call *in-beam calibration*—but a different, *dedicated calibration* observation can also be used which may be separated from the pulsar observation both spatially (i.e. looking at a different part of the sky) and temporally (be taken up to several hours before or after). The advantage of using a dedicated calibration observation is that fields can be selected that contain bright, steady sources that are ideal for calibration; the disadvantage is

that the ionospheric conditions can change on spatial and temporal scales that render the calibration solution inapplicable to the pulsar observation. For the MWA observations presented in this thesis, calibration was carried out using the Real Time System (RTS) software package described in Mitchell et al. (2008).

Once the data have been calibrated, they are beamformed towards the desired pulsar. The mathematical operations that constitute beamforming are now described. Overall, the beamforming process amounts to a weighted sum of the 128 complex-valued samples in each time and frequency bin generated by each polarisation of each MWA tile. For a given time step and channel, let

$$D_a = \begin{bmatrix} d_{a,X} \\ d_{a,Y} \end{bmatrix} \tag{2.4}$$

be the pair of complex-valued samples corresponding to antenna a with polarisations X and Y. The incoherent sum over the tiles and polarisations is achieved by

$$\begin{aligned} B_{\text{incoh}} &= \sum_a D_a^\dagger D_a \\ &= \sum_a (|d_{a,X}|^2 + |d_{a,Y}|^2), \end{aligned} \tag{2.5}$$

where the dagger denotes the Hermitian transpose. Note that B_{incoh} is a single, real-valued quantity.

Coherent summation incorporates the phase corrections gleaned from the calibration steps and the geometric and cable delays outlined above. The calibration solution takes the form of a 2×2 complex matrix, one for each tile, that is treated as constant over the duration of the observation. The matrix, called the *Jones matrix* is represented by J_a, and its direct (left) multiplication to D_a constitutes the application of the calibration solution to the pulsar observation[4]. The geometric delays are recalculated every second (necessary by virtue of the fact that

[4]In practice, the solutions output by the RTS are usually called the Jones matrices, and it is the *inverse*, J^{-1}, which is multiplied to D_a. However, the distinction is semantic, so here I am opting for the notationally simpler J for the quantity that is multiplied to D_a.

the desired look direction is changing as the Earth rotates) and are combined with the cable delays into another 2×2 matrix, called the *weights matrix*, W_a. The geometric and cable terms of the weights matrix are independent of polarisation, so the off-diagonal elements of W_a are always identically zero.

Having obtained J_a and W_a, the beamforming operation becomes

$$B_{\mathrm{coh}} = \begin{bmatrix} b_X \\ b_Y \end{bmatrix} = \sum_a B_a \quad = \sum_a J_a W_a D_a. \tag{2.6}$$

Note that whereas B_{incoh} is a single real, "detected" quantity, B_{coh} is complex-valued and retains both polarisations.

The final step is to convert B_{coh} into a set of full Stokes parameters. Rather than just using the components of B_{coh}, one final correction is made: subtraction of the autocorrelations. For a sufficiently large number of tiles which are dominated by noise, this has the benefit of reducing the noise by a much larger fraction than any astrophysical signal buried within it. We thus define the autocorrelation to be

$$N = \begin{bmatrix} n_{XX} & n_{XY} \\ n_{YX} & n_{YY} \end{bmatrix} = \sum_a B_a B_a^\dagger. \tag{2.7}$$

The Stokes parameters can then be calculated:

$$\begin{aligned} I &= \frac{1}{w}\Big((|b_X|^2 - n_{XX}) + (|b_Y|^2 - n_{YY}) \Big) \\ Q &= \frac{1}{w}\Big((|b_X|^2 - n_{XX}) - (|b_Y|^2 - n_{YY}) \Big) \\ U &= \quad 2\,\mathrm{Re}\left[\frac{1}{w}\Big(b_X b_Y^\dagger - n_{XY} \Big) \right] \\ V &= -2\,\mathrm{Im}\left[\frac{1}{w}\Big(b_X b_Y^\dagger - n_{XY} \Big) \right] \end{aligned} \tag{2.8}$$

where w is a weighting factor equal to the number of antennas used in the sums (which may be < 128 if tiles are flagged due to radio frequency interference or other forms of data corruption). The Stokes products obtained by Eq. (2.8)

correspond directly to the quantities in Eq. (1.1). This final product is then packed into the PSRFITS file format (Hotan et al., 2004) for further processing.

An alternative data processing pipeline is available, which is identical to the above pipeline up to the beamforming stage represented by Eq. (2.6), but then applies a special filter to the data. This filter is designed to invert the second, "fine" PFB stage, recovering a sample rate of 1.28 MHz ($\sim 0.78\,\mu$s time resolution) at the cost of reverting back to 1.28 MHz frequency resolution (i.e. the width of a "coarse" channel)[5]. The data are then packed directly into the VDIF file format (Whitney et al., 2009), and conversion to Stokes parameters is performed at a later stage of processing by third-party software (see §2.2). This resultant data product is amenable to coherent dedispersion, and thus to attain higher (optimal) time resolution by eliminating any temporal smearing due to residual dispersion.

2.1.2 The Giant Metrewave Radio Telescope (GMRT)

The GMRT is an array of 30×45-metre, fully steerable radio frequency dishes located ~ 90 km north-east of Pune, India. 12 of the dishes form a compact, pseudo-random cluster in the centre, and the remaining dishes form an approximate 'Y' shape, i.e. 3 arms of 6 dishes each. The maximum baseline between antennas is ~ 25 km, and the full array has an effective area of $\sim 30,000\,\mathrm{m}^2$. The original GMRT (known as the "legacy system") can operate in 5 discrete radio bands, ~ 32 MHz wide, ranging from 150 to 1420 MHz (Swarup et al., 1991; Ananthakrishnan, 1995).

In 2017, the GMRT underwent an upgrade, which is described in Section (§2.1.2.1). Consequently, data for this project were obtained both from before and after the upgrade. The earlier data sets used the bandwidth centred on ~ 610 MHz, split into 512×65.1 kHz channels ranging from 591 to 624 MHz.

Users can opt to use the GMRT in either an incoherent mode (IA), in which

[5]For archival data, this is only way to achieve a higher resolution; the MWA and VCS design did not provide any means for accessing the data stream before the fine PFB stage. However, work is currently in progress to allow for such access.

Figure 2.2 A few of the dishes that make up the Giant Metrewave Radio Telescope, near Pune, India. (Image credit: *National Centre for Radio Astrophysics/Tata Institute of Fundamental Research*).

the power detected at each antenna is summed together, or a phased array mode (PA) in which the phases are adjusted in real time to form a tied-array beam in the desired look-direction (Gupta et al., 2000). These modes are analogous to (but different in detail from) the MWA's incoherent and coherent beamforming modes described in the previous section. In particular, the PA mode will deliver a better signal to noise ratio than the IA mode by a factor of $\sqrt{N}$, where N is the number of antennas used in the sum. There is some flexibility in the choice of which antennas to include: the array can be arbitrarily split into subarrays, whose signals are individually processed by the GMRT Software Backend, capable of observing, processing, and recording pulsar signals over the whole bandwidth in real time (Gupta et al., 2000; Roy et al., 2010).

A common strategy is to use a subarray consisting of the 14 innermost antennas, in order to reduce the difficulty of finding calibration solutions over the largest baselines. Calibration is done by periodically observing steady, compact radio sources in a nearby region of the sky. Calibration solutions obtained in this way last for a limited time due to changing ionospheric conditions; after some time (approximately one hour), the solution becomes less and less accurate, and the telescope must be re-calibrated. For pulsar observations, the incoming data can be folded in real time so that the strength of the (pulsar) signal can be monitored as a proxy for estimating the goodness of the calibration solution. Doing so for a short period near the start of an observing run ensures that the calibration solution is indeed correct, and that the pulsar can be seen clearly.

For this thesis, the selected observing mode resulted in a final data stream containing 16-bit samples with 512 frequency channels and a sampling time of $122.88\,\mu$s.

2.1.2.1 The Upgraded Giant Metrewave Radio Telescope (uGMRT)

A few of the data sets were collected after the GMRT underwent an upgrade. For the purposes of this project, the most important aspects of this upgrade

were (1) the introduction of a new correlator that is capable of an instantaneous bandwidth of up to 400 MHz (cf. the earlier 32 MHz), and (2) an increase in sensitivity and accompanying improvement in dynamic range. In particular, we made use of Band 3, which offers 200 MHz of instantaneous bandwidth in the range 300 to 500 MHz (Gupta et al., 2017; Reddy et al., 2017), split into 4096 × 48.8 kHz individual channels. The sampling time was 163.84 μs. Except for these differences, the GMRT and uGMRT data sets are alike.

2.2 Further data processing

This chapter describes the generic post-processing routines, designed especially for pulsar observations, as implemented in three software packages: the Pulsar Exploration and Search Toolkit (PRESTO), DSPSR, and PSRCHIVE. These programs are designed to handle the output data formats of a variety of radio telescopes, including the telescopes used in this thesis (described in §2.1). These standard software packages convert the telescope-specific data formats into standard file formats designed for pulsar observations, and contain utilities for examining the resulting pulsar data sets in an intuitive way.

2.2.1 PRESTO

PRESTO (Ransom, 2001) was originally conceived as an implementation of a new, efficient technique to search for accelerated pulsars (i.e. pulsars in binary systems whose orbital velocity changes significantly with respect to the observer over the duration of an observation). It is, however, fully equipped to perform standard processing tasks even for known pulsars with zero acceleration (i.e. isolated pulsars)—this is the mode required for the pulsars studied in this thesis.

PRESTO's primary output is a diagnostic plot showing various aspects of the candidate pulsar signal, for example, its persistence in time and frequency, and the signal to noise as a function of DM, P, and $\dot{P}$. An example of such a

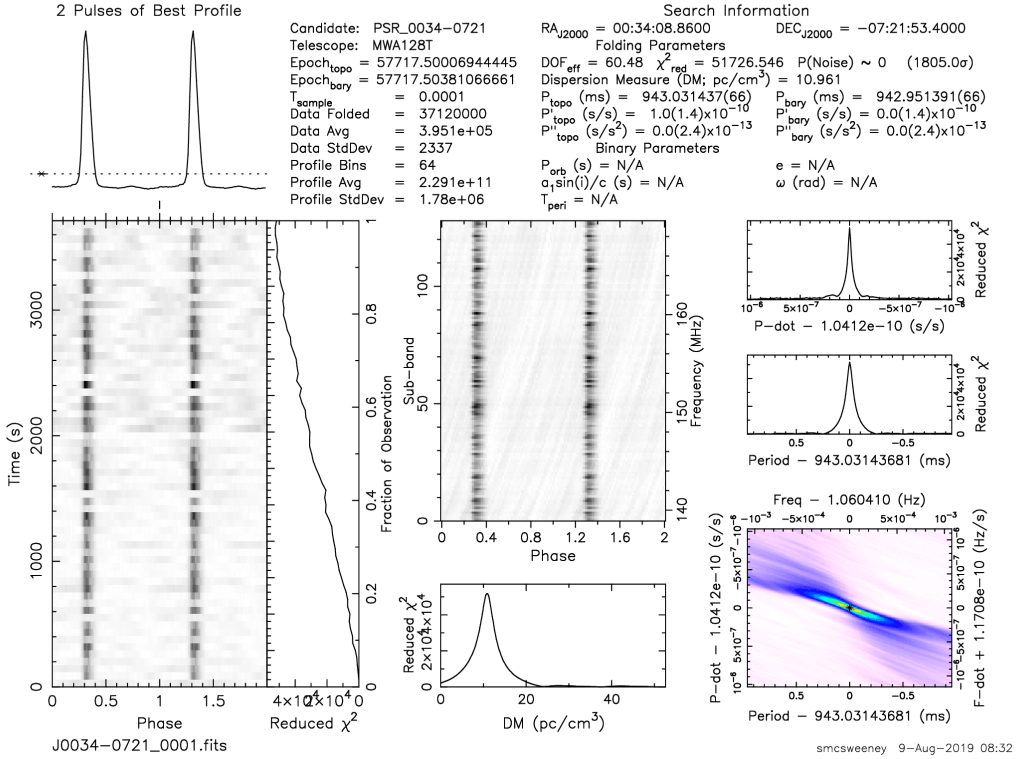

Figure 2.3 An example of a PRESTO diagnostic plot, showing an observation of B0031−07 by the MWA. The data have been dedispersed and folded with the pulsar's DM and rotation period, respectively.

diagnostic plot is provided in Fig. 2.3. It is standard practice to allow PRESTO to search in (DM, P, $\dot{P}$) parameter space. This is particularly useful if one or more of these parameters is variable, or known with only limited precision. In this "known pulsar" mode, the input signal is incoherently dedispersed according to the formulae in §1.2.5.1, and then folded according to Eq. (1.6), using TEMPO2 to determine the topocentric period of the pulsar (Hobbs et al., 2006).

2.2.2 DSPSR

DSPSR (van Straten and Bailes, 2011) grew out of early software designed to perform coherent dedispersion algorithms entirely in memory. Originally designed to work with a limited number of telescopes, it has since evolved to cater for a

wide range of telescope data, including the GMRT, and the PSRFITS and VDIF output formats of the MWA (see §2.1). As well as enabling coherent dedispersion, it converts the input data into the PSRCHIVE data format, which organises the data into multi-dimensional blocks (frequency, sub-integration[6], pulse phase, polarisation) called *archives*. These archives can then be further processed by the suite of tools that comprise the PSRCHIVE software suite.

2.2.3 PSRCHIVE

PSRCHIVE (Hotan et al., 2004; van Straten et al., 2009a,b, 2011, 2012) consists of a suite of applications for the manipulation, analysis, and visualisation of pulsar data in the PSRFITS format, or in pulsar archives archives created, e.g., by DSPSR. Although originally designed primarily for pulsar timing experiments, it has grown to include a vast array of general-purpose algorithms applicable to pulsar data sets, such as:

- polarimetric calibration,
- pulse arrival time,
- measuring the Faraday rotation,
- statistics of pulsar profiles and their variability.

For the purposes of this project, the most useful feature of PSRCHIVE is its array of plotting commands. Using the PGPLOT[7] software as its plotting library, it can display data in various formats, such as dynamic spectra, folded spectra (i.e. integrated power as a function of frequency and pulse phase), integrated profiles (with full polarisation, if available), and—especially useful for single pulse studies—pulse stacks.

[6] A "sub-integration" is an integration performed over several pulses. In this thesis, single pulses need to be retained, so here "sub-integration" is synonymous with "pulse (number)". In other contexts, such as pulsar timing, sub-integrations of several tens or even hundreds of pulses are desirable.

[7] `http://www.astro.caltech.edu/~tjp/pgplot/`. Last accessed 5 September 2018.

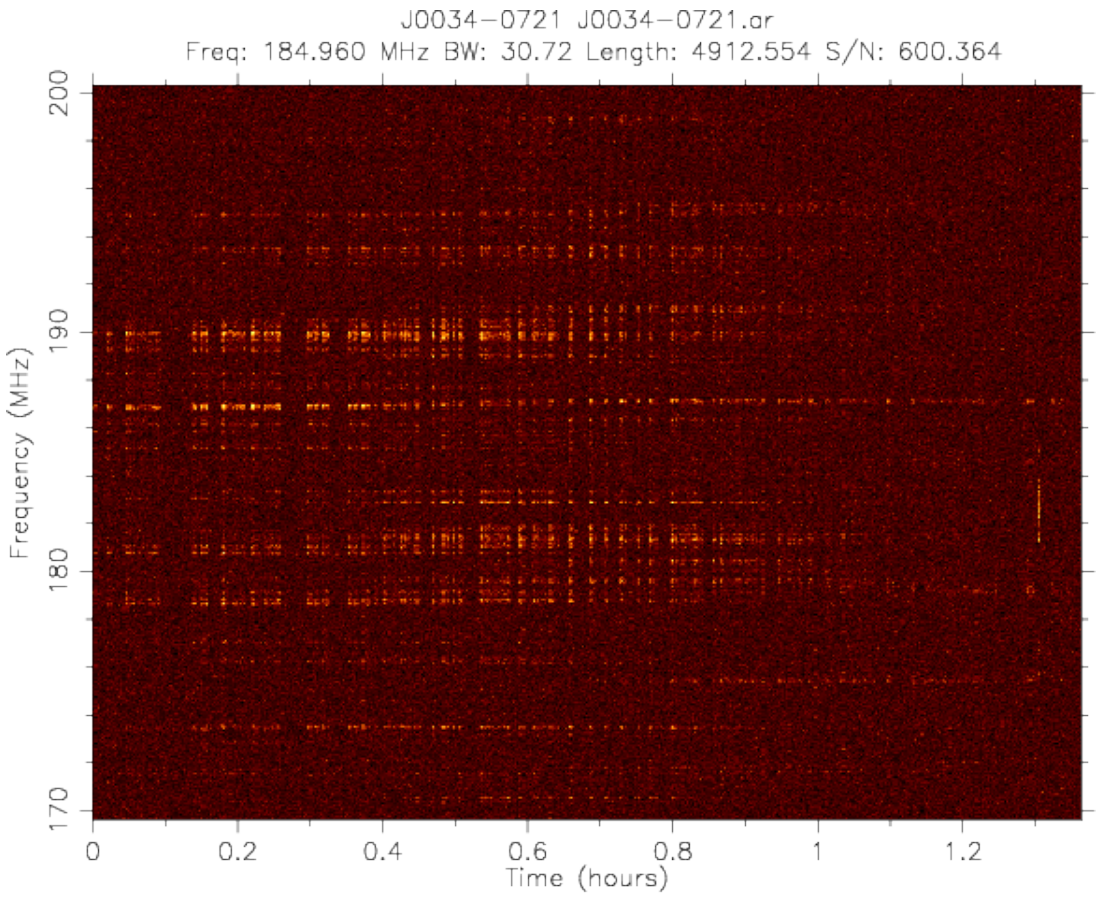

Figure 2.4 The dynamic spectrum obtained from an MWA observation of B0031−07. The modulation in frequency is due to scintillation (Section 1.2.5.3), and the sharply defined intervals of time where the signal is absent is due to nulling (Section 1.3.3). A burst of intermittent, RFI is visible at approximately 1.3 hours.

The analyses carried out in this thesis are specific to single pulse observations, which PSRCHIVE is not specifically designed to handle. Thus, once some feature of interest has been identified in the plots generated by PSRCHIVE, further analysis required the development of original code and algorithms.

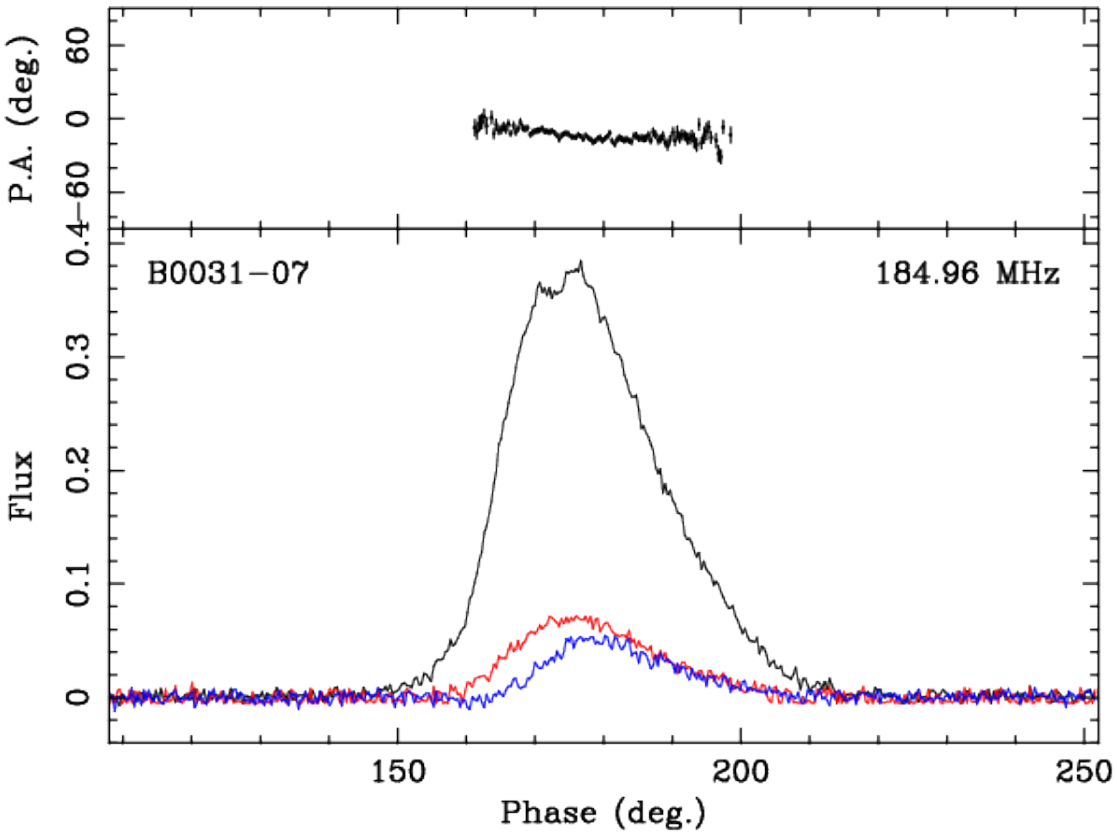

Figure 2.5 The polarisation profile of B0031−07. The bottom panel shows the total intensity profile (black), the linear polarisation (red), and the circular polarisation (blue). The PPA is shown in the upper panel.

Chapter 3

Low-frequency Observations of the Subpulse Drifter PSR B0031−07 with the Murchison Widefield Array

The data analysis begins with an in-depth study of the drift rate of B0031−07 and how it varies on small time scales. This chapter is a faithful reproduction of the author's publication (McSweeney et al., 2017), as per Curtin University's policy. It differs from the original in only minor respects, including the formatting of both the text and the images, the numbering of the equations and figures, and the use of Australian spelling. Also, the "J name" of the pulsar (J0034−0721) has been replaced throughout with its (original) "B name" (B0031−07), in keeping with the convention used in this thesis. In both this and subsequent chapters, the end matter (Acknowledgements, References) of the original papers have been shifted to the relevant sections of this dissertation.

3.1 Abstract

The phenomenon of subpulse drifting may hold the key to understanding the pulsar emission mechanism. Here, we report on new observations of B0031−07 carried out with the Murchison Widefield Array at 185 MHz. We observe three distinct drift modes whose "vertical" drift band separations (P_3) and relative abundances are consistent with previous studies at similar and higher frequencies. The drift bands, however, are observed to change their slopes over the course of individual drift modes, which can be interpreted as a continuously changing drift rate. The implied acceleration of the intrinsic carousel rotation cannot easily be explained by plasma models based on $\vec{\boldsymbol{E}} \times \vec{\boldsymbol{B}}$ drift. Furthermore, the implication of a continuously changing value of P_3 calls into question the wisdom in characterizing this pulsar's drift modes by its P_3 values. The "horizontal" separation between drift bands (P_2) is found to be larger at later rotation phases within the pulse window, which is inconsistent with the established effects of retardation, aberration, and the motion of the visible point. Longer observations spanning many thousands of pulsar rotations may help investigate these aspects further.

3.2 Introduction

Despite nearly half a century of observational and theoretical investigations, the physical mechanisms responsible for the radio emission from pulsars remain unresolved (Michel, 1991; Beskin et al., 2006; Melrose and Yuen, 2016). Some features of observed pulsar emission are considered vitally important to furthering our understanding of these fundamental processes. Chief among these is the phenomenon of subpulse drifting, which is the systematic shift in pulse phase of substructures within individual pulses over time (Drake and Craft, 1968). Also critical is nulling, in which the radio emission appears to switch off temporarily (Backer, 1970b; Ritchings, 1976), a widespread phenomenon closely linked to

the coherent emission process. B0031−07 is a bright, long-period ($P_1 = 0.943\,\mathrm{s}$) pulsar with dispersion measure DM = $10.9\,\mathrm{pc\,cm^{-3}}$ that exhibits both subpulse drifting (Backer, 1970b; Huguenin et al., 1970) and extensive nulling ($\sim 45\%$ of the time, Vivekanand 1995), and thus is an important object which can potentially reveal vital clues to the underlying emission mechanisms.

Subpulses are thought to represent "subbeams" caused by discrete emission regions that are stable over many pulsar rotations, which in some cases may be arranged in a "carousel" pattern centered on the magnetic dipole axis and rotating around it at some rate[1], $\overline{D}$ (Ruderman and Sutherland, 1975; Rankin, 1986). Strong observational support for this view came with the work of Deshpande and Rankin (1999, 2001), who were able to determine that the regular drifter PSR B0943+10, has a stable carousel consisting of 20 discrete emission regions. One of the earliest and most successful emission models (Ruderman and Sutherland, 1975) invoked $\vec{\boldsymbol{E}} \times \vec{\boldsymbol{B}}$ drift to explain the carousel's circular motion; however, there are some outstanding issues with its quantitative predictions. First, the measured drift rate for at least some pulsars are known to be many times greater than that predicted by $\vec{\boldsymbol{E}} \times \vec{\boldsymbol{B}}$ drift (e.g. Mitra and Rankin, 2008). Second, the drift rate of some pulsars is not constant, but varies over time. The most common manifestation of this is the presence of temporally distinct drift modes, characterised by an abrupt change in the drift rate, usually with a timescale less than a single stellar rotation (e.g. Redman et al., 2005). Variations in drift rate can also occur over longer timescales, without sudden drift modes changes, (e.g. Biggs et al., 1985; Bhattacharyya et al., 2009). B0031−07 exhibits both long and short timescale drift rate variations, with three distinct drift modes designated Modes A, B, and C (Huguenin et al., 1970; Wright and Fowler, 1981), and with drift rate variations occurring within each mode (Vivekanand and Joshi, 1996).

The methodology of Deshpande and Rankin (2001) involves mapping the in-

[1]The published version of this chapter does not include the "bar" notation, e.g. $\overline{D}$. It is included here to make the notation consistent with the rest of the thesis. It is introduced formally (with justification) in Ch. 5.

tensity sequences from the drifting subpulses onto a coordinate system centered on the magnetic axis (the so-called "cartographic transform"), Ideally, this can be applied to other drifters, such as B0031−07, allowing us to determine the geometry and dynamics of the emission regions. This is not always possible, mainly due to the difficulty in resolving the presence of aliasing, in which the true carousel drift rate is different from the measured drift rate because of the sub-Nyquist sampling of the emitting region due to the star's rotation. A carousel with an integer number of subbeams admits only a discrete (but possibly infinite) set of solutions to any given observed drift band pattern, with higher drift rates corresponding to higher order aliasing. Determining the true carousel rate, and hence the order of aliasing present, is difficult because different sets of parameter values (viewing geometry, as well as aliasing) can give rise to identical-looking drift bands. This is especially true for B0031−07, whose multiple drift modes complicate the issue, and whose viewing geometry is not precisely known (Smits et al., 2007). Nevertheless, it is vital to resolve the aliasing order so we can understand the configuration of emission regions of this pulsar and the relationship between its three different drift modes.

The regularity of both the stellar rotation and of the observed drift bands allows us to define a number of periodicities, often used in subpulse drifting analyses (e.g. Deshpande and Rankin, 1999; Edwards and Stappers, 2002). P_1, P_2, and P_3 are respectively defined as (1) the pulsar's rotation period, (2) the temporal separation between two subpulses within a single rotation, and (3) the time it takes for a subpulse to arrive at the same rotation phase as its predecessor. The drifting subpulses appear as diagonal *drift bands* in the pulse stack, which is the (one-dimensional) time series plotted in a two-dimensional array, with each row corresponding to 360° of rotation, and time progressing along the vertical axis (Fig. 3.1). Visually, P_2 and P_3 are realised as the horizontal and vertical separations (respectively) of consecutive drift bands. The slope of the drift bands

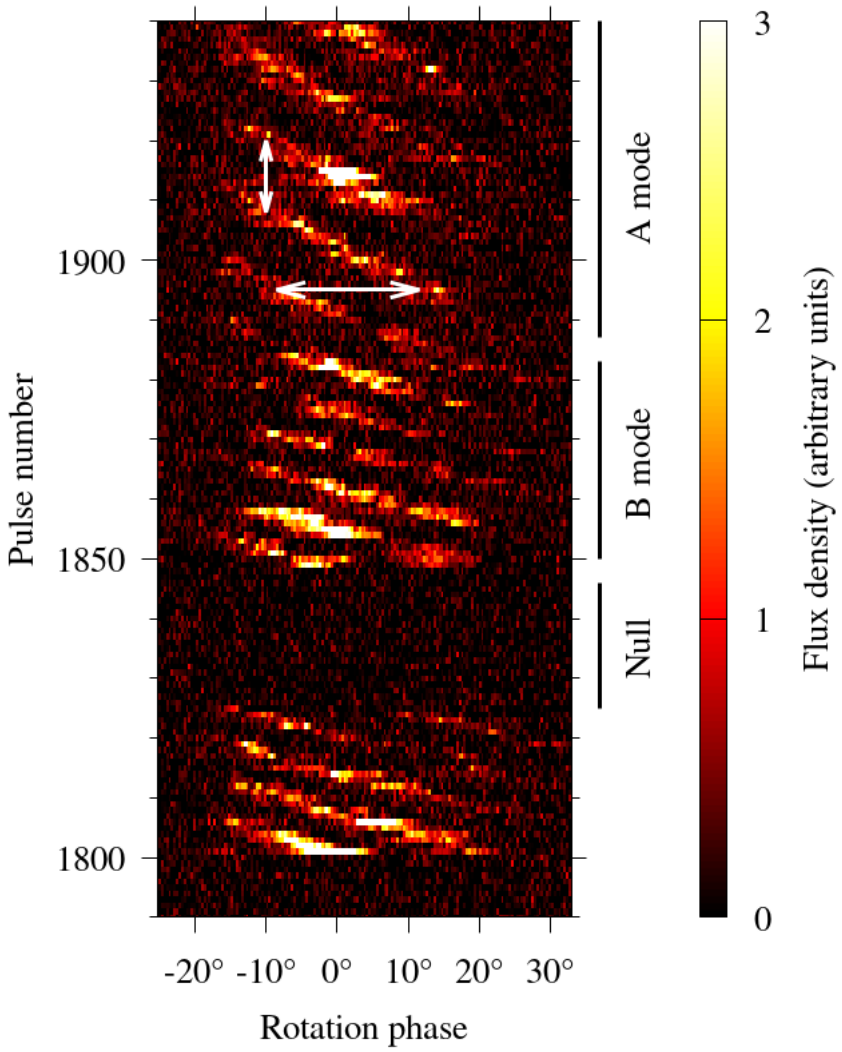

Figure 3.1 A subset of the stacked pulses of B0031−07, from MWA observations at 185 MHz. The drift bands are clearly visible. The horizontal and vertical separations between consecutive drift bands (indicated by the overlaid white arrows) are P_2, measured in degrees, and P_3, measured in units of P_1, respectively. Two of the three drift modes, A and B, are exemplified here, distinguished by markedly different P_3 values and drift rates. A typical null sequence is also present.

is the observed drift rate, defined as

$$\overline{D} \equiv \frac{\mathrm{d}\varphi}{\mathrm{d}p} = \frac{P_2}{P_3}, \tag{3.1}$$

where φ is the phase, p is the pulse number. In this paper, we adopt the convention that a positive drift rate corresponds to the scenario in which subpulses

drift towards earlier phases.

Drift modes are usually characterised by their P_3 value, which is generally found to remain stable over the course of a drift sequence (defined here as a set of contiguous pulses all belonging to the same drift mode). Early work on B0031−07 measured P_3 values of 12.5, 6.8, and $4.5\,P_1$ for Modes A, B, and C respectively (Huguenin et al., 1970; Wright and Fowler, 1981), with individual drift sequences lasting from a few to hundreds of pulse periods (Vivekanand and Joshi, 1996). Interestingly, the subpulse phases appear to be correlated across the nulls (Joshi and Vivekanand, 2000), indicating organised motion of the supposed carousel configuration even during nulls.

Smits et al. (2005, 2007) investigated the behavior of these drift modes at widely separated frequencies of 157 MHz and 4.85 GHz. Their analysis revealed that the drift bands of Mode B were largely undetectable at the higher frequency. They offered a geometric interpretation, placing the Mode B emission regions at a higher magnetic latitude than the Mode A emission regions (the assumed radius-to-frequency mapping implies that at higher frequencies, the Mode B emission regions do not intersect the line of sight). The physical cause of the change of magnetic latitude, however, was not explored.

Indeed, no physical explanation has been offered for several key properties of B0031−07's drift modes, such as their average duration, the order in which they appear, their relationship to the null sequences, and the variation (albeit small) in their respective P_3 measurements. Crucially, the presence or absence of aliasing in B0031−07 has not been determined; however, Smits et al. (2007) estimate the number of discrete emissions in the carousel to be about 9, under the assumption that aliasing is not present.

In this paper we present new observations of B0031−07 made with the Murchison Widefield Array (MWA, Tingay et al. 2013), a low frequency precursor to the Square Kilometre Array (SKA). We attempt to characterise the pulsar's observed drifting behavior in terms of a small number of parameters that remain

constant over the course of individual drift sequences. The data acquisition and pre-processing are described in §3.3. Our analysis of the drift bands, and the investigation of their time-varying behaviour are described in §3.4. The theoretical implications of a variable drift rate are discussed in §3.5, and our conclusions are presented in §3.6.

3.3 Observations and data processing

The data were taken with the MWA, a low frequency aperture array located in remote Western Australia. The MWA is now geared for high time resolution science, with the recently commissioned Voltage Capture System mode (VCS; Tremblay et al. 2015). The VCS enables the recording of the raw voltages from each of the MWA's 128 tiles, which are downloaded from site to the dedicated data storage facility at the Pawsey Supercomputing Centre[2].

We recorded 42 minutes (~ 18.5 TB) of VCS data on 19th January 2016. The data were processed following a procedure similar to Bhat et al. (2016), which is summarised here. Calibration of the data was performed with the Real Time System (RTS) software (Mitchell, in prep), using an observation of Pictor A taken immediately prior to the pulsar observation. Using the calibration solution, the raw voltages were phased up to form a pencil beam (~ 2 arcmins in diameter) on B0031−07.

The resulting data set (stored in the PSRFITS format, Hotan et al. 2004) consisted of 24×1.28 MHz coarse frequency channels ranging from 169.60 to 200.32 MHz, and a time resolution of 100 μs. The data from only the central 88 out of 128 (10 kHz) fine channels of each coarse channel were kept because of aliasing effects inherent in the polyphase filter bank, which attenuates the response of the antennas at the edges of the coarse channels. The best solution was found by calibrating on 115 out of the available 128 antenna tiles, so the data from the remaining tiles were rejected from the pulsar analysis.

[2] `https://www.pawsey.org.au/`

Finally, the resulting frequency-time data was processed in DSPSR (van Straten and Bailes, 2011) and PSRCHIVE (Hotan et al., 2004) to produce a single-pulse archive and a time series. The time resolution of the time series was 0.921 ms, corresponding to 1024 phase bins across one pulsar period. The data set is of very high quality, with an average S/N of ~ 9 per pulse (without excising null pulses), approximately a factor of 8.5 times higher than that of the same observation processed incoherently (i.e. with the signal power detected at each tile summed together), $\sim 20\%$ less than the theoretical expectation. This paper presents the first study of individual pulses for pulsar emission science undertaken with the MWA (but see, e.g., Oronsaye et al. 2015 for previous single-pulse studies with the MWA).

3.4 Subpulse drifting analysis

The analysis in this paper is aimed at exploring how the behaviour of the drift bands of B0031−07 varies both between different drift modes, and within individual drift sequences. We analysed only data within the on-pulse window, which was chosen to fall between the first and last phase bins whose average flux densities were 4σ above the off-pulse noise (the noise statistics were obtained from phase bins more than 90° away from the profile peak). The pulse window was thus determined to be between $-25.3° \leq \varphi \leq 33.0°$, where the point $\varphi = 0°$ was defined to be the center of the phase bin which contained the largest average flux density.

3.4.1 Determining the drift mode boundaries

Traditional methods of drift mode analysis include the Harmonic Resolved Fluctuation Spectrum (HRFS; Deshpande and Rankin, 2001) and the mathematically equivalent Two-Dimensional Fluctuation Spectrum (2DFS; Edwards and Stappers, 2003). These methods are designed to measure P_2 and P_3 by means

of Fourier analyses of the time series. The fluctuation spectra of pulsars with multiple drift modes will contain the Fourier components corresponding to the (P_2, P_3) pairs of each drift sequence and a delocalised component corresponding to the distribution of the drift modes, as can be seen, for example, in the HRFS of PSR B2303+30 (Redman et al., 2005).

Because B0031−07 exhibits multiple drift modes and long-duration nulls, the components corresponding to the three drift modes are not easily resolved in the fluctuation spectra (e.g., Fig. 8 of Karuppusamy et al., 2011). Any realistic measurement of P_2 and P_3 (and hence the drift rate) can therefore only be achieved by first determining the precise locations of the transitions between different drift modes, and treating each drift sequence separately. For this pulsar, the drift modes appear to switch on a timescale no longer than a single rotation period, and so it becomes possible to associate each pulse with a distinct mode.

One can use the sliding two-dimensional fluctuation spectrum (S2DFS; Serylak et al., 2009) to obtain a map of temporal changes to the drift modes, but the coarse resolution inherent in the technique cannot resolve sudden changes on the time scales of individual pulses. We therefore followed the method of Smits et al. (2005), which measures the average P_3 in a candidate drift sequence by computing the phase-averaged power spectrum (PAPS), which is the sum of the amplitudes of the DFT of each phase bin. The beginning and ending boundaries of the drift sequence were then adjusted incrementally until the peak value in the PAPS divided by the rms of the rest of the PAPS was maximised. The resulting map of drift modes is shown in the top panel of Fig. 3.2, and a summary table of drift mode statistics is given in Table 3.1.

The distribution of drift modes in the MWA observation strongly resembles that of Smits et al. (2005, 2007), who observed the pulsar for a similar length of time at similar frequencies (157, 243, 325 MHz and above). In particular, we note the following similarities: Mode A sequences are generally longer than modes B and C, and mode A sequences are often sandwiched between two mode

Table 3.1. Statistics of drift mode measurements

Mode	Number of sequences	Mean P_2 (°)	Mean P_3 (PAPS) (P_1)	Mean P_3 (Quad) (P_1)	Occurrence fraction (%)	Mean duration (P_1)
A	9	18.9 ± 1.1	11.9 ± 2.0	12.5 ± 0.8	18.4	54.6
B	31	19.8 ± 0.5	7.0 ± 0.5	7.0 ± 0.2	34.5	29.6
C	2	19.1 ± 2.9	5.9 ± 3.6	4.6 ± 0.3	0.8	11.0
Null	38	-	-	-	45.5	31.9
Unknown[a]	6	19.9 ± 3.2	-	-	0.8	3.7

[a]Sequences that were too short to yield a reliable measurement of P_3 were uncategorised.

B sequences with minimal nulling between them.

3.4.2 Linear fits to drift bands

The simplest way to characterise individual drift bands is to treat them as independent line segments. By fitting a line to each drift band, we hope to assess whether there are any systematic changes in the drift rate over the course of a drift sequence.

Each pulse was convolved with a narrow Gaussian (FWHM = $2^\circ \approx 10\%$ of P_2) in order to smooth out high frequency noise fluctuations. The phase bin containing the most power in each pulse was identified, and the phase of the interpolated peak (using a cubic spline to get a sub-bin estimation) was taken as the phase of a subpulse. P_2 has previously been measured to be $\sim 20^\circ$ at low frequencies (see Fig. 3.4), so the second highest peak was identified with the same method, but with the constraint that it was not closer than 10° to the first bin. For the vast majority of pulses, a maximum of two drift bands were visible in any given pulse, so we did not attempt to find a third subpulse peak.

An algorithm was designed to find connected series of subpulse peaks that belong to the same drift band. Starting at the beginning of the observation, and assuming that the subpulses found in the first pulse do in fact "belong" to genuine drift bands, we assigned the subpulses in the succeeding pulse to the already identified drift bands if the subpulse phases are within 10° of the drift

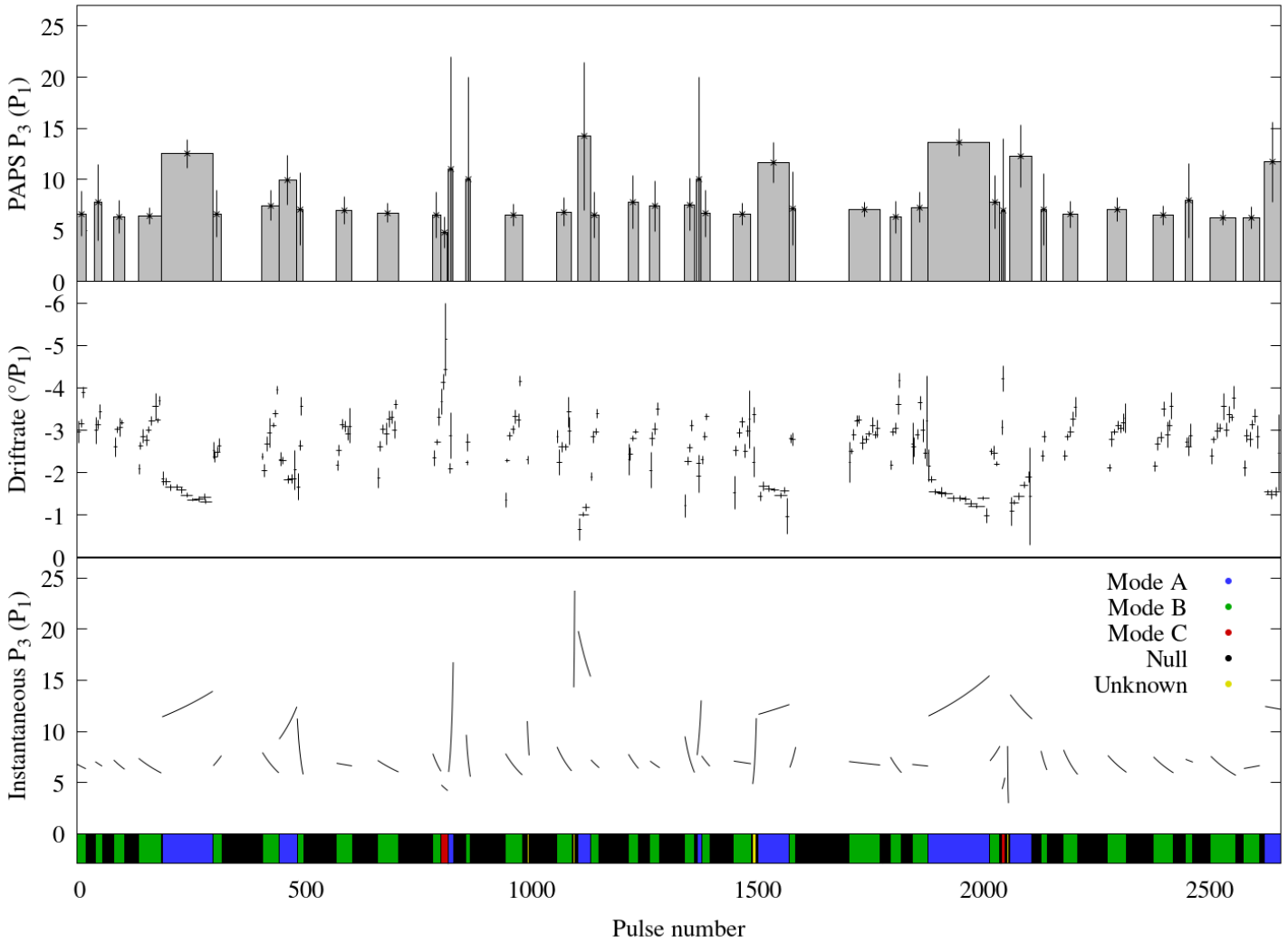

Figure 3.2 *Top*: Distribution of P_3 values calculated via the PAPS method of Smits et al. (2005). *Middle*: The slopes of drift bands containing at least 4 subpulses, from the linear fit described in §3.4.2. The horizontal length indicates the extent of the given drift band; the vertical length indicates the error of the drift rate. *Bottom*: The values of continuously changing P_3 as predicted by the quadratic fits described in §3.4.3. The P_3 values of Mode B (green) and Mode C (red) appear to be confined to narrow regions (between 6 and 8 P_1 for B; 3 and 5 P_1 for C), but those of Mode A (blue) vary dramatically. *Color panel*: These are the determined modes, by colour: mode A, mode B, mode C, nulls are in black, unclassified in yellow.

band's projected phase at the pulse in question. The projected phases were determined by a weighted least squares fit to each subpulse already associated with a drift band, where the weighting was proportional to the peak amplitude of the subpulse. However, the variation in subpulse position requires that a statistically significant number of pulses be already assigned to a drift band in order to obtain a reliable extrapolation of the drift band location. Thus, if a drift band has so far only been assigned 4 subpulses or fewer, we assume a nominal drift rate[3] of $-2.5^\circ/P_1$ and only perform least squares regression to find the phase offset. If a subpulse was found with a phase more than 10° to the right of the projected phases, it was assigned to the beginning of a new drift band. The process continues until the onset of a null sequence, and the entire algorithm is repeated for each drift sequence. Once all determined subpulses had either been assigned to a drift band or rejected as an outlier (if it didn't fall within 10° of any projected drift band), the subpulse positions were fit by a weighted least squares regression as before, except that this was also applied to even short (i.e. containing 4 or fewer subpulses) drift bands. The results of this algorithm for a subset of the pulse stack are illustrated by red lines in Fig. 3.3.

The errors on the slopes of the drift bands are calculated to be

$$m_{\rm unc} = \sqrt{\frac{1}{n-2}\frac{\sum_i (w_i(\varphi_i - \hat{\varphi}))^2}{\sum_i (w_i(p_i - \bar{p}))^2}}, \tag{3.2}$$

where the sums are iterated over the subpulses within a given drift band; n is the number of pulses within a drift band; φ and $\hat{\varphi}$ are respectively the measured subpulse phase and the phase predicted from the linear fit; p is the pulse number; and $\bar{p} = \frac{1}{n}\sum_i p_i$.

Having obtained a model for each drift band, we can now assess how the drift band slopes vary over the course of individual drift sequences (Fig. 3.2, middle

[3]For this pulsar, drift rates appear to range between $\sim 0.5^\circ/P_1$ and $\sim 4.5^\circ/P_1$, as evident in the results.

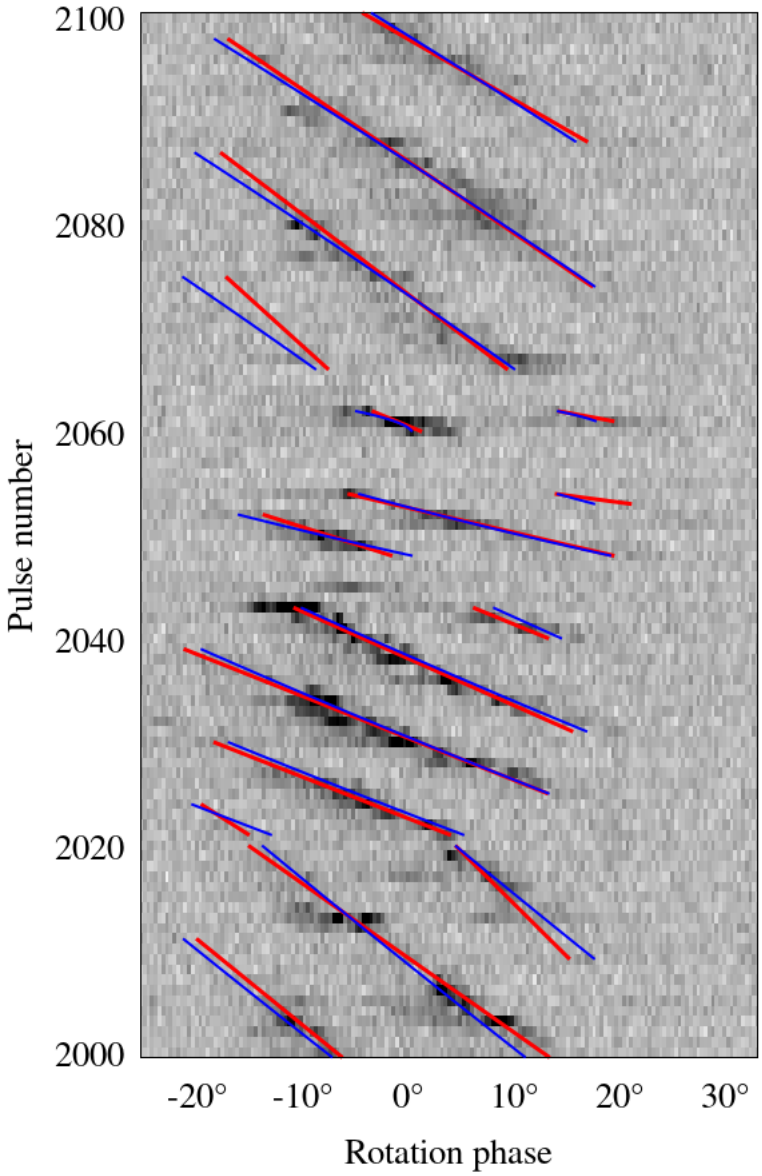

Figure 3.3 Pulse stack showing 101 pulses of B0031−07. The image is saturated at 25%, meaning that any pixel containing a value more than 25% of the maximum value in that window is displayed as a black pixel. Overlaid are red lines showing the linear fits to the drift bands using weighted least squares regression, described in §3.4.2, and blue lines showing the quadratic curves fit with fewer parameters, described in §3.4.3.

panel). Mode A drift bands tend to become steeper (i.e. the drift rate decreases), but those of mode B tend to become shallower (i.e. the drift rate increases), but not exclusively.

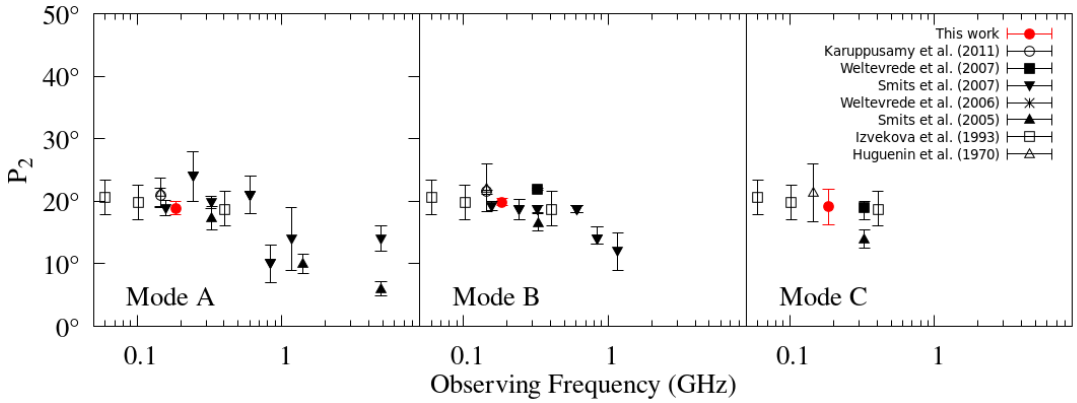

Figure 3.4 Comparison of available measurements of P_2, with the panels from left to right showing measurements of modes A, B, and C respectively. The fact that P_2 is consistent with being uniform across all three modes at any given frequency suggests that the angular spacing of the emission regions around the magnetic axis does not change between mode switches.

3.4.3 Quadratic fits to drift bands

The linear fits to the drift bands suggest that the drift rate varies quasi-linearly over the course of each drift sequence (to a first order approximation, cf. middle panel of Fig. 3.2). Assuming that this is the case, and also assuming that P_2 does not vary over the course of the observation, we write the following functional form for the nth drift band within a given drift sequence:

$$\varphi(p) = a_1 p^2 + a_2 p + a_3 + a_4 n, \tag{3.3}$$

where p is the pulse number starting from the beginning of the drift sequence, and a_1, a_2, a_3, and a_4 are free parameters to be fit. The drift rate, P_2, and P_3 can be derived from these parameters thus:

$$\begin{aligned} \frac{\mathrm{d}\varphi}{\mathrm{d}p} &= 2a_1 p + a_2, \\ P_2 &= a_4, \\ P_3 = \frac{P_2}{\mathrm{d}\varphi/\mathrm{d}p} &= \frac{a_4}{2a_1 p + a_2}. \end{aligned} \tag{3.4}$$

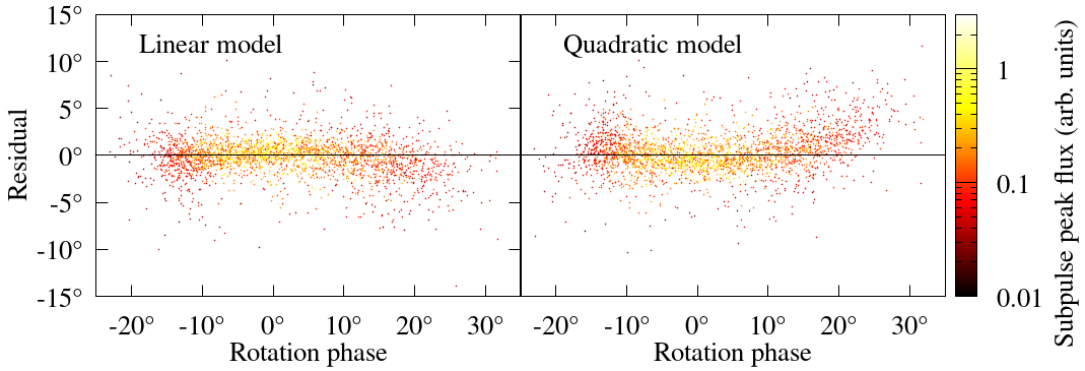

Figure 3.5 The residuals for both the linear fits to the drift bands (left panel) and the quadratic fits (right panel). The colour scale indicates the amplitude of the peak of the subpulses, which were used as weights in the regression fits. The linear fits appear to generate slightly smaller residuals, but requires many more free parameters. Both fits perform worse at the edges of the pulse window than in the central region, suggesting that P_2 is a weak function of rotation phase.

Note that the drift rate is linear in p, and P_2 is constant, as desired.

Because Eq. (3.3) is linear in a_1, a_2, a_3, a_4, they can be fit to the subpulse position data using least-squares regression. A weighted[4] linear fit was performed with the subpulses in each drift sequence, resulting in quadratic drift band fits shown in Fig. 3.3.

The quadratic fits described by Eq. (3.3) employ four free parameters per drift sequence, while the linear fits employ two free parameters per drift band. Both types of fit successfully identify the drift bands, but the subpulse position residuals suggest that the linear method fits the subpulses at the extremes of the pulse window slightly better than the quadratic method (Fig. 3.5). We note, however, that the quadratic fit method can potentially be used to correct a misidentification of a drift mode and/or drift mode boundaries, which occurred three times in the present data set. In the first instance, the quadratic fit failed to find a close fit to a set of drift bands when they were erroneously assumed to belong to the same drift mode. In the second instance, the drift sequence boundaries determined via the PAPS method had to be slightly adjusted in order to produce a good quadratic fit. Finally, the Mode C drift sequence at approximately pulse number

[4]The weights used were the amplitudes of the subpulse peaks, as before.

2050 was too short for the PAPS method to yield a reliable P_3 measurement, but was easily identified as Mode C using the quadratic fit method. Indeed, the striking difference between the average P_3 values for Mode C shown in Table 3.1 is due to the inability of PAPS to deal with such a short sequence.

3.4.4 Characterizing P_2

The value of P_2 in B0031−07 is consistent with being constant in time, irrespective of drift mode (Smits et al. 2005, but see Vivekanand and Joshi 1996 for evidence of the contrary). However, it has been observed to decrease at higher observing frequencies, in accordance with the radius-to-frequency mapping (Cordes, 1978, see Fig. 3.4 and references therein). Here, we report that P_2 is also dependent on the rotation phase, i.e. where the subpulses fall in the pulse window.

The average P_2 value is commonly measured by means of an ACF applied to the pulse stack. Here, we measure P_2 for each pulse individually, by simply taking the difference of phases of the two subpulse peaks detected by the peak-finding algorithm described in §3.4.2. The resulting P_2 measurements are plotted in Fig. 3.6 against the average (absolute) phase of the two subpulses. There is a noticeable positive correlation between P_2 and (average) phase—i.e. subpulses at later phases are generally spaced more widely apart.

To confirm this trend, we performed the identical quadratic fits described above to smaller subsets of subpulses. Within each drift sequence, the subpulses were divided into three subsets, based on their absolute phases. The phase boundaries were not the same for each drift sequence; instead, they were chosen to ensure that the number of subpulses in each subset were the same (or differed only by one, if the total number of subpulses was not divisible by three). P_2, as measured by the fit parameter a_4 (cf. Eq. (3.3)) for each subset is shown plotted against the average phase of the subset in the right-hand panel of Fig. 3.6. A similar upward trend is evident. We note, in passing, that the three modes do not appear to be drawn from different distributions of P_2, which is contrary to the finding of

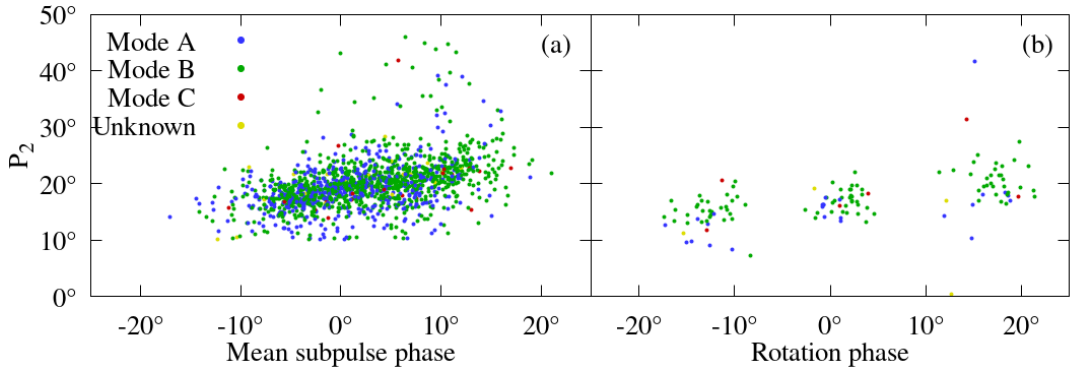

Figure 3.6 *Left*: The phase difference of two subpulses (P_2 measured for each pulse) against the phase of the midpoint between them. The fact that no P_2 was measured below 10° is a consequence of the algorithm used to measure the subpulse phases. *Right*: The value of the a_4 parameter (P_2 measured for each drift sequence) against the central phase of the swath used in the fit. Both methods indicate that P_2 is positively correlated with rotation phase.

Vivekanand and Joshi (1996) who reported a weakly negative correlation between P_2 and drift rate from analysis of their observations at 325 MHz.

3.5 Discussion

We have demonstrated the presence of two effects in B0031−07 that have previously not been studied in detail. Firstly, the drift rate in B0031−07 varies gradually within individual drift modes as well as sharply between them (Fig. 3.2). Secondly, P_2 appears to be positively correlated with rotation phase; i.e. subpulses on the right hand side of the pulse window (when viewed in the pulse stack) are more widely separated than those on the left hand side (Fig. 3.6).

Both of these effects were observed in B0826−34 (Gupta et al., 2004, hereafter GGKS04), another long-period ($P_1 = 1.85\,\mathrm{s}$) drifter, although different from B0031−07 in many respects. B0826−34 has a very wide profile, with up to 13 distinct drift bands being observed across all 360°. It appears to exhibit nulling, but weak emission (at the 2% level, at 1374 MHz) has been detected during null periods, enabling the tracing of the drift bands continuously over several hundred pulses (Esamdin et al., 2005). Bhattacharyya et al. (2008), however, report no

emission during nulls (at the 1% level) in their observations at 157, 325, 610, and 1060 MHz. B0826−34 and B0031−07 are suspected to have similar viewing geometries, with α (the angle between the rotation axis and the magnetic axis) and β (the angle between then magnetic axis and the line of sight at closet approach) both being very small ($< 10°$). The parameters α and β are often estimated by fitting the polarisation angle sweeps to the magnetic pole model (Radhakrishnan and Cooke, 1969). However, for both pulsars, there are several combinations of α and β that reproduced the observed polarisation curve, and current estimates give $1°.5 \leq \alpha \leq 5°.0$ and $0°.6 \leq \beta \leq 2°.0$ for B0826−34 (GGKS04) and $\alpha \approx \beta$ around $2°.0$ to $4°.0$ (Smits et al., 2007). A final difference is that, unlike B0031−07 whose drift rate always maintains the same direction and changes only gradually throughout any given drift sequence, the drift rate of PSR B0826−34 fluctuates about a mean value of $\sim 0°/P_1$, changing sign in a quasi-periodic manner.

3.5.1 Variable drift rate by stellar surface temperature fluctuations

Given the apparent similarity with B0826−34, we assess if the explanations that GGKS04 offer for the appearance of these features in B0826−34 would be applicable to B0031−07 as well. The variability of the drift rate is suggested to arise from fluctuations in the stellar surface temperature, which indirectly influences the $\vec{\boldsymbol{E}} \times \vec{\boldsymbol{B}}$ drift rate. Moreover, the apparent change in drift direction is attributed to an aliasing effect; with higher-order aliasing, the direction will appear to change if the true value of P_3 fluctuates over a small range that straddles an integral multiple of P_1. In this scenario, small fractional variations in the true drift rate can appear to observers as large fractional variations in measured drift rate. GGKS04 calculate that only up to 8% change in the true drift rate is required to explain the measured variation, and that this upper limit requires only a 0.14% fluctuation in the surface temperature.

Even though the observed drift rate in B0031−07 is ubiquitously unidirec-

tional, the fractional variation is very large ($\approx 67\%$) and can only be realistically explained by the same mechanism of fluctuating surface temperature if higher order aliasing is invoked to bring the true drift rate variation down to a few percent. For the geometry assumed by Smits et al. (2005), with 9 subbeams viewed at $\alpha \approx \beta \approx 4.5^\circ$, we find that the true drift rate becomes approximately $(10/k)\%$ for aliasing order $k \geq 1$. Thus, even aliasing order $k \gtrsim 2$ would bring the true drift rate to a level consistent with the 8% inferred for B0826−34. However, this cannot explain both the gradual change in drift rate within drift sequences and the abrupt change in drift rate between them, unless the temperature fluctuated at two distinct timescales. Even if aliasing is present, one is still left with a "cuspy" evolution of drift rate (cf. Esamdin et al. 2005, who point out the existence of such cusps in the drift rate of B0826−34). Thus, in keeping with the observed timescale of drift rate variation observed in B0826−34 (~ 100 pulses $\approx 180\,\mathrm{s}$), we surmise that if the surface temperature is indeed responsible for the intra-sequence drift rate variation, then some other, possibly unrelated mechanism must drive the drift mode changes.

The above discussion raises the interesting possibility that the true drift rate is in reality continuous (even if "cuspy" at drift mode boundaries), and that the apparent discontinuities are solely a side-effect of observing effects such as aliasing. In this scenario, the correct aliasing order and number of subbeams may be recognised by their ability to "connect up" the drift rates of pairs of adjacent drift sequences. Thus, the presence of multiple drift modes which are usually thought to be a hindrance to determining the true carousel drift rate, may in fact turn out to be the key. This, however, requires a much longer data set than presented here because of the fact that most drift sequences in B0031−07 are bordered by nulls (see Fig. 3.2). Based on the number of mode transitions in our data set, we estimate a rate of approximately 40 suitable mode transitions per $10,000$ pulses.

3.5.2 The P_2 dependence on rotation phase

GGKS04 invoke a new idea to explain the positive correlation between the measured P_2 and rotation phases. They suggest that the carousel pattern is centered not on the magnetic dipole axis, but around some other nearby axis (dubbed the "local pole") that arises perhaps due to a more dominant multipolar component near the surface. In their case, they were able to determine that a local pole which is offset from the dipole axis by $\sim 3^\circ$ is able to reproduce the observed P_2 dependence on rotation phase. We hope that a similar analysis will be able to find a local pole solution for B0031−07. This analysis, however, also depends on a known (or assumed) number of beams and aliasing order, which cannot yet be inferred from current observations.

Other explanations for this effect are not forthcoming. For example, retardation and aberration effects are traditionally invoked to explain the asymmetry in pulsar profiles. Unfortunately, as discussed in Gupta and Gangadhara (2003), and emphasised in Dyks et al. (2004), these effects serve to "stretch" out profile features at lower phases and "compress" features at higher phases. The upshot is to cause P_2 to be *longer* at lower phases, which is exactly the opposite to that observed in B0031−07.

Another possible explanation is the motion of the visible point (Yuen and Melrose, 2014; Yuen et al., 2016), which takes into account the direction of the dipolar magnetic field at the emission site, an effect that has traditionally been neglected in the interpretation of P_2 measurements. They showed that measurements of P_2 can dramatically underestimate the true subbeam separation when the angle between the rotation and magnetic axes, α, is sufficiently small, which is believed to be the case for B0031−07 (e.g. Smits et al., 2005, 2007). However, they also showed that the discrepancy in P_2 is symmetrical about the fiducial point, which the measured P_2 increasing as one moves away (in either direction) from the fiducial point. Again, this is at odds with what is seen from our observations, where P_2 appears to increase monotonically across the pulse window. Even

though invoking the effect of a moving visible point may explain the variation in P_2, it will require the assumption that the fiducial point lies somewhere to the left of the on-pulse region. However, attempts to constrain the fiducial point of B0031−07 have not met with success, owing to its complex polarisation profile, which contains orthogonal polarisation modes and differs between drift modes (Karuppusamy et al., 2011). Thus we are not able to comment on the likelihood of this scenario.

3.6 Conclusion

We have conducted a detailed analysis of new observations of B0031−07 with the MWA at 185 MHz, a first-of-its-kind demonstration of this instrument's capability of producing high quality single-pulse data, in line with its intended science aims (Bowman et al., 2013). Our analysis shows that the drift bands of B0031−07 exhibit more complex behavior than what has been inferred from previous studies. In particular, (1) the measured drift rate changes continuously within individual drift sequences, with a characteristic variation time scale apparently longer than the typical duration of individual drift sequences; and (2) P_2 is positively correlated with rotation phase. Both of these effects were observed and studied in B0826−34 by Gupta et al. (2004), who explain the variable drift rate by linking it to surface temperature fluctuations, and the P_2 dependence on rotation phase by determining the position of a "local pole" around which the carousel is assumed to rotate. However, the applicability of their proposed physical explanations to B0031−07 requires the knowledge of the aliasing order and the number of subbeams in the carousel, which are currently unknown for B0031−07. However, we note that resolving the aliasing order and number of subbeams may be helped by assuming that the true drift rate varies continuously over drift mode boundaries, but such an investigation requires significantly longer observations than have been presented here.

Chapter 4

On the geometry of curvature radiation and implications for subpulse drifting

McSweeney et al. (2017) reported that the subpulses of B0031−07 experienced a phase shift that depended on both the observing frequency and on the drift mode, and similar behaviour has been reported for other pulsars. This chapter is a reproduction of the author's publication (McSweeney et al., 2019), which introduces a numerical code whose purpose is to study the effects of aberration and retardation on the arrival times of individual subpulses. As in Chapter 3, only cosmetic changes have been made from the original.

Abstract

The phenomenon of subpulse drifting offers unique insights into the emission geometry of pulsars, and is commonly interpreted in terms of a rotating carousel of "spark" events near the stellar surface. We develop a detailed geometric model for the emission columns above a carousel of sparks that is entirely calculated in the observer's inertial frame, and which is consistent with the well-understood

rotational effects of aberration and retardation. We explore the observational consequences of the model, including (1) the appearance of the reconstructed beam pattern via the cartographic transform and (2) the morphology of drift bands and how they might evolve as a function of frequency. The model, which is implemented in the software package PSRGEOM, is applicable to a wide range of viewing geometries, and we illustrate its implications using PSRs B0809+74 and B2034+19 as examples. Some specific predictions are made with respect to the difference between subpulse evolution and microstructure evolution, which provides a way to further test our model.

4.1 Introduction

The phenomenon of subpulse drifting (Drake and Craft, 1968; Backer, 1973) offers unique insights into the emission physics of pulsars, if the correct interpretation can be found. One popular interpretation has its basis in the carousel model, originally proposed by Ruderman and Sutherland (1975), in which the geometry of the emitted pulsar beam is intimately connected with the geometry of a circular pattern of sparks near the stellar surface that rotate around the magnetic pole. More recently, Deshpande and Rankin (1999, 2001) developed a technique for mapping the two-dimensional emission beam that overcomes the inherent difficulty arising from the fact that a fixed observer's line of sight only ever makes a one-dimensional cut through it. This "cartographic transform" technique requires sufficiently long and stable pulse sequences[1] in order to "fill in" the map completely enough to see the beam's global structure.

The cartographic transform involves a number of parameters, including α, the angle between the rotation and magnetic axes, ζ, the angle between the rotation axis and the line of sight, N, the number of beamlets in the carousel, and P_4, the rotation time of the carousel. If these parameters are either not known

[1]Pulse sequences can be interrupted by nulls and mode changes on quasi-random time scales, whose statistics are different from pulsar to pulsar.

beforehand, or are coarsely estimated by other means, the cartographic transform can be used to test the viability of sets of parameters. In general, if one or more of the parameters put into the transform are slightly incorrect, the resulting polar beam pattern will be smeared and hence would be relatively devoid of structure. Then, a pulse sequence reconstructed from it will not correlate well with the original pulse sequence. However, the test is not entirely sufficient for finding the correct set of parameters as degeneracies may exist (e.g. due to aliasing of the rotating spark pattern modulo the pulsar rotation), which would have to be resolved by other means.

In the case of PSR B0809+74, Rankin et al. (2006) found that frequent mode changes, nulls, and "memory" of drift band phase across the nulls, all conspired to make it difficult to distinguish between a handful of solutions that all produced credible beam emission maps (see their paper, and references therein, for a full account of the difficulties encountered in their analysis). One of their solutions ($\alpha \approx 9°$, $\zeta \approx 13.5°$, $N = 10$) produced a polarised beam map with a striking asymmetry, where the beamlets of one of the orthogonal polarisations appear to be skewed in a common azimuthal direction (see their Fig. 4).

Under the assumption that the geometric parameters are correct, the authors connect this asymmetrical feature to "absorption" (Rankin et al., 2006), which is an empirical phenomenon, currently lacking physical justification. Here, we ask whether this kind of beam asymmetry can possibly arise from purely geometric considerations once rotational effects are taken into account. In this context, the primary relevant rotational effects are aberration and retardation (hereafter, AR effects), which are both height-dependent effects that cause emission to appear at an earlier phase than otherwise expected (Blaskiewicz et al., 1991; Dyks et al., 2004).

The treatment of aberration begins by making a few simple assumptions about how the emitted radiation would appear in the corotating frame (CF), and then using the principles of relativistic aberration to translate the Poynting vector into

the observer's inertial frame (IF). Dyks et al. (2004) show that if you assume that the Poynting vector is parallel to the tangent of the local magnetic field at the emission point, then the angle between the Poynting vector and the tangent of the local magnetic field in the IF, $\eta_{\rm ab}$, is, to first order,

$$\eta_{\rm ab} \approx r' \sin\theta_z, \tag{4.1}$$

where $r' = r/r_L$, r is the distance of the emission point from the origin placed at the stellar centre, $r_L = c/\Omega$ is the light cylinder radius, $\Omega = 2\pi/P$ is the angular frequency of pulsar rotation, and θ_z is the angle that the position vector of the emission point makes with the rotation axis $\hat{\boldsymbol{\Omega}} \equiv \hat{\boldsymbol{z}}$. The observable effect of this aberrational correction is a shift of the profile towards earlier phases,

$$\Delta\phi_{\rm ab} \approx \frac{\eta_{\rm ab}}{\sin\zeta}. \tag{4.2}$$

Dyks et al. (2004) point out, however, that the assumption of parallel vectors in the CF requires that the Lorentz factors of the emitting particles are relatively high, a requirement that is necessary in any case for curvature radiation to be in the observed range of radio frequencies.

The necessity of translating between the CF and the IF would not be required if the trajectories of the particles were already known in the IF. In this case, the Poynting vector of the curvature radiation could simply be identified with the instantaneous velocity of the particles (and of course across the width of the individual particle beam, which goes as $\sim 1/\gamma$). It is well established that the magnetic field lines are "frozen into" the corotating magnetosphere, and that particles are tightly constrained to move along magnetic field lines (at least, well within the light cylinder radius) as "beads on a wire" (e.g. Goldreich and Julian, 1969; Sturrock, 1971; Ruderman and Sutherland, 1975).

The problem of determining the trajectory of a particular particle on a particular field line from first principles is a non-trivial exercise. In Thomas and

Gangadhara (2007), the equations of motion for a particle in the (vacuous) magnetosphere are derived and evaluated numerically to produce particle trajectories that depend on both the functional form of the magnetic field and the magnetic inclination angle α. They found that there is significant contribution, due to rotation effects, to the curvature of field lines on the leading side of the magnetic axis as compared to those on the trailing side. Indeed, even particles on field lines very close to the magnetic axis have trajectories with significant rotation-induced curvature even though the field lines themselves have very small curvature.

Thomas and Gangadhara (2007) remind us that in the emission region, the various forces acting on a magnetospheric particle are expected to balance in such a way that the particle is tightly constrained to remain on a single field line. This is because, in the words of Radhakrishnan and Deshpande (2001), "any transverse momentum and energy would be radiated away 'instantly', and the charged particles would be in their lowest Landau levels." This implies that in regions where this balance is maintained, there is a relatively simple way to deduce the velocities of particles in the emission region by geometric arguments, without needing to evaluate the competing forces acting on the particles. Indeed, a sufficient set of assumptions to derive a particle's trajectory are that (1) we know the time-dependent magnetic field in the IF (and that the observer is at rest with respect to the centre of the star), (2) particles (in the emission region) move one-dimensionally along field lines as beads on a wire, and (3) we know the particle's speed in the IF, $\beta \equiv v/c$. In Section §4.2 we derive the particle velocities under the above assumptions, using a simple dipole field, and compare the results of this derivation to the more traditional approach via aberration as presented by Dyks et al. (2004) and others. We then proceed in Section §4.3 to use the derived analytical expression of the velocity field to predict the shape of the beam, both analytically in the case of an aligned rotator, and numerically in the general case. The geometric model is then applied in Section §4.5 to PSRs B0809+74 and B2034+19, two subpulse drifters with contrasting drift band morphologies,

to demonstrate the viability of the geometric approach. Finally, we include a discussion on the conditions required to observe various geometric effects in drift bands.

4.2 Derivation of the velocity and acceleration fields

The requirement of particles to stay on a corotating field line provides a strong geometric constraint on the possible trajectories of the particle. Let $\vec{C}(s,t)$ be a parametrisation of a given field line. Then corotation implies that $\vec{C}(s,t+\Delta t) = R_z(\Delta t)\vec{C}(s,t)$, where $R_z(\Delta t)$ is the matrix representing constant-speed rotation about the z-axis after time Δt. An observer in the IF who measures a particle at times t and Δt will see the particle move at some non-zero angle, η, to the local magnetic field. The average speed measured in the IF is completely determined by the motion of the field line, which is known, and the angle η. Indeed, the fact that the particle's speed in the IF is necessarily $v < c$ is equivalent to a finite range of allowed values of η, as illustrated in Fig. 4.1. Moreover, the extreme values of η correspond to the limit $v \to c$.

To find which values of η correspond to a given velocity, we take the vector sum illustrated in Fig 4.1 in the limit $\Delta t \to 0$. In this limit, the vector $\overline{PP'}$ becomes the particle's instantaneous velocity as measured in the IF, the vector $\overline{PQ}$ becomes the azimuthal velocity, and the vector $\overline{QP'}$ is tangent to the local magnetic field line at P. Thus, $\overline{PP'} = \overline{PQ} + \overline{QP'}$ becomes a vector triangle for which we know two sides (the particle's measured or assumed speed and the azimuthal velocity) and an angle (between the azimuthal direction and the local magnetic field), and which therefore can be solved completely.

As implied by Fig. 4.1, there are in general two solutions for a given particle speed. By solving the vector triangle for $v \approx c$, the normalised velocity vector

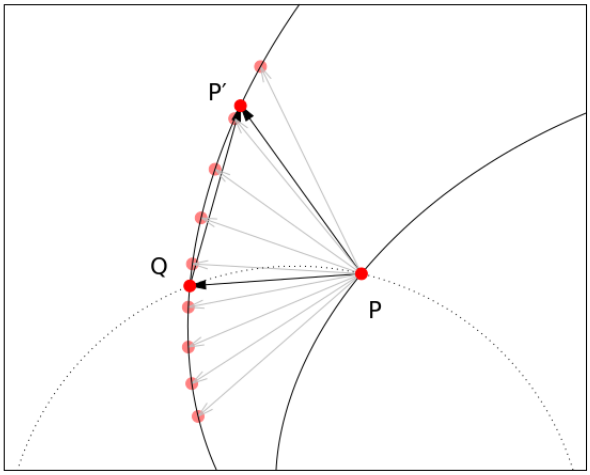

Figure 4.1 A schematic of the possible trajectories of a particle corotating with a magnetic field line. In the absence of any radial motion, a particle located at P at time t would end up at Q at time $t + \Delta t$. In general, the particle may move in a limited range of directions, as illustrated by the grey arrows, each corresponding to a specific speed measured by an observer in the IF. One arbitrary direction in this range is indicated by the point P' and the black arrows.

can be expressed as

$$\hat{\boldsymbol{v}} = \rho' \hat{\boldsymbol{\phi}} + \left[-\rho' (\hat{\boldsymbol{\phi}} \cdot \hat{\boldsymbol{B}}) \pm \sqrt{1 - (\rho')^2 (1 - (\hat{\boldsymbol{\phi}} \cdot \hat{\boldsymbol{B}})^2)} \right] \hat{\boldsymbol{B}} \tag{4.3}$$

where $\rho' = \rho / r_L$ is the azimuthal corotation speed normalised to the speed of light, ρ is the point's perpendicular distance from the $\hat{\boldsymbol{z}}$-axis, $\hat{\boldsymbol{\phi}}$ is the azimuthal unit vector, and $\hat{\boldsymbol{B}}$ is the unit tangent to the local magnetic field in the inertial observer frame. In most cases in the region of interest (i.e. above the polar cap), the positive solution corresponds to outward-flowing particles and the negative solution to inward-flowing particles. Throughout the rest of this paper, we will consider only positive solution. Moreover, because Eq. (4.3) is defined at all points in the magnetosphere, it describes a unique vector field (up to the sign of the radical), from which all other geometric properties can be directly derived, as is shown later in §4.3.

The particle acceleration field can be directly computed from the velocity

field. Like the magnetic field, the velocity field "corotates" with the pulsar, and in the context of a time-dependent velocity field, the acceleration field must be identified with the material derivative

$$\vec{\boldsymbol{a}} = \frac{\partial \vec{\boldsymbol{v}}}{\partial t} + v_x \frac{\partial \vec{\boldsymbol{v}}}{\partial x} + v_y \frac{\partial \vec{\boldsymbol{v}}}{\partial y} + v_z \frac{\partial \vec{\boldsymbol{v}}}{\partial z}. \tag{4.4}$$

Because the velocity $\vec{\boldsymbol{v}}$ has been constructed to have constant magnitude ($v \approx c$), the acceleration can be reduced to

$$\vec{\boldsymbol{a}} = c \left(\frac{\partial \hat{\boldsymbol{v}}}{\partial t} + v_x \frac{\partial \hat{\boldsymbol{v}}}{\partial x} + v_y \frac{\partial \hat{\boldsymbol{v}}}{\partial y} + v_z \frac{\partial \hat{\boldsymbol{v}}}{\partial z} \right). \tag{4.5}$$

Eqs. (4.3) to (4.5) were derived with an arbitrary magnetic field, but one must be careful to use only (time-dependent) magnetic fields that are physically meaningful in the IF. For an investigation of first-order effects, a static rotating dipole is a sufficiently good approximation, but throughout this paper, and in the accompanying numerical code[2], we have implemented the vacuum field derived originally by Deutsch (1955) (cf Arendt and Eilek 1998; Dyks and Harding 2004).

4.3 Construction of the beam

The salient feature of the velocity field as defined by Eq. (4.3) is that there is a unique emission direction associated with each emission location. Therefore, assuming that magnetospheric propagation effects are negligible (which may very easily not be the case, e.g. see Barnard and Arons 1986), the beam shape can be predicted for a given set of emission regions. A complete model also requires that the spectral output of each point is known, but in this analysis we will ignore any frequency dependence and only consider emission to be either on or off.

Before presenting the numerical beam shapes, we review the treatment of beam shapes in the slow rotation limit, and then derive the distortions introduced

[2]PSRGEOM, obtainable from `https://github.com/robotopia/psrgeom`

by finite rotation speeds. In this and following sections, (r, θ, ϕ) refer to spherical coordinates aligned with the magnetic axis. That is, r, θ, and ϕ are the radial distance, the magnetic colatitude, and the magnetic azimuth, respectively.

In the absence of rotation, the velocity field is everywhere parallel to the magnetic field, as can be confirmed by letting $r_L \to \infty$ (i.e. $\rho' \to 0$) in Eq. (4.3). In this case, emission will be axisymmetric about the magnetic axis, $\hat{\boldsymbol{\mu}}$, and we can define the beam magnetic colatitude[3] to be $\Gamma = \cos^{-1}(\hat{\boldsymbol{B}} \cdot \hat{\boldsymbol{\mu}})$. In the same limit, the Deutsch field reduces to a static dipole, and in this case, this colatitude becomes (for a fuller treatment, see Gangadhara and Gupta, 2001; Gangadhara, 2004)

$$\Gamma_{\rm nr} = \tan^{-1}\left(\frac{3\sin\theta\cos\theta}{3\cos^2\theta - 1}\right), \tag{4.6}$$

with the well known small angle approximation $\Gamma \approx (3/2)\theta$. The subscript "nr" here indicates non-rotation. The emission, like the magnetic field, will have no azimuthal component in the magnetic coordinate system.

With rotation, the important quantity for the beam shape is the angle between the velocity field and the magnetic axis, i.e. the deflected beam colatitude $\Gamma = \cos^{-1}(\hat{\boldsymbol{v}} \cdot \hat{\boldsymbol{\mu}})$. The expression of this quantity in terms of spherical coordinates is a formidable exercise in algebra, but we can compare in more detail the more simplified case of an aligned rotator, $\alpha = 0$. Then,

$$\cos\Gamma = (3\cos^2\theta - 1)\sqrt{\frac{1 - (r'\sin\theta)^2}{3\cos^2\theta + 1}}. \tag{4.7}$$

In the small angle approximation, we find

$$\Gamma \approx \sqrt{(r')^2 + \frac{9}{4}}\,\theta + O(\theta^3), \tag{4.8}$$

showing that the beam is dilated by an extra factor that depends on the emission

[3]Ordinarily, the term "half opening angle" is used for this quantity, which makes sense in the context of conal beam shapes, but here we use "beam colatitude" to emphasise the fact that the quantity is defined for all points in the magnetosphere, regardless of the global shape of the actual, observed beam.

height.

In the context of a given field line, r' and θ are coupled. For a dipole geometry, the relationship between them is: $r \propto \sin^2\theta$, where the constant of proportionality is the field line's maximal distance from the origin. Here, we follow the convention of Gangadhara and Gupta (2001) and others, and identify a field line by the magnetic colatitude of the point at which it pierces the pulsar surface, i.e. the "footpoint" colatitude θ_p. Moreover, we normalise the footpoint colatitude to the colatitude of the last open field lines, $\theta_L = \sin^{-1}\sqrt{r_p/r_L}$, so that the quantity $s \equiv \theta_p/\theta_L$ equals 0 at the magnetic pole and unity at the polar cap radius. By fixing s, we can make the substitution

$$r' \to \frac{r_p \sin^2\theta}{r_L \sin^2(s\theta_L)}, \tag{4.9}$$

in which case the approximation (4.8) reduces to $\Gamma \approx (3/2)\theta$ as before, with the s term only making an appearance in the 5th order term in θ.

As well as a slight expansion, the beam also acquires an azimuthal component, which due to axisymmetry also depends only on r' and θ. If the intensity of the pulsar beam is also axisymmetric, the azimuthal component becomes irrelevant (for the aligned rotator), since it only serves to rotate the beam around the common axis. However, the intensity profile generated by a rotating carousel is (or may be) only axisymmetric after averaging over a carousel rotation. In order to appreciate the effects of aberration on the global beam shape, we momentarily neglect the effects of carousel rotation by considering the slow rotation limit (i.e. $P_4 \to \infty$). In this limit, each beamlet originates from a narrow tube of field lines emerging from a discrete spark at the tube's base. The beam shape due to a single narrow tube will in general be some form of spiral, as emission from different heights along the tube is deflected by different amounts. Of course, the whole spiral will not necessarily be present because the emission is presumably only generated within a finite range of heights at a given frequency. Nevertheless, for a given line of sight cut, it may be the case that a large enough range of heights

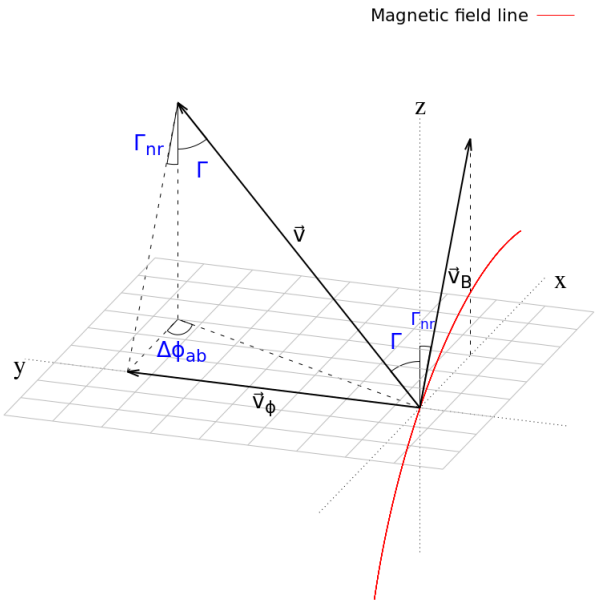

Figure 4.2 The geometry of rotationally deflected emission for an aligned rotator. The red line is a magnetic field line in the xz-plane. The vector $\vec{\boldsymbol{v}}$ is deflected from the tangent to the magnetic field line, such that $\Gamma > \Gamma_{\rm nr}$ and $\Delta\phi > 0$. The vectors $\vec{\boldsymbol{v}}_\phi$ and $\vec{\boldsymbol{v}}_B$ correspond to the first and second terms of Eq. (4.3), respectively.

are sampled that the map produced by the cartographic transform reveals the spiral nature of the individual beamlets.

To find the beam's azimuthal component (in the aligned case), we first compute the quantity $\Delta\phi_{\rm ab} = \tan^{-1}(-v_y/v_x)$. Axisymmetry allows us to calculate the azimuthal aberration by simply evaluating $\Delta\phi_{\rm ab}$ in the xz-plane (i.e. when $\phi = 0$). This gives

$$\tan(\Delta\phi_{\rm ab}) = -\frac{r'}{3\cos\theta}\sqrt{\frac{3\cos^2\theta + 1}{1 - (r'\sin\theta)^2}}. \tag{4.10}$$

The above result may be more simply derived by noting that in Fig. (4.2), the common sides of the triangles formed by $\vec{\boldsymbol{v}}$, $\vec{\boldsymbol{v}}_\phi$, and $\vec{\boldsymbol{v}}_B$ must be related by

$$\cos(\Delta\phi_{\rm ab}) = \frac{\tan\Gamma_{\rm nr}}{\tan\Gamma}, \tag{4.11}$$

and then substituting in the Eqs. (4.6) and (4.7).

Having obtained a complete description of the deflected emission beam, we must now incorporate the effects of retardation into the analysis. Similarly to Γ above, we can define the retardation angle, $\Delta\phi_{\rm ret}$, as a valid quantity at every point in the magnetosphere, regardless of whether or not the observer is in the direction to observe it:

$$\Delta\phi_{\rm ret} = -r'(\hat{\boldsymbol{r}} \cdot \hat{\boldsymbol{v}}), \tag{4.12}$$

which, for an aligned rotator becomes

$$\begin{aligned} \Delta\phi_{\rm ret} &= -2r' \cos\theta \sqrt{\frac{1-(r'\sin\theta)^2}{3\cos^2\theta + 1}} \\ &= -\frac{2r'\cos\theta\cos\Gamma}{3\cos^2\theta - 1} \end{aligned} \tag{4.13}$$

The negative sign serves the same purpose as that in Eq. (4.10), namely, to shift the observed emission to earlier rotation phases. This shift is equivalent to a further azimuthal distortion of the overall beam pattern, which in the aligned case serves to enhance the curvature of the spiral shape of the beam. For a dipolar field, Eq. (4.12) reduces to the approximation $\Delta\phi_{\rm ret} \approx -r' + O(r'^3)$, in agreement with Dyks et al. (2004).

By choosing a fixed s, the equations above constitute a complete description of the spiral beam pattern, as illustrated in Fig. 4.3. The foregoing construction is also valid (albeit algebraically daunting) for pulsars of arbitrary inclination angle α.

Emission from field lines with smaller s suffer from greater azimuthal distortion. This makes intuitive sense: the curvature of these field lines is smaller, and so the particles must climb to greater heights in order to produce beams of equivalent apparent magnetic colatitude. In the case of any one particular pulsar, however, it generally remains unknown exactly which magnetic field lines are the active ones. On the other hand, if azimuthal distortion of the beam can be measured, and assuming there are no significant additional distorting effects, the

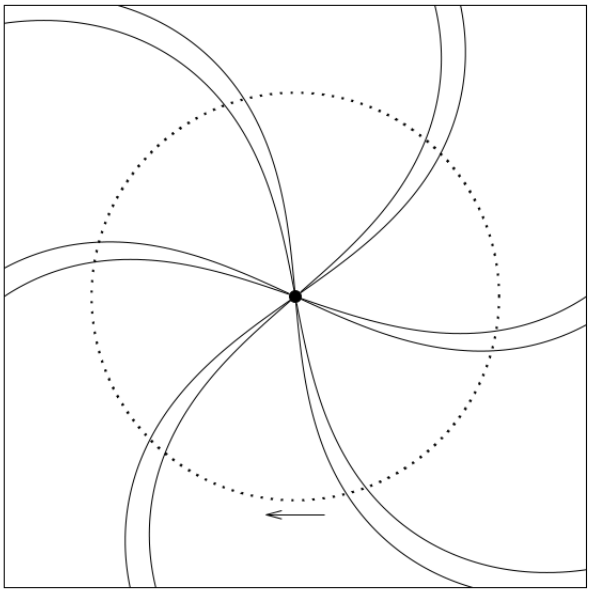

Figure 4.3 A schematic diagram of the spiral structure of beamlets arising from carousel sparks for an aligned rotator—once rotation effects and retardation have been factored in—if the emission were allowed to come from all heights. Note that the beam pattern itself would only be axisymmetric for a perfectly aligned rotator. In general, the line of sight (dotted line) cuts through the beamlets at an oblique angle that depends on the emission height, visible as an azimuthal distortion of the beam pattern. The line of sight cuts from right to left, as indicated by the arrow. The directional sense of the distortion is the same as the sense of stellar rotation, i.e. clockwise when viewed from above.

footpoints colatitudes can be constrained.

4.4 Simulating pulse stacks

A true comparison of the predictions of the present model and the polar maps generated by the cartographic transform requires the simulation of pulse stacks which can then be transformed. In this section, we describe in detail the process of producing simulated pulse stacks from the geometric model outlined above.

Clearly the geometric framework alone is insufficient to simulate observed pulse stacks; it can only say when emission from a given location in the magnetosphere would be seen by the observer, not how bright that emission would be at

a given frequency. However, the primary consideration here is the morphology of the drift bands, i.e. when the subpulses in successive pulses arrive in relation to each other. By virtue of the underlying assumption of the carousel model—that the emissivity of a field line is directly related to the spark activity at its base—we can use a simple model for estimating the observed intensities from specific emission locations in which they are proportional to the spark activity at their respective footpoints.

For an observer whose line of sight makes an angle ζ to the rotation axis, the only points on a given magnetic field line that are potentially visible are those for which

$$\hat{\boldsymbol{v}} \cdot \hat{\boldsymbol{\Omega}} = \cos\zeta \tag{4.14}$$

(in the aligned case, this condition is equivalent to $\Gamma = \zeta$). When $\zeta > \alpha$, there is a unique height on each magnetic field line above the polar cap where this condition is satisfied. On the other hand, when $\zeta < \alpha$, field lines on the equatorial side of the magnetic axis start at the surface with associated velocities that make an angle to the rotation axis $> \alpha$, and this angle only increases at greater emission heights as the field line drops away, never becoming equal to ζ. Then $\zeta < \alpha < \cos^{-1}(\hat{\boldsymbol{v}} \cdot \hat{\boldsymbol{\Omega}})$, so Eq. (4.14) can never be satisfied and these field lines never come into view of the observer. Field lines on the poleward side, however, initially curve "upwards" and then "backwards", so that the angle $\cos^{-1}(\hat{\boldsymbol{v}} \cdot \hat{\boldsymbol{\Omega}})$ starts at some value $< \alpha$, decreases through ζ until some minimum value is reached, and then increases again as the magnetic field drops away on the other side. These field lines therefore include visible points at two different heights, whose exact values can be found by solving Eq. (4.14) numerically. Since the second visible point is typically much higher than the first and appears near the anti-fiducial point, they are not expected to be observed in type S_d pulsars (i.e. whose profiles consist of a single conal component) and we hereafter consider only the lower visible point.

The fact that each visible magnetic field line is only observed at most at one

height implies that *any* arbitrary intensity profile or pulse stack can be obtained by a careful choice of (dynamic) spark pattern on the surface. However, we note that multiple field lines can contribute to the emission observed at a given phase, so that at all phases a range of heights is (potentially) observed. In this geometric model, having a range of emission heights is necessary to produce a spread in the polarisation angle at a given rotational phase, because just as each point in the magnetosphere has associated with it a unique velocity from Eq. (4.3), each point also has a unique acceleration vector from Eq. (4.4), and therefore a unique polarisation angle. Thus, a realistic model requires that a full, two dimensional spark pattern is used, in order that a range of heights and therefore a range of polarisation angles are sampled at each phase. However, for ease of computation, the simulated pulse stacks presented here are generated from a one-dimensional carousel at a fixed value of s whose "sparks" have Gaussian profiles in magnetic azimuth. By choosing only a single s value and making the rest of the polar cap "inactive", we are forcing the polarisation angle to adopt a unique value at each phase—that is, every pulse will have the exact same sweep of polarisation angles—which we will interpret as the "average" polarisation angle.

The steps to create a pulse stack are then as follows. For each footpoint in the (one dimensional) carousel, the field line is traversed numerically using Runge-Kutta integration until a point is found that has the property that $\hat{\boldsymbol{v}} \cdot \hat{\boldsymbol{\Omega}} = \cos\zeta$, where $\hat{\boldsymbol{v}}$ is calculated from Eq. (4.3). This is the so-called "visible point" of that field line. The polarisation angle associated with the visible point is then calculated by projecting the acceleration vector of Eq. (4.4) onto the observer's sky plane (i.e. normal to $\hat{\boldsymbol{v}}$). This is done to verify that the chosen parameters are consistent with the observed (average) polarisation swing.

The observed phase is determined by calculating $\Delta\phi_{\rm ab} + \Delta\phi_{\rm ret}$. The first term gives the rotation phase at which the emission must have taken place, and the second term is the retardation shift due to photon flight times. Next, we find the rotation phase at which a spark event at the field line's footpoint would have

occurred in order that the resulting particle stream (assumed to be travelling at ultra-relativistic speeds) would reach the visible point at phase $\Delta\phi_{\rm ab}$,

$$\Delta\phi_{\rm sp} = \Delta\phi_{\rm ab} - \ell', \tag{4.15}$$

where $\ell' \equiv \ell/r_L$, and ℓ is the distance traversed by a particle as it corotates with the pulsar and climbs from the surface to the emission point, which is calculated numerically at the same time that the visible point is being found. For pulse number p in the pulse stack, $\Delta\phi_{\rm sp}$ is converted (via the pulsar rotation period, P_1) into a time $t_{\rm sp} = P_1(p + \Delta\phi_{\rm sp}/2\pi)$, which can then in turn be converted into an intensity via the carousel model

$$I(t_{\rm sp}, \phi) \propto \sum_{n=1}^{N} \exp\left[-\frac{(\phi - 2\pi(\frac{n}{N} + \frac{t_{\rm sp}}{P_4}))^2}{2\sigma^2}\right], \tag{4.16}$$

where ϕ is the magnetic azimuth of the footpoint and σ parametrises the angular width of the individual spark profiles.

4.4.1 Phase-dependent intensity modulation

The foregoing procedure will produce a pulse stack where emission is "observed" across all 360° of longitude, regardless of the local conditions at the emission point, as illustrated in Fig. 4.4. In other words, it follows the assumption of the carousel model that spark activity at the footpoint of a field line is a necessary, but not a sufficient condition for coherence to occur on that field line. Some extra condition, presumably connected to the emission mechanism, must therefore be imposed in order to decide how the drift bands are modulated over pulse phase.

If a mechanism such as particle bunching is assumed (as first suggested by Ruderman and Sutherland 1975, but see, e.g., Melrose 2017 for arguments against bunching as a viable mechanism), then the beam intensity is proportional to N^2, where N is the number of particles in a "bunch" (i.e. within a volume element

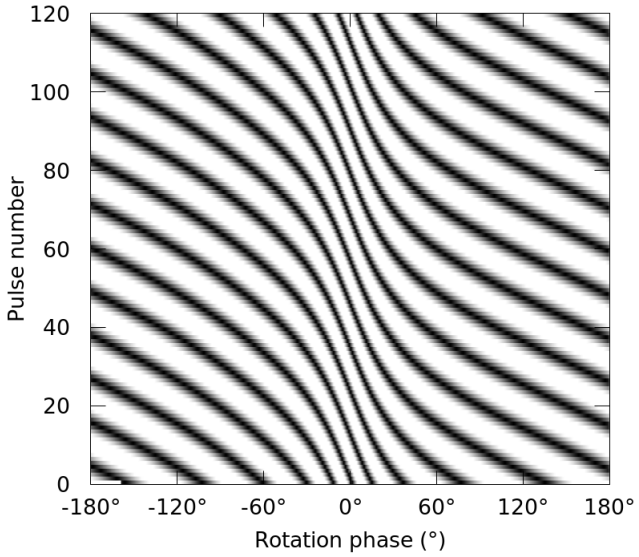

Figure 4.4 A simulated pulse stack showing drift bands across all 360° of rotation phase, using parameters drawn from one of the proposed viewing and carousel geometries of PSR B0809+74 (see §4.5.2 for details of the chosen parameters).

with its linear dimension smaller than the emitted wavelength in the co-moving frame). In this case, the observed emission pattern for curvature radiation from a single particle can be calculated, and scaled up by the square of the local plasma density at each emission site. Thomas et al. (2010) describe one possible method for doing such a calculation, although it should be noted that they incorporate the phase-shifting effects of aberration and retardation post hoc. To our knowledge, no similar method exists for estimating intensity profiles assuming other possible mechanisms, such as maser mechanisms (Ginzburg and Zhelezniakov, 1975) or plasma wave instabilities (Cheng and Ruderman, 1977).

It should be realised, however, that the positions of the drift bands in observed rotation phase are, under the assumptions of the carousel model, agnostic to which emission mechanism is ultimately adopted[4]. If, therefore, the goal is to study how the drift bands are affected by the geometry of the magnetosphere, one can avoid (or at least defer) the unenviable task of choosing and modelling one particular

[4]This statement does not allow for the minor apparent shift caused by the profile modulation itself, which will serve to skew the drift bands slightly towards the centres of the profile components.

coherent emission mechanism at the expense of the others. If a comparison with real data is still needed, it suffices to modulate the simulated pulse stack with an actual average profile at the desired frequency, which would include asymmetries, if any, resulting from both the emission physics and geometrical considerations.

4.5 Observable predictions of the geometric model

4.5.1 Drift band morphology

The drift bands in Fig. 4.4 show clear and significant curvature over the full range of rotation phases, due to the phase-dependent rate at which the visible point cuts across the carousel beam at different rotation phases. From the construction outlined in the previous section, the drift bands as they appear on the pulse stack have the dual properties (common to pulsars with drifting subpulses, as stated in Edwards and Stappers, 2002, and references therein) that the horizontal "distance" between them (i.e. the time between successive subpulses, P_2) is a pure function of pulse phase, and the vertical "distance" (P_3) is a pure function of pulse number. If aliasing is present, the vertical spacing of the drift bands will be $P_3 \neq \hat{P}_3 = P_4/N$ (see, e.g., Deshpande and Rankin 2001 for a detailed discussion), but this will not affect the constancy of either P_3 or $\hat{P}_3$ as long as P_4 and N remain constant (which is not always the case, e.g., McSweeney et al. 2017).

The shape of each simulated drift band is identical. This, of course, precludes the possibility of accurately modelling pulsars whose subpulse drifting properties undergo any kind of evolution over time, such as nulling, mode switching, or a changing drift rate (see McSweeney et al., 2017, for an example of all three occurring in the same pulsar, PSR B0031−07). In these cases, it is assumed that N, P_4, s, or some combination of them are not constant in time (e.g. Smits et al., 2005).

4.5.2 Appearance of reconstructed beamlets

The simulated pulse stacks can be subjected to all the standard analyses used to study subpulse drifting. In particular, they are amenable to the reconstruction of polar beam maps via the cartographic transform of Deshpande and Rankin (2001). As a case study, we investigate one of the viewing geometries proposed by Rankin et al. (2006) for PSR B0809+74, whose transformed beam map shows a remarkable azimuthal skewing of the beam maps (see their Fig. 4). The viewing geometry assumed $\alpha = 9°$, $\zeta = 13.5°$, and number of sparks $N = 10$. Even though the authors emphasise the difficulty of distinguishing between many sets of viable parameters, they argue that in this case aliasing is not present, in which case $P_3 \approx 11.1\, P_1$ is the time interval between successive drift bands at a fixed rotation phase, giving $P_4 = N \times P_3 \approx 143\,\mathrm{s}$.

One parameter remains free: the (normalised) radius of the carousel, s. We first tested which values in the range $0 < s < 1$ produced polarisation angle curves consistent with the observations (for one of the orthogonal polarisation modes only). Fig. 4.5 shows the polarisation angle curves predicted by the geometric model. As expected, values for relatively large s agree better, as these correspond to relatively low emission heights, at which the geometric model more closely approximates the rotating vector model, which was employed in the determination of the viewing geometry parameters. In particular, we note that values in the range $0.4 \lesssim s \lesssim 1.0$ agree sufficiently well with the polarisation angles in the pulse window.

After choosing a value for s, the pulse stack can be simulated according to the procedure described in Section §4.4. Fig. 4.6 shows a simulated intensity pulse stack for pulsars B0809+74 and B2034+19, using parameters reported in Rankin et al. (2006) and Rankin (2017) respectively. The average profile used to modulate the pulse stack was a $\sim 150\,\mathrm{MHz}$ profile retrieved from the European Pulsar Network database[5], supplied by Noutsos et al. (2015). The authors

[5] `http://www.epta.eu.org/epndb/`

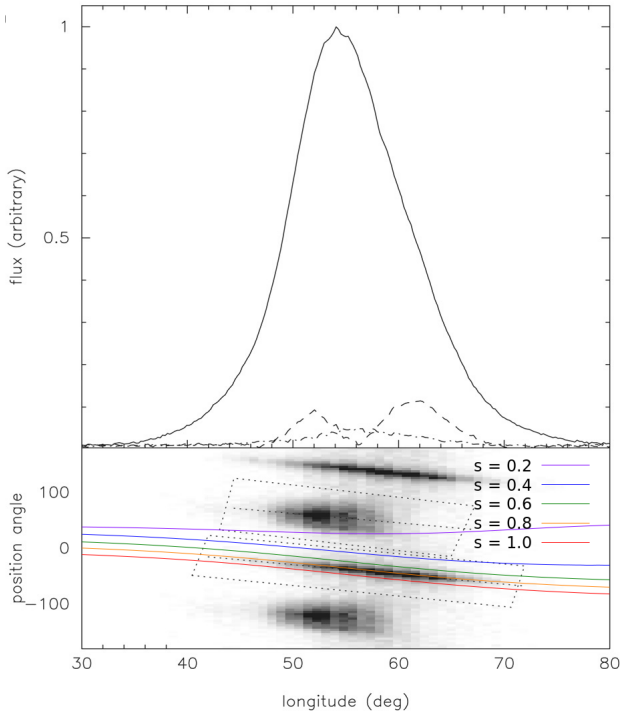

Figure 4.5 The pulse profile and polarisation angle histogram of B0809+74 at 328 MHz, reproduced from Rankin et al. (2006), and overlaid with the predictions of the polarisation angle curves for various values of the normalised radius of the carousel, s. The vertical offsets are arbitrary.

assigned the fiducial point in their profile by means of a Rotating Vector Model (RVM; Radhakrishnan and Cooke, 1969; Komesaroff, 1970) fit to the observed polarisation curve. Since (by virtue of Fig. 4.5) the simulated polarisation curve is sufficiently close to the RVM for the range $0.4 < s < 1.0$, the association with their empirically determined fiducial point with the simulated fiducial point is justified. Varying s within this range does not significantly alter the shape of the drift bands.

Having obtained a simulated pulse stack, we then applied the cartographic transform in order to obtain a simulated polar map of the pulsar beam. Fig. 4.7 shows the results for two choices of footprint polar radius, $s = 0.5$ and $s = 0.25$. When s values are chosen in the range $0.4 \leq s \leq 1.0$, no significant azimuthal distortions were observed, but smaller values of s yield very noticeable azimuthal distortions with similar characteristics as that observed by Rankin et al. (2006).

Curiously, the direction of the azimuthal distortions differ, with the simulated beamlets being skewed in the counter-clockwise (CCW) direction, while the real data is skewed in the clockwise (CW) direction. This is discussed further in the next section.

4.6 Discussion

4.6.1 Comparison of simulated and real data

The geometric model described in this work is capable of producing simulated pulse stacks from a set of parameters describing the viewing geometry and the underlying carousel of sparks near the surface. We have assumed that the appearance and morphology of drift bands is entirely determined by which field lines are "active" (i.e. those whose footpoints coincide with a spark event at a given time), and that the coherent emission mechanism itself is only responsible for how the whole drift band pattern is modulated over 360° of rotation phase. The unknown details of the emission mechanism have not been investigated here; rather, we have modulated our simulated pulse stacks with the profiles of real data taken at some desired frequency.

Our purpose has been to show that the geometric model is sufficient to reproduce the essential characteristics of the drift band patterns actually observed, without committing to any one particular coherent emission mechanism. The two simulated pulse stacks in Fig. 4.6 illustrate the application of the geometric model to two pulsars with very different viewing geometries. Except for the absence of nulls, the simulated pulse stacks exhibit very similar morphologies to their real counterparts; in particular, the similar curvature of the drift bands of B0809+74 and the odd-even subpulse modulation over the pulse sequence in B2034+19 (discussed in Rankin, 2017).

We have not attempted an exhaustive search in these case studies for the best fitting carousel parameters. For the latter pulsar, we have adopted the

following parameters: $N = 5$, $P_4 = 6.65\,\mathrm{s}$, spark size $\sigma = 20°$, and that the direction of the carousel motion has the opposite sense to the rotation of the pulsar. Assuming the double cone model of Rankin (2017), we modelled the two components (at approximate rotation phases $-5°$ and $-3.5°$) separately, assigning them carousel radii of $s = 1$ and $s = 0.8$ respectively. In order to approximate the profile contributions from the relevant drift mode, we fit four Gaussians to the total profile and discarded the two rightmost components, which appear to come mainly from the other drift mode. The sparks of the inner cone were set midway in magnetic azimuth between the sparks of the outer cone. Other sets of parameters were found to result in a similar morphology, and a comprehensive search for the best fitting set should include, for example, a comparison of the fluctuation spectra. This, however, is beyond the scope of the present work, primarily aimed to highlight the wide variety of simulated pulse stacks that are possible with the geometric model. A comprehensive model of B2034+19's drift bands in both its modes (here, only the first mode was simulated) is deferred to a future work.

4.6.2 Effect on the interval between successive subpulses (P_2)

An important feature of the geometric model is the inclusion of the time taken for the spark information to reach the visible point, a non-negligible time, which to our knowledge is entirely lacking in other models of carousel behaviour. The quantity P_2, which measures the elapsed time between the observation of two adjacent sparks, must therefore include not only AR effects and continuous carousel rotation (affecting the *apparent* spacing between the sparks, a theme discussed in Yuen et al. 2016), but also the difference of path lengths of the respective particle trajectories. The length of the trajectories traced by particles in the IF (ℓ') are necessarily different from the path length along the magnetic field lines on which they reside—rotation effects should not be neglected.

As described above, the trajectory lengths are calculated numerically, but we can get a sense of the magnitude and behaviour of the effect by taking the first-order approximation $\ell' \approx r'$. Then the interval between the arrival of successive subpulses will depend on how far the carousel rotates in time $\sim \Delta r/c$, which in radians is $\frac{\Delta r' P_1}{P_4}$. On the leading side of the fiducial point, the emission heights start large, approach a minimum near the fiducial point, and grow large again on the trailing side (see Fig. 4.8). The inclusion of trajectory lengths therefore either serves to artificially augment or diminish the observed value of P_2 during leading phases (depending on whether the line of sight cuts across the beam pattern in the same or opposite directional sense, respectively, as the carousel rotation) and to have the opposite effect on P_2 on the trailing side. This is similar to retardation, except that retardation always compresses the observed emission on the trailing side (Dyks et al., 2010). Therefore, the present effect can either enhance or suppress the effect of retardation, depending on the relative signs of P_1, P_4, and $\beta = \zeta - \alpha$.

4.6.3 Effect of finite spark size

A similar comparison can be made between sparks with the same magnetic azimuth but with different magnetic colatitudes, i.e. different values of s. In this case, we can assume to first order that the aberration angles are the same ($\Delta\phi_{\mathrm{ab},1} \approx \Delta\phi_{\mathrm{ab},2}$), and that therefore any difference in arrival time is due to the combined difference of particle trajectory length and photon flight time (retardation). Here, second order effects become necessarily important, because the inclusion of only first order effects implies that the total path length of the spark information is the sum of the distance from the surface to the emission point, $\sim r$, and the distance from the emission point to the observer, $\sim (D - r)$ (where D is the distance between the centre of the pulsar and the observer), which reduces to the constant distance D. In reality, if the sparks span a large enough range of s values, the inner parts of the spark (i.e. nearest the magnetic pole) may be

ultimately observed measurably later in phase than the outer parts, which would be observed as a broadening of the drift bands in phase.

It has been suggested that changing drift modes is caused by a change in the radius of the spark carousel of PSR B0031−07 (Smits et al., 2005). In their model, the observed difference of emission heights between the two most prominent drift modes is a function of observing frequency. If this is the case, then the geometric model predicts that there should be a different rotational phase shift between the drift bands of each mode viewed simultaneously across a sufficiently wide frequency band, which has indeed been observed (McSweeney et al., 2017).

Similar frequency-dependent effects have also been observed in PSR B0809+74 by Hassall et al. (2013) and PSR B0943+10 by Bilous (2018). The latter argue that the evolution (in phase) of the drift bands can be understood in terms of the radius-to-frequency mapping (RFM; whereby the opening angle of the beam emerging from the same surface sparks increases at lower frequencies), affecting the projected phases at which the beamlets pass through the line of sight. Our model is in principle consistent with RFM, but requires the implementation of two-dimensional surface sparks in order to make a qualitative comparison with the work of Bilous (2018), since in our (one-dimensional) model each field line is associated with only a single visible point at a geometrically determined height.

For the same reason, our model also predicts that (broadband) microstructure would *not* show a frequency-dependent phase separation, assuming that the emission regions associated with micro-pulses span a sufficiently small number of field lines—again, because the location of the visible point (and thereby the degree to which AR effects are present) of a given emission column is independent of observing frequency. Thus, the geometric model predicts that subpulses appear to move about in phase when viewed simultaneously across a wide frequency range (because different field lines are sampled), whereas the individual micro spark events that make up a spark "patch", if they do indeed occur on a small fixed set of field lines, would appear at the same phase at all frequencies. Since B0031−07

is known occasionally to emit particularly bright pulses (Tuoheti et al., 2011; Nizamdin et al., 2011), it may provide a way to test the present geometric model, if sufficiently high time resolution observations of bright microstructure across a wide frequency band can be obtained (see, e.g., the temporal stability of Crab microbursts across ~ 2 octaves of frequency, presented in Fig. 2 of Hankins et al., 2016).

4.6.4 The rotational asymmetry of B0809+74's reconstructed beam

We have shown that it is possible to simulate pulse stacks that, when the cartographic transform is applied to them, appear azimuthally skewed in a way that is at least qualitatively expected from AR effects. Although this exercise was motivated by the azimuthal asymmetries observed by Rankin et al. (2006) for B0809+74, there are two major reasons why the effect described in this paper cannot provide an adequate explanation for their particular case.

The first reason is the direction of the asymmetry: Rankin et al.'s beamlets appear to be skewed in the CW direction, whereas the simulated polar maps are skewed CCW. Both polar maps were produced with the same set of parameters, which assume that the line of sight is cutting through the beam from right to left, with $\zeta > \alpha$. In this scenario, height-dependent aberration always tends to shift the observed emission towards earlier rotation phases, which equates to the beamlets being skewed towards the right at the bottom of the polar map, with the net result of a CCW skew.

The second reason is the failure to find a consistent value of s that can produce both the correct polarisation angle curve ($s \gtrsim 0.4$) and the azimuthal asymmetry ($s \lesssim 0.3$). For the geometry of B0809+74, the former condition is equivalent to the restriction $r' \lesssim 0.02$ ($r \lesssim 100\,\mathrm{km}$), and the latter, $r' \gtrsim 0.04$ ($r \gtrsim 250\,\mathrm{km}$), which is demonstrated by the solid height curves in Fig. 4.8. This difficulty is not necessarily insurmountable, because the RVM implicitly assumes sufficiently

low heights that rotational effects are negligible. As can be seen in Fig. 4.5, the polarisation angle curve tends to flatten when lower values of s (and therefore greater emission heights) are chosen. Therefore, there may well be a viewing geometry for the which the RVM would predict a steeper polarisation angle curve, but which agrees with the data for a sufficiently low value of s that would make the azimuthal asymmetry significant. If a change in the viewing geometry is required, then there is no reason to continue assuming that the other parameters of Rankin et al.'s model are correct, including the number of sparks in the carousel, and the degree of drift band aliasing (currently assumed to be zero). Finding such a geometry is beyond the scope of the present work, but could, in principle, be found by extending the RVM to include the rotational effects implicit in the equation for the acceleration field, Eq. (4.4).

One major difference between the analysis of Rankin et al. (2006) and the present work is that the azimuthal asymmetry was seen in only one OPM, whereas our analysis assumes (incorrectly) that all the observed emission belongs to the same OPM. The polarisation plots in Fig. 4 of Ramachandran et al. (2002) suggest that the dominance of the OPMs depends very strongly on where in the drift band the emission in question occurs. Choosing only one OPM is therefore tantamount to significantly changing the appearance of the drift bands, which will inevitably affect the appearance of the transformed beamlets. In B0809+74's case, the way the OPMs are divided in the pulse stack would make the apparent drift rate larger (i.e. the drift bands more horizontal). However, experimenting with the simulation parameters shows that one of the effects of increasing s (but leaving the other model parameters the same) is to increase the apparent drift rate in the pulse stack, which would lead us to expect that selecting just one OPM would cause the polar map to increase in skewness in the CCW direction, opposite to what is observed. Furthermore, the other OPM's polar map skewness would be similarly boosted because its drift bands would also be flattened—this is also not observed. In summary, we consider the rotational asymmetry observed by

Rankin et al. (2006), if real (and assuming their viewing geometry to be correct), to be due to something other than the geometric effects described in this work.

4.6.5 Other considerations

We briefly remark on the difference between using the Deutsch field and the simpler, but strictly incorrect rotating "static" dipole on the numerical results presented in this paper. In all cases a comparison found that the difference at emission heights $\lesssim 10\%$ of the light cylinder radius was negligible. A comparison of the predicted emission heights of B0809+74 between the full Deutsch vacuum model and the dipole model is shown in Fig. 4.8.

Finally, our analysis has ignored the possibility of magnetospheric propagation effects (e.g. Barnard and Arons, 1986), which may affect the viewing angle of the subpulses (and thus the morphology of the drift bands). This may ultimately be responsible for the azimuthal asymmetry, but it remains to be shown whether the relatively small height differences involved can account for the large "pitch angle" of the skewed beamlets. The assumption of negligible magnetospheric effects also implies that the polarisation angle is entirely determined by the acceleration vector of the particle as it passes through the visible point, as per Eq. (4.4). In that case, the spread of the polarisation angles observed at any given phase (e.g. the histogram in the bottom panel of Fig. 4.5), if significant, is a direct measure of the range of heights that are sampled, and hence the range of s values, providing another means of constraining the emission geometry. This will be explored more thoroughly in future applications of the geometric model to pulsars with measured polarisation angle histograms.

4.7 Conclusion

We have described a geometric model for pulsar emission that assumes coherent curvature radiation from a corotating, relativistic plasma, consistent with AR ef-

fects. The further assumption (implicit in the carousel model) that the "activity" along field lines is only dependent on the spark activity at their footpoints near the stellar surface enables the model to predict the morphology of drift bands without reference to any particular coherent emission mechanism.

We have explored two specific pulsars, PSRs B0809+74 and B2034+19, with contrasting viewing geometries (nearly-aligned and oblique rotators, respectively) and shown that the geometric model can reproduce the essential characteristics of the observed pulse stacks, including the modulation periodicity P_2, and drift band curvature. In the case of B0809+74, we have shown how the geometric model is capable of generating rotational asymmetries in the polar maps produced by the cartographic transform, qualitatively similar to those observed by Rankin et al. (2006). However, in this particular case, the directional sense of the asymmetries and the emission height range needed to reproduce them in simulation are difficult to reconcile with their interpretation in the current geometric context.

The geometric model presented in this paper is, we believe, a necessary consequence of the assumptions of curvature radiation, and is therefore applicable to all radio pulsars for which some form of coherent curvature radiation is believed to be the primary emission mechanism, including but not limited to the class of subpulse drifters. The most telling tests of the validity of this model require high time resolution, broadband observations of individual pulses, especially where microstructure can be resolved—a kind of observation that is scarce, due to the difficulty of coordinating multiple telescopes for a wide spectral coverage. However, with several broadband instruments coming online (e.g. the ultra-wideband receiver at Parkes, the upgraded GMRT, and the RRI-GBT multiband receiver; Maan et al. 2013), in-depth investigations of these subtle effects will become possible in the near future.

4.8 Appendix: Coordinate systems

The derivation of Eq. (4.8) and, in general, any Taylor expansion about the magnetic axis that depends on Eqs. (4.3) and (4.4), requires the conversion between the *observer* coordination system and the *magnetic* coordinate system.

The observer coordinate system is defined as follows. The origin is placed at the centre of the pulsar. The pulsar's rotation axis is identified with the z-axis. The x-axis is chosen to lie in the plane spanned by the z-axis and the line of sight, $\hat{\boldsymbol{n}}$, such that positive x points towards the distant observer (i.e. $\hat{\boldsymbol{n}} \cdot \hat{\boldsymbol{x}} \geq 0$). Finally, $\hat{\boldsymbol{y}} = \hat{\boldsymbol{z}} \times \hat{\boldsymbol{x}}$.

The magnetic coordinate system is related to the observer coordinate system by a rotation about the y-axis by the magnetic inclination angle α, followed by a rotation about the z-axis by the rotation phase angle ϕ. This brings the z-axis into alignment with the magnetic axis, $\hat{\boldsymbol{\mu}}$. When $\phi = 0$, the magnetic axis is in the plane spanned by the x- and z-axes. We note that although the magnetic coordinate system does not represent an inertial frame, the magnetic field ($\vec{\boldsymbol{B}}$), the velocity field $\vec{\boldsymbol{V}}$, and the acceleration field ($\vec{\boldsymbol{A}}$) are all static in the co-rotating frame. That is to say, an inertial observer would find that these fields all corotate with the pulsar, so that a measurement of the entire fields at two different times would be related by a simple rotation about the z-axis (see also Appendix A of Dyks and Harding, 2004).

Therefore, there is no loss of generality by evaluating these fields at a single rotation phase, say at the fiducial point ($\phi = 0$) and rotating it a posteriori, or equivalently letting the line of sight "rotate" in the opposite direction by the same amount. In many cases, this makes the evaluation of Eq. (4.3) and other derived quantities much simpler since they can be expressed independently of ϕ. Furthermore, because the only radiation that would be observed is that produced by particles whose velocity vector is parallel to the line of sight, we can simply replace all instances of $\hat{\boldsymbol{n}}$ with $\hat{\boldsymbol{v}}$ and tacitly ignore times and locations in the magnetosphere where they are not parallel.

The rotation matrices are given many times in the literature, and are not repeated here. For example, the Appendix of Yuen et al. (2016) includes the relevant transformation matrices, as well as the matrix used to convert between Cartesian and spherical polar coordinates, which is also used in this work to Taylor expand about the magnetic axis (i.e. about $\theta = 0$).

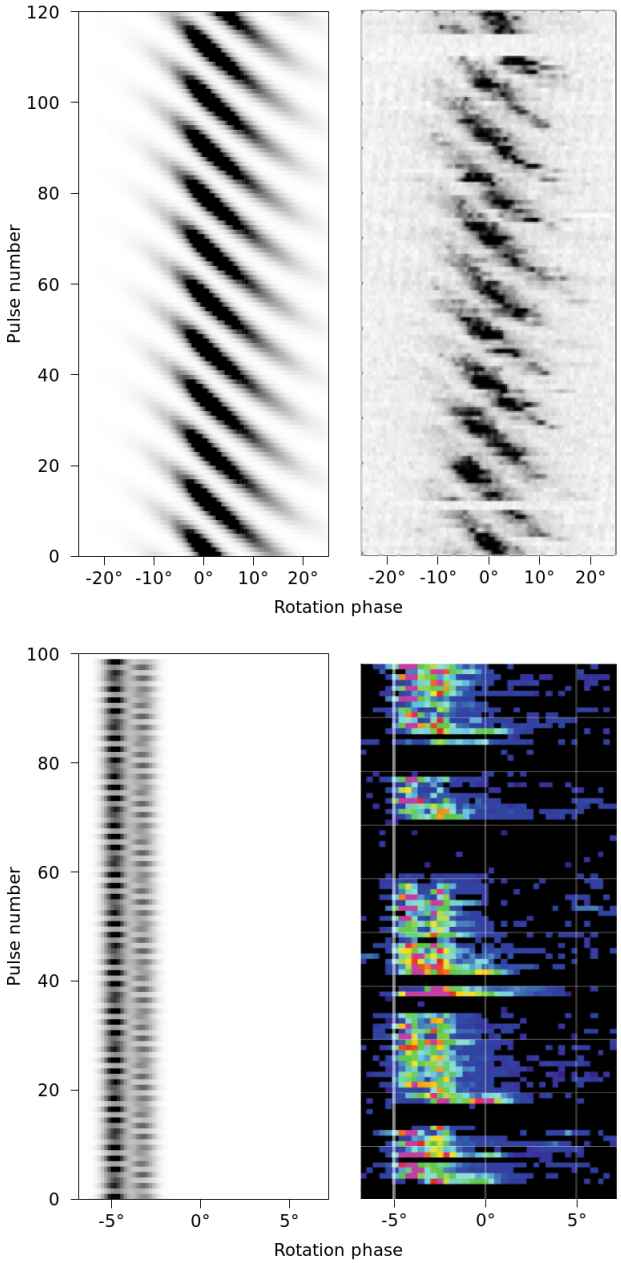

Figure 4.6 (Top left) A simulation of PSR B0809+74's drift bands, generated using the parameters given in Rankin et al. (2006), assuming $s = 0.5$ and spark size $\sigma = 6°$. The pulse stack was modulated with a 150 MHz profile from the European Pulsar Network database (see text for details). The drift bands are distinctly (albeit slightly) curved, in agreement with observation. (Top right) A comparable pulse sequence from an observation of B0809+74 taken at 313 MHz (Gajjar et al., 2014). The sequence contains several short null sequences, which the simulation lacks. (Bottom) Same as above, but for pulsar B2034+19 (see text for chosen parameters). The modulating profiles for the two components (at $-5°$ and $-3.5°$) were constructed from the profile given in Rankin (2017).

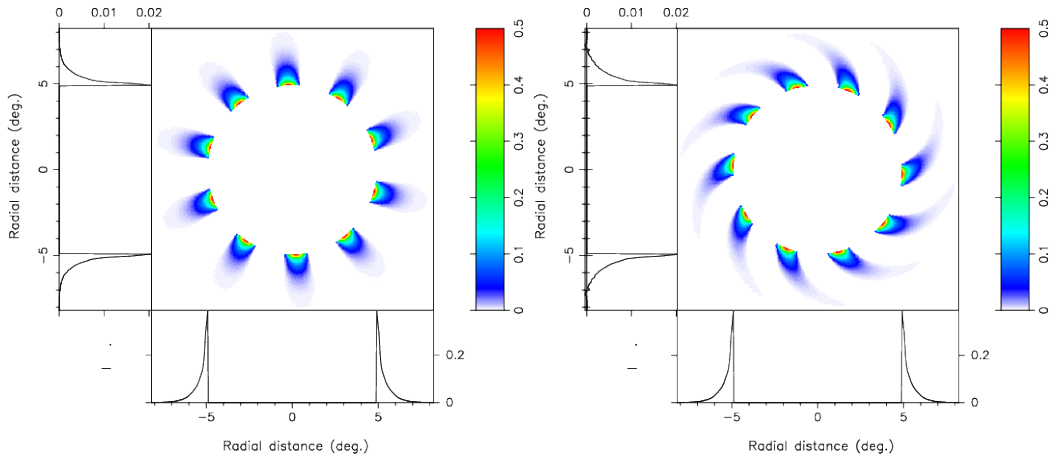

Figure 4.7 Two polar maps made from simulated data. On the left, $s = 0.5$ was used, and on the right, $s = 0.25$. The azimuthal distortions, argued here to be primarily due to the greater aberration associated with greater emission heights, are clearly present in the right-hand plot, but *have the opposite sense to that seen by Rankin et al. (2006)* (cf. their Fig. 4).

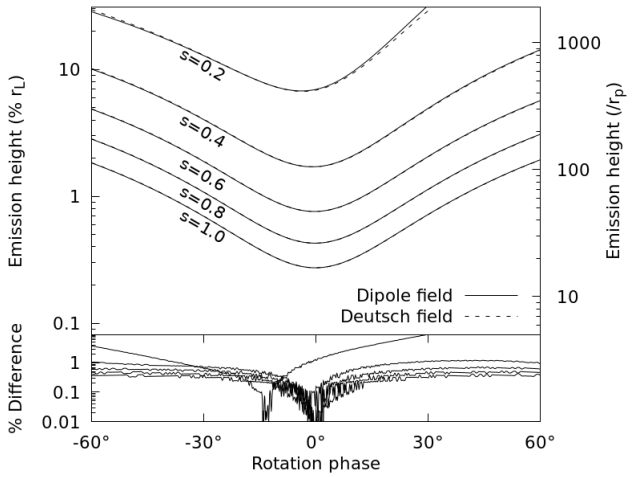

Figure 4.8 *Top*: Numerical emission heights for B0809+74's proposed geometry, for both a dipolar magnetic field and a Deutsch field, assuming a stellar radius of 10 km. The left and right y-axes are equivalent, but presented in terms of the light cylinder radius, r_L, and the pulsar radius, r_p, respectively. *Bottom*: The absolute percentage difference between the dipolar and Deutsch derived heights, normalised to the dipolar height. At the lower heights ($s \geq 0.4$), the two are almost indistinguishable ($< 1\%$ difference). The two coincide at a height-dependent phase, with the $s = 0.2$ curve showing the left-most minimum. The roughness of the curves is due to numerical noise in the PSRGEOM algorithm.

Chapter 5

The frequency-dependent behaviour of subpulse drifting: I. Carousel geometry and emission heights of PSR B0031−07

Encouraged by the general numerical results of Chapter 4, an explanation for B0031−07's frequency-dependent behaviour was now sought. However, in order to make quantitative arguments, B0031−07's correct carousel configuration had to be deduced (or at least constrained). Similar to previous chapters, this chapter is reproduced from the author's publication (McSweeney et al., 2019). Apart from trivial changes to the formatting, an extra row has been added to Table 5.4 (B0834+06), which wasn't included in the published version.

Abstract

The carousel model of pulsar emission attributes the phenomenon of subpulse drifting to a set of discrete sparks located very near the stellar surface rotating around the magnetic axis. Here, we investigate the subpulse drifting behaviour of

PSR B0031−07 in the context of the carousel model. We show that B0031−07's three drift modes (A, B, and C) can be understood in terms of a single carousel rotation rate if the number of sparks is allowed to change by an integral number, and where the different drift rates are due to (first-order) aliasing effects. This also results in harmonically-related values for P_3 (the time it takes a subpulse to reappear at the same pulse phase), which we confirm for B0031−07. A representative solution has $[n_A, n_B, n_C] = [15, 14, 13]$ sparks and a carousel rotation period of $P_4 = 16.4\,P_1$. We also investigate the frequency dependence of B0031−07's subpulse behaviour. We extend the carousel model to include the dual effects of aberration and retardation, including the time it takes the information about the surface spark configuration to travel from the surface up to the emission point. Assuming these effects dominate at B0031−07's emission heights, we derive conservative emission height differences of $\lesssim 2000$ km for mode A and $\lesssim 1000$ km for modes B and C as seen between 185 MHz and 610 MHz. This new method of measuring emission heights is independent of others that involve average profile components or the polarisation position angle curve, and thus provides a potentially strong test of the carousel model.

5.1 Introduction

Subpulse drifting, first observed by Drake and Craft (1968) not long after pulsars were discovered (Hewish et al., 1968) is a widespread phenomenon affecting more than half of all known pulsars (Weltevrede et al., 2006, 2007). When individual pulses are stacked vertically to form a two dimensional pulse stack, the individual components of pulses, termed *subpulses*, are observed to undergo a regular modulation pattern in both amplitude and phase, which visually resemble a set of discrete diagonally-oriented burst regions called *drift bands*. The slope of the drift bands is called the drift rate, and it represents the apparent advance or lag of subpulses per stellar rotation.

Drifting subpulses found an early explanation in the seminal polar gap the-

ory of Ruderman and Sutherland (1975) (hereafter RS), who suggested that the pattern of radio waves that ultimately escape the magnetosphere is the emission signature of a set of discrete, localised pockets of quasi-stable electrical activity called *sparks* that exist very near the pulsar surface. These sparks are the sites of particles accelerated through the polar gap to energies of 10^{12} V, seeding an avalanche of secondary particles which stream along magnetic field lines at relativistic speeds to produce curvature radiation. Charged particles generated by the sparks partly screen the electric potential along the magnetic field at the surface, causing them to move relative to the polar cap surface about the magnetic axis (the $\mathbf{E} \times \mathbf{B}$ drift), in an arrangement resembling a fairground "carousel". The emission beam would then also have a spatial structure composed of discrete "beamlets" that reflects the magnetic azimuthal arrangement of sparks on the surface. With each rotation, an Earth-bound observer perceives a different intensity pattern as the line of sight cuts through a slightly rotated carousel, producing the observed drifting behaviour.

The carousel model has been heavily criticised on (at least) two different grounds. Firstly, its reliance on a coherent form of curvature radiation is difficult to justify from known plasma physics (e.g. Melrose, 1992). Secondly, there are a number of secondary phenomena associated with subpulse drifting that present challenges for, or at least require extensions of, the simple geometric picture described above (Edwards, 2006). These include, among others, drift mode switching (Huguenin et al., 1970), bi-drifting (Qiao et al., 2004), nulling (Backer, 1970a), and subpulse "memory" across nulls (Lyne and Ashworth, 1983).

Despite these criticisms, the carousel model, along with its implied conal emission beams, remains a popular model for interpreting subpulse drifting, as it is capable of explaining (qualitatively at least) several features of pulsar morphology and behaviour (Rankin, 1983, and subsequent papers in the series). As a result, there have arisen two schools of thought, one which believes the basic model is correct in principle but whose details are complicated and have yet to

be worked out on a pulsar-by-pulsar basis, and one which believes the model is fundamentally incorrect. What is lacking is a robust test that can distinguish, once and for all, between these alternatives. A strong candidate for such a test, if it can be found, is one that exploits the model's unique emission geometry, namely, that although the observed photons are emitted at some height dictated by the magnetic field geometry, the subpulse modulation pattern is dictated by events very close to the surface. This feature of the carousel model makes specific predictions about how the observed subpulse modulation changes as a function of observing frequency.

In this two-part paper series that will focus on B0031−07, we investigate the frequency dependence of subpulse drifting. We start by recognising that the basic carousel model predicts that the rotation phases at which subpulses appear is invariant with frequency (Edwards and Stappers, 2002, 2003), a point that is sometimes confused with the expected radius-to-frequency mapping (RFM) behaviour of average profiles (e.g. Smits et al., 2007; Yuen et al., 2016). Nevertheless, frequency-dependent behaviour of subpulses *is* observed, most notably in the way that the time between successive subpulses (the so-called "secondary period", P_2) changes as a function of frequency (Taylor et al., 1975; Bartel et al., 1980). Several ideas have been advanced to explain this within the context of the carousel model, including non-dipolar field geometries (e.g. Davies et al., 1984) and the finite size and shape of beamlets, which present a slightly-shifted cross section to the line of sight as the frequency-dependent beamlets move in magnetic colatitude (Edwards and Stappers, 2003; Bilous, 2018). Edwards and Stappers (2003) also speculate that aberration and retardation (AR) effects must be present, although they argue that the subpulse phase shifts they observe in PSR B0320+39 and PSR B0809+74 imply emission heights that are much larger than the heights expected from other arguments.

In this paper, we develop this idea further to obtain quantitative predictions of how subpulses shift with frequency if AR effects are the dominant cause. We apply

the model to the interesting and well-studied case of PSR B0031−07 whose P_2 is also known to have a measurable longitude dependence (McSweeney et al., 2017) and whose known frequency-dependent subpulse phase shifts are also dependent on which of the pulsar's three drift modes is present (Huguenin et al., 1970; Vivekanand and Joshi, 1996; McSweeney et al., 2017). In Sections §5.3.1 and §5.3.2 the relationship (initially neglecting AR effects) between the drift bands and the underlying carousel geometry are laid out, with particular emphasis on the degeneracy introduced by the possibility of aliasing effects. We then generalise the model to include AR effects in Section §5.3.3, calculating their effect on the subpulse phase shift (§5.3.3.1) and on P_2 (§5.3.3.2). A discussion of the results and our final conclusions are presented in Sections §5.4 and §5.5.

This is the first of a two-part series, both of which deal with the relationship between frequency-dependent effects and subpulse drifting in B0031−07. This paper deals exclusively with effects that can be observed in Stokes I observations. In the subsequent paper, we investigate how the subpulse phase (which encodes information about the magnetic azimuth) is related to the polarisation position angle and use this relationship to place further constraints on the carousel and viewing geometries.

5.1.1 Definitions and Notation

The rotation axis ($\vec{\omega}$), the magnetic axis ($\vec{\mu}$), and the LoS define three points of a spherical triangle which relate the rotation phase (φ), the viewing geometry (α, ζ), the half-beam opening angle (Γ), the PPA (ψ), and the magnetic azimuth (σ). In this paper, α and ζ are always relative to the rotation axis defined by the right hand rule, so that $0° \leq \alpha < 180°$ and $0° \leq \zeta < 180°$. These angles are illustrated in Fig. 1.15. An asterisk is used to denote the supplementary angles $\alpha^* = 180° - \alpha$ and $\zeta^* = 180° - \zeta$, i.e. measured from the opposite rotation axis. The impact angle is defined as $\beta = \zeta - \alpha$, with $\beta^* = \zeta^* - \alpha^* = -\beta$.

As is common in the literature, we use P_1 for rotation period of the pulsar,

Table 5.1. Data sets recorded on MJD 57556

Telescope	Centre frequency (MHz)	Bandwidth (MHz)	# pulses	S/N per pulse
MWA	185	30.72	4631	14.2
GMRT	610	33.33	8487	9.8

P_2 for the subpulse separation, P_3 for the time it takes a subpulse to reappear at the same rotation longitude, and P_4 for the rotation period of the carousel. Conventionally, P_2 is often expressed in degrees of rotation, and P_3 in units of P_1, but in order to keep the notation consistent throughout this work, we reserve the unadorned P_x to have units of time. To denote quantities normalised by P_1, we introduce the overline notation, e.g., $\overline{P}_3 \equiv P_3/P_1$. In addition, we define $P_2^{(\circ)} \equiv \overline{P}_2 \times 360^\circ$ to express periods in degrees of rotation.

The drift rate, D, is traditionally expressed in units of degrees per pulse. To keep this consistent with the foregoing notation, we define

$$D \equiv \frac{P_2}{\overline{P}_3}, \quad \overline{D} \equiv \frac{\overline{P}_2}{\overline{P}_3} \quad \text{and} \quad D^{(\circ)} \equiv \frac{P_2^{(\circ)}}{\overline{P}_3}. \tag{5.1}$$

5.2 Observations

We have taken two simultaneous observations of B0031−07, one using the Murchison Widefield Array (MWA; Tingay et al., 2013) centred at 185 MHz, and the other using the Giant Metrewave Radio Telescope (GMRT; Swarup et al., 1991), centred at 610 MHz. The details are summarised in Table 5.1.

The MWA observation was processed in the same way as McSweeney et al. (2017). The MWA voltages were recorded using the Voltage Capture System (VCS; Tremblay et al., 2015), and a tied-array beam was formed (Ord et al., 2019) in the direction of the pulsar. The calibration solution was obtained using a separate, dedicated observation of the calibrator source 3C444. During the

calibration process, it was deemed necessary to exclude five MWA tiles (out of 128) from the coherent sum, due to corrupted data. The resulting data set had a time resolution of 100 μs and a frequency resolution of 10 kHz. At the time of the observation (June 2016), only total intensity data products were available, but the recent verification of MWA polarimetry (Xue et al., 2019) has made it possible to reprocess the original recorded voltages to produce a data product with full Stokes parameters.

The GMRT observations were made with the 13 central antennas in the phased array mode. However, only the total intensity was recorded. The output time resolution was 123 μs and the frequency resolution was 65 kHz.

Both MWA and GMRT data sets were processed with DSPSR (van Straten and Bailes, 2011) and PSRCHIVE (Hotan et al., 2004; van Straten et al., 2011) to produce single-pulse archives. A small percentage of frequency channels contaminated by local radio frequency interference (RFI) were removed, and impulsive RFI was identified by eye on a pulse-by-pulse basis; pulses that were contaminated by RFI were replaced by zeros. The resulting Stokes I average profiles are shown in Fig. 5.1.

The analysis in this paper will naturally benefit from knowledge of the exact clock offset between the two telescopes, which unfortunately was unavailable at the time of recording due to the fact that the MWA had not yet embarked on any timing programs that could verify the VCS time stamps. The correspondence between pulses was therefore found by aligning the null sequences, which are known in the case of B0031−07 to be a broadband phenomenon (Smits et al., 2007). The total number of pulses observed simultaneously at both telescopes was 4780. A section of the pulse stacks, showcasing all three drift modes, is shown in Fig. 5.2.

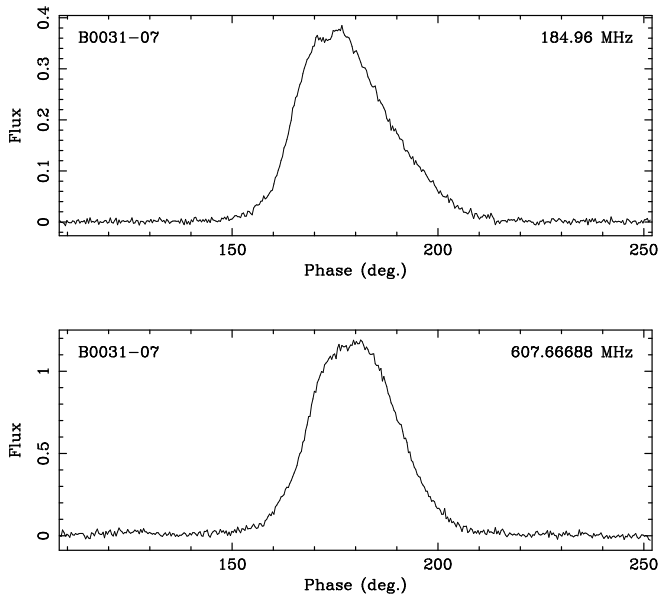

Figure 5.1 Average intensity profiles of B0031−07 made from the MWA observation (upper panel) and the GMRT observation (lower panel). The alignment of the profile centres was done by eye.

5.3 Analysis & Results

5.3.1 Using P_3 to constrain the carousel geometry

In the simplest version of the carousel model, in which the surface sparks are equally spaced in magnetic azimuth, the behaviour of the drift bands is determined by the number of sparks in the carousel, n, and the carousel rotation rate, P_4. If the carousel rotation is constant, the observed P_3 at any given longitude will also be constant. This is true regardless of either the radial distance of the spark from the magnetic axis, or the sparks' radial extent. Without aliasing, P_3 is identical to P_4/n, but with aliasing,

$$\frac{1}{\overline{P}_3} = \left| \frac{n}{\overline{P}_4} - k \right|, \tag{5.2}$$

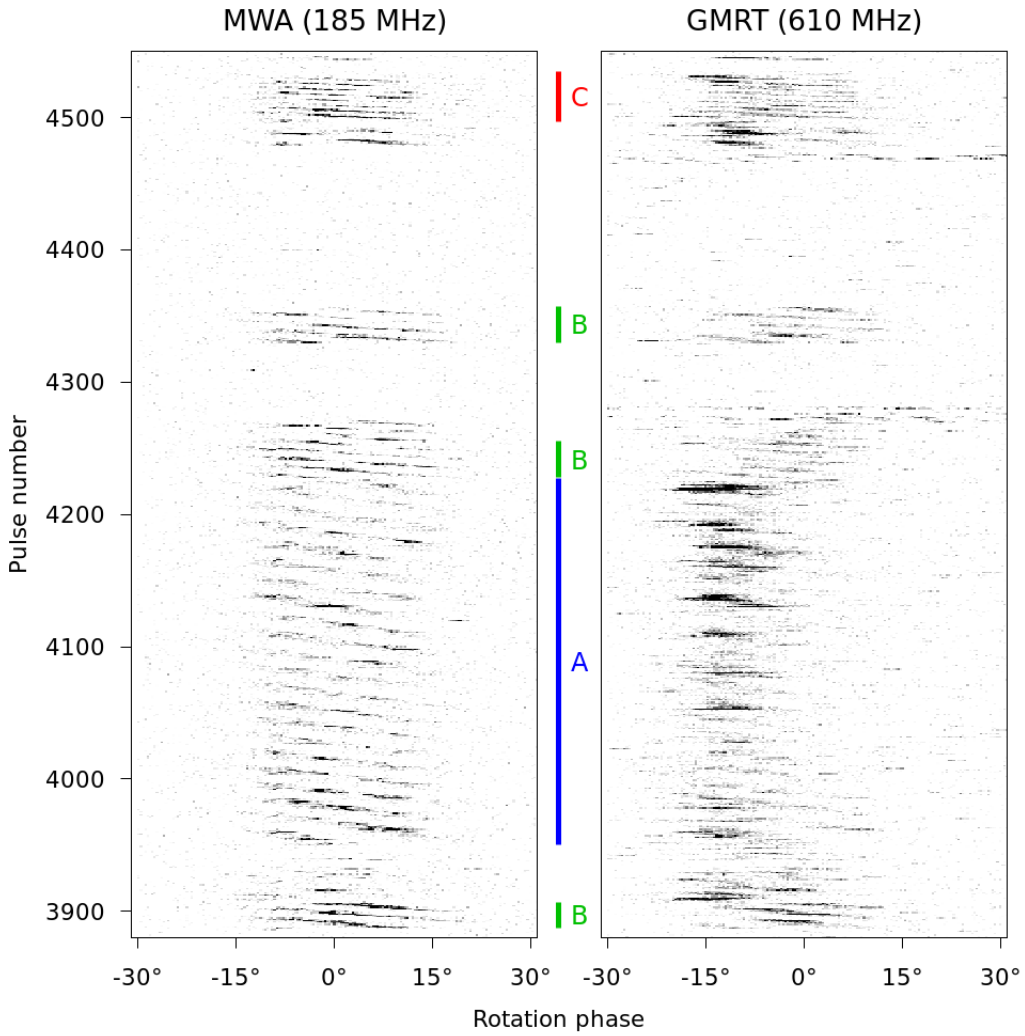

Figure 5.2 A sequence of 671 simultaneous pulses observed at the MWA (left) at 185 MHz and at the GMRT (right) at 610 MHz. All three drift modes can be seen (including the rare C mode), along with interspersed null sequences. The dynamic ranges have been adjusted by eye to give comparable contrast. Some pulses contaminated with RFI can be seen in the GMRT data set. As in Fig. 5.1, the central phase at 0° was chosen by eye to approximate the centre of the pulse window.

where $k = [n/\overline{P}_4]$ is the aliasing order[1], and where the square brackets denote rounding to the nearest integer. Eq. (5.2) is the same as that derived by Rankin et al. (2013), but generalised for arbitrary aliasing orders.

The fact that P_3 is different for each of B0031−07's three drift modes can therefore be explained by a change in n, P_4, or both. In general, it is difficult to find the correct aliasing order k, because solutions for Eq. (5.2) can always be found for any k due to the free choice of P_4 for each mode. However, the carousel rotational speed is thought to be set by the magnetic and electric fields near the surface, which cannot easily change their magnitudes and/or directions on the time scales on which drift mode changes are observed to take place (< 1 rotation). Therefore, it is an interesting question to ask whether the behaviour of the different modes might be brought about by only a change in n, and keeping P_4 constant, an idea first introduced by Rankin et al. (2013) for PSR B1918+19. In this case, it is immediately clear that k cannot be 0 for all three drift modes, since otherwise the drift rate would be the same at all times. If we assume that k is the same for all three drift modes, we find that the quantities $1/\overline{P}_{3A}$, $1/\overline{P}_{3B}$, and $1/\overline{P}_{3C}$ (for modes A, B, and C, respectively) are members of an arithmetic sequence whose nth term corresponds to a carousel with n sparks. Furthermore, if n_A, n_B, and n_C are themselves an arithmetic sequence, then the respective values of $\overline{P}_3$ will be harmonically related, as originally suggested by Wright and Fowler (1981). It also immediately follows that

$$\frac{1}{\overline{P}_{3B}} = \frac{1}{2}\left(\frac{1}{\overline{P}_{3A}} + \frac{1}{\overline{P}_{3C}}\right). \tag{5.3}$$

which can be readily verified in the case of B0031−07. In the special case that the number of sparks differs only by one, then the terms of the arithmetic sequence are consecutive, and the difference between any adjacent pair yields the carousel

[1]Under this definition of the aliasing order, the sign of k is always the same as the sign of P_4, which in this work is chosen to be positive when the carousel is rotating anticlockwise when viewed from "above" the magnetic axis. The phrase "first order aliasing" can be taken to mean $k = \pm 1$.

Table 5.2. Values of P_2 and P_3 for the drift modes of B0031−07, from McSweeney et al. (2017)

Drift mode	$P_2^{(\circ)}$	$\overline{P}_3$
A	$18^\circ.9 \pm 1.1$	12.5 ± 0.8
B	$19^\circ.8 \pm 0.5$	7.0 ± 0.2
C	$19^\circ.1 \pm 2.9$	4.6 ± 0.3

rotation rate directly, e.g.

$$\left| \frac{1}{\overline{P}_{3A}} - \frac{1}{\overline{P}_{3B}} \right| = \left| \frac{1}{\overline{P}_4} \right|. \tag{5.4}$$

Then n can be found by substituting the derived value of $\overline{P}_4$ back into Eq. (5.2).

An alternative approach rearranges Eq. (5.2) to leverage the expectation that the number of sparks changes by an integer value. Continuing under the assumption that the carousel rotation does not change between drift modes, $\overline{P}_4$ can be eliminated to yield

$$\frac{n_A}{\Delta n} = \frac{\overline{P}_{3B}(1 - k\overline{P}_{3A})}{\overline{P}_{3B} - \overline{P}_{3A}}, \tag{5.5}$$

where $\Delta n = n_A - n_B$. Using measured values for $\overline{P}_{3A}$ and $\overline{P}_{3B}$ (from McSweeney et al., 2017, summarised in Table 5.2), this becomes

$$\frac{n_A}{\Delta n} \approx (-1.3 \pm 0.2) + (15.9 \pm 1.7)k. \tag{5.6}$$

Plugging in candidate values for n_A and k, we find near-integral solutions for Δn, with the first order solutions given in Table 5.3. As expected, no solutions were found for $k = 0$. The same procedure was repeated using modes B and C in Eq. (5.5) instead of A and B, with the same results.

Eq. (5.6) shows that if a change in n is indeed the cause of different drift

Table 5.3. Carousel parameters deduced for B0031−07

n_A	n_B	n_C	k	$\sim \overline{P}_4$	Δn
13	12	11	1	14.1	0.89
14	13	12	1	15.2	0.96
15	14	13	1	16.4	1.02
15	16	17	-1	-14.0	-0.87
16	17	18	-1	-14.8	-0.93
17	18	19	-1	-15.7	-0.99

modes, then the predicted number of sparks must increase rapidly for higher aliasing orders, and more so for higher values of Δn. If Δn is kept constant, then n increases approximately linearly with k, and therefore $\overline{P}_4$ must stay relatively constant (since $k = [n/\overline{P}_4]$), but will be much larger (i.e. the carousel rotates much slower) for higher values of Δn. Thus, the approximate solution for $\overline{P}_4$ represents the fastest possible carousel rotation speeds consistent with the observed $\overline{P}_3$ values, without significant difference for higher aliasing orders. By contrast, the theoretical value of $\overline{P}_4$ predicted by the RS model is

$$\overline{P}_{4,\mathrm{RS}} \approx 5.7 \times \left(\frac{P_1}{\mathrm{s}}\right)^{-3/2} \left(\frac{\dot{P}}{10^{-15}}\right)^{1/2} \tag{5.7}$$

which is $\overline{P}_{4,\mathrm{RS}} \approx 4$ for B0031−07. Thus, we argue that a modest carousel rotation period ($14 \lesssim |\overline{P}_4| \lesssim 17$) and a modest number of sparks ($13 \leq n_A \leq 17$) is the most plausible, since it is much closer to the above theoretical value than a no-aliasing solution (for instance, $\overline{P}_4 = n\overline{P}_3 = 9 \times 12.5 = 112.5$ for mode A in Smits et al. 2005). These carousel properties are similar to those found by Rankin et al. (2013) for PSR B1918+19.

On the possible harmonicity of the drift modes, we note that the finding of Vivekanand and Joshi (1996) that they are *not* harmonically related appears to be based on the argument that the *drift rates* are not harmonically related.

However, this is not the same as the claim that the values of P_3 are harmonically related. Indeed, since $P_{2A} \approx P_{2B} \approx P_{2C}$, the harmonicity of P_3 implies that the drift rates should be linearly related, which is in fact consistent with their measurements.

5.3.2 Using P_2 to constrain the viewing geometry

The preceding section dealt solely with P_3, a quantity which is independent of pulse longitude, as evident in Eq. (5.2). P_2, on the other hand, encodes information about the angular distance between successive sparks, and is generally a longitude-dependent quantity. We now proceed to investigate how P_2 may be used to constrain the carousel parameters and the viewing geometry.

P_2 can be measured by correlation methods (e.g. Smits et al., 2005) or methods using fluctuation spectra (Backer, 1971; Wolszczan et al., 1981). For our purposes, the latter are the most suitable for obtaining measurements of P_2 as a function of longitude. This involves computing the longitude-resolved fluctuation spectrum (LRFS), which is done by applying the Discrete Fourier Transform to each longitude bin within a given drift sequence. If the drift band separation remains constant throughout the sequence, a narrow, strong feature will appear at all longitudes in the frequency bin corresponding to the value of P_3. The relative phases of the feature, which we denote by $\theta(\varphi)$, constitute the so-called "subpulse phase track", which encodes information about P_2:

$$\frac{1}{\overline{P}_2(\varphi)} = \left| \frac{\mathrm{d}\theta}{\mathrm{d}\varphi} \right|. \tag{5.8}$$

The subpulse phase that is visible at a given rotation phase involves the computation of two quantities: (1) the magnetic azimuth, σ, of the field lines coplanar with the LoS, and (2) the spark activity at the footpoint (i.e. where the magnetic field line intersects the stellar surface). The consideration of (1) is what Yuen et al. (2016) mean by the "motion of the visible point." For a carousel of n sparks

rotating at rate $1/\overline{P}_4$, the subpulse phase is the difference between the sampled magnetic azimuth and the amount that the carousel has rotated in the same time:

$$\theta(\varphi) = n\left(\sigma(\varphi) - \frac{\varphi}{\overline{P}_4}\right) + \theta_0, \tag{5.9}$$

where the dependence on pulse phase has been made explicit, and θ_0 is the subpulse phase when $\varphi = 0$. An example of a mode B sequence, observed simultaneously with the MWA and the GMRT, with their respective profiles, LRFS, pulse energies, and subpulse phase tracks, is shown in Fig. 5.3.

To recover the expression for $\overline{P}_2$, we differentiate with respect to the phase, yielding[2]

$$\frac{1}{\overline{P}_2(\varphi)} = n\left|\frac{\mathrm{d}\sigma}{\mathrm{d}\varphi} - \frac{1}{\overline{P}_4}\right|. \tag{5.10}$$

By multiplying through by $\overline{P}_3$ and by using Eq. (5.2) to eliminate n, the drift rate can be equivalently expressed as

$$\frac{1}{\overline{D}} = \left(\overline{P}_3 k \pm 1\right)\left(\overline{P}_4\frac{\mathrm{d}\sigma}{\mathrm{d}\varphi} - 1\right). \tag{5.11}$$

In this form, it is easily seen that if $k = 0$, the dependence on P_3 vanishes and a constant carousel rotation speed implies the same drift rate for all three drift modes. Furthermore, any observed curvature of the drift bands is necessarily inherited from the $d\sigma/d\varphi$ term unless the angular speed of the sparks is a function of magnetic azimuth.

If the drift mode changes are, in fact, characterised by only a change in the number of sparks, then Eq. (5.10) predicts only small changes in $\overline{P}_2$ for sufficiently large values of n. This is because $\overline{P}_4$ is assumed constant, and both σ and $\frac{\mathrm{d}\sigma}{\mathrm{d}\varphi}$ are pure functions of the viewing geometry. Therefore, the fractional change in $\overline{P}_2$

[2]One must be careful when comparing this equation with similar-looking equations in Yuen et al. (2016), as both the definitions and notations of the terms involved, as well as the derivation itself, differ.

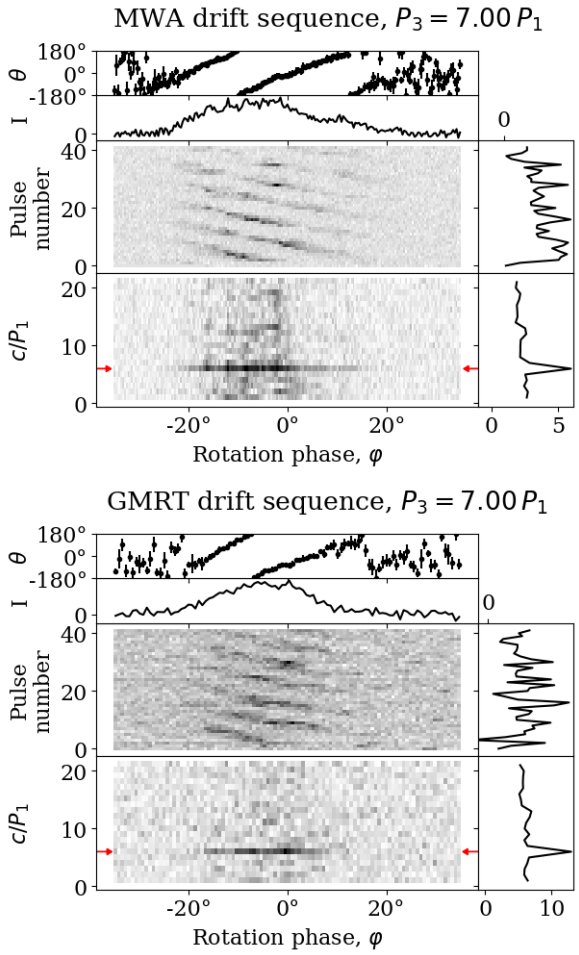

Figure 5.3 A mode B drift sequence observed with the MWA (top figure) and the GMRT (bottom figure). The central panel shows the pulse stack with clearly identifiable drift bands and pulse energies to the right. The LRFS is in the lower panel, with the red arrows marking the frequency bin corresponding to the vertical separation between the drift bands (P_3), and its integrated spectrum on the right. Immediately above the pulse stack is the integrated profile, and the subpulse phase track (i.e. the phases of the highlighted LRFS row) is at the very top. The phase centres ($\varphi = 0°$) have been aligned by eye.

should be equal to the fractional change in n, or

$$\frac{\overline{P}_{2A}}{\overline{P}_{2B}} = \frac{n_B}{n_A}, \tag{5.12}$$

and similarly for modes A and C, etc. The smallest integral values of n that are consistent with the reported values of P_2 in McSweeney et al. (2017) are approximately $n \gtrsim 6$. This is a weaker constraint than the constraint derived using P_3 because of the relatively large measurement errors on P_2 (obtained using correlation methods).

The relative magnitudes of the two terms in the brackets of Eq. (5.10) determine the overall drift band behaviour. For a sufficiently slowly rotating carousel, the value of P_2 is dominated by $d\sigma/d\varphi$. If the carousel rotates in the opposite sense to the motion of the visible point in the pulse window (i.e. P_4 is negative), then increasing the carousel speed causes P_2 to decrease. However, if the carousel rotates in the same direction as the motion of the visible point, P_2 will initially increase until the two terms balance and the subpulse drift appears stationary. As the carousel rotates faster still, the sparks overtake the visible point and the subpulse drift resumes, but now with each successive subpulse coming from the trailing spark.

Regardless of the carousel configuration, $d\sigma/d\varphi$ is in general a function of rotation phase, and thus so is P_2. It follows that the drift rate can never be stationary at all phases simultaneously. In the presumably rare case that the value of $1/\overline{P}_4$ falls between the maximum and minimum value of $d\sigma/d\varphi$, one would see the subpulse drift adopt opposite directions at distinct rotation phases, a phenomenon that has been observed in a few pulsars and known as "bi-drifting" (Wright and Weltevrede, 2017, and references therein). Thus, Eq. (5.10) potentially provides a natural framework for understanding bi-drifting.

In the case of B0031−07, we can estimate the relative contributions of the two competing terms in Eq. (5.10) by considering what parameter values give rise to the measured P_2 value. Taking, for example, the B mode of the second

line in Table 5.3 ($n = 13$, $\overline{P}_4 = 15.2$), a value of $d\sigma/d\varphi = 1.46$ is required to reproduce $\overline{P}_2^{\circ} = 19.8^{\circ}$. Thus, even though the carousel is rotating fast enough to produce aliasing $k = 1$, the motion of the visible point is far more dominant, since $d\sigma/d\varphi \gg 1/\overline{P}_4$. In this case, we can then write

$$\frac{\mathrm{d}\sigma}{\mathrm{d}\varphi} \approx \pm\frac{1}{n\overline{P}_2}, \tag{5.13}$$

which becomes an exact equality in the stationary carousel limit. For the same viewing geometry (i.e. keeping $d\sigma/d\varphi$ fixed), the contribution by the carousel rotation only becomes appreciable when either the aliasing order increases to $k \gtrsim 5$ or the number of sparks drastically increases (or some combination of both). A similar conclusion is reached for all the entries in Table 5.3.

If we assume a small k for B0031−07, we may draw another conclusion from the observation that in the pulses immediately following the onset of a drift sequence after a null, the drift rate appears to undergo a decay until it reaches a nominally stable value (McSweeney et al., 2017). During this decay period, both P_2 and the subpulse width appear visually exaggerated, suggesting that the relative speed of the visible point and the sparks is less. However, when the motion of the visible point dominates, there are only two possibilities. Either (1) the directional sense of both the carousel drift and the motion of the visible point is the same, in which case the relaxation of the drift rate implies a slowing down of the carousel rotation, or (2) the direction senses are different, in which case the carousel must be speeding up. Given that the drift rate of other pulsars which are thought to be free of aliasing effects is observed to increase after a null (e.g. Lyne and Ashworth, 1983), we therefore favour the second possibility. Note that this does not necessarily imply that the carousel and the *pulsar* are rotating in the same directional sense, since the sign of $d\sigma/d\varphi$ depends, in part, on the sign of β, which is still unknown.

5.3.3 Generalisation for AR effects

The P_2 model derived in the previous section has no frequency dependence whatsoever. However, P_2 has long been known to be a function of frequency for pulsars generally (Taylor et al., 1975) and for B0031−07 in particular (Bartel et al., 1980). More recently, McSweeney et al. (2017) showed that the frequency-dependent shift in subpulse phase also depends on which drift mode is present.

One might expect that the dependence of P_2 on observing frequency is a simple side-effect of RFM, where the "space" between the drift bands grows in proportion to the opening angle of the emission cone (e.g. Smits et al., 2007; Yuen et al., 2016). However, it cannot be so, as discussed at length in Edwards and Stappers (2002, 2003). While it is true that the line of sight would cut through the emission cone at different phases depending on the frequency, the image of a single spark projected onto the pulsar's sky would not change relative to the line of sight traverse. Observationally, this implies that different parts of drift bands are illuminated when viewed at different frequencies, not that the drift bands themselves shift in phase.

Despite the preceding argument, a radius-to-frequency mapping remains a necessary (if not a sufficient) condition to explain the P_2 dependence on frequency. For example, Bilous (2018) explains the drift band shifts observed in PSR B0943+10 in terms of the offset phase of the centroid of the line of sight traverse through a beamlet of finite size and shape, as the beamlet changes its magnetic colatitude with frequency.

In this section, we consider the possibility that the frequency-dependence of the subpulse phase shift and of P_2 is due to aberration and retardation (AR) effects, as suggested by Edwards and Stappers (2003). If AR are the dominant effects, such a generalised model can be used to extract information about the emission heights from multi-frequency measurements of the subpulse phase.

5.3.3.1 Derivation of the subpulse phase shift

Dyks et al. (2004) and others showed that pulsar emission will be shifted earlier in phase according to

$$\varphi' \approx \varphi - 2r', \tag{5.14}$$

where φ' is the observed phase, $r' = r/r_L$, and $r_L = cP_1/(2\pi)$ is the light cylinder radius. One r' comes from the aberration of the emission angle from the tangent to the field line, and the other comes from retardation, or the finite time it takes the light to travel from the emission point to the observer.

Although Eq. (5.14) applies to all emission, a correct determination of the observed subpulse modulation must also account for the finite time it takes the information about the subpulse phase to travel from the surface to the emission height. To first order, the trajectory of relativistic particles climbing from the surface to the emission point along a corotating field line is simply r, with a corresponding travel time equal to a phase rotation of r'. This means that the observed subpulse phase does not represent the spark activity at the footpoint of the field line at the time of emission, say, at phase φ, but rather the spark activity at the time when the phase was $\varphi - r'$. Thus, emission that comes from a given magnetic azimuth will be observed at phase $\varphi' \approx \varphi - 2r'$ and have subpulse phase

$$\begin{aligned} \theta'(\varphi') &= n\left(\sigma(\varphi) - \frac{\varphi - r'}{\overline{P}_4}\right) + \theta_0 \\ &= \theta(\varphi) + \frac{n}{\overline{P}_4} r'. \end{aligned} \tag{5.15}$$

Let L and H represent two field lines that have the same magnetic azimuth, σ, but whose footpoints have different magnetic colatitudes. In the absence of AR effects, the two lines come into view at the same phase, φ, at which moment the geometry is represented by the same fundamental triangle. Let L represent the line whose footpoint has the smaller colatitude. For a dipolar field, one expects from geometric arguments (neglecting rotation effects on curvature, as discussed in Thomas and Gangadhara 2007 and Thomas et al. 2010) that the lower

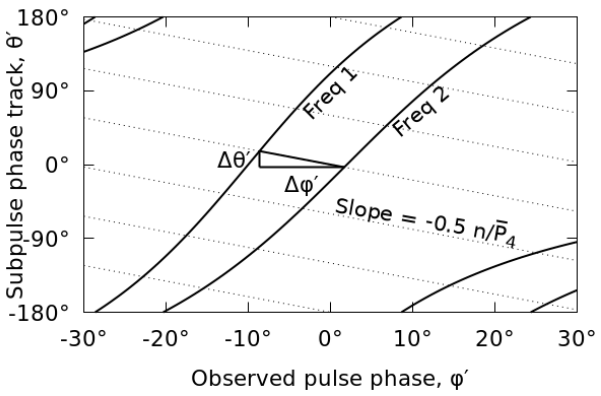

Figure 5.4 An illustration of the method for determining the emission height difference from the subpulse phase tracks at two different frequencies.

frequency emission will be observed from L and the higher frequency emission from H, and that the emission occurs at a greater altitude for L than for H. From Eq. (5.15),

$$\begin{aligned} \theta'_{\rm L}(\varphi'_{\rm L}) - \theta'_{\rm H}(\varphi'_{\rm H}) &= \frac{n}{\overline{P}_4}(r'_{\rm L} - r'_{\rm H}) \\ &= -\frac{n}{2\overline{P}_4}(\varphi'_{\rm L} - \varphi'_{\rm H}), \end{aligned} \tag{5.16}$$

where we have used Eq. (5.14) in the second equation. The corresponding point on the subpulse phase track will appear to have moved vertically by $\Delta\theta' = \theta'_{\rm L}(\varphi'_{\rm L}) - \theta'_{\rm H}(\varphi'_{\rm H})$ and horizontally by $\Delta\varphi' = \varphi'_{\rm L} - \varphi'_{\rm H}$ when viewed simultaneously at two distinct frequencies. Curiously, the slope of this apparent motion is constant:

$$\frac{\Delta\theta'}{\Delta\varphi'} = -\frac{n}{2\overline{P}_4} = -\frac{1}{2}\left(k \pm \frac{1}{\overline{P}_3}\right). \tag{5.17}$$

The shift of a whole subpulse phase track is schematically illustrated in Fig. 5.4. If k is known, the two phase tracks can be directly compared, and the phase difference gives a direct measure of the difference of the emission heights at the two frequencies:

$$\Delta r' \approx -\frac{1}{2}\Delta\varphi', \tag{5.18}$$

in accordance with Eq. (5.14). Note that although the direction of the subpulse phase track shift is fixed by the carousel geometry, the magnitude of the shift

depends on r', which may well be a strong function of pulse phase (e.g. Gangadhara, 2004; Thomas et al., 2010). This can introduce further distortions in the shape of the subpulse phase track as it appears at different frequencies.

The phase shift of individual subpulses can be estimated by Taylor expanding the rotation phase shift as a function of the corresponding subpulse phase shift and the slope of the subpulse phase track:

$$\Delta\varphi'_{\rm hor} \approx \Delta\varphi' + \Delta\theta' \frac{{\rm d}\varphi'}{{\rm d}\theta'}. \tag{5.19}$$

By applying Eq. (5.16) and identifying $\overline{P}'_2 = d\varphi'/d\theta'$ as the AR-corrected subpulse separation actually measured by the observer, we find

$$\Delta\varphi'_{\rm hor} \approx \Delta\varphi' \left(1 - \frac{n\overline{P}'_2}{2\overline{P}_4}\right), \tag{5.20}$$

which by virtue of Eq. (5.18) can be rearranged to yield

$$\Delta r' \approx \frac{\Delta\varphi'_{\rm hor}}{2 - k\overline{P}'_2 \pm \overline{D}'}, \tag{5.21}$$

which directly relates the phase shift of individual subpulses to the difference of emission heights at two simultaneously observed frequencies.

5.3.3.2 Derivation of P_2

The preceding analysis can be recast explicitly in terms of P_2 rather than the subpulse drift phase. It follows from Eq. (5.15) that the measured value of $\overline{P}'_2$ (where, as before, the primes on $\overline{P}'_2$ and φ' denote values measured in the observer's AR-corrected frame) is

$$\frac{1}{\overline{P}'_2} = \frac{{\rm d}\theta'}{{\rm d}\varphi'} \approx \frac{\rm d}{{\rm d}\varphi'} \left(\theta + \frac{n}{\overline{P}_4} r'\right). \tag{5.22}$$

In order to relate this to the $\overline{P}_2$ of Eq. (5.10), we may apply the chain rule, noting that

$$\frac{\mathrm{d}}{\mathrm{d}\varphi'} = \frac{\mathrm{d}\varphi}{\mathrm{d}\varphi'}\frac{\mathrm{d}}{\mathrm{d}\varphi} \approx \frac{1}{1 - 2\frac{\mathrm{d}r'}{\mathrm{d}\varphi}}\frac{\mathrm{d}}{\mathrm{d}\varphi}, \tag{5.23}$$

where we have taken the derivative of Eq. (5.14) with respect to φ. Although it is possible to express these equations in terms of $dr'/d\varphi'$, which is the rate of change of emission height with AR-corrected longitude as it would appear in the observer's frame, $dr'/d\varphi$ is easier to relate to the emission geometry. Then Eq. (5.22) becomes

$$\frac{1}{\overline{P}_2'} = \frac{1}{1 - 2\frac{\mathrm{d}r'}{\mathrm{d}\varphi}}\left(\frac{1}{\overline{P}_2} + \frac{n}{\overline{P}_4}\frac{\mathrm{d}r'}{\mathrm{d}\varphi}\right). \tag{5.24}$$

Two simplifying assumptions can be made. First, as before, we expect the $n/\overline{P}_4$ term to be small compared to $1/\overline{P}_2$. Second, $dr'/d\varphi$ itself must be small on average, since the maximum height is not expected to be more than a few percent of the light cylinder radius. If β is very small, then r' may change rapidly near the fiducial point, but otherwise we assume $dr'/d\varphi \ll 1$. Thus, neglecting the $n/\overline{P}_4$ term and Taylor expanding the fraction,

$$\frac{1}{\overline{P}_2'} \approx \frac{1}{\overline{P}_2}\left(1 + 2\frac{\mathrm{d}r'}{\mathrm{d}\varphi}\right). \tag{5.25}$$

Thus, the observed subpulse separation includes both a fixed, frequency-independent term equal to the subpulse separation that would be observed in the absence of AR effects, and a frequency-dependent term that depends on the rate of change of the observed emission height with rotation phase.

In B0031−07, $\overline{P}_2'$ follows the same trend as the separation of average components, i.e. it becomes smaller at higher frequencies. Thus, the frequency-dependent term must be positive. Since the smallest emission height is expected to be observed at the fiducial point, this supports the idea, suggested by McSweeney et al. (2017), that the fiducial point lies on the leading side of the pulse window.

Eq. (5.25) is almost in a form that can be used to fit historical measurements of P_2 against observing frequency. If the RFM is independent of magnetic azimuth, the emission height can be written in the form $r' = \Phi(\varphi)\nu^\eta$, where $\Phi(\varphi)$ encapsulates the fact that the magnetic colatitudes of the footpoints of the observed field lines is a function of phase, as illustrated in the geometry of Gangadhara and Gupta (2001) and Gangadhara (2004). It then follows that, for a given fixed observing frequency ν,

$$\frac{\mathrm{d}r'}{\mathrm{d}\varphi'} = \frac{\mathrm{d}\Phi}{\mathrm{d}\varphi'}\nu^\eta \tag{5.26}$$

and

$$\frac{1}{\overline{P}'_2} \approx \frac{1}{\overline{P}_2}\left(1 + 2\frac{\mathrm{d}\Phi}{\mathrm{d}\varphi'}\nu^\eta\right). \tag{5.27}$$

5.3.4 Application of the model to B0031−07

Frequency-dependent subpulse behaviour can be thought of in terms of an absolute phase shift (a bulk shift towards earlier or later phases) and a changing P_2 (a compression or expansion of the subpulse modulation pattern). However, measuring the absolute phase shift for our dual-frequency observation of B0031−07 proved problematic because the exact time offset between the clocks at the two telescopes was unknown. The average profiles for each drift mode are known to evolve significantly with frequency, so they cannot be used to align the phases reliably[3]. Alternatives, such as methods involving the alignment of single pulses (e.g. via cross-correlating the time series), would mask any average subpulse phase shift that does exist between the two frequencies. Therefore, the best that can be done with our present data sets is to show how the estimated emission height difference depends on an assumed clock offset between the two telescopes. Using $k = 1$ and the measured average values of $\overline{P}_2$ and $\overline{P}_3$ for the three drift modes, the relative emission height differences between the two frequencies are

[3]A wide-band observation using a single telescope would obviate this problem, unless the profile evolution interferes with the correct determination of DM.

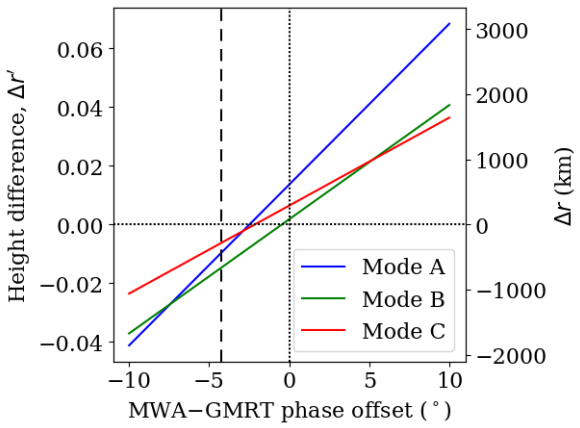

Figure 5.5 The relative emission height differences at MWA and GMRT frequencies for each drift mode, as a function of the assumed clock offset between the two telescopes, expressed in terms of rotation phase. A positive $\Delta r'$ means that the low-frequency emission (observed at the MWA) occurs at greater altitudes than the high-frequency emission (GMRT). The zero-axes are drawn as dotted lines for reference. The 0° phase offset corresponds to the assumption that the phase bin with the greatest average intensity at the MWA aligns with the analogous phase bin at the GMRT. The dash line at −4.2° is the offset assuming that a "giant" pulse that appears at both frequencies occurs at the same true phase.

plotted for each mode in Fig. 5.5. The measured value of $\varphi'_{\rm hor}$ was derived by cross correlating each pulse at the two frequencies, and average all the resulting correlation curves for pulses belonging to the same drift mode. The resulting average correlation curves were smoothed with a Savitzky-Golay filter (Savitzky and Golay, 1964) using a fifth order polynomial and then using cubic-spline interpolation to identify the location of the primary peak.

Although the MWA-GMRT clock offset is unknown, we mark two offsets of interest in Fig. 5.5. The first corresponds to assumption that the peaks of the profiles at the two respective profiles correspond to the same rotation phase. This offset defines the zero point of the x-axis used in the figure. The second offset uses the peak of a particularly bright, narrow burst that appears at both frequencies (pulse number 579 in the MWA data set, equivalent to pulse number 149 in the GMRT data set) to align the clocks. The possibility that the two pulses occur at the same "true" rotation phase is founded on the identification

of the bright emission as a candidate "giant pulse", which are known to come from very narrow phase ranges at some frequencies (Kuzmin and Ershov, 2004; Tuoheti et al., 2011; Nizamdin et al., 2011). If a broadband burst comes from a sufficiently small volume of the magnetosphere, as would be the case for a highly localised surface spark event that generates a large range of particle energies, then the phase shift due to AR effects would apply to all frequencies equally, and the burst would appear at a fixed longitude at all frequencies. However, since Fig. 5.5 shows that this assumption leads to negative height differences in this model (the vertical dashed line at $-4.2°$), we conclude that the bright emission must also come from a range of heights, thus making the derived clock offset erroneous. We note the possibility that the GMRT bright pulse is actually a burst of RFI, as it resembles other instances of off-pulse RFI found in the data set, but we do not investigate this further.

Fig. 5.5 shows that the height differences for all three modes are positive when the MWA-GMRT phase offset $\gtrsim -0.°5$. In this region, the mode with the greatest Δr is mode A, with the height differences in modes B and C being smaller but similar to each other. For phase offsets less than $5°$, $\Delta r \lesssim 2000\,\mathrm{km}$ for mode A and 1000 km for modes B and C (all within a few percent of the light cylinder radius). In contrast, the height differences found by Smits et al. (2007) were $\sim 10\,\mathrm{km}$ across a much wider frequency range (157 MHz to 4850 MHz); however, their model was based (in part) on the idea that P_2 is a direct manifestation of RFM, which, as we have argued above, is an incorrect interpretation.

The unknown clock offset does not affect measurements of P_2, which is related only to the relative phase shift of subpulses at different longitudes. Fig. 5.6 shows a fit for historical measurements of P_2 during mode B drift sequences (mode B is the most common mode with the most reliable data, and has been observed at a much wider range of frequencies than either mode A or mode C), over a wide range of frequencies. There is a clear general trend that P_2 gets smaller with increasing frequency, as previous authors have noted. As indicated in the figure,

some of the early, low-frequency measurements of P_2 relied on single polarisation telescope feeds. It is unclear to what extent this would affect the measurements, given the known complexity of B0031−07's subpulse polarisation (Taylor et al., 1975; Gould and Lyne, 1998) and similar examples of P_2 ambiguity in other pulsars (e.g. Rankin et al., 2005). However, even if these particular observations were omitted, we find that there is still strong support for a frequency-dependent (i.e. non-constant) P_2, especially if one accepts the data from Smits et al. (2007), whose method for measuring P_2 was identically used for (sometimes simultaneous) observations across a broad range of frequencies, albeit using three different telescopes. We thus proceed on the cautious assumption that all the historical measurements presented in Fig. 5.6 are valid. Using Eq. (5.27), the fitted parameters are $\overline{P}_2^{(\circ)} = 23.^\circ6 \pm 3.^\circ8$, $d\Phi/d\varphi' = 0.3 \pm 0.1$, and $\eta = 0.70 \pm 0.34$, which is also plotted on the figure for comparison. A discussion of this result and its implications is deferred until Section §5.4.2.

5.4 Discussion

5.4.1 Carousel geometry

We have attempted to find plausible, quantitative explanations for two interesting features of B0031−07's subpulse modulation pattern: (1) the changing P_3 and drift rate associated with its three distinct drift modes (A, B, and C), and (2) the dependence of subpulse arrival phases on observing frequency and on drift mode. The interpretation of both of these effects depend on the carousel model, assumed in this analysis, which connects the observed modulation pattern of subpulses to a set of sparks near the pulsar's surface rotating around the magnetic axis. Measuring the number of sparks, n, and the carousel rotation period, P_4, is an important step in verifying the predictions of the carousel model. However, these measurements are difficult to make, as there are often degenerate sets of parameters that produce similar looking drift bands in the pulse window. We have

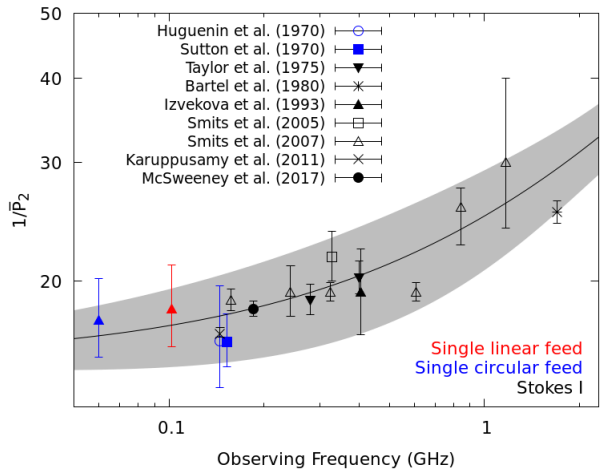

Figure 5.6 A re-creation of Fig. 3.4, but presented on log-scale axes, with the ordinate representing the quantity $1/\overline{P}_2$ instead of P_2, and including a few data points omitted previously. The errors are those reported in the respective source papers, except for Sutton et al. (1970), which did not report measurement errors for P_2, and for which we have adopted a "typical" error of $\pm 2°$. The solid line is a fit of Eq. (5.27) to the data points. The best fit yields $\overline{P}_2^{(\circ)} = 23.°6 \pm 3.°8$ and $\eta = 0.70 \pm 0.34$. The grey shading shows the $\leq 1\sigma$ uncertainty region derived by propagating the (assumed Gaussian) errors of the fitted parameters. Omitting measurements made with single polarisation feeds still shows clear evidence that P_2 is a non-constant function of frequency.

argued that the most likely carousel configuration is one in which the subpulses are aliased ($k = \pm 1$), with the number of sparks being $n \approx 15$, and where n_A, n_B, and n_C differ by 1 in turn.

This solution explains a number of otherwise puzzling features of B0031−07's drift modes. Firstly, the relationship between the modes' respective P_3 values has long been suspected to be a harmonic one. We have shown that this is a mathematical consequence of the number of sparks differing by a constant amount (in this case, one). Also, the similarity of P_2 in all three modes favours solutions with a relatively large number of sparks, as per Eq. (5.12), which is incompatible with a no-aliasing solution by virtue of Eq. (5.6). This solution has the added benefit that the different drift rates of the three modes can be understood in terms of a changing number of sparks rather than a change in the carousel drift rate itself (Rankin et al., 2013). This is more consistent with the original claim of

RS that the carousel speed is a (constant) function of the electric and magnetic field strengths at the surface, which are not expected to change rapidly on small time scales.

The absolute magnitude of the carousel rotation period is also an important prediction of the RS and competing models. The solutions presented in Table 5.3 all predict a similar carousel rotation period; taking one example ($[n_A, n_B, n_C] = [15, 14, 13]$), the carousel rotation period is $\overline{P}_4 = \pm 16.4$. The time (per rotation period) it takes one spark to reach the location of its predecessor is of order $\overline{P}_4/n \approx 1$, as expected for a solution with first-order aliasing. This is much smaller than the time that would be inferred directly from $\overline{P}_3$ if aliasing were assumed to be absent (12.5, 7.0, 4.6 for modes A, B, and C respectively).

In Table 5.4, we compare our measurement of P_4 (for a particular carousel configuration from Table 5.3) alongside measurements for other pulsars. The carousel rotation period predicted from RS, $\overline{P}_{4,\mathrm{RS}}$, is calculated from Eq. (5.7). We have included both the unaliased and (first order) aliased values of P_4 for each pulsar in the table except B0826−34, whose drift bands frequently change directions, and whose unaliased P_4 value is therefore ambiguous. The preferred P_4 (according to the cited work) is indicated in the table notes, with the other value being extrapolated assuming the same number of sparks. We have not indicated whether $k = 1$ or $k = -1$, but this can be worked out using the table values and Eq. (5.2).

In almost all cases, the unaliased carousel rotation period is much larger than the value predicted by RS, a point that is noted by all authors who advance the unaliased model as the preferred one. It is commonly recognised that aliasing could be a way to account for (or at least mitigate) this discrepancy, except in the case of B0809+74, in which the "memory" of subpulse phases across null sequences was used to show that only the unaliased model is consistent with the data. Even if aliasing were possible for this and other pulsars, there still remains a large discrepancy between the measured $\overline{P}_4$ and the RS value, most significantly

Table 5.4. Carousel rotation rates of selected pulsars

Pulsar	Modes	n	$\sim \lvert\overline{P}_4\rvert$		$\overline{P}_{4,\mathrm{RS}}$	Reference
			$k = 0$	$\lvert k\rvert = 1$		
B0031−07	[A,B,C]	[15,14,13]	[187,98,60]	16.4	4.0	[This work]
B0809+74	-	$\gtrsim 15$	$\gtrsim 165$[a]	$\gtrsim 14$	1.6	van Leeuwen et al. (2003)
B0818−41	-	20	370[a]	18.3[a]	1.9	Bhattacharyya et al. (2007)
B0826−34	-	13	Fluctuates in both directions	13[a]	2.3	Gupta et al. (2004); Esamdin et al. (2005); Bhattacharyya et al. (2008)
B0834+06	-	8	17.4	14.8[a]	10.3	Asgekar and Deshpande (2005)
B0943+10	B	20	43	37[a]	9.3	Deshpande and Rankin (2001)
B1237+25	-	18[b]	~ 60	26[a]	3.4	Maan and Deshpande (2014)
B1819−22	[A,B,C]	[12,11,10]	[204,80,46]	12.8[a]	2.6	**?**
B1857−26	-	20	147[a]	18	5.4	Mitra and Rankin (2008)
B1918+19	[A,B,C]	[10,9,7]	[61,34,17]	12[a]	7.3	Rankin et al. (2013)

[a] P_4 values in the cited texts

[b] Derived for the outer ring of their 'A' sequence

for B0826−34, B0818−41, and B1237+25, where there is approximately an order of magnitude difference. It is possible that in some of these cases, an even higher aliasing order may be present.

Alternative theories of spark circulation obviate the need for invoking higher order aliasing, such as the spark model of Gil and Sendyk (2000), which generally predicts much longer carousel rotation periods than RS. They analyse B0031−07, concluding that its carousel consists of five sparks in a single annulus with a radius of $s = 0.7$ of the polar cap distance, rotating at $\overline{P}_4 \approx 34$. While this reproduces an unaliased value of P_3 that agrees well with the observed value for P_3, they do not discuss how their model may be applied to modes A and C. However, we note that their theory predicts a maximum allowed number of sparks of $n_{\max} = 16$, which is consistent with the $k = +1$ solutions in Table 5.3.

A final point to note is that, in many cases, the first order aliasing solution predicts a value of $\overline{P}_4$ that is comparable to the number of sparks, and hence $n/|\overline{P}_4| \sim 1$. This is not surprising, as first order aliasing implies $0.5 \leq |k| = [n/|\overline{P}_4|] \leq 1.5$.

5.4.2 Frequency-dependent effects

Armed with a plausible solution for the configuration and rotation period of the carousel, we have attempted to make sense of the frequency-dependence of its subpulse modulation pattern. It is important to remember that the carousel model (ignoring AR and finite-spark-size effects) predicts that any given subpulse should appear at the same rotation phase at any observing frequency, regardless of the location (or movement) of their parent sparks in the polar cap, and regardless of the emission height. Clearly, however, the subpulses of B0031−07 *do* exhibit frequency- and mode-dependent phase shifts, as has been demonstrated many times in the literature, and confirmed by our own observations.

The qualitative behaviour of the subpulses can be summarised as follows. In any given drift mode, the horizontal separation of the drift bands (i.e. P_2) decreases with increasing frequency (however, mode A may behave more erratically at higher frequencies, see Smits et al., 2007) by roughly the same amount. There is also an absolute, frequency-dependent phase shift of the whole subpulse pattern which is different for the three modes.

5.4.2.1 Absolute phase shift and implications for emission heights

We have derived a model for the frequency-dependence of subpulse phases due to AR effects. Regardless of whether this turns out to be the correct explanation for B0031−07, the derived formulas quantify the subpulse phase shift that must be present due to AR effects. Importantly, we have included in this model the time it takes information about the spark modulation to travel from the surface to the emission height, a point which (to the best of our knowledge) has not been considered in previous studies of the frequency-dependence of subpulses. This makes the model a potentially powerful tool for testing the carousel model in cases where AR effects are indeed dominant, and where the emission heights can be measured by other (independent) means.

Our attempt to apply this model to B0031−07, however, encountered several

difficulties. Firstly, the exact time offset between the data obtained at the two different telescope facilities is unknown, so that the absolute phase shifts of the subpulse modulation pattern in each drift mode could not be confidently measured. This analysis is therefore only practical if the time offset is known precisely (to within a fraction of the subpulse width, ∼a few milliseconds for B0031−07), or if large instantaneous bandwidths are available at a single telescope, so that the frequency evolution of the drift bands is unambiguous. Using the relative phase shifts between the three drift modes, we have deduced that if the time offset is no more than 13 ms (equivalent to 5° in pulse longitude) from the offset obtained by aligning the average profile peaks at the two frequencies, then the emission height differences between the modes is $\lesssim 2000$ km for mode A and $\lesssim 1000$ km for modes B and C, or approximately a few percent of the light cylinder radius.

Within this small range of time offsets, there appears to be a greater inferred height difference generally between the drift bands of mode A than for the other two modes. If this is true, then there should also be a correspondingly greater degree of profile evolution for mode A sequences. This is indeed observed, as can be seen in both Fig. 5.2 and the mode-separated profiles of Smits et al. (2005). However, a more robust comparison requires a more precise determination of the emission heights than we have been able to accomplish here.

5.4.2.2 Subpulse separation, P_2

The fact that the drift bands bunch together at higher frequencies has led many authors to incorrectly associate the frequency behaviour of P_2 with the frequency behaviour of the average profile. However, they must be considered independently from each other owing to the fact that any frequency dependence of the former must be explained in the context of the geometry of a single field line, whereas the latter considers the (flaring) geometry of the global magnetic field structure. That the two effects are independent is evidenced by PSRs B0826−34 and B2020+28, whose P_2 appears to evolve in the opposite sense to their average

profiles (Bhattacharyya et al., 2008). In both effects, however, the RFM plays an important role, since it relates the emission frequency to the local field geometry. We can expect, therefore, that a correct determination of the RFM, coupled with a correct understanding of which frequency-dependent effects dominate at different emission heights, would provide a quantitative explanation for both the single pulse and the average profile behaviour.

The connection between P_2 and the RFM is made explicit in Eq. (5.26), which led to the prediction of how $\overline{P}_2'$ changes with frequency in Eq. (5.27). The functional form of (5.27) reveals the relationship between single pulse (i.e. P_2) and average pulse behaviour. The overall shape of the curve is set by the signs of of $d\Phi/d\varphi'$ and η, and it is instructive to consider the possibilities. When $d\Phi/d\varphi' < 0$, the resulting curve has a vertical asymptote at a (maximum or minimum, depending on the sign of η) frequency of

$$\nu_{\rm asymptote} = \left(-2\frac{\mathrm{d}\Phi}{\mathrm{d}\varphi'} \right)^{-1/\eta}, \tag{5.28}$$

at which point P_2 explodes. However, no such drastic qualitative change in P_2 has ever been observed, so we can rule out this scenario. When $d\Phi/d\varphi' > 0$, Eq. (5.27) predicts that P_2 should change in the *opposite* sense to the average profile components. As noted above, this sort of behaviour has been observed (in B0826−34 and B2020+28), but it is far less common than the alternative. It is also troubling that $d\Phi/d\varphi' > 0$ implies (in the geometry of Gangadhara (2004)) that we are always seeing the subpulses on the trailing side of the fiducial point, which is unlikely to be true for most pulsars, especially those with large duty cycles. Only at the fiducial point does $d\Phi/d\varphi' = 0$, at which point the frequency dependence vanishes altogether.

Another challenge for this model is the high-frequency prediction that P_2 should continue to decrease at an ever greater rate. On this point, the erratic behaviour of P_2 for mode A as reported by Smits et al. (2007) has already been mentioned. Recent work by Ilie et al. (2019, submitted) have measured a mode B

value of $P_2^{(\circ)} = (20^{+7}_{-5})^\circ$ at $\sim 1.4\,\mathrm{GHz}$, which is notably smaller than measurements at similar frequencies shown in Fig. 5.6. Thus, P_2 may also behave similarly in modes A and B at high frequencies, both of which stand in stark contrast to the high-frequency prediction of the present model.

Thus, there are a number of problems with our model of how P_2 should change with frequency if AR are the dominant effects. In the particular case of B0031−07, the fit of Eq. (5.27) to the historical measurements of P_2 yields positive values for both $d\Phi/d\varphi'$ and η. However, a positive value for the index, η, should be viewed with strong scepticism. All known models of RFM (see, e.g., Thorsett, 1992, and references therein) predict a negative index. Some pulsars *are* known to show unusual profile evolution, such as B1944+17, whose profile components move outward at higher frequencies (Kloumann and Rankin, 2010), and others whose more central components shift in phase much less (or not at all!) than the outer components. However, even in the unlikely scenario that these anomalies imply an unusual RFM, this cannot be the case for B0031−07. Low frequency observations of B0031−07 reveal that the primary profile component becomes double at $< 100\,\mathrm{MHz}$ (Izvekova et al., 1993; Suleimanova and Pugachev, 2002). This implies (within the context of the carousel model) that the observed footpoints are indeed at smaller colatitudes at lower frequencies, i.e. the line of sight cuts the carousel more centrally at lower frequencies. The assumed dipolar geometry of the magnetic field requires that the emission height along inner field lines is higher than for outer field lines. We can therefore conclude that there is nothing unusual about the RFM of B0031−07 that requires exceptional consideration, and that B0031−07 is similar to most pulsars whose P_2 follows the same trend as the average profile components.

Given this, can we make sense of our measurement of a positive η? One possibility is that the RFM is a strong function of magnetic azimuth (and therefore of rotation phase), rendering Eq. (5.26) invalid. This idea has been explored by Thomas and Gangadhara (2007) and Thomas et al. (2010), who showed how the

curvature of the field lines on the leading side is augmented by rotation effects, while on the trailing side the curvature is diminished. A more complete modelling of P_2 vs frequency for B0031−07 that takes rotation-induced curvature is beyond the scope of this analysis—we only note here that this effect (or some other effect that we haven't considered) may be necessary for a complete understanding of the observed frequency-dependent behaviour of P_2 in B0031−07 if AR effects are the dominant cause.

Alternatively, AR effects may not be the dominant frequency-dependent effects at play here, which would naturally affect our analysis of the absolute phase shifts seen in the three drift modes (Fig. 5.5). If this is the case, one alternative is the effect of the sparks having finite size and shape, as studied in B0320+39 and B0809+74 by Edwards and Stappers (2003) and in B0943+10 by Bilous (2018). We do not attempt a similar analysis for B0031−07 here, but this could now be fruitfully attempted using the carousel configuration we have derived. In general, it would be useful to compare the spark-size model with the present AR-augmented model to see which of them dominates for a given emission geometry (i.e. carousel configuration and emission height). Alternative models, such as the fan-beam model of Dyks and Rudak (2015), may also be compared.

5.5 Conclusions

We have presented a new solution for the carousel configuration of B0031−07, showing that the subpulse behaviour of the three drift modes can be explained with a single carousel rotation rate. This is possible because of aliasing effects, which produce different apparent drift rates and P_3 values by only changing the number of sparks in the carousel. Among the solutions consistent with the drift rates (given in Table 5.3), we give as a representative solution a carousel rotation rate of $\overline{P}_4 = 16.4$ and number of sparks in each drift mode $[n_A, n_B, n_C] = [15, 14, 13]$. We have explained how first-order aliasing solutions in which the number of sparks differs between drift modes by a constant amount ($\Delta n = 1$, in

this case) produce P_3 values that are harmonically related, which we confirm in the case of B0031−07. Moreover, this carousel rotation period is much closer to the theoretical value predicted by RS than estimates that assume no aliasing.

We have extended the carousel model to include AR effects and shown how they affect the pulse phase at which subpulses appear. However, we found several problems with the model's ability to interpret the frequency dependence of P_2, and that these problems were not limited to B0031−07 alone, but also to the wider pulsar population in which P_2 usually behaves in a similar way to the average profile components (smaller separation at higher frequencies). This indicates that either the AR-theory is incomplete (e.g. rotation induced curvature has not been included) or AR effects are not typically the dominant cause of frequency-dependent behaviour. In either case, the inferred emission height differences for the three drift modes ($\lesssim 2000$ km for mode A and $\lesssim 1000$ km for modes B and C, between 185 and 610 MHz), as conservative as they are, should be nevertheless regarded with caution.

Despite these difficulties, the model describes the effect that AR *must* have on subpulses in the carousel model. As such, it provides a new method for estimating emission height differences that uses the frequency evolution of the drift bands, making it independent from other methods which use the average profile. If it can be shown that AR effects dominate the frequency-dependent behaviour of a given pulsar, this method provides a strong test of the carousel model, which uniquely assumes that the behaviour of the subpulses is governed by spark events located very close to the pulsar surface, thereby dictating the magnitude of phase shift that will be observed for a given emission height. Therefore, applications of this AR-augmented model to other bright pulsars which exhibit subpulse drifting and whose emission heights are known or estimated by other methods will be able to conclusively determine whether the observed phase shift is consistent with the carousel model.

Chapter 6

Discussion and Conclusions

The underlying theme of this thesis has been to investigate the mechanism that generates the bright radio emission beams around pulsars that are observed as a series of regular pulses. The fact that the details of the emission mechanism are still unclear after more than half a century of research and the observation of thousands of pulsars, speaks to the difficulty of the problem. Bottom-up approaches suffer from a lack of understanding of how relativistic plasmas behave in ultra-strong magnetic and gravitational fields, while the sheer variety of pulsar signal morphologies (integrated profiles, single-pulse behaviour) make top-down approaches challenging.

It is widely regarded that single-pulse studies offer the greatest insights into the emission mechanism, since single pulses reveal the stochastic nature of the emission process, which is masked by the process of forming integrated profiles. Taking this approach naturally limits such studies to pulsars that are bright enough to be seen in single pulses. Among such pulsars are many whose subpulses drift regularly in time across the pulse window, a phenomenon which has been the main focus of this thesis.

Subpulse drifting is popularly taken as evidence that the emission beam has a regular structure, consisting of discrete beamlets rotating steadily around the pulsar's magnetic axis. One of the earliest models, that of Ruderman and Suther-

land (1975), suggested that beamlets were the emission signatures of a carousel of sparks that occur in the polar gap, a region just above the pulsar's surface where charged particles are accelerated to relativistic energies and which are also subject to an azimuthal drift that carry the sparks around the magnetic pole. This model makes specific predictions about the behaviour of the sparks and the resulting emission beamlets, three of which have been investigated in detail in this thesis, namely,

1. that the carousel rotates with a constant period;

2. that the rotation period is set by the $\vec{\boldsymbol{E}} \times \vec{\boldsymbol{B}}$ drift, and has a magnitude given by Eq. (1.62); and

3. that the phase at which individual subpulses appear is independent of observing frequency.

All three of these predictions are known to fail in many instances, and a large amount of effort by proponents of the carousel model has been spent trying to understand ways in which the model might be extended in order to accommodate such exceptions. This thesis has focused on one pulsar in particular, B0031−07, which has been demonstrated in the preceding chapters to apparently violate all three predictions.

The ideal resolution to this problem would be to find some unifying principle which can explain all the peculiarities of B0031−07 (and pulsars with similar behaviour) in one go. Unfortunately, this is impossible within the context of the carousel model. Predictions (1) and (2) relate to the physical (hence, frequency independent) dynamics of the sparks on the surface, while the violation of (3) is necessarily a magnetospheric effect, i.e. due to the specifics of the radiation mechanism in the emission region far above the surface, which produces a frequency-dependent emission beam. Thus, at least two disparate ideas are needed to account for B0031−07's subpulse behaviour. While this by no means renders the (extended) carousel model inadmissible as a possible explanation, it

does increase the likelihood that some other, simpler model might be found that can more parsimoniously explain all of B0031−07's observed properties.

The test of any model requires the observed behaviour (or departure from the predicted behaviour) to be quantified. As is evident in the preceding chapters, however, this can prove difficult when there are multiple possible solutions to the carousel configuration, all of which produce similar-looking drift bands within the pulse window. Indeed, only a small number of pulsars have had their carousel configurations determined with any degree of confidence (see Table 5.4). Most of these determinations have only been possible because of some argument for why one particular aliasing order should be favoured. The argument for B0031−07 is similar to B1819−22 and B1918+19: if the drifting behaviour is first-order aliased, the apparently different drift rates of their respective multiple drift modes can be explained in terms of a single carousel rotation rate. This naturally supports the carousel model, which no longer (at least, for these three pulsars) has to explain how the carousel rotation rate can change sporadically and suddenly between drift modes.

On the other hand, it remains unclear why the number of sparks should change equally sporadically and suddenly. The original Ruderman and Sutherland (1975) model does not make a specific prediction of how many sparks there should be, stating only that the presence of a spark discharging at one location "would be expected to inhibit the formation of another simultaneous discharge within a distance $\sim h$," where h is the height of the polar gap. This implies a minimum distance between sparks, which in turn implies a maximum number of sparks that can fit around 360° of azimuth for some given magnetic colatitude. This idea has been notably further developed in the spark model of Gil and Sendyk (2000), in which the whole polar cap is filled with sparks forming possibly multiple concentric rings (instead of consisting of a single circumferential ring of sparks, as per the Ruderman and Sutherland (1975) model). Unfortunately, this model also predicts that the number of sparks in any given ring is constant, at odds

with the solution for B0031−07 derived here. Thus, there is a need to explain how and why this happens on rapid time scales.

Nevertheless, assuming the number of sparks can change on short ($< P_1$) time scales, the carousel configuration derived in Chapter 5 is a major step forward in understanding the behaviour of B0031−07's carousel. The implications of this carousel configuration are now discussed in further detail.

6.1 Evolving drift rates: synthesising the results from Chapters 3 and 5

The novelty of the derived carousel configuration of B0031−07 is that it obviates the need for multiple carousel rotation rates to explain the different drift rates seen in its three modes (A, B, and C). However, the gradual change in drift rate investigated in Chapter 3 cannot be so easily explained. It will be noted that the study presented in Chapter 3 was published before the first-order aliased solution of Chapter 5 was found, and so it is appropriate to revisit the discussion of the earlier results in this new light.

In other pulsars where similar behaviour is seen, the drift rate appears to relax from some initial rate to a steady value (characteristic of the present drift mode) until it is interrupted by either a drift mode change or the onset of a null sequence (Lyne and Ashworth, 1983). Given the effort to explain all subpulse drifting behaviour with a constant carousel rotation rate, is it possible that the gradually changing drift rate is merely a side effect of the individual sparks shifting into a different configuration, while the average rotation rate remains constant? For example, suppose that when a spark vanishes (say, during a transition from mode A to mode B), the remaining sparks initially remain in their places, only gradually relaxing into a new configuration in which they are, once again, equally spaced in magnetic azimuth. In this view, the "extra" motion of an individual spark is due to interactions between the sparks (presumably related to the $\sim h$

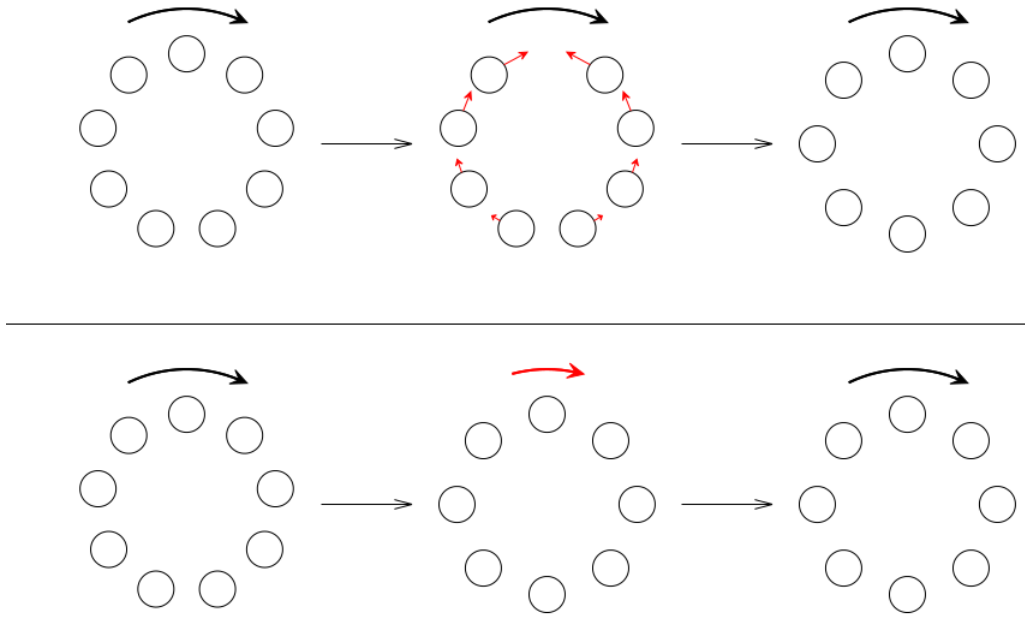

Figure 6.1 Two models which can explain the gradually changing drift rate after a drift mode change caused by the reduction of the number of sparks by one. These possibilities are merely examples and do not represent an exhaustive list of the possibilities. In this cartoon, the carousel begins with 9 sparks equally spaced in magnetic azimuth and end with 8 sparks, also equally spaced. In the first model (top row), one spark vanishes and the remaining sparks only gradually move into the new configuration while the average rotation speed of the carousel remains constant. In the second model (bottom row), the sparks immediately change configuration and the carousel rotation suddenly slows, only gradually relaxing back to its usual, steady rate.

length scale introduced above), while the bulk motion is still fixed by $\vec{\boldsymbol{E}} \times \vec{\boldsymbol{B}}$ drift. This is illustrated in the top row of Fig. 6.1.

The "vanishing spark model" just described has three immediately testable consequences. Firstly, the vanished spark would occasionally be "seen" as a missing subpulse, and subpulses on either side of it would shift from the drift expected from steady rotation in opposite directions to each other. The same is true for the case when the spark number increases, except that the new spark would appear either between two existing drift bands or as a subpulse that bifurcates. This effect would only be visible when the spark disappears (or appears) while its cor-

responding beamlet is in a section of the emission beam that is concurrently being traversed by the line of sight. This would only happen occasionally, depending on the number of sparks and the viewing geometry, and so many instances of drift mode changing would have to be observed in order to catch it in action.

Secondly, the subpulse separation, P_2, would change continuously (albeit not necessarily smoothly) from its old values to its new values. This is a consequence of the extant sparks themselves not changing their azimuthal spacing discontinuously in this model. Whether or not this actually occurs in B0031−07 was not tested, and the empirical model used in Chapter 3 explicitly assumed that P_2 remains constant throughout. Nevertheless, there are instances in the data sets where P_2 appears slightly larger at the beginning of some drift sequences, as noted in Chapter 5. Interestingly, B0809+74 was found to take on a different value of P_2 at the beginning of some drift sequences (van Leeuwen et al., 2002), but in that case P_2 is smaller.

Thirdly, since the azimuthal speed of the sparks is allowed to change discontinuously, so too, might the apparent drift rate. The new drift rate, as well as its relaxation back to a steady value, depends on the motion of the individual sparks whose corresponding beamlets are passing through the line of sight during the relaxation period. If the carousel happens to be oriented so that the locally observed sparks have individual rotation speeds less than the average rotation speed, one would expect (in the absence of aliasing effects) the apparent drift rate to either increase or decrease depending on the relative motion of the carousel with respect to the motion of the visible point. However, if the observed sparks have rotation speeds more than the average, the drift rate would change in the opposite direction.

This third consequence, as well as the former two, are complicated by aliasing, if present. However, a full investigation of aliasing in this context, and how it affects measurements of the drift rate and P_2, is not carried out here.

An alternative model, in which the average carousel rotation rate temporar-

ily changes (see the bottom row of Fig. 6.1), makes three different predictions. First, no extraneous or missing subpulses would be expected. Second, P_2 would change discontinuously at the drift mode boundary. Finally, the drift rate would also change discontinuously, but its relaxation back to a steady value would depend only on average carousel properties, and not which azimuthal section of the emission beam was being observed.

Although the post-null properties of subpulses have been studied for many individual pulsars, it remains unclear which of these models best describes the data in general, or whether the transition between carousel states unfolds in a different way than the two possibilities considered here (illustrated in Fig. 6.1). The first step of such a study is to accurately quantify the effects described above for each model. A general treatment is beyond the scope of this thesis, but a beginning can be made by generalising the formalism of Chapter 5 for an accelerating carousel, to see if it can possibly tally with the empirical model developed in Chapter 3.

6.1.1 Generalisation for accelerating carousels

In Chapter 5, an expression for the subpulse phase, Eq. (5.9), was derived assuming a constantly rotating carousel, which is repeated here:

$$\theta(\varphi) = n\left(\sigma(\varphi) - \frac{\varphi}{\overline{P}_4}\right) + \theta_0. \tag{6.1}$$

For a carousel whose rotation rate can vary with time, the second term inside the brackets must be replaced by the integral representing the total amount of carousel rotation that has occurred during some time interval. As this is no longer a pure function of rotation phase, the generalised formula must be expressed as a function of time. For two arbitrary times, $t_1 < t_2$, the difference between the

observed subpulse phases is

$$\Delta\theta = n\left(\Delta\sigma - \int_{t_1}^{t_2} \omega_4(t')\,dt'\right) \tag{6.2}$$

where $\Delta\theta \equiv \theta(t_2) - \theta(t_1)$ (similarly for $\Delta\sigma$), and $\omega_4(t) = 2\pi/P_4(t)$. The function $\omega_4(t)$ must now be chosen in order to make progress.

6.1.2 The exponential relaxation model

Let us assume the functional form suggested by the analysis of Lyne and Ashworth (1983), an exponential decay[1] from some initial rotation rate, $\omega_{4,i}$, to an asymptotic final, "steady" rate $\omega_{4,f}$:

$$\omega_4(t) = (\omega_{4,i} - \omega_{4,f})e^{-t/\tau} + \omega_{4,f}, \tag{6.3}$$

where $\tau > 0$ is the characteristic time scale of the exponential decay. Integrating and substituting this into Eq. (6.2),

$$\Delta\theta = n\Big(\Delta\sigma + \Delta\omega_4\tau - \omega_{4,f}\Delta t\Big), \tag{6.4}$$

where, of course, $\Delta t = t_2 - t_1$. In order to interpret this equation in terms of an observed drift rate, t_1 and t_2 must be chosen to coincide with the centres of two subpulses that appear in the same drift band in consecutive pulses. If the reference time $t = 0$ is chosen to occur within the pulse window of an initial pulse ($p = 0$), then the following approximations can be made:

$$t_1 \approx pP_1, \tag{6.5}$$

$$\Delta t = P_1 + D \approx P_1, \tag{6.6}$$

[1]Note that van Leeuwen et al. (2003) argue that the exponential decay rate is only apparent, resulting from averaging over many drift sequences where the start time of the relaxation period after a null is variable. There are also examples of "wandering" (i.e. not as predictable as "drifting") subpulses, such as B0826−34 (e.g. Esamdin et al., 2005) and B2303+30 (Redman et al., 2005), suggesting a more stochastic cause for gradual drift rate changes.

where the second approximation also assumes $D \ll P_1$. Since $\sigma(t)$ is periodic with the rotation period,

$$\begin{aligned}\sigma(t_2) - \sigma(t_1) &= \sigma(t_1 + P_1 + D) - \sigma(t_1) \\ &= \sigma(t_1 + D) - \sigma(t_1),\end{aligned} \tag{6.7}$$

and hence,

$$\Delta\sigma \approx \frac{\mathrm{d}\sigma}{\mathrm{d}t} D = 2\pi \frac{\mathrm{d}\sigma}{\mathrm{d}\varphi} \overline{D}. \tag{6.8}$$

Also,

$$\Delta\omega_4 \approx (\omega_{4,f} - \omega_{4,i})(1 - e^{-1/\overline{\tau}})e^{-p/\overline{\tau}}, \tag{6.9}$$

where $\overline{\tau} = \tau/P_1$, following the notational convention introduced in Chapter 5. Finally, note that the subpulse phase difference between the two chosen subpulses is

$$\Delta\theta = \begin{cases} 2\pi(n-k), & \beta > 0, \\ -2\pi k, & \beta < 0 \end{cases} \tag{6.10}$$

where k is the aliasing order, as usual, and the extra $2\pi n$ in the $\beta > 0$ case comes about by virtue of the fact that the visible point makes a complete circuit around the magnetic pole[2]. For simplicity, $\beta < 0$ is assumed in what follows, but care should be taken to add in the extra $2\pi n$ term whenever $\beta > 0$.

The above approximations can now be combined to give an explicit solution for the drift rate as a function of the pulse number and the exponential decay parameters τ, $\omega_{4,i}$, and $\omega_{4,f}$:

$$\begin{aligned}-2\pi k &\approx n\left(\frac{\mathrm{d}\sigma}{\mathrm{d}t} D + \tau(\omega_{4,f} - \omega_{4,i})(1 - e^{-1/\overline{\tau}})e^{-p/\overline{\tau}} - \omega_{4,f}(P_1 + D)\right) \\ -k &\approx n\left(\frac{\mathrm{d}\sigma}{\mathrm{d}\varphi}\overline{D} + \overline{\tau}\left(\frac{1}{\overline{P}_{4,f}} - \frac{1}{\overline{P}_{4,i}}\right)(1 - e^{-1/\overline{\tau}})e^{-p/\overline{\tau}} - \frac{1+\overline{D}}{\overline{P}_{4,f}}\right),\end{aligned} \tag{6.11}$$

[2]Alternatively, one can define $\sigma(t)$ to be "unwrapped" in phase, so that $\sigma(t+P_1) = \sigma(t) + 2\pi$ when $\beta > 0$.

from which

$$\begin{aligned}\overline{D}(p) &\approx \frac{\frac{1}{\overline{P}_{4,f}} - \frac{k}{n} - \overline{\tau}\left(\frac{1}{\overline{P}_{4,f}} - \frac{1}{\overline{P}_{4,i}}\right)(1 - e^{-1/\overline{\tau}})e^{-p/\overline{\tau}}}{\frac{\mathrm{d}\sigma}{\mathrm{d}\varphi} - \frac{1}{\overline{P}_{4,f}}} \\ &\approx \overline{D}_f - \overline{A}e^{-p/\overline{\tau}},\end{aligned} \tag{6.12}$$

where

$$\overline{A} = n\overline{P}_{2,f}\overline{\tau}\left(\frac{1}{\overline{P}_{4,f}} - \frac{1}{\overline{P}_{4,i}}\right)(1 - e^{-1/\overline{\tau}}) \tag{6.13}$$

is constant for a given drift sequence, and where $\overline{P}_{2,f}$ and $\overline{D}_f$ are the asymptotic values of $\overline{P}_2$ and $\overline{D}$ respectively. In this form, it is easily seen that the exponential term becomes negligible when $p \gg \overline{\tau}$, leaving $\overline{D} \approx \overline{D}_f$. Eq. (6.12) shows that the relaxation of the drift rate appears exponential even in the presence of aliasing, as long as the aliasing number doesn't change over the course of the carousel acceleration.

Finally, the functional form of the drift bands as a function of pulse number can be approximated by summing the drift contribution of each successive pulse. A drift band that starts at phase φ_i in pulse $p = 0$ will have shifted to

$$\begin{aligned}\varphi(p) &\approx \varphi_i + 2\pi \sum_{p'=0}^{p-1} \overline{D}(p') \\ &\approx \varphi_i + 2\pi\overline{D}_f p - 2\pi\overline{A} \sum_{p'=0}^{p-1} e^{-p'/\overline{\tau}},\end{aligned} \tag{6.14}$$

by pulse p. The first two terms describe the asymptotic (i.e. "steady state") drift in which the subpulse phase position progresses linearly with the pulse number, p. The last term represents the departure from the asymptotic drift rate due to the exponential relaxation.

6.1.3 Comparison with the quadratic model

The empirical model used in Chapter 3 was motivated by the observation that the drift rate of B0031−07 changes steadily over the course of entire drift bands. The chosen strategy was to model this behaviour as simply as possible by fitting straight lines to the drift rate as a function of pulse number. Since the drift rate is the rate of change of subpulse position, this led to modelling the shapes and positions of the drift bands as quadratic functions of pulse number.

In a sense, the exponential relaxation model is equally empirical, except that the assumed functional form is applied to the physical carousel rotation instead of directly to the measured subpulse positions. Nevertheless, it is important to remember that there is no *a priori* reason to expect the carousel to behave in any way other than constant rotation (but see Section §6.2 below). In this section the relationship between the exponential relaxation model and the quadratic model is derived, in order to learn which of the two models is better able to describe the data.

If the drift rates are well-fit by lines of constant slope, as the analysis of Chapter 3 suggests, then the relaxation time scale must be relatively long, otherwise the drift rate would flatten out significantly before the end of the drift sequences. Thus, the exponential term in Eq. (6.12) can be Taylor expanded about $p/\overline{\tau} = 0$. Neglecting terms quadratic and higher, one is left with

$$\begin{aligned} \overline{D}(p) &\approx \overline{D}_f - \overline{A}\left(1 - \frac{p}{\overline{\tau}}\right) \\ &\approx \frac{\overline{A}}{\overline{\tau}}p + \overline{D}_f - \overline{A}, \end{aligned} \tag{6.15}$$

whose coefficients can be directly related to the parameters of the quadratic model:

$$\begin{aligned} a_1 &= \frac{4\pi\overline{A}}{\overline{\tau}} \\ a_2 &= 2\pi(\overline{D}_f - \overline{A}). \end{aligned} \tag{6.16}$$

The extra factor of 2π is included to convert the dimensionless quantities to radi-

ans. Eq. (6.16) thus gives physical significance to the first two fitted parameters of the quadratic model, which was not attempted in Chapter 3.

Is the exponential relaxation model any better at describing the drifting behaviour of B0031−07 than the quadratic model? Only if $\overline{\tau}$ is sufficiently small that the change of drift rate ceases to be well-described by straight lines. Demonstrating that this is true will require a careful analysis of the data, which is not attempted here. However, given the fluctuation in subpulse morphology and position, there is a natural upper limit on how precisely the instantaneous values of D, P_2 and P_3 can be measured. Thus, such an analysis will have to be statistic in nature, measuring the drift rate "relaxation" in many drift sequences in order to show that the rate of change of drift rate (see the middle panel of Fig. 3.2) are not purely linear functions of pulse number.

6.1.4 Drift band curvature and polarisation

In Chapter 3, it was shown that overall, the quadratic model performed just as well as, if not better than, linear fits to individual drift bands. However, there were clearly systematic effects that caused both models to perform poorly at the edges of the pulse window (see Fig. 3.5), indicating that the curvature of the drift bands is not accounted for in either model. The quadratic model does, of course, introduce some curvature into the fits, but the fact that this model appears to perform slightly worse at the edges than the linear model indicates that the fitted parabolas curve in the opposite direction to the true curvature of the drift bands.

Curvature is expected in the drift bands even for a constantly rotating carousel, due to the spherical trigonometric relationship between the magnetic azimuth, σ, and the rotation phase, φ (Edwards and Stappers, 2002). Curvature is also expected in the exponential relaxation model, which can be most easily seen by noting the (implicit) dependence of both terms of Eq. (6.14) on φ (via $\overline{P}_{2,f}$). It would be possible to ascertain whether or not Eq. (6.14) produces similar systematic errors if fit with the linear and quadratic models considered in Chapter

3; however, it is surely a more direct approach to use Eq. (6.14) to fit the data directly, and compare the goodness-of-fit and systematic errors directly with the other models. The utility of such an analysis (which is left for the future) is to place further constraints on the viewing geometry, since the drift band curvature depends on α and ζ.

In the remainder of this section, the relationship between drift band curvature and the PPA is investigated, and some useful formulas for future investigation are derived. The following assumes a constant carousel rotation speed, in order that the curvature (manifest as a phase-dependent P_2) can be accurately measured from the LRFS. Recall that whether or not a particular spark is observed at a given time depends on the magnetic azimuth of both the spark and the line of sight, as expressed in Eq. (5.9). At any moment in time, the fundamental triangle (Fig. 1.15) is completely defined by α and ζ (which are fixed), and φ (which of course varies periodically with time). Unfortunately, α and ζ are never perfectly known, and estimates of these two quantities are usually obtained by fitting the RVM model to the PPA, as outlined in Section §1.5.2. Incidentally, the PPA is also used to identify the location of the fiducial point, which is otherwise only assumed to coincide with the centre of the integrated profile.

The expression connecting the PPA with the viewing geometry is an example of an identity of spherical triangles, which in general relate four of the triangle's six angles together. Many other identities exist—in fact, one can always find an identity relating any four angles together. It is also possible to derive identities relating the rates of change of angles with respect to other angles. In the case of the fundamental triangle, one is almost always interested in the rates of change with respect to φ, since these are the most easily measured. Since all such derivatives are also completely determined by φ, it follows that the derivatives "contain" just as much information about the state of the fundamental triangle as any of the angles. Thus, the full set of quantities relating to the state of the fundamental triangle includes the "sides" (α, ζ, Γ), the angles (ψ, σ, φ), and the

non-trivial derivatives[3]:

$$\frac{\mathrm{d}\psi}{\mathrm{d}\varphi}, \quad \frac{\mathrm{d}\sigma}{\mathrm{d}\varphi}, \quad \text{and} \quad \frac{\mathrm{d}\Gamma}{\mathrm{d}\varphi}. \tag{6.17}$$

Any subset of four will be related by a corresponding identity.

With the identification of $\mathrm{d}\psi/\mathrm{d}\varphi$ with the slope of the PPA curve and the strong connection between $\mathrm{d}\sigma/\mathrm{d}\varphi$ and the subpulse drifting phenomenon, these two quantities are arguably the most easily measured or inferred from an assumed carousel configuration. With the relevant identities in hand, full polarisation measurements of pulsars exhibiting subpulse drifting can potentially provide useful constraints on other pairs of angles. Here, just one such identity is derived, relating the four quantities α, ζ, $\mathrm{d}\psi/\mathrm{d}\varphi$, and $\mathrm{d}\sigma/\mathrm{d}\varphi$. This identity is planned to be exploited in the further analysis of the MWA observation of B0031−07 studied in Chapter 5 (note that only Stokes I was used in that analysis even though full Stokes parameters were available).

First, the familiar identity relevant to the RVM is restated:

$$\tan\psi = \frac{\sin\alpha\sin\varphi}{\sin\zeta\cos\alpha - \cos\zeta\sin\alpha\cos\varphi}. \tag{6.18}$$

We can change this (and any other) identity to an equivalent symmetrical one by making the "left-right" substitutions $\alpha \leftrightarrow \zeta$, $\psi \leftrightarrow \sigma$ (but φ and Γ map to themselves). Then

$$\tan\sigma = \frac{\sin\zeta\sin\varphi}{\sin\alpha\cos\zeta - \cos\alpha\sin\zeta\cos\varphi}. \tag{6.19}$$

[3]As the fundamental triangle has only one degree of freedom, they are expressed as full, and not partial, derivatives of the angle φ.

Implicit differentiation of Eq. (6.18) with respect to φ yields

$$\begin{aligned}\frac{1}{\cos^2\psi}\frac{\mathrm{d}\psi}{\mathrm{d}\varphi} &= \frac{\sin\alpha\cos\varphi(\sin\zeta\cos\alpha-\cos\zeta\sin\alpha\cos\varphi)-\sin^2\alpha\cos\zeta\sin^2\varphi}{(\sin\zeta\cos\alpha-\cos\zeta\sin\alpha\cos\varphi)^2}\\ &= \frac{\sin\alpha\cos\alpha\sin\zeta\cos\varphi-\sin^2\alpha\cos\zeta(\cos^2\varphi+\sin^2\varphi)}{(\sin\zeta\cos\alpha-\cos\zeta\sin\alpha\cos\varphi)^2}\\ &= \frac{\tan^2\psi(\sin\alpha\cos\alpha\sin\zeta\cos\varphi-\sin^2\alpha\cos\zeta)}{\sin^2\alpha\sin^2\varphi}\end{aligned} \tag{6.20}$$

$$\begin{aligned}\frac{\mathrm{d}\psi}{\mathrm{d}\varphi} &= -\frac{\sin^2\psi(\sin\alpha\cos\zeta-\cos\alpha\sin\zeta\cos\varphi)}{\sin\alpha\sin^2\varphi}\\ &= -\frac{\sin^2\psi\sin\zeta\sin\varphi}{\sin\alpha\sin^2\varphi\tan\sigma},\end{aligned} \tag{6.21}$$

where the last step follows from Eq. (6.19). The spherical sine rule applied to the fundamental triangle gives the identities

$$\frac{\sin\alpha}{\sin\psi}=\frac{\sin\zeta}{\sin\sigma}=\frac{\sin\Gamma}{\sin\varphi}, \tag{6.22}$$

which allows simplification of the above to

$$\frac{\mathrm{d}\psi}{\mathrm{d}\varphi}=-\frac{\sin\alpha\cos\sigma}{\sin\Gamma}=-\frac{\sin\psi\cos\sigma}{\sin\varphi}. \tag{6.23}$$

By symmetry, the equivalent expressions for the rate of change of magnetic azimuth can be written down immediately:

$$\frac{\mathrm{d}\sigma}{\mathrm{d}\varphi}=-\frac{\sin\zeta\cos\psi}{\sin\Gamma}=-\frac{\sin\sigma\cos\psi}{\sin\varphi}. \tag{6.24}$$

Eq. (6.18) can be converted to an expression for α using the equivalent polar triangle,

$$\tan\alpha=\frac{\sin\psi\sin\Gamma}{\sin\sigma\cos\psi+\cos\sigma\sin\psi\cos\Gamma} \tag{6.25}$$

which gives

$$\frac{\mathrm{d}\sigma}{\mathrm{d}\varphi} + \frac{\mathrm{d}\psi}{\mathrm{d}\varphi}\cos\Gamma = -\frac{\sin\sigma\cos\psi + \cos\sigma\sin\psi\cos\Gamma}{\sin\varphi} = -\frac{\sin\psi\sin\Gamma}{\tan\alpha\sin\varphi} = -\cos\alpha. \tag{6.26}$$

By "left-right" symmetry,

$$\frac{\mathrm{d}\psi}{\mathrm{d}\varphi} + \frac{\mathrm{d}\sigma}{\mathrm{d}\varphi}\cos\Gamma = -\cos\zeta. \tag{6.27}$$

By multiplying Eqs. (6.26) and (6.27) by $\frac{\mathrm{d}\sigma}{\mathrm{d}\varphi}$ and $\frac{\mathrm{d}\psi}{\mathrm{d}\varphi}$ respectively and subtracting to eliminate the $\cos\Gamma$ term, one obtains

$$\left(\frac{\mathrm{d}\sigma}{\mathrm{d}\varphi}\right)^2 - \left(\frac{\mathrm{d}\psi}{\mathrm{d}\varphi}\right)^2 = -\frac{\mathrm{d}\sigma}{\mathrm{d}\varphi}\cos\alpha + \frac{\mathrm{d}\psi}{\mathrm{d}\varphi}\cos\zeta. \tag{6.28}$$

These results can be applied to any pulsar for which both the PPA and the subpulse drift can be measured for individual drift sequences with a stable rotation rate. The application of these results to B0031−07 are planned for the sequel paper to Chapter 5.

6.1.5 Continuity of the carousel rotation rate

At first glance, the investigation into the evolving drift rate of B0031−07 in Chapter 3 seems to be fundamentally at odds with the main argument of Chapter 5, which seeks a solution for the carousel geometry that can explain the drift rates of the three drift modes with a single, unchanging carousel rotation rate. There is no real contradiction here: the two types of drift rate change under discussion represent two physically distinct phenomena, owing to the very different time scales on which they operate[4]. As long as the variance in carousel rotation speed required to explain the slowly evolving drift rate is relatively small compared to

[4]It is worth noting that, in principle, accurate measurements of P_2 would be able to distinguish between the scenario in which the carousel configuration changes by means of a changing number of sparks on one hand, and a varying carousel rotation rate on the other. However, as demonstrated in Chapter 5, the fractional change in P_2 is in both cases smaller than the precision to which P_2 can be presently measured.

the average rotation speed, this is perfectly consistent (within uncertainties) with the single rotation rate solution found in Chapter 5.

For this reason, aliased solutions are favoured over non-aliased solutions, since aliasing can amplify a small $\Delta\omega_4$ into a relatively large ΔD. Thus, for some given, slowly fluctuating drift rate, higher aliasing implies both a larger physical carousel rotation rate and a smaller variance thereof, which conspire to imply a very small *fractional* change in the carousel rotation rate. As an example, consider one of the carousel configurations presented in Chapter 5 as a possible solution, where mode B has 14 sparks and a carousel rotation period of $\overline{P}_4 \approx 16.4$. In this case, a 1% change in carousel rotation rate appears as roughly a 6% change in drift rate.

Taking the slowly changing drift rate as evidence of an accelerating carousel rotation rate (whether exponential or otherwise), it is interesting to consider how the rotation changes when the pulsar switches to a different drift mode. The primary assumption in the analysis of Chapter 5 was that a sudden change in the number of sparks in the carousel is not accompanied by an equally sudden change in the carousel rotation rate (within measurement errors). This assumption led directly to the set of first order aliasing solutions presented in Table 5.3. The extension of this assumption to the context of a gradually changing drift rate is that the carousel rotation rate is *continuous* across drift mode boundaries.

If the carousel rotation rate is, in fact, continuous across drift mode boundaries, then this may furnish the means for distinguishing the true carousel configurations among the possibilities listed in Table 5.3. Choosing the wrong configuration will result in carousel rotation rates that are not necessarily continuous across drift mode boundaries. If there is an intervening null sequence, this may prove difficult to test; fortunately, there are many instances where the transition between drift modes occurs without nulls, or without nulls lasting only a few pulses.

For an assumed aliasing order and number of sparks, the drift rate and the drift

band spacing are sufficient to derive the carousel rotation rate. Given that P_2, P_3 and D must all change continuously while P_4 is changing, it may prove difficult to obtain accurate, instantaneous measurements. The LRFS-based methods of Chapters 3 and 5 are inappropriate because they rely on information that has been averaged over whole drift sequences. As a result, measuring the instantaneous value of P_2 may therefore prove the most difficult to measure accurately, since the only alternative method of measuring the instantaneous value requires the correlation of subpulses across a large fraction of the pulse window, where the systematics due to drift band curvature come into effect. However, linear fits to the subpulses of each drift band provide measurements of D for each drift band at a single (arbitrarily selected) rotation phase. It is expected that the uncertainty in these measurements is dominated by the uncertainty of the subpulse positions, and not by systematic errors introduced by drift band curvature. The vertical spacing between the fitted drift band lines (at the selected rotation phase) also provides an estimate of P_3 between successive drift bands.

Thus, for B0031−07, measuring the instantaneous values of D and P_3 directly is likely to be far more robust than than measuring P_2. Once they have been obtained, Eq. (5.11) provides a direct connection between the carousel rotation rate, the observed drift rate, and P_3. Rearranging it slightly,

$$\overline{P}_4 \frac{\mathrm{d}\sigma}{\mathrm{d}\varphi} = \frac{1}{\overline{D}(\overline{P}_3 k \pm 1)} + 1. \tag{6.29}$$

Both $\overline{D}$ and $\overline{P}_3$, which are now treated as functions of time (or pulse number) can be measured directly at an arbitrarily chosen pulse phase. Although the viewing geometry is unknown, $d\sigma/d\varphi$ is constant at a fixed rotation phase. Thus, if $\overline{P}_4$ is continuous, then so is the product $\overline{P}_4(d\sigma/d\varphi)$. It will be noted that Eq. (6.29) has no explicit dependence on n, so this method is only capable of finding the correct aliasing order, k. However, if the value of $d\sigma/d\varphi$ can be independently estimated (see, for example, Section §6.1.4 above), the instantaneous value of $\overline{P}_4$, and thence n, can be ascertained. The use of this method to verify the results of

Chapter 5 (or, at least, to test the continuity of P_4) is planned for an upcoming publication.

6.2 The (average) carousel rotation rate: a summary of the main results of Chapter 5

One of the main successes of the analysis of Chapter 5 is the fact that the derived carousel rotation rate of B0031−07 is much closer to the value predicted by the Ruderman and Sutherland (1975) model than previous estimates. This is a general feature of all first-order aliasing solutions, as evident in Table 5.4. However, there is still an unaccounted discrepancy between theory and observation in the case of B0031−07 as well as other pulsars for which P_4 has been measured (see Table 5.4). This can be partially accounted for by the inclusion of a factor that depends on the inclination angle, α, which was omitted from Eq. (5.7), the formula derived for an aligned rotator.

One can hardly avoid noticing, however, that higher-order aliasing ($|k| \geq 2$) can potentially bring the measured P_4 values into even closer alignment with the theoretical value. There is no *a priori* reason why such solutions could not exist, except to note in the case of B0031−07 that such solutions generally favour much larger numbers of sparks, n, where the difference of n between the three drift modes is $\Delta n \geq 2$. Given that there is currently no physical model to justify the appearance or disappearance of even a single spark at a time, these higher-order solutions should not be immediately rejected; however, the first-order solutions still seem the most parsimonious.

It should be remembered that the Ruderman and Sutherland (1975) prediction of the value P_4 given in Eq. (1.62) is a first order approximation, and thus the first-order aliasing solution is broadly consistent with it. Nevertheless, there have been several attempts to hone the original argument in order to produce a more rigorous prediction; e.g., Gil et al. (2003); Fung et al. (2006). In particular,

van Leeuwen and Timokhin (2012) undertake a more complete derivation of the original Ruderman and Sutherland (1975) expression, and show that the drift velocity of the sparks is proportional to the *gradient* of the voltage drop across the polar cap (as opposed to the total voltage drop, which is erroneously assumed to be fixed in the derivation of Eq. (1.62)). This fact allows for the possibility of slower drift velocities, as well as variations in the drift velocity—both of which can potentially bring theory in line with observation.

The theoretical refinements mentioned above, however, can only be tested robustly if P_4 can be measured accurately, which can only happen if the carousel geometry is known with confidence. To summarise, the discovery that B0031−07's three drift modes can all be modelled with a single rotation rate (albeit with minor variations) provides strong constraints on the true carousel rotation period, which can guide future investigations into the various models of spark drift that have been advanced since the original Ruderman and Sutherland (1975) model. Any further information that can be leveraged to constrain the number of sparks in B0031−07's carousel will serve to make the P_4 measurement all the more reliable.

6.3 Frequency-dependent effects: an explanation of the results of Chapters 4 and 5, and future lines of investigation

Both Chapters 4 and 5 have sought to explain the observed frequency-dependent phase shift of subpulses in B0031−07 by appealing to AR effects. This effort was only partially successful: the resulting model made predictions about how P_2 should change with frequency that did not square well with what was expected from B0031−07's profile evolution and its implied RFM. As concluded in Chapter 5, it is likely that AR effects are not solely responsible for the observed subpulse phase shift. However, other possible causes have not been quantitatively applied

to B0031−07, so it would be premature to speculate on which is the most likely. Nevertheless, the analyses of Bilous et al. (2016) and Wright and Weltevrede (2017), which rely on assuming the spatial structure of the sparks, have been identified as two possibilities. The spatial structure of the sparks is intimately connected to the observed frequency behaviour of the subpulses and the energy distribution of the emitting particles. To understand the connection between the spatial structure of the sparks and the different frequency behaviour, one can consider simplified (idealised) spark shapes. In the following sections, four such shapes are considered: (1) point sparks, (2) one-dimensional sparks aligned along lines of constant magnetic colatitude, (3) one-dimensional sparks aligned along lines of constant azimuth, and (4) two-dimensional sparks. These are illustrated schematically in Fig. 6.2.

6.3.1 Point sparks

Consider first the extreme case where the sparks are (zero-dimensional) points on the surface, or in other words, occupy the footpoint of a single magnetic field line (at a single time). As discussed at length in Chapter 4, there is (in general) only a single point along that field line and one point in rotation phase where a relativistic particle's velocity in the observer's inertial frame is parallel to the line of sight. Consequently, all observed emission from that field line[5] is emitted at a single height and appears to the observer as a delta function at a single pulse phase[6]. This is true for all frequencies, even when AR effects have been accounted for, since both the aberration angle and the time of flight are unique functions of the emission height. The spectrum of the delta function would therefore be uniquely determined by the energy distribution of the particles at the emission point. However, because this kind of "subpulse" changes only in amplitude and not in pulse phase at different observing frequencies, it is clear that other spark

[5]Here, as everywhere, some form of coherent curvature radiation is assumed.

[6]Since subpulses have finite width, this is clearly too simple a model, but may have applications to microstructure and nanostructure.

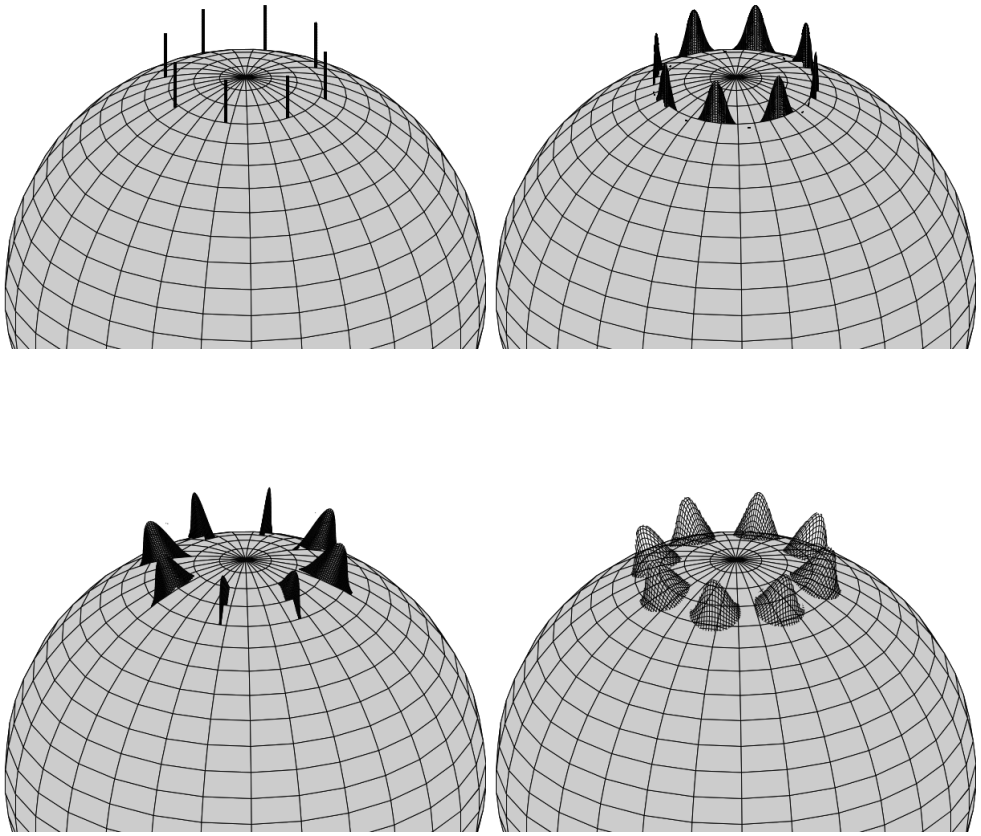

Figure 6.2 Schematic diagrams of four different idealised spark shapes. *Top left*: Point sparks. *Top right*: One-dimensional sparks aligned along lines of constant magnetic colatitude. *Bottom left*: One-dimensional sparks aligned along lines of constant azimuth. *Bottom right*: Two-dimensional sparks.

shapes must be considered.

6.3.2 One-dimensional latitudinal sparks

The next simplest spark shape to consider is a one-dimensional spark. First, let the spark be oriented so that its finite length occupies a range of magnetic azimuths, but has only a single colatitude. This is precisely the kind of spark that was used in Chapter 4 to generate simulated pulse stacks using PSRGEOM. In that case, the "shape" of the spark was chosen to be a Gaussian function in

azimuth; however, in the discussion that follows, the shape is unimportant. Every footpoint in the spark is associated with a unique field line, and by the same arguments as given above, a unique emission height and observed rotation phase. Similarly, the phase-dependent spectrum is uniquely set by the particle energy distribution at each emission point. Since both this energy distribution and the curvature of the particles' trajectory are generally functions of the emission location, the spectra are also expected to be phase-dependent.

Nevertheless, some general statements can be made about how such subpulses may change their appearance at different observing frequencies. Firstly, if the particle energy distribution is assumed to be the same at all heights (a reasonable assumption given that the energy lost to curvature radiation is a negligibly small fraction of the total energy of the relativistic particle[7]), then the difference between the spectra observed at two phases is mainly due to the curvatures of the particles' trajectories at the respective emission points. Because all footpoints have the same colatitude (by assumption), the emission height is smallest for field lines near the fiducial plane and larger at more peripheral azimuths. This implies that the "observed" radius of curvature[8] is also smallest for the field line in the fiducial plane and greater at peripheral azimuths. The spectrum will therefore be shifted towards lower frequencies at more peripheral pulse phases.

This suggests a mechanism by which subpulses can appear to shift in phase at different frequencies. Consider a spark centred at magnetic azimuth σ and has width $\Delta\sigma$. The maximum width of the corresponding subpulse is the "subpulse window", $\Delta\varphi_{\rm sp,lat}$. For sparks near the fiducial point (see Section 6.1.4 for a partial derivation),

$$\Delta\varphi_{\rm sp,lat} \approx \frac{|\sin\beta|}{\sin\zeta}\Delta\sigma. \tag{6.30}$$

[7]This is precisely the condition noted in Ternov (1995) under which the classical theory of synchrotron radiation—and, by extension, curvature radiation—becomes invalid, requiring a full quantum treatment.

[8]Rotation-induced curvature (Thomas and Gangadhara, 2007; Thomas et al., 2010) is neglected here, so that the curvature of a particle's trajectory is assumed to equal the curvature of the field line it follows.

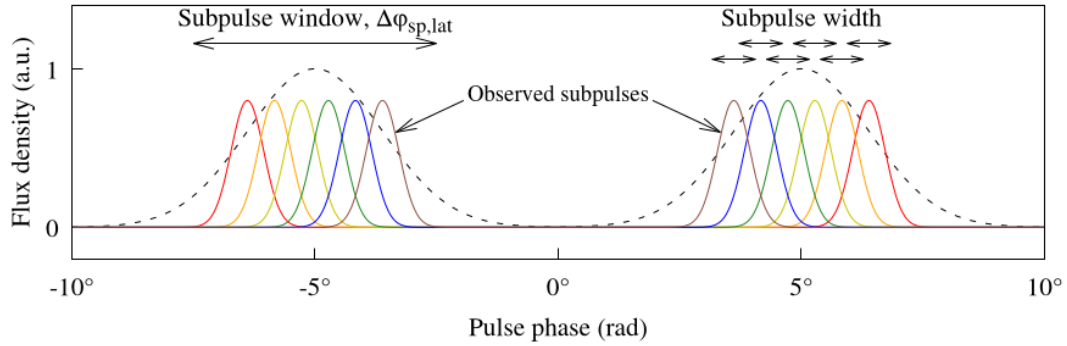

Figure 6.3 The apparent frequency-dependent phase shift of subpulses within the subpulse window set by the azimuthal extent of a latitudinally-aligned spark. In order to see a shift, the subpulse width must be smaller than the subpulse window, which implies a relatively narrow distribution of particle energies along the observed field lines. This is because the emission height (and hence, the curvature and characteristic frequency of curvature emission) for each field line is fixed set by the geometry. Therefore, the spectrum at each rotation longitude is a pure function of the particle energy distribution.

In order for a phase shift of the subpulse to be possible, the width of the subpulse at a particular frequency must be narrower than $\Delta\varphi_{\rm sp,lat}$ in order for it to have "room" to move about (Fig. 6.3). This in turn requires the energy distribution to be narrow enough that the (phase-dependent) amplitudes peak within the subpulse window. However, because the emission heights are fixed for each magnetic field line, and because the lowest heights occur at the fiducial point, there is a one-to-one mapping between emission frequencies and rotation phases for a given particle energy (actually, a one-to-*two* mapping, with pairs of rotation phases appearing symmetrically on either side of the fiducial point). Subpulses within the correct phase range would appear to shift outwards (i.e. away from the fiducial point) at lower frequencies as the amplitude peak shifts within the subpulse window. The similarity between this predicted behaviour and that of integrated profile components is notable, even though the cause usually invoked to explain profile evolution (in the context of the carousel model) is quite different to the model described here. In particular, the qualitative agreement between this model and the behaviour of P_2 as observed in B0031−07 is strongly suggestive

that the azimuthal extent of the underlying sparks may be a key missing ingredient from the analysis of Chapter 5 that prevented the AR model from producing sensible results.

On the other hand, if the energy distribution is too wide, there will still be an amplitude gradient across the subpulse, but the whole subpulse window will be illuminated. In that case, the mean subpulse position will be a much weaker function of observing frequency, and only appear to shift as the slope of the gradient changes.

It should be noted that even though the Chapter 4 pulse stack simulations generated by PSRGEOM assumed the same one-dimensional spark shape as being discussed here, the intensity profile of the subpulse was chosen to be a fixed function of magnetic azimuth without any frequency dependence. Therefore, the effect just described would not have appeared in the PSRGEOM simulations. Instead, the frequency dependence studied in that chapter is that which arises from shifting the colatitude of the subpulses; ironically, this effect is better understood by considering one-dimensional sparks oriented along lines of magnetic longitude, which is discussed in the next section.

6.3.3 One-dimensional longitudinal sparks

The previous section discussed one-dimensional sparks that were aligned along lines of constant colatitude, and it was shown in a qualitative way how there may arise a frequency-dependent phase shift owing to the fact that different parts of the spark are associated with different emission heights and, hence, different trajectory curvatures and spectra. If, on the other hand, one-dimensional sparks are aligned along lines of constant azimuth, then the whole spark will appear at the same rotation phase in the absence of AR effects, or with a maximum width that depends on the colatitudinal range of the spark if AR effects are included. In Chapter 5 it was argued that the contribution from retardation is, to first order, zero because the total path length of the information from the surface

spark to the observer is the same, and does not depend on the height at which the information-carrying particles are converted into information-carrying radio photons.

The PSRGEOM simulations in Chapter 4 show a phase shift which depends on spark colatitude; for longitudinal sparks, this is manifest as a smearing of the delta function across a similar phase range, resulting in subpulse windows with width $\Delta\varphi_{\rm sp,long}$. However, this smearing time scale is only fully realised if the particle energy distribution is sufficiently wide and the resulting spectra sufficiently flat. The parts of the spark nearest the magnetic pole will have observed emission points at greater heights and corresponding greater radii of curvature than those parts of the spark farthest from the magnetic pole. Thus, a narrow particle energy distribution will cause the lower frequencies to be observed in a narrow (i.e. $< \Delta\varphi_{\rm sp,long}$) peak at more leading phases than higher frequencies, but where the maximum shift is not more than $\Delta\varphi_{\rm sp,long}$.

The size of $\Delta\varphi_{\rm sp,long}$ is related to the length of the spark. As mentioned above, retardation effects are considered negligible, so the main contribution to $\Delta\varphi_{\rm sp,long}$ comes from aberration,

$$\Delta\varphi_{\rm sp,long} \approx |\Delta\varphi_{\rm ab}| \approx |\Delta r'|, \tag{6.31}$$

where $r' = r/r_L$ is the emission height normalised to the light cylinder radius. For a dipole geometry,

$$r' = R' \sin^2\theta \approx \frac{4\sin^2\beta}{9s^2}, \tag{6.32}$$

where $R' = R/r_L$ is the (normalised) maximum distance of the field line from the origin, and s is the colatitude of the footpoint normalised to the colatitude of the last open field lines of an aligned rotator. The approximation $R' \approx 1/s^2$ is obtained by expressing R' in terms of s and Taylor expanding about $s = 0$, and the approximation $\beta \approx \Gamma \approx \frac{3}{2}\theta$ is valid near the fiducial point. Since the kind of

sparks under consideration are aligned along lines of magnetic longitude,

$$\Delta\varphi_{\rm sp,long} \approx \Delta r' \approx \frac{\partial r'}{\partial s}\Delta s \approx \frac{8\sin^2\beta}{9s^3}\Delta s, \tag{6.33}$$

which is valid when $\Delta s \ll s$. That is, the observed shift is greater (per unit change in colatitude) at smaller footpoint colatitudes (s), which are sampled at lower frequencies. Thus, applying the cartographic transform to two simultaneous observations at two different frequencies would reveal the phase shift, $\Delta\varphi_{\rm sp,long}$, as a rotational offset between the two computed cartographic maps.

6.3.4 Two-dimensional sparks

The one-dimensional sparks discussed above are merely abstractions designed to investigate how frequency-dependent phase shifts of the resulting subpulses might come about. Sparks are usually considered to have finite width in both azimuthal and colatitudinal directions, commonly assumed to have rotational symmetry (e.g. a two-dimensional Gaussian). In this case, the width of subpulse window, $\Delta\varphi_{\rm sp}$, will depend on which of the two quantities $\Delta\varphi_{\rm sp,lat}$ and $\Delta\varphi_{\rm sp,long}$ dominates.

Consider, then, a carousel of n sparks at colatitude s, where each spark subtends an angle at the magnetic axis which is some fraction, $0 < \chi < 1$, of the angular spacing of the sparks,

$$\Delta\sigma \approx \frac{2\pi\chi}{n}. \tag{6.34}$$

For rotationally symmetric sparks, the physical size of the spark in the azimuthal and colatitudinal directions are the same. On the polar cap ($s < 1$), the carousel can be approximated by a flat circle with radius s, so that sparks have size

$$\Delta s \approx s\Delta\sigma = \frac{2\pi\chi s}{n}, \tag{6.35}$$

Hence, near the fiducial point, the respective subpulse windows are

$$\Delta\varphi_{\rm sp,lat} \approx \frac{|\sin\beta|}{\sin\zeta}\frac{2\pi\chi}{n} \tag{6.36}$$

and

$$\Delta\varphi_{\rm sp,long} \approx \frac{8\sin^2\beta}{9s^2}\frac{2\pi\chi}{n} \tag{6.37}$$

The size of the subpulse window is dominated by the spark's size in magnetic azimuth when

$$\frac{\Delta\varphi_{\rm sp,lat}}{\Delta\varphi_{\rm sp,long}} \approx \frac{9s^2}{8\sin\zeta|\sin\beta|} > 1 \tag{6.38}$$

Unless s is very small (which is not expected on physical grounds), this condition is easily met because β is expected to be small.

This does not guarantee that any observed frequency-dependent subpulse phase shift is due to the azimuthal extent of the spark, unless the observed phase shift is greater than $\Delta\varphi_{\rm sp,long}$. The analyses in Chapters 4 and 5 do, however, support the view that the frequency-dependent shift of B0031−07's subpulses is more likely due to the sparks' azimuthal extent than their colatitudinal extent. The former showed that significant changes in subpulse phase were only achieved at relatively low values of s; the latter, at relatively high emission altitudes—the two conditions are equivalent.

Considering the above arguments, the observed frequency-dependent subpulse phase shifts, if due at all to the finite size and shape of the sparks, are more likely due to their azimuthal extent than their colatitudinal extent. This possibility has yet to be investigated quantitatively.

6.3.5 Sparks as conglomerations of point discharges

The above analyses have assumed that sparks can be modelled as smoothly varying spatial structures on the pulsar's surface, and where the observed intensity at a particular pulse phase is a weighted sum (or integration) of the "intensity" of the spark that is visible to the observer at that moment in time. In reality, subpulses

show a great deal of stochastic behaviour, and the smooth, regular spark shapes assumed above and in the PSRGEOM simulations are a fiction. Given the observational evidence for microstructure, and even nanostructure (albeit for giant pulses), it is possible that subpulses in general are conglomerations of intense, short-duration bursts (Cordes et al., 1990). Such microbursts (and nanobursts) can only arise from events on very small spatial scales, and if they are akin to spark discharge events, they are arguably better modelled by the "point" sparks discussed above in Section 6.3.1.

This has interesting implications for subpulses whose phase is frequency dependent. By the arguments given above, a given micro-spark will appear at the same phase at all frequencies, since the emission height is a fixed function of its magnetic field line geometry. Thus, the only way for a subpulse to have a frequency-dependent phase shift is by modulating the amplitudes of its component micro-sparks. Since the spectrum of micro-spark is entirely dictated by the distribution of particle energies along a given field line, the frequency-dependent subpulse phase shift is also determined by the particle energy distribution. The only ambiguity that must be resolved is the case where micro-sparks at two (or more) distinct locations within a spark fall into the same observed phase bin. In general, however, the spectra of micro-structure can potentially reveal the underlying particle energy distribution (see, e.g., Lange et al., 1998).

6.4 Conclusions

In this thesis, the study of the physical mechanism responsible for pulsed radio emission observed from pulsars has been approached from a largely geometric point of view. One of the most popular models, namely the carousel model, makes specific predictions about when individual millisecond-long bursts of emission ("subpulses") should arrive at the telescope, and deviations from this expected behaviour have been studied in detail for PSR B0031−07. Both numerical and analytical techniques have been applied, resulting in a much greater understand-

ing of the underlying dynamics of this very interesting pulsar.

It has been found that the aspects of B0031−07's behaviour that have historically been the most challenging to understand in terms of the carousel model are greatly aided by the discovery of a particular (small) set of solutions for the geometry and dynamics of its underlying spark carousel. First and foremost among these aspects is the different subpulse drift rates of its three drift modes, which can now be ascribed to a single carousel rotation rate. The carousel rotation rate itself is much closer to the theoretical prediction than previous estimates, and the systematic variations in drift rate seen *within* a drift mode are consistent with predictions of surface temperature fluctuations, as postulated for B0826−34. Modelling B0031−07's drift rate variations has been an important step towards the broader goal of mapping this pulsar's emission beam via the cartographic transform.

The dependence of subpulse behaviour on observing frequency has been less satisfactorily explained, but this is largely because only a single possible cause for this behaviour (namely, AR effects) has been modelled, whereas other frequency-dependent effects probably dominate at the expected emission heights for B0031−07. Nevertheless, the formulas derived for the frequency-dependence of subpulses are a necessary consequence of AR, and may be applicable to pulsars in which emission altitudes are sufficiently high. For more well-behaved pulsars (with longer, more stable drift sequences), models of the frequency-dependence can be tested by measuring the rotational offset of the spark pattern made by the cartographic transform at widely-separated frequencies.

This thesis has also presented a new numerical code, PSRGEOM (documented in Chapter 4), which can be used to create simulated pulse stacks from a given set of carousel parameters. PSRGEOM potentially has many more applications beyond those which have been presented here. In particular, it can be extended to simulate arbitrary spark shapes, providing a way to numerically confirm the ideas outlined in this chapter. In addition, it calculates the curvature

of a particle's trajectory in the observer's inertial frame, thus incorporating the work of Thomas and Gangadhara (2007) and Thomas et al. (2010), who argue for the significance of rotation-induced curvature. It is currently limited to infinitely narrow (unidirectional) particle beams which are 100% linearly polarised and monochromatic (at the characteristic frequency). Future versions of PSRGEOM will include finite-width, polarised particle beams, realistic curvature radiation spectra, and micro- and nano-sparks.

In summary, the major results of this thesis include:

- A new model of B0031−07's carousel that has enabled it, for the first time, to be used as a test for the Ruderman and Sutherland (1975) carousel model.
- A quantitative analysis of the drift rate variations of B0031−07's subpulses, which may (in the future) be used to confirm the suspected aliasing order, $k = 1$.
- The first general derivation of AR effects on subpulse phase shifts, applicable to any pulsar exhibiting subpulse drifting.
- A derivation of the first-order effects of spark shape on subpulse phase shifts.
- The publication of PSRGEOM, a software suite capable of producing simulations of subpulses that are fully consistent with both AR effects and effects arising from different spark shapes.

There are still many unanswered questions surrounding B0031−07 and other similar pulsars. Some have been asked almost since pulsars were discovered, while others have been motivated by the results in this thesis. They include:

- What triggers the drift mode changes and nulls, and what determines how often they occur and how long they last?
- Are the subpulse phases stationary during B0031−07's nulls, as argued for B0809+74?

- Is the carousel rotation rate continuous across drift mode boundaries, and is the variation predictable?
- Can the PPA curve be used in addition to P_2 and P_3 to constrain the carousel parameters?
- If AR effects are not responsible for the frequency- and mode-dependent behaviour of B0031−07's subpulses, can it be explained in terms of the finite size of sparks?
- What are the smallest structures that make up sparks, and what sets this size scale?

Just as B0031−07 has proven a fruitful target of study owing to its apparent departure from the predictions of the Ruderman and Sutherland (1975) model, it is fully expected that other pulsars which exhibit unusual behaviour may also benefit from similarly in-depth analyses as those undertaken in this thesis. In particular, given the widespread (but erroneous) conflation of profile evolution with the frequency dependence of P_2 in the literature, a promising line of attack is to study the correlation between profile components and subpulse shifts across wide frequency ranges. In this regard, pulsars such as B1944+17, B0826−34, and B2020+28 stand out as worthy of further investigation, the former because of its unusual ("reverse") profile evolution, and the latter two because the profile components apparently change in the opposite sense to P_2 with frequency. Newly discovered pulsars, such as J1926−0652 discovered with the Five-hundred-meter Aperture Spherical Telescope (FAST) (Zhang et al., 2019) also offer promising new insights into the subpulse drifting phenomenon.

The above open questions are ripe for investigation, owing in part to the high quality of the data sets obtainable with latest-generation telescopes. For instance, in the course of this study, it has become apparent that studies of frequency-dependent behaviour will benefit greatly from the ultra-wide band receivers that are being commissioned at Parkes and the GMRT. Also, the recently implemented

functionality of the MWA to recover sub-microsecond time resolutions from VCS data is paving the way to study routinely the micro-structure of sparks. In the longer-term future, planned upgrades for the MWA will allow for greater sensitivity and higher native time resolutions. All of this work has implications for impending pulsar studies with SKA-low and SKA-mid (one of its key science goals), which have been, and continue to be, informed by the success of the studies conducted as part of this thesis—in particular, the first systematic, single-pulse studies of pulsars using the MWA.

Appendices

Appendix A

Agreement of co-authors

This section is to comply with the requirement that all co-authors of work included in this thesis outline their contributions. In communicating this statement to the co-authors, they were also informed that the lack of a response would be taken as unconditional tacit approval. Otherwise, all co-authors have read and agreed to the following statement, and their responses can be found below. In the following, "Paper 1" refers to the contents of Chapter 3, "Paper 2" refers to the contents of Chapter 4, and "Paper 3" refers to the contents of Chapter 5.

A.1 Statement of originality

All three papers: I wrote the drafts, which were distributed to all co-authors (with the exception of Dr Kudale, Paper 3) for several rounds of proofreading and editing. After each round, I incorporated the feedback in the manuscripts directly, and this iterative process continued until the co-authors gave their approval.

Paper 1: "Low Frequency Observations of the Subpulse Drifter PSR J0034-0721 with the MWA"
The MWA-VCS observations were scheduled and undertaken by Dr Steven Tremblay, and processed with the beamformer software by myself under the supervision of Dr Ramesh Bhat, Dr Steven Tremblay, and Dr Stephen Ord. Further analysis

of the data (including the development of bespoke software) was undertaken by myself, under close supervision of, and with many suggestions from, Dr Ramesh Bhat, Dr Steven Tremblay, and Dr Avinash Deshpande.

Paper 2: "On the Geometry of Curvature Radiation and Implications for Subpulse Drifting"
I wrote the numerical code that underpins this paper (PSRGEOM). Error (and sanity) checking the code was achieved through multiple discussions with all the co-authors. Dr Ramesh Bhat and Dr Avinash Deshpande guided the discussion relating the simulations to real data, and Dr Avinash Deshpande provided the SPULSES software that was used to make cartographic maps of the simulated beam. Dr Geoff Wright provided derivations of results relating to AR effects that made possible the connection between our results and previous works on AR effects.

Paper 3: "The frequency-dependent behaviour of subpulse drifting: I. Carousel geometry and emission heights of PSR B0031-07"
The MWA and GMRT observations were planned by myself, Dr Ramesh Bhat, and Dr Steven Tremblay. Dr Steven Tremblay scheduled and executed the MWA-VCS observations; Dr Ramesh Bhat and Dr Sanjay Kudale coordinated and executed the GMRT observations. The idea to argue for a first-order-aliasing solution came originally from Dr Geoff Wright, and I undertook the subsequent analysis of the data under the supervision of Dr Ramesh Bhat, Dr Avinash Deshpande, and Dr Geoff Wright. These three also provided many suggestions and insight into the theory relating AR effects to subpulse phase shifts, which I originally derived, and the discussion thereof.

A.2 Co-author responses

Ord, Stephen <Stephen.Ord@csiro.au>

Agreed!

Geoff Wright <geoffw44@btinternet.com>

I'm in full agreement

Sanjay Kudale <kudale.sanjay@gmail.com>

Agreed.

Avinash Deshpande <avideshi@gmail.com>

Agree.

Ramesh Bhat <ramesh.bhat@curtin.edu.au>

I fully agree. All the best.

Bibliography

Ahuja, A., D. Mitra, and Y. Gupta (2007, may). The effect of pulse profile evolution on pulsar dispersion measure. *Monthly Notices of the Royal Astronomical Society 377*(2), 677–686.

Ananthakrishnan, S. (1995). The Giant Metrewave Radio Telescope. *Journal of Astrophysics and Astronomy 16*, 427–435.

Arendt, P. N. and J. A. Eilek (1998). The Shape of Pulsar Polar Caps.

Asgekar, A. and A. Deshpande (2005, mar). Fluctuation properties and polar emission mapping of pulsar B0834+06 at decametre wavelengths. *Monthly Notices of the Royal Astronomical Society 357*, 1105–1112.

Baade, W. and F. Zwicky (1934). Remarks on super-novae and cosmic rays. *Physical Review 46*(1), 76–77.

Backer, D. (1970a, oct). Pulsar Nulling Phenomena. *Nature 228*, 42–43.

Backer, D. (1971). *Radio Intensity Fluctuations in Pulsars.* Ph. D. thesis, CORNELL UNIVERSITY.

Backer, D., S. Hama, S. van Hook, and R. Foster (1993, feb). Temporal Variations of Pulsar Dispersion Measures. *Astrophysical Journal 404*, 636.

Backer, D. C. (1970b). Correlation of subpulse structure in a sequence of pulses from pulsar PSR 1919+21. *Nature 227*(5259), 692–5.

Backer, D. C. (1970c). Peculiar Pulse Burst in PSR 1237+25. *Nature 228*(5278), 1297–1298.

Backer, D. C. (1973). Pulsar Fluctuation Spectra and the Generalized Drifting-Subpulse Phenomenon. *ApJ 182*, 245–276.

Backer, D. C. and J. M. Rankin (1980). Statistical Summaries of Polarized Pulsar Radiation. *The Astrophysical Journal Supplement Series 42*, 143–173.

Bagnulo, S., L. Fossati, J. D. Landstreet, and C. Izzo (2015). The FORS1 catalogue of stellar magnetic field measurements. *Astronomy & Astrophysics 583*(March 2009), A115.

Barnard, J. J. and J. Arons (1986). Wave Propagation in Pulsar Magnetospheres: Refraction of Rays in the Open Flux Zone. *The Astrophysical Journal 302*, 138–162.

Bartel, N., D. Morris, W. Sieber, and T. H. Hankins (1982). The mode-switching phenomenon in pulsars. *The Astrophysical Journal 258*, 776.

Bartel, N., W. Sieber, and A. Wolszczan (1980, oct). Pulse to pulse intensity modulation from radio pulsars with particular reference to frequency dependence. *Astronomy and Astrophysics 90*, 58–64.

Basu, R., D. Mitra, G. I. Melikidze, K. Maciesiak, A. Skrzypczak, and A. Szary (2016). Meterwavelength Single-Pulse Polarimetric Emission Survey. Ii. the Phenomenon of Drifting Subpulses. *The Astrophysical Journal 833*(1), 29.

Bates, S., D. Lorimer, and J. Verbiest (2013, may). The pulsar spectral index distribution. *Monthly Notices of the Royal Astronomical Society 431*, 1352–1358.

Baym, G., C. Pethick, D. Pines, and M. Ruderman (1969, nov). Spin Up in Neutron Stars : The Future of the Vela Pulsar. *Nature 224*(5222), 872–874.

Beskin, V. S., A. V. Gurevich, and Y. N. Istomin (1988). Theory of the Radio Emissions of Pulsars. *Astrophysics and Space Science 146*, 205–281.

Beskin, V. S., A. V. Gurevich, and Y. N. Istomin (2006). *Physics of the Pulsar Magnetosphere*. Cambridge University Press.

Bhat, N. D. R., J. M. Cordes, and S. Chatterjee (2003). A CLEAN-based Method for Deconvolving Interstellar Pulse Broadening from Radio Pulses. *The Astrophysical Journal 584*(2), 782–790.

Bhat, N. D. R., Y. Gupta, M. Kramer, A. Karastergiou, a. G. Lyne, and S. Johnston (2007). Simultaneous Single-Pulse Observations of Radio Pulsars: V. On the Broadband Nature of The Pulse Nulling Phenomenon in PSR B1133+16. *Astronomy and Astrophysics 462*(1), 257–268.

Bhat, N. D. R., S. M. Ord, S. E. Tremblay, S. J. McSweeney, and S. J. Tingay (2016). Scintillation Arcs in Low-Frequency Observations of the Timing-Array Millisecond Pulsar Psr J0437–4715. *The Astrophysical Journal 818*(1), 86.

Bhattacharyya, B., Y. Gupta, and J. Gil (2008). Results from multifrequency observations of PSR B0826-34. *Monthly Notices of the Royal Astronomical Society 383*(4), 1538–1550.

Bhattacharyya, B., Y. Gupta, and J. Gil (2009). Exploring the remarkable subpulse drift and polarization properties of PSR B0818-41. *Monthly Notices of the Royal Astronomical Society 398*(3), 1435–1449.

Bhattacharyya, B., Y. Gupta, J. Gil, and M. Sendyk (2007). Discovery of a remarkable subpulse drift pattern in PSR B0818-41. *Monthly Notices of the Royal Astronomical Society: Letters 377*(1), 10–14.

Biggs, J. D., P. M. McCulloch, P. A. Hamilton, R. N. Manchester, and A. G. Lyne (1985). A study of PSR 0826—34 - a remarkable pulsar. *Monthly Notices of the Royal Astronomical Society 215*, 281–294.

Bilous, A. (2018). PSR B0943+10: low-frequency study of subpulse periodicity in the Bright mode with LOFAR. *Astronomy & Astrophysics 616*, A119.

Bilous, A., V. Kondratiev, M. Kramer, E. Keane, J. Hessels, B. Stappers, V. Malofeev, C. Sobey, R. Breton, S. Cooper, H. Falcke, A. Karastergiou, D. Michilli, S. Osłowski, S. Sanidas, S. ter Veen, J. van Leeuwen, J. Verbiest, P. Weltevrede, P. Zarka, J. M. Grießmeier, M. Serylak, M. Bell, J. Broderick, J. Eislöffel, S. Markoff, and A. Rowlinson (2016, jun). A LOFAR census of non-recycled pulsars: average profiles, dispersion measures, flux densities, and spectra. *Astronomy & Astrophysics 591*, A134.

Blaskiewicz, M., J. M. Cordes, and I. Wasserman (1991). A relativistic model of pulsar polarization. *The Astrophysical Journal 370*, 643.

Bowman, J. D., I. Cairns, D. L. Kaplan, T. Murphy, D. Oberoi, L. Staveley-Smith, W. Arcus, D. G. Barnes, G. Bernardi, F. H. Briggs, S. Brown, J. D. Bunton, A. J. Burgasser, R. J. Cappallo, S. Chatterjee, B. E. Corey, A. Coster, A. Deshpande, L. DeSouza, D. Emrich, P. Erickson, R. F. Goeke, B. M. Gaensler, L. J. Greenhill, L. Harvey-Smith, B. J. Hazelton, D. Herne, J. N. Hewitt, M. Johnston-Hollitt, J. C. Kasper, B. B. Kincaid, R. Koenig, E. Kratzenberg, C. J. Lonsdale, M. J. Lynch, L. D. Matthews, S. R. McWhirter, D. a. Mitchell, M. F. Morales, E. H. Morgan, S. M. Ord, J. Pathikulangara, T. Prabu, R. a. Remillard, T. Robishaw, A. E. E. Rogers, A. a. Roshi, J. E. Salah, R. J. Sault, N. U. Shankar, K. S. Srivani, J. B. Stevens, R. Subrahmanyan, S. J. Tingay, R. B. Wayth, M. Waterson, R. L. Webster, A. R. Whitney, A. J. Williams, C. L. Williams, and J. S. B. Wyithe (2013). Science with the Murchison Widefield Array. *Publications of the Astronomical Society of Australia 30*, e031.

Brentjens, M. and A. de Bruyn (2005, oct). Faraday rotation measure synthesis. *Astronomy & Astrophysics 441*(3), 1217–1228.

Burn, B. (1966, jan). On the depolarization of discrete radio sources by Faraday dispersion. *Monthly Notices of the Royal Astronomical Society 133*, 67.

Cheng, A. F. and M. A. Ruderman (1977). Bunching mechanism for coherent curvature radiation in pulsar magnetospheres. *Astrophysical Journal 212*, 800–806.

Clark, R. R. and F. G. Smith (1969). Polarization of Radio Pulses from Pulsar CP 0328. *Nature 221*(5182), 724–726.

Cordes, J. (1981). Radio observational constraints on pulsar emission mechanisms. In *Pulsars: 13 Years of Research on Neutron Stars*, Volume 95, pp. 115–131.

Cordes, J. and T. Lazio (2002, jul). NE2001.I. A New Model for the Galactic Distribution of Free Electrons and its Fluctuations. *ArXiv Astrophysics e-prints*.

Cordes, J., A. Pidwerbetsky, and R. Lovelace (1986, nov). Refractive and Diffractive Scattering in the Interstellar Medium. *Astrophysical Journal 310*, 737.

Cordes, J., R. Shannon, and D. Stinebring (2016, jan). Frequency-dependent Dispersion Measures and Implications for Pulsar Timing. *Astrophysical Journal 817*(1), 16.

Cordes, J., J. Weisberg, and T. Hankins (1990, dec). Quasiperiodic Microstructure in Radio Pulsar Emission. *Astronomical Journal 100*, 1882.

Cordes, J. M. (1978). Observational limits on the location of pulsar emission regions. *The Astrophysical Journal 222*, 1006–1011.

Cordes, J. M. (1979). Coherent radio emission from pulsars. *Space Science Reviews 24*(4), 567–600.

Cordes, J. M., J. M. Weisberg, and V. Boriakoff (1985). Small-scale electron density turbulence in the interstellar medium. *The Astrophysical Journal 288*, 221.

Davies, J., A. Lyne, F. Smith, V. Izvekova, A. Kuzmin, and I. P. Shitov (1984, nov). The magnetic field structure of PSR 0809+74. *Monthly Notices of the Royal Astronomical Society 211*, 57–68.

Demorest, P. B. (2011). Cyclic spectral analysis of radio pulsars. *Monthly Notices of the Royal Astronomical Society 416*(4), 2821–2826.

Deshpande, A. A. and J. M. Rankin (1999). Pulsar Magnetospheric Emission Mapping: Images and Implications of Polar Cap Weather. *The Astrophysical Journal 524*(2), 1008–1013.

Deshpande, A. A. and J. M. Rankin (2001). Topology and Polarisation of Subbeams Associated With Pulsar 0943+10's "Drifting"-Subpulse Emission: I. Analysis of Arecibo 430- and 111-MHz Observations. *Monthly Notices of the Royal Astronomical Society 322*(3), 438–460.

Deutsch, A. J. (1955). The electromagnetic field of an idealized star in rigid rotation in vacuo. *Annales d'Astrophysique 18*(1), 1–10.

Drake, F. D. and H. D. Craft (1968). Second Periodic Pulsation in Pulsars. *Nature 220*(5164), 231–235.

Dyks, J. (2008). Altitude-dependent polarization in radio pulsars. *Monthly Notices of the Royal Astronomical Society 391*(2), 859–868.

Dyks, J. and A. K. Harding (2004). Rotational Sweepback of Magnetic Field Lines in Geometric Models of Pulsar Radio Emission. *The Astrophysical Journal 614*(2), 869–880.

Dyks, J., A. K. Harding, and B. Rudak (2004). Relativistic effects and polarization in three high-energy pulsar models. *Astrophysical Journal 606*(2003), 49.

Dyks, J. and B. Rudak (2015, jan). The origin of the frequency-dependent behaviour of pulsar radio profiles. *Monthly Notices of the Royal Astronomical Society 446*(3), 2505–2522.

Dyks, J., B. Rudak, and a. K. Harding (2004). On the methods of determining the radio emission geometry in pulsar magnetospheres. *Astrophysical Journal 607*(2), 939–948.

Dyks, J., G. A. E. Wright, and P. Demorest (2010). Rotational asymmetry of pulsar profiles. *Monthly Notices of the Royal Astronomical Society 405*(1), 509–519.

Edwards, R. T. (2006). Polarised views of the drifting subpulse phenomenon. *Chinese Journal of Astronomy and Astrophysics Supplement 6*, 18–23.

Edwards, R. T., G. B. Hobbs, and R. N. Manchester (2006). TEMPO2, a new pulsar timing package - II. The timing model and precision estimates. *Monthly Notices of the Royal Astronomical Society 372*(4), 1549–1574.

Edwards, R. T. and B. W. Stappers (2002). Drifting sub-pulse analysis using the two-dimensional Fourier transform. *Astronomy and Astrophysics 393*(2), 733–748.

Edwards, R. T. and B. W. Stappers (2003). The frequency-dependence of drifting subpulse patterns. *Astronomy and Astrophysics 410*, 961–966.

Ekers, R. D. and A. T. Moffet (1969). Polarization of Pulsating Radio Sources. *Astrophysical Journal 158*, L1.

Esamdin, A., A. G. Lyne, F. Graham-Smith, M. Kramer, R. N. Manchester, and X. Wu (2005). Mode switching and subpulse drifting in PSR B0826-34. *Monthly Notices of the Royal Astronomical Society 356*(1), 59–65.

Espinoza, C. M., A. G. Lyne, B. W. Stappers, and M. Kramer (2011). A study of 315 glitches in the rotation of 102 pulsars. *Monthly Notices of the Royal Astronomical Society 414*(2), 1679–1704.

Event Horizon Telescope Collaboration, K. Akiyama, A. Alberdi, W. Alef, K. Asada, R. Azulay, A.-K. Baczko, D. Ball, M. Baloković, J. Barrett, D. Bintley, L. Blackburn, W. Boland, K. L. Bouman, G. C. Bower, M. Bremer, C. D. Brinkerink, R. Brissenden, S. Britzen, A. E. Broderick, D. Broguiere, T. Bronzwaer, D.-Y. Byun, J. E. Carlstrom, A. Chael, C.-k. Chan, S. Chatterjee, K. Chatterjee, M.-T. Chen, Y. Chen, I. Cho, P. Christian, J. E. Conway, J. M. Cordes, G. B. Crew, Y. Cui, J. Davelaar, M. De Laurentis, R. Deane, J. Dempsey, G. Desvignes, J. Dexter, S. S. Doeleman, R. P. Eatough, H. Falcke, V. L. Fish, E. Fomalont, R. Fraga-Encinas, W. T. Freeman, P. Friberg, C. M. Fromm, J. L. Gómez, P. Galison, C. F. Gammie, R. Garc\'\ia, O. Gentaz, B. Georgiev, C. Goddi, R. Gold, M. Gu, M. Gurwell, K. Hada, M. H. Hecht, R. Hesper, L. C. Ho, P. Ho, M. Honma, C.-W. L. Huang, L. Huang, D. H. Hughes, S. Ikeda, M. Inoue, S. Issaoun, D. J. James, B. T. Jannuzi, M. Janssen, B. Jeter, W. Jiang, M. D. Johnson, S. Jorstad, T. Jung, M. Karami, R. Karuppusamy, T. Kawashima, G. K. Keating, M. Kettenis, J.-Y. Kim, J. Kim, J. Kim, M. Kino, J. Y. Koay, P. M. Koch, S. Koyama, M. Kramer, C. Kramer, T. P. Krichbaum, C.-Y. Kuo, T. R. Lauer, S.-S. Lee, Y.-R. Li, Z. Li, M. Lindqvist, K. Liu, E. Liuzzo, W.-P. Lo, A. P. Lobanov, L. Loinard, C. Lonsdale, R.-S. Lu, N. R. MacDonald, J. Mao, S. Markoff, D. P. Marrone, A. P. Marscher, I. Mart\'\i-Vidal, S. Matsushita, L. D. Matthews, L. Medeiros, K. M. Menten, Y. Mizuno, I. Mizuno, J. M. Moran, K. Moriyama, M. Moscibrodzka, C. Müller, H. Nagai, N. M. Nagar, M. Nakamura, R. Narayan, G. Narayanan, I. Natarajan, R. Neri, C. Ni, A. Noutsos, H. Okino, H. Olivares, G. N. Ortiz-León, T. Oyama, F. Özel, D. C. Palumbo, N. Patel, U.-L. Pen, D. W. Pesce, V. Piétu, R. Plambeck, A. PopStefanija, O. Porth, B. Prather, J. A. Preciado-López, D. Psaltis, H.-Y. Pu, V. Ramakrishnan, R. Rao, M. G. Rawlings, A. W. Raymond, L. Rez-

zolla, B. Ripperda, F. Roelofs, A. Rogers, E. Ros, M. Rose, A. Roshanineshat, H. Rottmann, A. L. Roy, C. Ruszczyk, B. R. Ryan, K. L. Rygl, S. Sánchez, D. Sánchez-Arguelles, M. Sasada, T. Savolainen, F. P. Schloerb, K.-F. Schuster, L. Shao, Z. Shen, D. Small, B. W. Sohn, J. SooHoo, F. Tazaki, P. Tiede, R. P. Tilanus, M. Titus, K. Toma, P. Torne, T. Trent, S. Trippe, S. Tsuda, I. van Bemmel, H. J. van Langevelde, D. R. van Rossum, J. Wagner, J. Wardle, J. Weintroub, N. Wex, R. Wharton, M. Wielgus, G. N. Wong, Q. Wu, K. Young, A. Young, Z. Younsi, F. Yuan, Y.-F. Yuan, J. A. Zensus, G. Zhao, S.-S. Zhao, Z. Zhu, J.-C. Algaba, A. Allardi, R. Amestica, J. Anczarski, U. Bach, F. K. Baganoff, C. Beaudoin, B. A. Benson, R. Berthold, J. M. Blanchard, R. Blundell, S. Bustamente, R. Cappallo, E. Castillo-Dom\'\inguez, C.-C. Chang, S.-H. Chang, S.-C. Chang, C.-C. Chen, R. Chilson, T. C. Chuter, R. Córdova Rosado, I. M. Coulson, T. M. Crawford, J. Crowley, J. David, M. Derome, M. Dexter, S. Dornbusch, K. A. Dudevoir, S. A. Dzib, A. Eckart, C. Eckert, N. R. Erickson, W. B. Everett, A. Faber, J. R. Farah, V. Fath, T. W. Folkers, D. C. Forbes, R. Freund, A. I. Gómez-Ruiz, D. M. Gale, F. Gao, G. Geertsema, D. A. Graham, C. H. Greer, R. Grosslein, F. Gueth, D. Haggard, N. W. Halverson, C.-C. Han, K.-C. Han, J. Hao, Y. Hasegawa, J. W. Henning, A. Hernández-Gómez, R. Herrero-Illana, S. Heyminck, A. Hirota, J. Hoge, Y.-D. Huang, C. V. Impellizzeri, H. Jiang, A. Kamble, R. Keisler, K. Kimura, Y. Kono, D. Kubo, J. Kuroda, R. Lacasse, R. A. Laing, E. M. Leitch, C.-T. Li, L. C. C. Lin, C.-T. Liu, K.-Y. Liu, L.-M. Lu, R. G. Marson, P. L. Martin-Cocher, K. D. Massingill, C. Matulonis, M. P. McColl, S. R. McWhirter, H. Messias, Z. Meyer-Zhao, D. Michalik, A. Montaña, W. Montgomerie, M. Mora-Klein, D. Muders, A. Nadolski, S. Navarro, J. Neilsen, C. H. Nguyen, H. Nishioka, T. Norton, M. A. Nowak, G. Nystrom, H. Ogawa, P. Oshiro, T. Oyama, H. Parsons, S. N. Paine, J. Peñalver, N. M. Phillips, M. Poirier, N. Pradel, R. A. Primiani, P. A. Raffin, A. S. Rahlin, G. Reiland, C. Risacher, I. Ruiz, A. F. Sáez-Mada\'\in, R. Sassella, P. Schellart, P. Shaw, K. M. Silva,

H. Shiokawa, D. R. Smith, W. Snow, K. Souccar, D. Sousa, T. Sridharan, R. Srinivasan, W. Stahm, A. A. Stark, K. Story, S. T. Timmer, L. Vertatschitsch, C. Walther, T.-S. Wei, N. Whitehorn, A. R. Whitney, D. P. Woody, J. G. Wouterloot, M. Wright, P. Yamaguchi, C.-Y. Yu, M. Zeballos, S. Zhang, and L. Ziurys (2019, apr). First M87 Event Horizon Telescope Results. I. The Shadow of the Supermassive Black Hole. *Astrophysical Journal Letters 875*(1), L1.

Fung, P. K., D. Khechinashvili, and J. Kuijpers (2006). Radio pulsar drifting sub-pulses and diocotron instability. *Astronomy & Astrophysics 445*(3), 779–794.

Gajjar, V., B. C. Joshi, M. Kramer, R. Karuppusamy, and R. Smits (2014). Frequency Independent Quenching of Pulsed Emission. *The Astrophysical Journal 797*(1), 18.

Gangadhara, R. T. (2004). Pulsar Radio Emission Altitude from Curvature Radiation. *Astrophysical Journal 609*(1), 335–339.

Gangadhara, R. T. and Y. Gupta (2001). Understanding the Radio Emission Geometry of PSR B0329+54. *The Astrophysical Journal 555*(1), 31–39.

Gil, J., G. I. Melikidze, and U. Geppert (2003). Drifting subpulses and inner acceleration regions in radio pulsars. *Astronomy & Astrophysics 407*, 315–324.

Gil, J. and M. Sendyk (2000, sep). Spark Model for Pulsar Radiation Modulation Patterns. *Astrophysical Journal 541*(1), 351–366.

Ginzburg, V. L. and V. V. Zhelezniakov (1975). On the pulsar emission mechanisms. *Annual review of astronomy and astrophysics 13*, 511–535.

Gold, T. (1968, may). Rotating Neutron Stars as the Origin of the Pulsating Radio Sources. *Nature 218*, 731–732.

Gold, T. (1969). Rotating Neutron Stars and the Nature of Pulsars. *Nature 221*, 25–27.

Goldreich, P. and W. H. Julian (1969). Pulsar Electrodynamics. *The Astrophysical Journal 157*, 869.

Gould, D. M. and a. G. Lyne (1998). Multifrequency polarimetry of 300 radio pulsars. *Monthly Notices of the Royal Astronomical Society 301*(1), 235–260.

Gupta, Y., B. Ajithkumar, H. S. Kale, S. Nayak, S. Sabhapathy, S. Sureshkumar, R. V. Swami, J. Chengalur, S. K. Ghosh, C. H. Ishwara-Chandra, B. Joshi, N. Kanekar, D. Lal, and S. Roy (2017). The upgraded GMRT: Opening new windows on the radio Universe. *Current Science 113*, 707–714.

Gupta, Y. and R. T. Gangadhara (2003). Understanding the Radio Emission Geometry of Multiple-Component Radio Pulsars from Retardation and Aberration Effects. *Astrophysical Journal 584*, 418–426.

Gupta, Y., J. Gil, J. Kijak, and M. Sendyk (2004). Unraveling the drift behaviour of the remarkable pulsar PSR B0826-34. *Astronomy and Astrophysics 426*, 229–245.

Gupta, Y., P. Gothoskar, B. Joshi, M. Vivekanand, R. Swain, S. Sirothia, and N. Bhat (2000). Pulsar Research with the GMRT: A Status Report. In M. Kramer, N. Wex, and R. Wielebinski (Eds.), *IAU Colloq. 177: Pulsar Astronomy - 2000 and Beyond*, Volume 202 of *Astronomical Society of the Pacific Conference Series*, pp. 277.

Hankins, T., J. Eilek, and G. Jones (2016, dec). The Crab Pulsar at Centimeter Wavelengths. II. Single Pulses. *Astrophysical Journal 833*, 47.

Hankins, T. and B. Rickett (1975). Pulsar signal processing. In B. Alder, S. Fernbach, and M. Rotenberg (Eds.), *Methods in Computational Physics. Volume 14 - Radio astronomy*, Volume 14, pp. 55–129.

Hankins, T. H., J. S. Kern, J. C. Weatherall, and J. a. Eilek (2003). Nanosecond Radio Bursts From Strong Plasma Turbulence In The Crab Pulsar. *Nature 422*, 141–144.

Hassall, T. E., B. W. Stappers, P. Weltevrede, J. W. T. Hessels, A. Alexov, T. Coenen, A. Karastergiou, M. Kramer, E. F. Keane, V. I. Kondratiev, J. V. Leeuwen, A. Noutsos, M. Pilia, J. van Leeuwen, M. Serylak, C. Sobey, K. Zagkouris, R. Fender, M. E. Bell, J. Broderick, J. Eislöffel, H. Falcke, J.-M. Grießmeier, M. Kuniyoshi, J. C. A. Miller-Jones, M. W. Wise, O. Wucknitz, P. Zarka, A. Asgekar, F. Batejat, M. J. Bentum, G. Bernardi, P. Best, A. Bonafede, F. Breitling, M. Brüggen, H. R. Butcher, B. Ciardi, F. de Gasperin, J.-P. de Reijer, S. Duscha, R. A. Fallows, C. Ferrari, W. Frieswijk, M. A. Garrett, A. W. Gunst, G. Heald, M. Hoeft, E. Juette, P. Maat, J. P. McKean, M. J. Norden, M. Pandey-Pommier, R. Pizzo, A. G. Polatidis, W. Reich, H. Röttgering, J. Sluman, Y. Tang, C. Tasse, R. Vermeulen, R. J. van Weeren, S. J. Wijnholds, and S. Yatawatta (2013). Differential frequency-dependent delay from the pulsar magnetosphere. *Astronomy & Astrophysics 552*(20764), A61.

Hewish, A., S. J. Bell, J. D. H. Pilkington, P. F. Scott, and R. A. Collins (1968). Observation of a Rapidly Pulsating Radio Source. *Nature 217*(5130), 709–713.

Hobbs, G., A. G. Lyne, M. Kramer, C. E. Martin, and C. Jordan (2004). *Long-term timing observations of 374 pulsars*, Volume 353.

Hobbs, G. B., R. T. Edwards, and R. N. Manchester (2006). TEMPO2, a new pulsar-timing package - I. An overview. *Monthly Notices of the Royal Astronomical Society 369*(2), 655–672.

Hotan, a. W., W. Van Straten, and R. N. Manchester (2004). PSRCHIVE and PSRFITS: An open approach to radio pulsar data storage and analysis. *Publications of the Astronomical Society of Australia 21*(3), 302–309.

Huguenin, G. R., J. H. Taylor, and T. H. Troland (1970). The Radio Emission from Pulsar MP 0031-07. *Astrophysical Journal 162*, 727–735.

Izvekova, V. A., A. D. Kuzmin, A. G. Lyne, Y. P. Shitov, and F. G. Smith (1993). Frequency dependence of characteristics of pulsars PSR 0031-07, 0320+39, 1133+16 and 2016+28. *Monthly Notices of the Royal Astronomical Society 261*, 865–872.

Jackson, J. D. (1975). *Classical Electrodynamics*. Wiley Eastern Limited.

Jankowski, F., W. van Straten, E. Keane, M. Bailes, E. Barr, S. Johnston, and M. Kerr (2018, feb). Spectral properties of 441 radio pulsars. *mnras 473*(4), 4436–4458.

Jessner, A., A. Słowikowska, B. Klein, H. Lesch, C. H. Jaroschek, G. Kanbach, and T. H. Hankins (2005). Giant radio pulses from the Crab pulsar. *Advances in Space Research 35*(6), 1166–1171.

Joshi, B. C. and M. Vivekanand (2000). A study of subpulse phase correlation across nulls in PSR B0031-07. *Monthly Notices of the Royal Astronomical Society 316*, 716–720.

Karuppusamy, R., B. W. Stappers, and M. Serylak (2011). A low frequency study of PSRs B1133+16 , B1112+50 , and B0031-07. *Astronomy and Astrophysics 525*, A55.

Kaur, D., N. Bhat, S. Tremblay, R. Shannon, S. McSweeney, S. Ord, A. Beardsley, B. Crosse, D. Emrich, T. Franzen, L. Horsley, M. Johnston-Hollitt, D. Kaplan, D. Kenney, M. Morales, D. Pallot, K. Steele, S. Tingay, C. Trott, M. Walker, R. Wayth1, A. Williams, and C. Wu (2019, jul). A high time resolution study of the millisecond pulsar J2241-5236 at frequencies below 300 MHz. *arXiv e-prints*, arXiv:1907.08916.

Kellermann, K. I. and I. I. K. Pauliny-Toth (1969). The Spectra of Opaque Radio Sources. *The Astrophysical Journal 155*, L71.

Kloumann, I. M. and J. M. Rankin (2010). On the long and short nulls, modes and interpulse emission of radio pulsar B1944+17. *Monthly Notices of the Royal Astronomical Society 408*(1), 40–52.

Komesaroff, M. M. (1970). Possible Mechanism for the Pulsar Radio Emission. *Nature 225*(5233), 612–614.

Kuzmin, A. D. and A. A. Ershov (2004). Giant pulses in pulsar PSR B0031-07. *Astronomy and Astrophysics 427*(2), 575–579.

Lange, C., M. Kramer, R. Wielebinski, and A. Jessner (1998). Radio pulsar microstructure at 1.41 and 4.85 GHz. *Astronomy and Astrophysics 332*, 111–120.

Lorimer, D. R. and M. Kramer (2005). *Handbook of Pulsar Astronomy*. Cambridge Observing Handbooks for Research Astronomers. Cambridge University Press.

Luo, Q. (1993). Coherent Curvature Emission in Pulsar Magnetospheres - Non-Dipolar Geometric Effects. In *Proceedings of the Astronomical Society of Australia, Vol. 10, Issue 3*, pp. 258.

Luo, Q. (1998). Plasma processes in pulsar magnetospheres and eclipsing binary pulsar systems. *Brazilian Journal of Physics 28*(3), 191–202.

Luo, Q. and D. B. Melrose (1992). Coherent curvature emission and radio pulsars. *Monthly Notices of the Royal Astronomical Society 258*(3), 616–620.

Luo, Q. and D. B. Melrose (1995). Curvature maser emission due to field line torsion in pulsar magnetospheres. *Monthly Notices of the Royal Astronomical Society 276*, 372–382.

Lyne, A. G. and M. Ashworth (1983). The effects of nulls upon subpulse drift in PSRs 0809+74 and 0818-13. *Monthly Notices of the Royal Astronomical Society 204*, 519–536.

Lyne, A. G. and F. G. Smith (1968). Linear Polarization in Pulsating Radio Sources. *Nature 218*(5137), 124–126.

Maan, Y. and A. A. Deshpande (2014). Inter-Relationship Between the Two Emission Cones of B1237+25. *The Astrophysical Journal 792*(2), 130.

Maan, Y., A. A. Deshpande, V. Chandrashekar, J. Chennamangalam, K. B. R. Rao, R. Somashekar, G. Anderson, M. S. Ezhilarasi, S. Sujatha, S. Kasturi, P. Sandhya, J. Bauserman, R. Duraichelvan, S. Amiri, H. A. Aswathappa, I. V. Barve, G. Sarabagopalan, H. M. Ananda, C. Beaudet, M. Bloss, D. B. Dhamnekar, D. Egan, J. Ford, S. Krishnamurthy, N. Mehta, A. H. Minter, H. N. Nagaraja, M. Narayanaswamy, K. O'Neil, W. Raja, H. Sahasrabudhe, A. Shelton, K. S. Srivani, H. V. Venugopal, and S. T. Viswanathan (2013). RRI-GBT Multi-band Receiver: Motivation, Design, and Development. *The Astrophysical Journal Supplement Series 204*(1), 12.

Manchester, R., G. Hobbs, A. Teoh, and M. Hobbs (2005, apr). The Australia Telescope National Facility Pulsar Catalogue. *Astronomical Journal 129*, 1993–2006.

Manchester, R. N., J. H. Taylor, and G. R. Huguenin (1975). Observations of pulsar radio emission. II - Polarization of individual pulses. *The Astrophysical Journal 196*, 83.

McSweeney, S. J., N. D. R. Bhat, S. E. Tremblay, and A. A. Deshpande (2017). Phase shifts in multi-frequency observations of the drift bands of J0034-0721. *Proceedings of the International Astronomical Union 13*(S337), 376–377.

McSweeney, S. J., N. D. R. Bhat, S. E. Tremblay, A. A. Deshpande, and S. M. Ord

(2017). Low Frequency Observations of the Subpulse Drifter PSR J0034-0721 with the MWA. *The Astrophysical Journal 836*(2), 224.

McSweeney, S. J., N. D. R. Bhat, S. E. Tremblay, A. A. Deshpande, and G. Wright (2019). On the Geometry of Curvature Radiation and Implications for Subpulse Drifting. *The Astrophysical Journal 870*(1), 48.

McSweeney, S. J., N. D. R. Bhat, G. Wright, S. E. Tremblay, and S. Kudale (2019). The frequency-dependent behaviour of subpulse drifting: I. Carousel geometry and emission heights of PSR B0031-07. *Astrophysical Journal (accepted)*.

Melrose, D. B. (1979). Propagation effect on polarization of pulsar radio emission. *Australian Journal of Physics 32*, 61.

Melrose, D. B. (1992). Coherent Radio Emission from Pulsars. *Phil. Trans. R. Soc. Lond. 341*, 105–115.

Melrose, D. B. (2017). Coherent Emission Mechanisms in Astrophysical Plasmas. *Reviews of Modern Plasma Physics 1*, 5.

Melrose, D. B. and R. Yuen (2016). Pulsar electrodynamics: an unsolved problem. *Journal of Plasma Physics 82*(2), 635820202.

Meyers, B. W., S. E. Tremblay, N. D. R. Bhat, R. M. Shannon, F. Kirsten, M. Sokolowski, S. J. Tingay, S. I. Oronsaye, and S. M. Ord (2017). Spectral Flattening at Low Frequencies in Crab Giant Pulses. *ApJ, accepted*.

Michel, F. C. (1991). *Theory of Neutron Star Magnetospheres*. Chicago : University of Chicago Press.

Mitchell, D. A., L. J. Greenhill, R. B. Wayth, R. J. Sault, C. J. Lonsdale, R. J. Cappallo, M. F. Morales, and S. M. Ord (2008). Real-time calibration of the Murchison Widefield Array. *IEEE Journal on Selected Topics in Signal Processing 2*(5), 707–717.

Mitra, D., R. Basu, K. Maciesiak, A. Skrzypczak, G. I. Melikidze, A. Szary, and K. Krzeszowski (2016). Meterwavelength Single-Pulse Polarimetric Emission Survey. *The Astrophysical Journal 833*(1), 28.

Mitra, D. and J. M. Rankin (2008). On the Subpulse Modulation, Polarization and Subbeam Carousel Configuration of Pulsar B1857-26. *Monthly Notices of the Royal Astronomical Society 385*(2), 606–613.

Nizamdin, B., A. Esamdin, Z.-Y. Liu, N. Wang, and C.-S. Zhao (2011). An Observational Study of the Strong Single Pulses of PSR J0034-0721. *Chinese Astronomy and Astrophysics 35*(1), 37–47.

Noutsos, A., C. Sobey, V. I. Kondratiev, P. Weltevrede, J. P. W. Verbiest, A. Karastergiou, M. Kramer, M. Kuniyoshi, A. Alexov, R. P. Breton, A. V. Bilous, S. Cooper, H. Falcke, J. M. Grießmeier, T. E. Hassall, J. W. T. Hessels, E. F. Keane, S. Oslowski, M. Pilia, M. Serylak, B. W. Stappers, S. ter Veen, J. van Leeuwen, K. Zagkouris, K. Anderson, L. Bähren, M. Bell, J. Broderick, D. Carbone, Y. Cendes, T. Coenen, S. Corbel, J. Eislöffel, R. Fender, H. Garsden, P. Jonker, C. Law, S. Marko, J. Masters, J. Miller-Jones, G. Molenaar, R. Osten, M. Pietka, E. Rol, A. Rowlinson, B. Scheers, H. Spreeuw, T. Staley, A. Stewart, J. Swinbank, R. Wijers, R. Wijnands, M. Wise, P. Zarka, and A. van der Horst (2015). Pulsar polarisation below 200 MHz: Average profiles and propagation effects. *Astronomy & Astrophysics 576*, A62.

Ord, S. M., S. E. Tremblay, S. J. McSweeney, N. D. R. Bhat, C. Sobey, D. A. Mitchell, P. J. Hancock, and F. Kirsten (2019). MWA tied-array processing I: Calibration and beamformation. *Publications of the Astronomical Society of Australia 36*, e030.

Oronsaye, S. I., S. M. Ord, N. D. R. Bhat, S. E. Tremblay, S. J. McSweeney, S. J. Tingay, W. van Straten, A. Jameson, G. Bernardi, F. Briggs, R. J. Cappallo, A. A. Deshpande, L. J. Greenhill, B. J. Hazelton, M. Johnston-Hollitt,

D. L. Kaplan, C. J. Lonsdale, S. R. McWhirter, D. A. Mitchell, M. F. Morales, E. Morgan, D. Oberoi, T. Prabu, N. U. Shankar, K. S. Srivani, R. Subrahmanyan, R. B. Wayth, R. L. Webster, A. Williams, and C. L. Williams (2015). Simultaneous Observations of Giant Pulses From the Crab Pulsar, With the Murchison Widefield Array and Parkes Radio Telescope: Implications for the Giant Pulse Emission Mechanism. *The Astrophysical Journal 809*(1), 51.

Ostriker, J. P. and J. E. Gunn (1969). On the Nature of Pulsars. I. Theory. *ApJ 157*, 1395.

Pilia, M., J. W. T. Hessels, B. W. Stappers, V. I. Kondratiev, M. Kramer, J. van Leeuwen, P. Weltevrede, a. G. Lyne, K. Zagkouris, T. E. Hassall, a. V. Bilous, R. P. Breton, H. Falcke, J.-M. Grießmeier, E. Keane, A. Karastergiou, M. Kuniyoshi, A. Noutsos, S. Osłowski, M. Serylak, C. Sobey, S. ter Veen, A. Alexov, J. Anderson, A. Asgekar, I. M. Avruch, M. E. Bell, M. J. Bentum, G. Bernardi, L. Bîrzan, A. Bonafede, F. Breitling, J. W. Broderick, M. Brüggen, B. Ciardi, S. Corbel, E. de Geus, A. de Jong, A. Deller, S. Duscha, J. Eislöffel, R. a. Fallows, R. Fender, C. Ferrari, W. Frieswijk, M. a. Garrett, a. W. Gunst, J. P. Hamaker, G. Heald, A. Horneffer, P. Jonker, E. Juette, G. Kuper, P. Maat, G. Mann, S. Markoff, R. McFadden, D. McKay-Bukowski, J. C. a. Miller-Jones, A. Nelles, H. Paas, M. Pandey-Pommier, M. Pietka, R. Pizzo, a. G. Polatidis, W. Reich, H. Röttgering, A. Rowlinson, D. Schwarz, O. Smirnov, M. Steinmetz, A. Stewart, J. D. Swinbank, M. Tagger, Y. Tang, C. Tasse, S. Thoudam, M. C. Toribio, a. J. van der Horst, R. Vermeulen, C. Vocks, R. J. van Weeren, R. a. M. J. Wijers, R. Wijnands, S. J. Wijnholds, O. Wucknitz, and P. Zarka (2016). Wide-band, low-frequency pulse profiles of 100 radio pulsars with LOFAR. *Astronomy & Astrophysics 586*, A92.

Qiao, G. J., K. J. Lee, B. Zhang, R. X. Xu, and H. G. Wang (2004). A Model for the Challenging "Bi-drifting" Phenomenon in PSR J0815+09. *Astrophysical Journal 616*, L127–L130.

Radhakrishnan, V. and D. J. Cooke (1969). Magnetic Poles and the Polarization Structure of Pulsar Radiation. *Astrophysical Letters 3*, 225.

Radhakrishnan, V. and A. Deshpande (2001, nov). Vela, its X-ray nebula, and the polarization of pulsar radiation. *Astronomy & Astrophysics 379*, 551–556.

Ramachandran, R., J. M. Rankin, B. W. Stappers, M. L. A. Kouwenhoven, and A. G. J. van Leeuwen (2002). Pulsar "drifting"-subpulse polarization: No evidence for systematic polarization-angle rotations. *Astronomy & Astrophysics 381*, 993–999.

Rankin, J. M. (1983). Toward an Empirical Theory of Pulsar Emission - I. Morphological Taxonomy. *The Astrophysical Journal 274*, 333–358.

Rankin, J. M. (1986). Toward an empirical theory of pulsar emission. III - Mode changing, drifting subpulses, and pulse nulling. *The Astrophysical Journal 301*, 901.

Rankin, J. M. (1993, mar). Toward an Empirical Theory of Pulsar Emission. VI. The Geometry of the Conal Emission Region. *Astrophysical Journal 405*, 285.

Rankin, J. M. (2017). Nulling, Mode-Changing and Drifting Subpulses in the Highly Asymmetric Conal Quadruple Radio Pulsar B2034+19. *Journal of Astrophysics and Astronomy 38*(3), 53.

Rankin, J. M., R. Ramachandran, and S. A. Suleymanova (2005). PSR B0809 + 74 : Understanding its perplexing subpulse-separation (P 2) variations. *Astronomy and Astrophysics 429*, 999–1006.

Rankin, J. M., R. Ramachandran, and S. A. Suleymanova (2006). Phenomenology of pulsar B0809+74's rotating subbeam system I. Geometry and profile "absorption". *Astronomy & Astrophysics 447*, 235–243.

Rankin, J. M., R. Ramachandran, J. van Leeuwen, and S. A. Suleymanova (2006). Phenomenology of pulsar B0809+74's rotating subbeam system. II. "Carousel" configuration and polarization. *Astronomy and Astrophysics 455*, 215–221.

Rankin, J. M., G. A. E. Wright, and A. M. Brown (2013). Drifting, moding and nulling: Another look at pulsar B1918+19. *Monthly Notices of the Royal Astronomical Society 433*(1), 445–456.

Ransom, S. (2001). *New search techniques for binary pulsars*. Ph. D. thesis, Harvard University.

Reddy, S. H., S. Kudale, U. Gokhale, I. Halagalli, N. Raskar, K. De, S. Gnanaraj, B. Ajith Kumar, and Y. Gupta (2017). A Wideband Digital Back-End for the Upgraded GMRT. *Journal of Astronomical Instrumentation 06*(01), 1641011.

Redman, S. L., G. A. E. Wright, and J. M. Rankin (2005). Pulsar PSR B2303+30: a single system of drifting subpulses, moding and nulling. *Monthly Notices RAS 357*(3), 859–872.

Ritchings, R. T. (1976). Pulsar single pulse intensity measurements and pulse nulling. *Monthly Notices of the Royal Astronomical Society 176*(Aug), 249–263.

Romani, R., R. Narayan, and R. Blandford (1986, may). Refractive effects in pulsar scintillation. *Monthly Notices of the Royal Astronomical Society 220*, 19–49.

Rosen, R., M. McLaughlin, and S. Thompson (2011, feb). A Non-radial Oscillation Model for Pulsar State Switching. *The Astrophysical Journal 728*(1), L19.

Roy, J., Y. Gupta, U.-L. Pen, J. B. Peterson, S. Kudale, and J. Kodilkar (2010, aug). A real-time software backend for the GMRT. *Experimental Astronomy 28*(1), 25–60.

Ruderman, M. A. and P. G. Sutherland (1975). Theory of pulsars - Polar caps, sparks, and coherent microwave radiation. *The Astrophysical Journal 196*, 51–72.

Savitzky, A. and M. J. E. Golay (1964). Smoothing and Differentiation of Data by Simplified Least Squares Procedures. *Analytical Chemistry 36*(8), 1627–1639.

Serylak, M., B. W. Stappers, and P. Weltevrede (2009). S2DFS: Analysis of temporal changes of drifting subpulses. *Astronomy and Astrophysics 506*(2), 865–874.

Shitov, Y. P. (1983). Period dependence of the spectrum and the phenomenon of twisting of the magnetic fields of pulsars. *Soviet Astronomy 27*(3), 314.

Smirnova, T. V., V. I. Shishov, M. V. Popov, C. R. Gwinn, J. M. Anderson, A. S. Andrianov, N. Bartel, A. Deller, M. D. Johnson, B. C. Joshi, N. S. Kardashev, R. Karuppusamy, Y. Y. Kovalev, M. Kramer, V. A. Soglasnov, J. A. Zensus, and V. I. Zhuravlev (2014). RADIOASTRON studies of the nearby, turbulent interstellar plasma with the longest space-ground interferometer baseline. *The Astrophysical Journal 786*(2), 115.

Smits, J. M., D. Mitra, and J. Kuijpers (2005). Frequency dependence of the drifting subpulses of PSR B0031-07. *Astronomy and Astrophysics 440*, 683–692.

Smits, J. M., D. Mitra, B. W. Stappers, J. Kuijpers, P. Weltevrede, A. Jessner, and Y. Gupta (2007). The Geometry of PSR B0031-07. *Astronomy and Astrophysics 465*, 575–586.

Sturrock, P. A. (1971). A Model of Pulsars. *The Astrophysical Journal 164*, 529.

Suleimanova, S. A. and V. D. Pugachev (2002). Polarization of individual pulses of radio pulsars at the low frequencies 40, 60, and 103 MHz. *Astronomy Reports 46*(4), 309–326.

Sutton, J., D. Staelin, R. Price, and R. Weimer (1970, feb). Three Pulsars with Marching Subpulses. *Astrophysical Journal Letters 159*, L89–L94.

Swarup, G., S. Ananthakrishnan, V. Kapahi, A. Rao, C. Subrahmanya, and V. Kulkarni (1991, jan). The Giant Metre-Wave Radio Telescope. *Current Science 60*, 95.

Tan, C. M., C. G. Bassa, S. Cooper, T. J. Dijkema, P. Esposito, J. W. T. Hessels, V. I. Kondratiev, M. Kramer, D. Michilli, S. Sanidas, T. W. Shimwell, B. W. Stappers, J. van Leeuwen, I. Cognard, J.-M. Grießmeier, A. Karastergiou, E. F. Keane, C. Sobey, and P. Weltevrede (2018, oct). LOFAR Discovery of a 23.5 s Radio Pulsar. *The Astrophysical Journal 866*(1), 54.

Taylor, J. H., G. R. Huguenin, R. M. Hirsch, and R. N. Manchester (1971). Polarization of the Drifting Subpulses of Pulsar 0809+74. *ApJL 9*, 205–208.

Taylor, J. H., R. N. Manchester, and G. R. Huguenin (1975). Observations of pulsar radio emission. I - Total-intensity measurements of individual pulses. *The Astrophysical Journal 195*, 513.

Ternov, I. M. (1995, apr). Synchrotron radiation. *Physics-Uspekhi 38*(4), 409–434.

Thomas, R. M. C. and R. T. Gangadhara (2007). Dynamics of charged particles in the radio emission region of pulsar magnetosphere. *Astronomy and Astrophysics 467*, 911–918.

Thomas, R. M. C., Y. Gupta, and R. T. Gangadhara (2010). Understanding the effects of geometry and rotation on pulsar intensity profiles. *Monthly Notices of the Royal Astronomical Society 406*(2), 1029–1048.

Thorsett, S. E. (1992). Radius-to-Frequency Mapping in the Radio Pulsar Emission Mechanism. *International Astronomical Union Colloquium 128*, 143–146.

Tingay, S. J., R. Goeke, J. D. Bowman, D. Emrich, S. M. Ord, D. A. Mitchell, M. F. Morales, T. Booler, B. Crosse, R. B. Wayth, C. J. Lonsdale, S. Tremblay, D. Pallot, T. Colegate, A. Wicenec, N. Kudryavtseva, W. Arcus, D. Barnes, G. Bernardi, F. Briggs, S. Burns, J. D. Bunton, R. J. Cappallo, B. E. Corey, A. Deshpande, L. DeSouza, B. M. Gaensler, L. J. Greenhill, P. J. Hall, B. J. Hazelton, D. Herne, J. N. Hewitt, M. Johnston-Hollitt, D. L. Kaplan, J. C. Kasper, B. B. Kincaid, R. Koenig, E. Kratzenberg, M. J. Lynch, B. McKinley, S. R. McWhirter, E. Morgan, D. Oberoi, J. Pathikulangara, T. Prabu, R. A. Remillard, A. E. E. Rogers, A. Roshi, J. E. Salah, R. J. Sault, N. Udaya-Shankar, F. Schlagenhaufer, K. S. Srivani, J. Stevens, R. Subrahmanyan, M. Waterson, R. L. Webster, A. R. Whitney, A. Williams, C. L. Williams, and J. S. B. Wyithe (2013). The Murchison Widefield Array: The Square Kilometre Array Precursor at Low Radio Frequencies. *Publications of the Astronomical Society of Australia 30*, 7.

Tremblay, S. E., S. M. Ord, N. D. R. Bhat, S. J. Tingay, B. Crosse, D. Pallot, S. I. Oronsaye, G. Bernardi, J. D. Bowman, F. Briggs, R. J. Cappallo, B. E. Corey, A. A. Deshpande, D. Emrich, R. Goeke, L. J. Greenhill, B. J. Hazelton, M. Johnston-Hollitt, D. L. Kaplan, J. C. Kasper, E. Kratzenberg, C. J. Lonsdale, M. J. Lynch, S. R. McWhirter, D. A. Mitchell, M. F. Morales, E. Morgan, D. Oberoi, T. Prabu, A. E. E. Rogers, A. Roshi, N. Udaya Shankar, K. S. Srivani, R. Subrahmanyan, M. Waterson, R. B. Wayth, R. L. Webster, A. R. Whitney, A. Williams, and C. L. Williams (2015, jan). The High Time and Frequency Resolution Capabilities of the Murchison Widefield Array. *Publications of the Astronomical Society of Australia 32*(2015), e005.

Tuoheti, A., A. Esamdin, H.-d. Hu, G.-L. Lu, N. Wang, and M. Abliz (2011). Strong pulses from pulsar PSR J0034-0721. *Research in Astronomical Astrophysics 11*(8), 974–980.

van Leeuwen, A., M. Kouwenhoven, R. Ramachand ran, J. Rankin, and B. Stap-

pers (2002, may). Null-induced mode changes in PSR B0809+74. *Astronomy and Astrophysics 387*, 169–178.

van Leeuwen, A. G. J., B. W. Stappers, R. Ramachandran, and J. M. Rankin (2003). Probing drifting and nulling mechanisms through their interaction in PSR B0809+74. *Astronomy and Astrophysics 399*, 223–229.

van Leeuwen, J. and A. N. Timokhin (2012, jun). On Plasma Rotation and Drifting Subpulses in Pulsars: Using Aligned Pulsar B0826-34 as a Voltmeter. *The Astrophysical Journal 752*(2), 155.

van Straten, W. and M. Bailes (2011). DSPSR: Digital signal processing software for pulsar astronomy. *Publications of the Astronomical Society of Australia 28*(1), 1–14.

van Straten, W., P. Demorest, J. Khoo, M. Keith, A. Hotan, and et Al. (2011). PSRCHIVE: Development Library for the Analysis of Pulsar Astronomical Data.

van Straten, W., P. Demorest, and S. Osłowski (2012). Pulsar data analysis with PSRCHIVE. *arXiv preprint arXiv:1205.6276*, 21.

van Straten, W., R. N. Manchester, S. Johnston, and J. Reynolds (2009a). PSRCHIVE and PSRFITS: Definition of the Stokes Parameters and Instrumental Basis Conventions. *Publications of the Astronomical Society of Australia 2822*, 7.

van Straten, W., R. N. Manchester, S. Johnston, and J. Reynolds (2009b). PSRCHIVE and PSRFITS: Definition of the Stokes Parameters and Instrumental Basis Conventions. (1966), 1–7.

Vivekanand, M. (1995). Observation of nulling in radio pulsars with the Ooty Radio Telescope. *Monthly Notices of the Royal Astronomical Society 274*, 785–792.

Vivekanand, M. and B. C. Joshi (1996). The Drifting Behavior of PSR B0031-07. *The Astrophysical Journal 477*(1), 431–438.

Walker, M. a., P. B. Demorest, and W. Van Straten (2013). Cyclic spectroscopy of the millisecond pulsar, B1937+21. *Astrophysical Journal 779*(2).

Wang, H.-G., J.-L. Chen, Z.-G. Wen, and F.-P. Pi (2012). On the mode switching timescales of pulsar PSR B0329+54. *Proceedings of the International Astronomical Union 8*(S291), 549–551.

Wang, N., R. N. Manchester, and S. Johnston (2007). Pulsar nulling and mode changing. *Monthly Notices of the Royal Astronomical Society 377*(3), 1383–1392.

Wayth, R. B., S. J. Tingay, C. M. Trott, D. Emrich, M. Johnston-Hollitt, B. McKinley, B. Gaensler, A. Beardsley, T. Booler, B. Crosse, T. Franzen, L. Horsley, D. Kaplan, D. Kenney, M. Morales, D. Pallot, G. Sleap, K. Steele, M. Walker, A. Williams, C. Wu, I. H. Cairns, M. Filipovic, S. Johnston, T. Murphy, P. Quinn, L. Staveley-Smith, R. Webster, and J. Wyithe (2018, nov). The Phase II Murchison Widefield Array: Design overview. *PASA 35*, 33.

Weltevrede, P., R. T. Edwards, and B. W. Stappers (2006). The subpulse modulation properties of pulsars at 21 cm. *Astronomy and Astrophysics 445*(1), 243–272.

Weltevrede, P., B. W. Stappers, and R. T. Edwards (2007). The subpulse modulation properties of pulsars at 92 cm and the frequency dependence of subpulse modulation. *Astronomy and Astrophysics 469*(2), 607–631.

Whitney, A., M. Kettenis, C. Phillips, and M. Sekido (2009). VLBI Data Interchange Format (VDIF). In *8th International e-VLBI Workshop*.

Wolszczan, A., N. Bartel, and W. Sieber (1981, jul). Frequency dependence of the P2 and P3 periods in four pulsars. *Astronomy and Astrophysics 100*, 91–96.

Wright, G. and P. Weltevrede (2017). Pulsar bi-drifting: implications for polar cap geometry. *Monthly Notices of the Royal Astronomical Society 464*(3), 2597–2608.

Wright, G. A. E. and L. A. Fowler (1981). PSR 0031–07: The Harmonic Pulsar. *Symposium - International Astronomical Union 95*, 211–212.

Xilouris, K., M. Kramer, A. Jessner, A. von Hoensbroech, D. Lorimer, R. Wielebinski, A. Wolszczan, and F. Camilo (1998, jul). The Characteristics of Millisecond Pulsar Emission. II. Polarimetry. *The Astrophysical Journal 501*(1), 286.

Xue, M., S. M. Ord, S. E. Tremblay, N. D. R. Bhat, C. Sobey, B. W. Meyers, S. J. McSweeney, and N. A. Swainston (2019). MWA tied-array processing II: Polarimetric verification and analysis of two bright southern pulsars. *Publications of the Astronomical Society of Australia 36*, e025.

Yao, J. M., R. N. Manchester, and N. Wang (2017). A New Electron-Density Model for Estimation of Pulsar and FRB Distances. *The Astrophysical Journal 835*(1), 1–32.

Yuen, R. and D. B. Melrose (2014). Visibility of pulsar emission: motion of the visible point. *Publications of the Astronomical Society of Australia 31*, e039.

Yuen, R., D. B. Melrose, M. A. Samsuddin, Z. Y. Tu, and X. H. Han (2016). Variations of P_2 in subpulse drifting pulsars. *Monthly Notices of the Royal Astronomical Society 459*(1), 603–609.

Zhang, L., D. Li, G. Hobbs, C. H. Agar, R. N. Manchester, P. Weltevrede, W. A. Coles, P. Wang, W. Zhu, Z. Wen, J. Yuan, A. D. Cameron, S. Dai, K. Liu, Q. Zhi, C. Miao, M. Yuan, S. Cao, L. Feng, H. Gan, L. Gao, X. Gu, M. Guo, Q. Hao, L. Huang, P. Jiang, C. Jin, H. Li, Q. Li, Q. Li, H. Liu, G. Pan, Z. Pan, B. Peng, H. Qian, L. Qian, X. Shi, J. Song, L. Song, C. Sun, J. Sun,

H. Wang, Q. Wang, Y. Wang, X. Xie, J. Yan, L. Yang, S. Yang, R. Yao, D. Yu, J. Yu, Y. Yue, C. Zhang, H. Zhang, S. Zhang, X. Zheng, A. Zhou, B. Zhu, L. Zhu, M. Zhu, W. Zhu, and Y. Zhu (2019, may). PSR J1926-0652: A Pulsar with Interesting Emission Properties Discovered at FAST. *The Astrophysical Journal 877*(1), 55.

Zwicky, F. (1939, apr). On the Theory and Observation of Highly Collapsed Stars. *Physical Review 55*(8), 726–743.

Index